NATURAL GAS HYDRATES – ISSUES FOR GAS PRODUCTION AND GEOMECHANICAL STABILITY

A Dissertation

by

TARUN GROVER

Submitted to the Office of Graduate Studies of
Texas A&M University
in partial fulfillment of the requirements for the degree of

DOCTOR OF PHILOSOPHY

August 2008

Major Subject: Petroleum Engineering

NATURAL GAS HYDRATES – ISSUES FOR GAS PRODUCTION AND GEOMECHANICAL STABILITY

A Dissertation

by

TARUN GROVER

Submitted to the Office of Graduate Studies of
Texas A&M University
in partial fulfillment of the requirements for the degree of

DOCTOR OF PHILOSOPHY

Approved by:

Co-Chairs of Committee,	Stephen A Holditch
	George J Moridis
Committee Members,	William D McCain
	Maria Barrufet
	Roger Sassen
Head of Department,	Stephen A Holditch

August 2008

Major Subject: Petroleum Engineering

ABSTRACT

Natural Gas Hydrates - Issues for Gas Production and Geomechanical Stability.
(August 2008)
Tarun Grover, B.En., Panjab University; M.S., University of Mississippi
Co-Chairs of Advisory Committee: Dr. Stephen A Holditch
Dr. George J Moridis

Natural gas hydrates are solid crystalline substances found in the subsurface. Since gas hydrates are stable at low temperatures and moderate pressures, gas hydrates are found either near the surface in arctic regions or in deep water marine environments where the ambient seafloor temperature is less than 10°C. This work addresses the important issue of geomechanical stability in hydrate bearing sediments during different perturbations.

I analyzed extensive data collected from the literature on the types of sediments where hydrates have been found during various offshore expeditions. To better understand the hydrate bearing sediments in offshore environments, I divided these data into different sections. The data included water depths, pore water salinity, gas compositions, geothermal gradients, and sedimentary properties such as sediment type, sediment mineralogy, and sediment physical properties. I used the database to determine the types of sediments that should be evaluated in laboratory tests at the Lawrence Berkeley National Laboratory.

The TOUGH+Hydrate reservoir simulator was used to simulate the gas production behavior from hydrate bearing sediments. To address some important gas production issues from gas hydrates, I first simulated the production performance from the Messsoyakha Gas Field in Siberia. The field has been described as a free gas reservoir overlain by a gas hydrate layer and underlain by an aquifer of unknown strength. From a parametric study conducted to delineate important parameters that affect gas production at the Messoyakha, I found effective gas permeability in the hydrate layer, the location

of perforations and the gas hydrate saturation to be important parameters for gas production at the Messoyakha. Second, I simulated the gas production using a hydraulic fracture in hydrate bearing sediments. The simulation results showed that the hydraulic fracture gets plugged by the formation of secondary hydrates during gas production.

I used the coupled fluid flow and geomechanical model “TOUGH+Hydrate-FLAC3D” to model geomechanical performance during gas production from hydrates in an offshore hydrate deposit. I modeled geomechanical failures associated with gas production using a horizontal well and a vertical well for two different types of sediments, sand and clay. The simulation results showed that the sediment and failures can be a serious issue during the gas production from weaker sediments such as clays.

DEDICATION

I dedicate this dissertation to my family; my mother and father, my brother, Arun and my sister, Aarti. It is only because of their love and support that I have reached this far in my life.

ACKNOWLEDGEMENTS

My graduate studies at Texas A&M have been rich in experience, both intellectually and professionally. I have had an excellent opportunity to work with some of the best and brightest minds in the world. The debt of gratitude I owe is too large to express in words, and any attempt to repay this debt remains meaningless.

I thank Dr. Steve Holditch, my co-advisor, for giving me an opportunity to pursue my research on the wonderful subject of gas hydrates, encouraging me to think independently and taking care of my financial well-being.

I am grateful to Dr. George Moridis, my co-advisor, for guiding me tirelessly, sharing his experience and insight on hydrates, teaching me how to use his amazing code TOUGH+Hydrate and always intellectually stimulating me.

I appreciate Dr. Yuri Makogon for sharing his excellent insight on hydrate fundamentals and Dr. Jonny Rutqvist at Lawrence Berkeley National Laboratory, for teaching me how to use his coupled model.

Thanks go to Dr. Roger Sassen for sharing his extremely valuable experience, knowledge and understanding on natural gas hydrates and to Dr. Maria Barrufet and Dr. Bill McCain for serving on my dissertation committee.

Thanks also to Dr. Matt Reagan and Dr. Mike Kowalsky at Lawrence Berkeley National Laboratory for sharing their experience on numerical simulation.

Thanks to all my Aggie buddies Danial, Deepak, Raj, Salil, Teddy and Uma for wonderful discussions and making my stay at Texas A&M a memorable one.

Thanks to my family, last in the list, always first in my thoughts, for everything.

NOMENCLATURE

LETTERS

Bcf	Billion cubic feet
C_0	Uniaxial compressive strength (Pa, psi)
d_{s}	Depth below seafloor (m)
d_{w}	Water depth (m)
g	Acceleration due to gravity, 9.81 $\mathrm{m/s^2}$
HBS	Hydrate-bearing sediments
h_{bottom}	Bottom of the hydrate layer
h_{top}	Top of the hydrate layer
k	Permeability ($\mathrm{m^2}$)
k_{rA}	Relative permeability to water
k_{rG}	Relative permeability to gas
N_H	Hydration number
n	Relative permeability exponent
p	Pressure (Pa)
p_{avg}	Average pressure in the free gas layer (Pa, psi)
p_0	Entry pressure (Pa, psi)
P_{e}	Equilibrium pressure (MPa)
$\mathrm{p_p}$	Pore pressure
r	radial direction
m	Slope of Mohr-Coulomb failure line
Q_{r}	Volumetric release rate in the reservoir (scf/day)
Q_{p}	Volumetric production rate at the well (scf/day)
V_{r}	Cumulative gas released in the reservoir (scf)
V_{p}	Cumulative gas produced at the well (scf)

RRR	Rate replenishment ratio
S	Saturation
S_0	Cohesion (Pa, psi)
S_{irA}	Irreducible water saturation
S_{irG}	Irreducible gas saturation
T	Temperature (°C)
T_0	Temperature at the seafloor (°C)
Tcf	Trillion cubic feet
VRR	Volumetric replenishment ratio
x	x-direction
y	y-direction
x^i_{A}	Mole fraction of inhibitor in the aqueous phase
x^i_{Ar}	Reference mole fraction of inhibitor in the aqueous phase

GREEK

α	Biot's effective stress parameter
Δd_{s}	Difference between subsurface depths (m)
Δp	Pressure difference
Δp_{max}	Maximum pressure drop at the wellbore (Pa, psi)
Δp_{tb}	Pressure difference between top and bottom of hydrate layer (psi)
Δp_{w}	Pressure difference between well and the reservoir
ΔT	Temperature difference (°C)
ΔT_{D}	Inhibitor induced temperature depression (K)
$\Delta T_{\mathrm{D,r}}$	Inhibitor induced temperature depression at reference mole fraction (K)
λ	Van Genutchen exponent
μ	Coefficient of friction

ε	Strain
ρ_w	Water density (kg/m3)
ρ_b	Sediment bulk density (kg/m^3)
σ'	Effective stress (Pa, psi)
σ_1	Maximum principal stress
σ_3	Minimum principal stress
σ'_{1c}	Maximum principal effective stress
σ'_3	Minimum principal effective stress
σ_v	Overburden stress (Pa, psi)
ϕ	Porosity
$\varphi_{wellbore}$	Porosity of the wellbore
$\phi_{fracture}$	Porosity of the fracture
ψ	Angle of friction (°)

SUBSCRIPTS

max	Maximum
aqu	Aquifer
p	pore
cap	capillary
rad	radial
eff	effective
A	Aqueous
G	gas
H	hydrate
I	Ice
w	Well

TABLE OF CONTENTS

Page

CHAPTER

LIST OF FIGURES

FIGURE Page

FIGURE Page

LIST OF TABLES

CHAPTER I

INTRODUCTION

Natural gas hydrates have been an area of active research in the oil and gas industry since their role in plugging or blocking fluid flow in oil and gas pipelines was demonstrated by Hammerschmidt (1934). Makogon (1965) first proposed that natural gas hydrates could exist in the earth's subsurface. Since then, research has been performed to estimate and quantify the volume of naturally occurring gas hydrates both onshore (beneath the permafrost) and offshore (in deepwater marine sediments). Although there is considerable uncertainty over the quantity and distribution of hydrates in the earth, there is general agreement that substantial volumes of gas hydrates do exist (Sloan and Koh, 2008). According to the latest data gathered by various expeditions for hydrates, the gas resource in hydrate ranges from 10^5 to 10^6 Tcf (US Department of Energy, 2007). The present interest in naturally occurring hydrates is two fold:

1. Hydrates as an energy resource.
2. Hydrates as a possible cause of seafloor instability and other safety hazards for the offshore oil and gas industry.

In this research, I have looked at certain aspects of both issues.

1.1 Motivation

Natural gas hydrate is a very concentrated form of natural gas storage. One cubic meter of a methane hydrate (solid) can hold up to 164 m^3 of gas at standard temperature and pressure (STP) (Makogon, 2007). The 164 m^3 (at STP) of methane is held in only 0.2 $m^3$of hydrate, with the other 0.8 m^3 occupied by water (Makogon et al., 2007). The large concentration of natural gas in the form of hydrates can be a very attractive energy source if it can be dissociated in an environmentally safe way to produce the gas and get it to a market.

This dissertation follows the style of Journal of Petroleum Science and Engineering.

In this research, I have used the numerical simulators TOUGH+Hydrate (hereafter referred to as T+H) and TOUGH+Hydrate-FLAC3D (hereafter referred to as T+F) (Moridis et al., 2008; Rutqvist, 2008) to evaluate several aspects of fluid flow and mechanical stability in naturally occurring gas hydrate formations. TOUGH is an acronym for Transport of Unsaturated Groundwater and Heat. FLAC is an acronym for Fast Lagrangian Analysis of Continua.

The Messoyakha field in Siberia has been described as a free gas reservoir overlain by hydrates and underlain by an aquifer of unknown strength. Although the Messoyakha field has been used by some as an example of how to produce gas from hydrate deposits at other parts of the world, no one has ever studied the Messoyakha field in detail using a reservoir simulator. Using T+H I have evaluated the feasibility of producing gas from the hydrate zone at Messoyakha. I believe that by delivering a better understanding of the gas production mechanisms at Messoyakha, I can do a better job of simulating possible gas production from deep water, marine gas hydrate deposits.

In soft, unconsolidated sediments, gas hydrates can actually be the cementing material that holds the sediments together. When gas hydrates dissociate in response to thermal or inhibitor loading without gas removal (e.g., when hydrate deposits are heated by pipelines carrying warm reservoir fluids ascending toward the surface), the generated gas creates an excess pore pressure (pressure above the initial equivalent hydrostatic pressure) in the sediments (Makogon, 2007; Xu and Germanovich, 2006). The magnitude of the excess pore pressure depends on sediment permeability, sediment compressibility, and the overall geological features. As the pore pressure increases, the effective stress in the sediments decreases. The reduction in effective stress can create weak zones in slope sediments and can trigger a slope failure.

During production from hydrate-bearing sediments, the dissociation of hydrates (a strong cementing agent) continuously weakens the structural strength of the sediments, which are often unconsolidated. Furthermore, the removal of the reservoir fluids (and the creation of large and expanding gas banks in the deposit) results in formation pressure changes, and, consequently, in an increasing load transfer to the porous media as the initial load-bearing solid phases volume (comprising the grains of the porous medium and the hydrate) shrinks in the process of hydrate dissociation. The resulting strains and stresses (and their anisotropic distribution) can lead to formation failure and wellbore instability. The possibility of such failures (with potentially catastrophic consequences) requires an in-depth examination of the physical and mechanical properties of hydrate-bearing sediments, and their response to different dissociation scenarios. Performing stress analysis using T+F helped me identify the geomechanical issues related to gas production from offshore hydrate deposits.

1.2 Research objectives

The overall aim of this research was to use numerical modeling to quantify several issues related to gas production from hydrate deposits and seafloor stability in hydrate bearing sediments. The work was divided into three main tasks.

1. I developed an MS/ Access database of offshore hydrate bearing sediments using publicly available literature. This database includes the following information:
    a. Water depths, geothermal gradients, gas compositions, and pore water salinity.
    b. Sedimentology data such as sediment type, mineralogy, physical properties, and thermal properties.
2. The numerical simulator T+H was used to simulate the gas production for two different problems. Those problems were:
    a. Reservoir performance of the Messoyakha gas hydrates deposit. In this study, I explained various field phenomena observed in the field and identified important parameters for gas production.
    b. Production from a hydraulic fracture in hydrate bearing sediments – In this study I simulated the production behavior from a hydraulic fracture and identified the production issues when a hydraulic fracture intersecting a well is used to produce gas from hydrates.

3. The coupled model T+F was used to study the geomechanical instability during gas production from an offshore hydrate deposit. I was able to identify the geomechanical issues for two different problems:
    a. Production from a horizontal well
    b. Production from a vertical well

1.3 Organization

This dissertation is organized into eight chapters.

Chapter I is the introduction.

Chapter II explains the preliminary concepts of gas hydrates and discusses the fundamental properties of hydrates. These properties are important to understand the gas production from hydrate deposits as well as geomechanical stability of hydrate bearing sediments. The important characteristics of gas hydrate deposits are discussed in detail.

Chapter III explains the data collected on offshore hydrate deposits and presents an explanation of the database constructed on the characteristics of offshore hydrate deposits. The database also presents the data measured from different laboratory experiments undertaken by different researchers. The importance of different parameters for gas production and geomechanical performance are explained.

Chapter IV explains the simulation tools used in this research including the reservoir simulation code, T+H and the coupled geomechanics code, T+F.

Chapter V deals with the detailed analysis as well as numerical study of Messoyakha Gas Field in Siberia. I used the T+H simulator for this study. I have used a real field example to explain the observed pressure data and other phenomena occurring at the field. Further, the controlling parameters for hydrate dissociation in porous media are quantified and a sensitivity study is presented.

Chapter VI presents the results of a simulation experiment done to evaluate the performance of a hydraulic fracture in a hydrate bearing layer. Using simulation results I have analyzed the contribution of a fracture to overall gas production in a hydrate bearing layer.

Chapter VII explains the change in stresses in hydrate bearing sediments under different perturbations of pressure and temperature. I used T+F for the study of this problem. I combined the important information collected in Chapter III concerning the characteristics of offshore hydrate deposits with modeling strategies explained in Chapter V. The evolution of in situ stresses is presented for three important problems. The first problem deals with the evolution of in situ stresses in hydrate bearing sediments during heating of the deposit with no production. The second problem deals with the evolution of in situ stresses in hydrate bearing sediments due to gas production from a horizontal well; the driving force for hydrate dissociation in horizontal well problem is simple depressurization. The third problem deals with the evolution of in situ stresses in hydrate bearing sediments due to gas production from a vertical well; the driving force for hydrate dissociation in vertical well problem is combination of thermal stimulation and depressurization.

Chapter VIII presents the conclusions and recommendations of this research.

CHAPTER II

CHARACTERISTICS OF GAS HYDRATE DEPOSITS

2.1 Introduction

Natural gas hydrates (NGH) are crystalline compounds formed by the association of molecules of water with natural gas. Makogon (1997) illustrates the methane hydrate formation reactions as:

$$\underset{\text{(Methane)}}{CH_4} + \underset{\text{(Water)}}{N_H H_2O} \Leftrightarrow \underset{\text{(Hydrate)}}{CH_4.nH_2O} + \Delta H_1 \qquad (2.1)$$

$$\underset{\text{(Methane)}}{CH_4} + \underset{\text{(Ice)}}{N_H H_2O} \Leftrightarrow \underset{\text{(Hydrate)}}{CH_4.nH_2O} + \Delta H_2 \qquad (2.2)$$

Where N_H is the hydration number approximately equal to 6 for methane hydrates (Sloan and Koh, 2008). The hydrate formation reaction is an exothermic process (generates heat) and the hydrate dissociation reaction is an endothermic process (absorbs heat). The heat of formation of methane hydrate from methane and liquid water is $\Delta H_1 =$ 54.2 kJ/mol and the heat of formation of methane hydrate from methane and ice is $\Delta H_2 =$ 18.1 kJ/mol.

NGHs are a subset of substances known as clathrates, which means “cage like structures”. Besides gases, some liquids like tetrahydrofuran (THF) can also react with water to form hydrates. The formation of natural gas hydrates depends on pressure, temperature, gas composition, and presence of inhibitors such as salts. NGHs are found in the subsurface in two distinct types of settings; that is, the permafrost in arctic regions and in deepwater marine environments. In the oil and gas industry, hydrates have been studied since Hammerschmidt (1934) demonstrated that plugging of pipelines can occur because of the formation of hydrates. Certain chemicals can be injected into the pipelines to either prevent hydrates from forming or to prevent them from sticking to the walls of the pipeline (Makogon, 1997; Sloan and Koh, 2008).

Ever since natural gas hydrates were discovered in the subsurface (Makogon, 1965), the research on naturally occurring gas hydrates has continued. The amount of gas present in the form of hydrates around the world has been estimated to range from 10^5 to 10^6 Tcf (US Department of Energy, 2007). The characterization of hydrate deposits involves collection and interpretation of geophysical, geochemical, sedimentological and thermal data. Several expeditions undertaken by the Ocean Drilling Program (Shipboard Scientific Party, 1996; Shipboard Scientific Party, 2003) and the US Department of Energy (US Department of Energy, 2007) have collected data to explain the distribution of hydrates in sediments The purpose of this chapter is to analyze the properties of hydrate bearing sediments that affect the gas production and geomechanical instabilities related to hydrates.

2.2 Properties of gas hydrates

The three basic crystalline structures of gas hydrates are called Structure I (sI), Structure II (sII) and Structure H (sH) (Fig. 2.1).

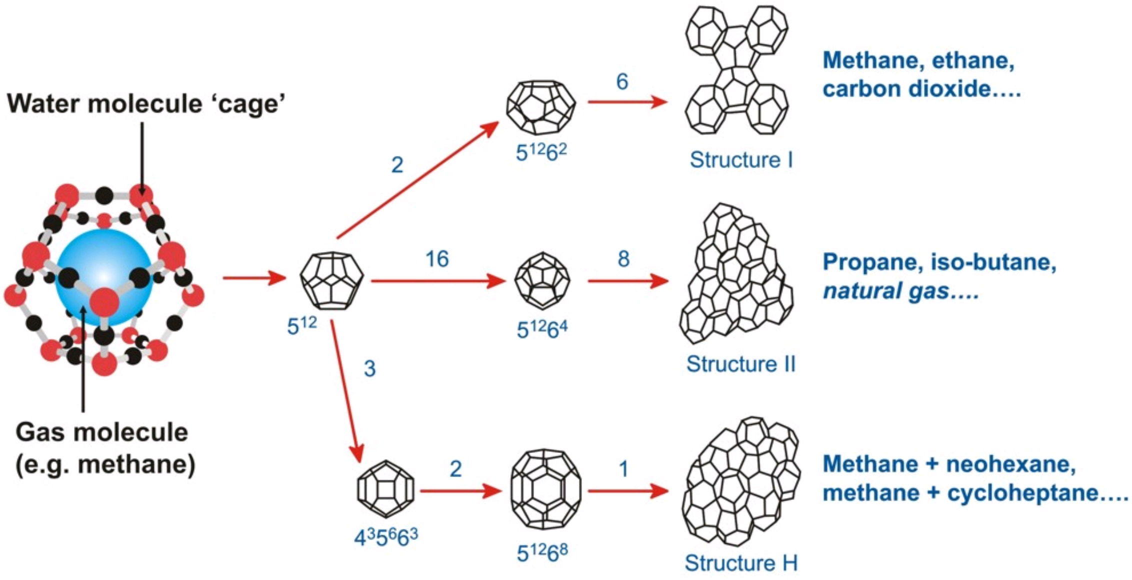

Fig. 2.1. Hydrate structures (From Center for Gas Hydrate Research – Heriot Watt University, 2007)

The crystal structures sI and sII were first identified by von Stackelberg (1949, 1954), von Stackelberg and Muller (1951), Claussen (1951) and Pauling and Marsh (1952) using the crystallography studies. The structure H (sH) was first discovered by Ripmeester (1987) (Sloan and Koh, 2008) Whether a gas mixture will form sI, sII or sH will depend on the gas composition. Pure methane and ethane form sI hydrate. For components larger than ethane (propane, butane), sII hydrate is formed. sH hydrate accommodates larger gas molecules than butane such as isopentane along with smaller molecules (C1-C4). sI hydrate is the most abundant structure in nature followed by sII hydrate. sH hydrates are much rarer and it is only recently that they have been found in natural systems (Sassen and Macdonald, 1994).

One cubic foot of methane hydrate can encapsulate up to 164 ft^3 of methane at standard temperature T and pressure P (Makogon, 1997). The large concentration of methane in methane hydrate, coupled with the vast amount of the global hydrate inventory, has brought to the foreground the question of exploiting natural hydrates as an energy resource, and is the driving force of the significant recent research on naturally occurring hydrates.

The density of gas hydrates can vary from 0.8 to 1.2 gm/cm^3 (as shown in Table 2.1) depending on the composition of gas that was used to form the hydrate, pressure p, temperature T (Makogon et al., 2007) and the texture of the hydrate. The texture of hydrate depends on the degree of filling of cavities in the hydrate crystal lattice. Since the density of methane hydrate is approximately 0.910 gm/ cm^3, methane hydrate is less dense than water. Hydrates crystals can have different morphologies depending on gas composition and conditions of crystal growth (Makogon, 1981).

Hydrate dissociation is an endothermic reaction. Fig. 2.2 (Makogon, 1997) shows the heat of dissociation of different hydrates.

Table 2.1

Properties of different hydrates (from Makogon, 1997)

Gas	Formula of hydrate	Hydrate density @ 273 K (gm/cm^3)
C1 (Methane)	$CH_4.6H_2O$	0.910
CO_2 (Carbon dioxide)	$CO_2.6H_2O$	1.117
C2 (Ethane)	$C_2H_6.7H_2O$	0.959
C3 (Propane)	$C_3H_8.17H_2O$	0.866
i-C4(Iso-butane)	$iC_4H_{10}.17H_2O$	0.901

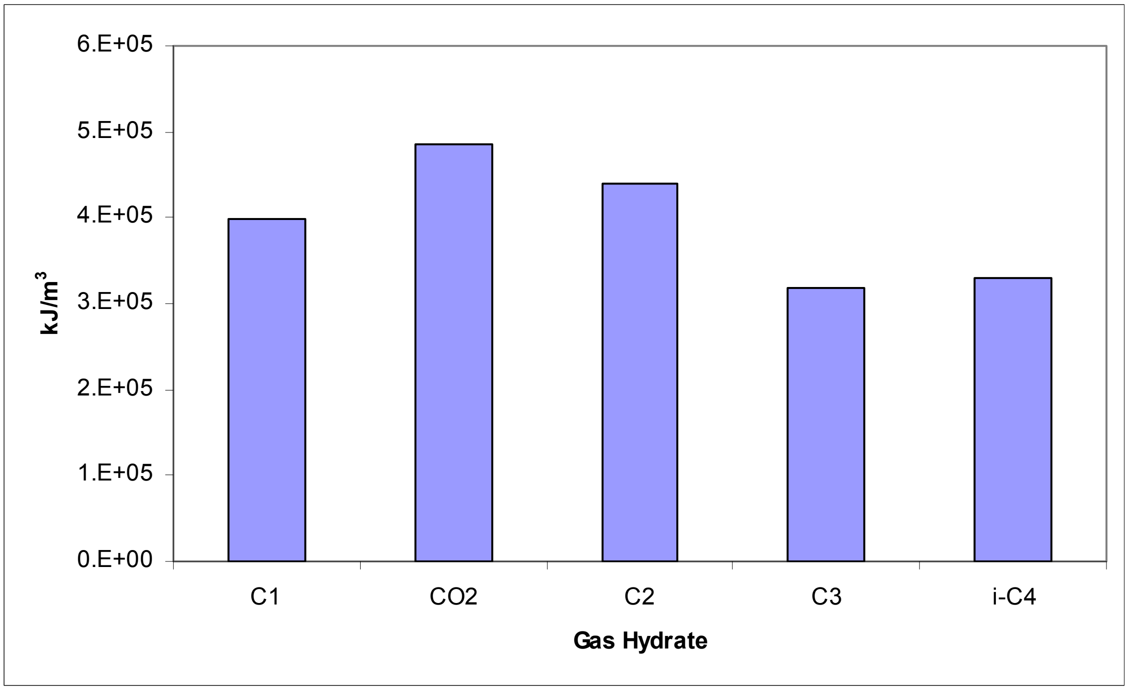

Fig. 2.2. Heat of dissociation of various gas hydrates (data from Makogon,1997).

2.3 Controls on hydrate stability

The stability of hydrates is controlled by parameters such as pressure, temperature gas composition and presence of inhibitors (such as salts). Fig. 2.3 illustrates the methane hydrate equilibrium curve with pure water for most of the naturally occurring temperature ranges. The pressure and temperature conditions considered in Fig. 2.3 do not include the other part of spectrum of hydrate stability, which is, below the ice-point. Fig. 2.3 is an exponential fit on a large number of data points experimentally measured by various researchers (Moridis et al., 2008). The equilibrium curve shifts to the left (red arrow in Fig. 2.2) with increasing concentration of salt or the other chemicals in the water; salts and alcohols act as hydrate inhibitors. Alcohols like methanol, ethylene glycol are injected in oil and gas transportation pipelines to inhibit the formation of hydrates. Makogon (1974; 1981) conducted extensive studies on the inhibition effect of alcohols and salts on the hydrate formation. The equilibrium curve shifts to the right (green arrow) when heavier hydrocarbons, along with methane participate in hydrate formation.

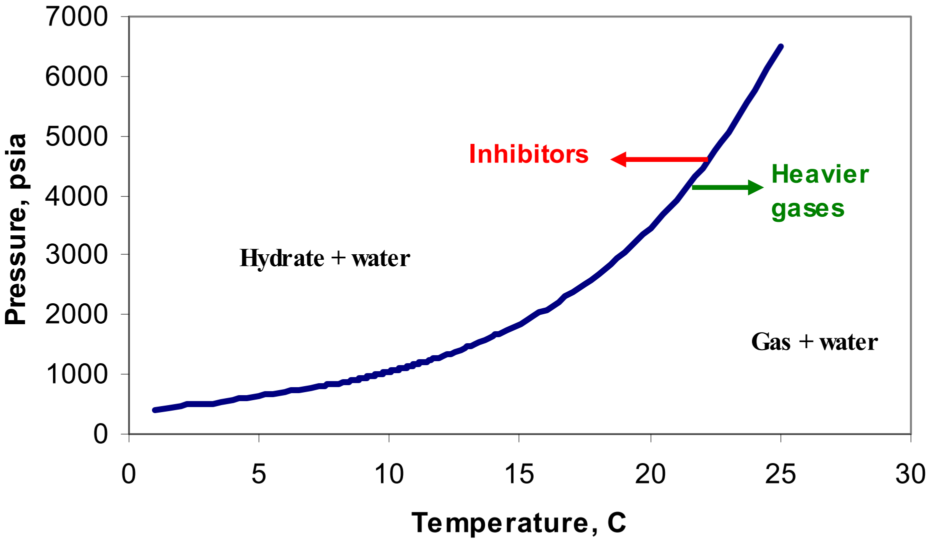

Fig. 2.3. Methane hydrate equilibrium curve (after Moridis et al., 2008).

2.4 Hydrate stability zone

Naturally occurring hydrates are known to exist in two different types of environments, arctic permafrost and deepwater oceanic sediments. A majority of the hydrates occur in oceanic sediments because of active production of methane by methanogenesis in marine sediments (Claypool and Kaplan, 1974). The methane formed then reacts with pore water and forms methane hydrate when the correct pressure and temperature conditions occur. This chapter deals with the detailed characteristics of offshore hydrate deposits, as the main purpose of this dissertation is to study the geomechanical stability of offshore hydrate-bearing sediments. Because so little data are available on gas hydrate deposits in the ocean, considerable uncertainty remains concerning how the gas hydrate is distributed in the sediment and how much gas is really trapped in the form of hydrates.

The amount of methane available as hydrates has been estimated by a number of researchers. Makogon (1966) first published the idea of occurrence of hydrates in nature and proved it through experimental work. He also first generated a methodology to estimate the in-place hydrates in the subsurface. A lot of studies to estimate the hydrate resource have been done since and has been described in detail by Milkov (2004).

Although knowledge on the total hydrate inventory and its global distribution is fraught with significant uncertainties, it is rather well established that the oceanic hydrate deposits constitute the bulk of natural hydrates (Sloan and Koh, 2008). In offshore environments, hydrates are stable in water depths greater than 200 to 600 meters depending on the gas composition and seafloor temperatures (Milkov and Sassen, 2002). Fig. 2.4 (data from Milkov and Sassen, 2003) shows the pressure and temperature conditions that can lead to a typical offshore hydrate deposit in Gulf of Mexico.

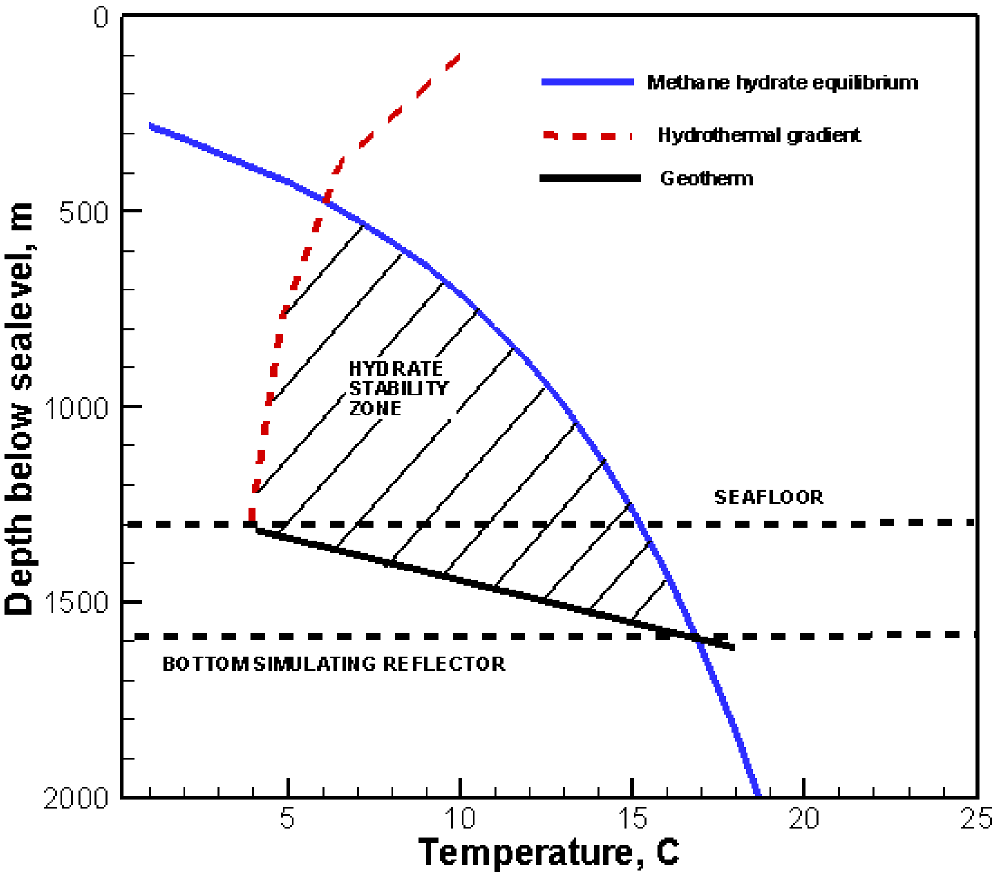

Fig. 2.4. Hydrate stability zone in offshore environments.

The “methane-water-hydrate” phase boundary is actually the equilibrium curve that depends on the gas composition as well as the pore water salinity. The term “hydrate stability zone” (HSZ) does not mean that hydrates will always be present there but just means that the hydrates, if formed, will be stable in that region. The other controlling parameter (apart from pressure, temperature, gas composition, and salinity) for hydrate formation in marine sediments is the methane supply in marine sediments. Methane has to be present above the solubility limit at respective pressures and temperatures to form hydrates.

Since water is always present in marine sediments, it is not a constraint in the formation of hydrates. At many places such as the Blake Ridge (Shipboard Scientific Party, 1996) and Cascadia Margin (Shipboard Scientific Party, 2003), a well-developed acoustic reflector is often (but not always) identified during acquisition of seismic data in the presence of hydrate deposits. The acoustic signal occurs because of the presence of free gas below the hydrate stability zone. The free gas occurs because the P and T conditions are either at or just outside those defining the stability (equilibrium) curve, i.e., the coexistence of gas, liquid and hydrate. Since the acoustic signal is roughly parallel to the seafloor, it is called the bottom-simulating reflector (BSR).

The methane supply can have two origins, biogenic or thermogenic (Claypool and Kaplan, 1974). Biogenic methane is produced by the action of microorganisms on the buried organic matter in an anoxic environment. The methane then forms hydrates when it exceeds the solubility in pore water. Biogenic methane is formed in relatively shallow sediments and it travels very short distances, on the order of tens to hundreds of meters, before forming hydrates (Milkov, 2005). Thermogenic methane is formed by the thermal cracking of higher hydrocarbons at greater depths and it migrates over long distances, on the order of hundreds to thousands of meters. The source of the thermogenic methane can be either oil or natural gas deposits deeper in the subsurface. The transport of thermogenic methane can occur along faults (Sassen et al., 1994), mud volcanoes (Milkov, 2000), and structurally deformed carrier beds (Milkov et al., 2005) to the hydrate stability zone.

Gas hydrates are widespread along the Continental margins (Max et al., 2006), because of the large sediment flux and hence rapid burial of organic content at these locations. The rapid burial of organic content creates oxygen deficient conditions (anoxic) and favors the conversion of organic matter to methane.

The thickness of the hydrate stability zone will vary along the continental margin (Fig. 2.5) which includes a Continental shelf, a Continental slope and a Continental rise (Kvenvolden and McMenamin, 1982). The thickness of hydrate stability zone increases along the slope as the water depth increases and the geothermal gradients remain constant throughout the Continental margin.

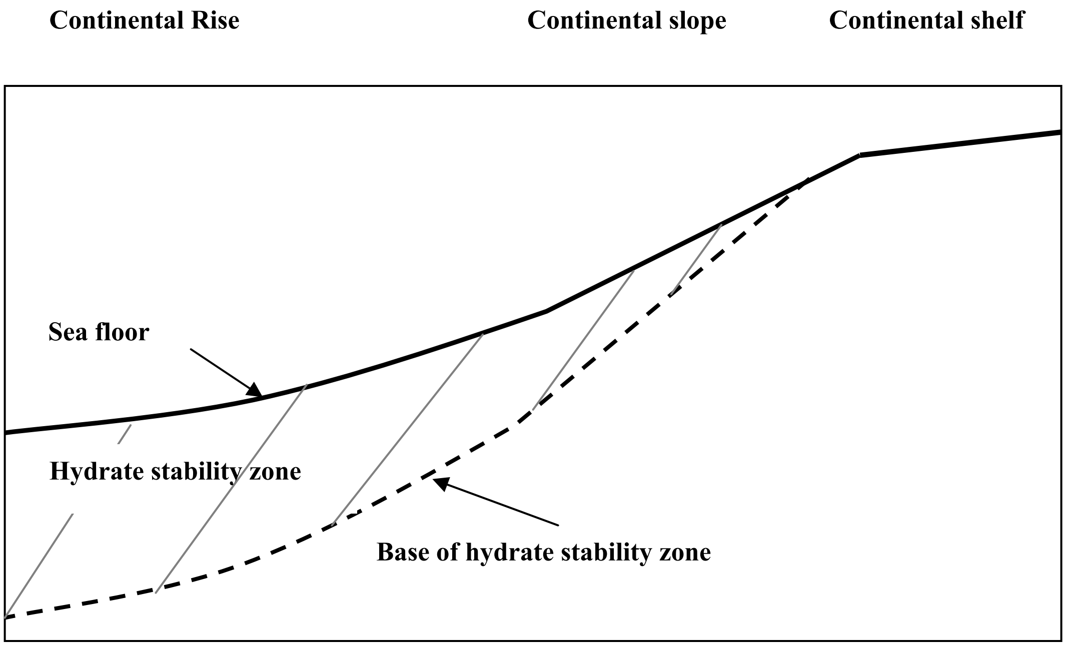

Fig. 2.5. Hydrate stability zone along the continental margins.

2.5 Hydrate accumulation models

Hydrate accumulation in nature is a complex phenomenon and many authors have proposed models of hydrate formation in marine sediments (Hyndman and Davis, 1992; Rempel and Buffett, 1997; Xu and Ruppel, 1999; Davie and Buffett, 2001; Klauda and Sandler, 2005; Liu and Flemings, 2007). The important parameters that have been suggested to affect the formation of hydrates in marine sediments are depth (pressure), temperature (geothermal gradient), pore water salinity, total organic content of sediments, sediment characteristics, and presence of faults and fractures. Typically one-dimensional hydrate-formation models delineate the importance of each of the factors controlling the hydrate formation in sediments. Davie and Buffett (2001) modeled the hydrate saturation as largest at the base of hydrate stability zone and decreasing towards the seafloor. Klauda and Sandler (2005) have developed an equilibrium thermodynamic hydrate accumulation model which includes the effects of salinity, pore-size distribution of sediments and hydrate confinement in pores.

These models predict that hydrate saturation will decrease towards the seafloor with a maximum concentration at the base of the hydrate stability zone. However, massive hydrate mounds have been found at the seafloor in the Gulf of Mexico (Sassen, 2007), an observation that has exposed a limitation of the hydrate formation models.

2.6 Hydrate dissociation mechanisms

Hydrates can be dissociated by the following three fundamental mechanisms (Makogon, 1966):

1. depressurization
2. thermal stimulation
3. the use of inhibitors

Fig. 2.6 illustrates these mechanisms of hydrate dissociation in the context of hydrates in the subsurface. Depressurization means the pressure in the hydrate bearing system is reduced to bring the pressure out of the hydrate-stability region. Thermal stimulation means heat is supplied to increase the temperature of the system so it moves out of the hydrate stability region. Inhibitor injection involves the injection of salts or solvents to shift the equilibrium curve so as to bring the hydrates out of hydrate stability region.

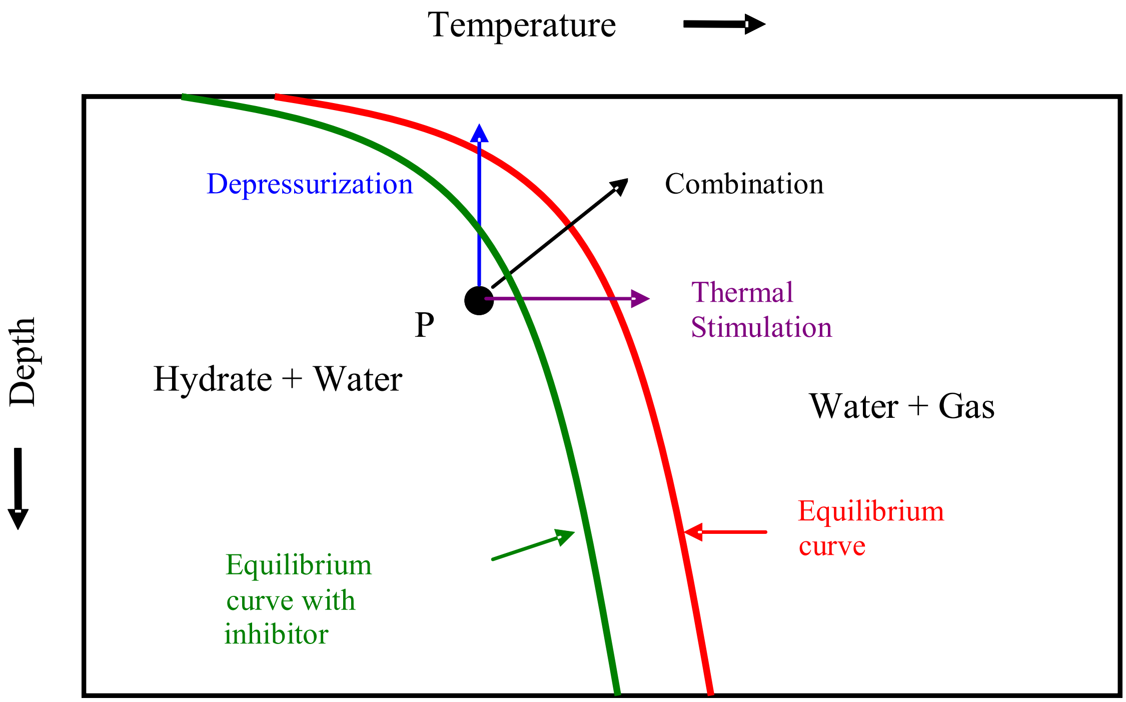

Fig. 2.6. Hydrate dissociation mechanisms in offshore hydrate deposits.

2.7 Classification of hydrate deposits

Moridis and Collett (2004) developed a classification system for hydrate-bearing geologic media. They classified the hydrate deposits into four classes, that is, Class 1, Class 2, and Class 3. Class 1 systems are those where a hydrate bearing layer is underlain by a zone of mobile water and free gas. Class 2 systems are those where a hydrate-bearing layer is underlain by water. Class 3 systems are those where a single hydrate-bearing layer exists with no underlying mobile fluids. Moridis and Sloan (2007) proposed Class 4 hydrate deposits, which they defined as low-saturation hydrate deposits without any bounding formations. The Class 4 hydrate deposits are typical of oceanic hydrate accumulations.

Another classification system suggests that geologically, most hydrate deposits in the offshore environments can be classified as either structural or stratigraphic (Milkov and Sassen, 2002). They can also exist as a combination of both of these settings (Fig. 2.7). Structural hydrate deposits generally form when the thermogenic gases from the deeper subsurface migrate to the hydrate stability zone (HSZ) along the faults or permeable channels, gas chimneys above petroleum reservoirs or mud volcanoes(Milkov, 2005). These gases then react with the water in the hydrate stability zone and form hydrates. The hydrates in structural deposits and their distribution in sediments are controlled mainly by heat flow, salinity variations in the sediments, and the occurrence of permeable pathways (Milkov, 2005). Gas hydrates can be concentrated locally around the faults and mud volcanoes (Milkov and Sassen, 2002). The northwestern Gulf of Mexico (Brooks et al., 1986; Macdonald et al., 1994; Sassen et al., 1999b; Milkov and Sassen, 2000) is one of the examples of structural gas hydrate accumulation. Other examples are Hydrate Ridge (offshore Oregon) (Trehu et al., 2006)and the Haakon Mosby mud volcano (offshore Norway). Typically, the structural accumulations occur at high fluid flux settings and occur as thick layers (Xu and Ruppel, 1999). However, because of high fluid flux and high pore water salinity, the HSZ is eliminated completely (Ruppel et al., 2005). BSRs are not common in structural hydrate occurrences because the hydrates are more or less vertically stacked in the high permeability conduits such as faults (Milkov and Sassen, 2002; Kleinberg, 2006). Therefore, the free gas does not parallel the seafloor and hence no BSRs are observed.

Stratigraphic hydrate accumulations are hydrate deposits formed by the biogenic gas in marine sediments. These types of deposits occur in low fluid flux environments or diffusion dominated environments (Xu and Ruppel, 1999). Hydrates are located well below the seafloor and have a large areal extent but may occur in very low saturations. BSRs occur more frequently beneath stratigraphic accumulations than at structural accumulations.

Combination accumulations are those settings where hydrates occur in permeable strata, but the supply of gas for hydrate formation occurs along conductive faults or diapirs.

Recently, Boswell's team (Smith et al., 2006; Boswell et al., 2007) introduced a new system to classify hydrate deposits into four major categories. Their classification system is based on a geological framework and lithology of the hydrate-bearing sediments. According to these researchers, the four major plays where hydrates are found are sand-dominated plays, fractured clay-dominated plays, massive gas-hydrate formations exposed at the seafloor, and low concentration hydrates disseminated in a clay matrix. A majority of hydrates in offshore sediments are clay-dominated (Boswell et al., 2007; Sassen, 2007). Frequently, the hydrates are hosted in fracture fillings in clay dominated systems in shallow sediments. A combination of hydrate-bearing sand and clays can also exist.

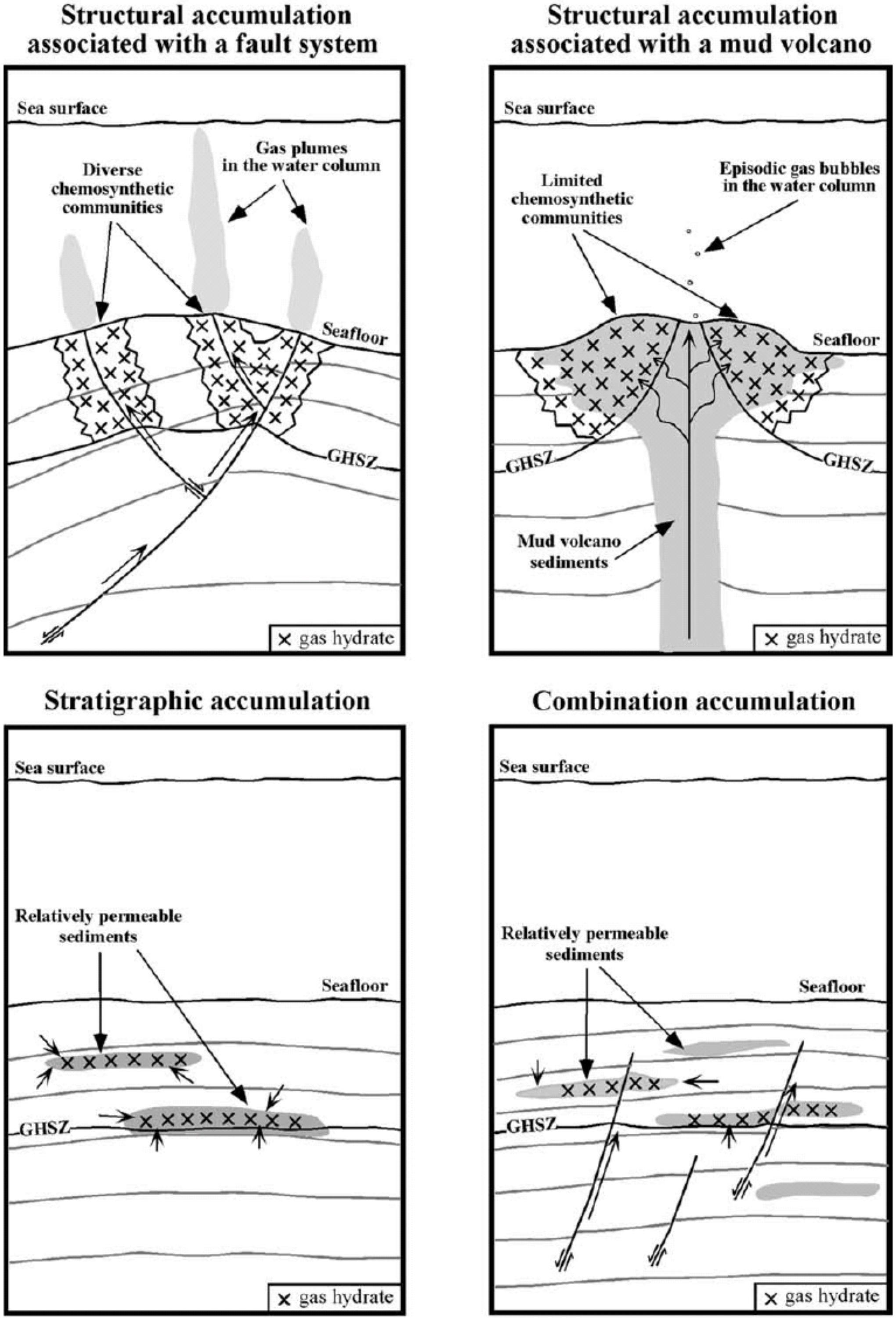

Fig. 2.7. Types of offshore hydrate accumulations (from Milkov and Sassen, 2002).

2.8 Detection of hydrates in sediments

2.8.1 Seismic techniques

Traditionally, the presence of a bottom simulating reflector (BSR) has been an important criterion for selecting a drilling location to collect hydrate cores. While BSRs may indicate the presence of hydrates, they may be misleading (Milkov and Sassen, 2002; Kleinberg, 2006). Relying on BSRs could lead to missing out the high hydrate location zones (Kleinberg, 2006). Hydrates may not exist above the BSR (Kleinberg, 2006) or they may exist and could form traps for the free gas below. Hydrates may also exist in areas where a BSR cannot be detected.

2.8.2 Coring techniques

Hydrate-bearing cores have been recovered by the scientific community during various scientific expeditions (Shipboard Scientific Party, 1996; Shipboard Scientific Party, 2003). The expeditions for offshore hydrate deposits have been led by the Ocean Drilling Program (in areas such as Blake Ridge, Cascadia Margin, and Hydrate Ridge) and the US Department of Energy (Gulf of Mexico, Offshore India). The expeditions for onshore (permafrost) hydrate deposits have been led by Geological Society of Canada (Mallik expeditions at Northwest Territories, Canada) and US Department of Energy (Mt. Elbert in Alaska). However, the most significant challenge has been the collection and retrieval of cores that contain gas hydrates with little or no change from the reservoir conditions. The common method to retrieve cores from the ocean bottom is with a piston core barrel. However, common piston coring techniques used during many expeditions have not been capable of retrieving hydrate-bearing cores to the surface for laboratory analysis before the hydrates dissociated (Paul and Ussler, 2001). When a hydrate-bearing core is retrieved using conventional piston cores, the pressure decreases and the temperature increases. The pressure decrease during coring destabilizes the hydrates in the cores and the hydrates dissociate. To overcome the problem of hydrate dissociation during piston-coring operations, new tools for collecting hydrate samples at in situ pressure had to be developed. The Pressure Core Sampler (PCS) and the Hydrate

Autoclave Coring Equipment (HYACE) (Shipboard Scientific Party, 2003) were effective in retrieving cores at Hydrate Ridge that still had hydrates in the cores.

Another recent advancement to estimate the hydrate concentrations in retrieved cores is described in Weinberger et al. (2005). The pressurized cores are collected from the sediment depths and are thermally imaged during the depressurization. Since hydrate dissociation is endothermic, it will lead to “cold spots” in the core wherever hydrates dissociate. These cold-spots can be identified by an Infra-red (IR) camera and can be used as a preliminary guess for locating hydrates in the recovered core samples.

2.8.3 Proxy indicators

Pore water chlorinity anomaly is often used as a proxy indicator of the presence of hydrates when piston-coring equipment is used and the hydrate disappears before it can be retrieved on board. During hydrate formation, water molecules are removed from sediments. The pore water in marine sediments is saline; however, salt is excluded from the hydrate structure during hydrate formation. The exclusion of salt in turn increases the pore water chlorinity. With geological time, this high chloride concentration decreases because of dissipation of chloride by advection and diffusion. When the hydrate cores are recovered, the hydrates dissociate, which in turn leads to freshening of pore water which causes a negative chloride anomaly that is estimated to be proportional to the amount of the hydrate present. The phenomenon of chloride anomaly has been discussed in details in various sources (Hesse and Harrison, 1981; Ussler and Paul, 2001). However, chloride anomalies can not always indicate the presence of gas hydrates. Other competing reactions occurring in the sediments, such as clay dehydration reactions, can be wrongly interpreted in the presence of gas hydrates. The measurement of temperature anomaly in combination with the chlorinity anomaly has been effective in estimating the distribution of hydrates in sediments (Trehu et al., 2004).

2.8.4 Well logging

Downhole logging tools are used for estimating the concentration of hydrates in the sediments. Since gas hydrates have unique properties (such as electrical resistivity, acoustic properties) downhole logging can be used to detect the hydrates in subsurface (Shipboard Scientific Party, 2003; Collett et al., 2005). The well logging models modified for gas hydrates can be used to estimate the saturations of gas hydrates in the sediments. The primary well logs used to estimate the gas hydrates in sediments are gamma, bulk density, electrical resistivity, and P-wave sonic logs.

All these measurements on the cores have greatly increased the understanding of distribution patterns of hydrates in marine as well as permafrost sediments. It is now widely believed that hydrate distribution is very heterogeneous in marine sediments and exist in different morphologies.

2.9 Hydrate patterns in sediments

Hydrates exist in various patterns in sediments. Fig. 2.8 shows various types of hydrate distribution patters collected during various research expeditions. Table 2.2 describes the characteristics of these hydrate patterns in these sediments. Study of the effect of hydrates on seafloor stability and gas production require understanding of the hydrate patterns existing in the geological framework. There are various factors which control the hydrate patterns in sediments:

1. Presence of faults/fractures in the sedimentary layers (Milkov and Sassen, 2002)
2. The flux of the migrating gases. High gas flux settings typically tend to form the massive hydrate layers
3. The geomechanical stress state in sediments (Kleinberg, 2006)

In the broader sense, disseminated hydrate patterns are found in coarser grained sediments; and veins, veinlets, lenses, and layers are found usually in finer grained sediments. When the hydrates crystallize in the sediment matrix, they generally deform the sediments because of the pressure of crystallization (Sassen, 2007). However, the magnitude of this crystallization pressure is not known.

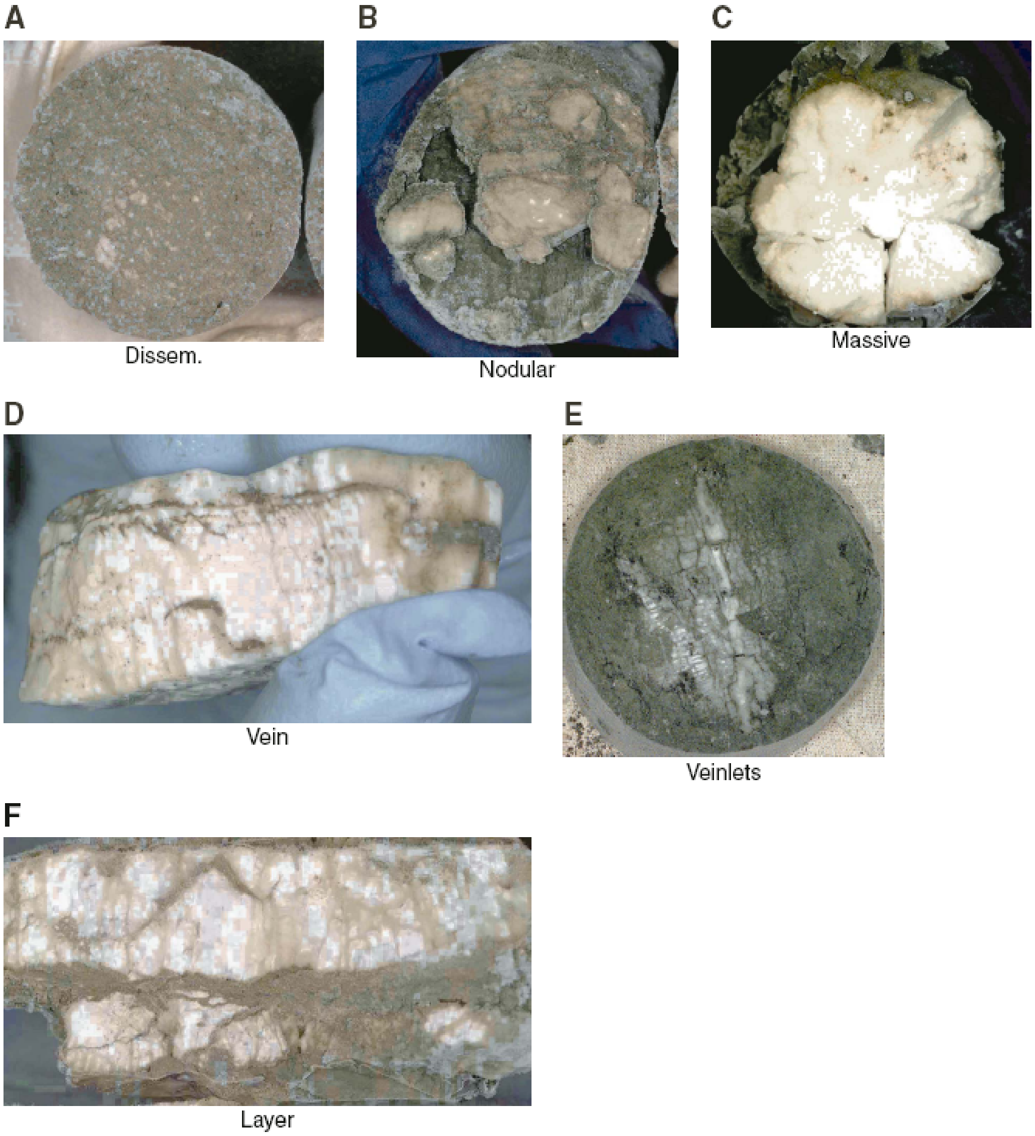

Fig. 2.8. Hydrate patterns in sediments (from Shipboard Scientific Party, 1996).

Table 2.2

Hydrate patterns in sediments (from Shipboard Scientific Party, 1996)

Pattern	Description
Layer	Plate like gas hydrate that transects the core conformable to bedding. Its apparent thickness is typically of the order of a few centimeters
Lens	A hydrate layer or other feature with tapering margin
Vein	Tabular gas hydrate feature that transects the core at an angle to the bedding. Its apparent thickness is of the order of a few centimeters
Veinlet	Thin, tabular gas hydrates ~1 mm thick or less, commonly present adjacent to veins or layers and oriented in mutually orthogonal directions
Nodular	Spherical to oblate features typically 1-5 cm in diameter.
Disseminated	Hydrate grains less than 3 mm distributed throughout the sediment matrix
Massive	The presence of hydrate in core greater than ~10 cm in thickness and with less than 25% intercalated cement

2.10 Data collection

I collected the data from various offshore hydrate cruises to understand the characteristics of marine hydrate bearing sediments. I collected data on only offshore hydrate-bearing sediments were collected as I wanted to study geomechanical instabilities during hydrate dissociation in marine sediments. The data collected were:

1. Water depths
2. Geothermal gradients
3. Gas composition
4. Pore water salinity
5. Sedimentology data

The properties defining each of the above sections will be discussed in detail in this section.

1 *Water depth (d_w)* is the representation of pressure. *Penetration* means the depth drilled below the seafloor. The hydrostatic pressure (p_hyd) experienced at a depth, d_s below the seafloor is given by equation 2.3

$$p_\mathrm{hyd} = (d_\mathrm{w} + d_\mathrm{s})\rho_\mathrm{w} g \qquad (2.3)$$

where g is the acceleration due to gravity and ρ_w is water density

2 *Geothermal gradient* ($\frac{\Delta T}{\Delta d_\mathrm{s}}$) means the rate of temperature increase in the subsurface. The temperature, *$T(d_s)$* at any depth, d_s meters below the seafloor is given by equation 2.4

$$T(d_\mathrm{s}) \;=\; T_0 \;+\; \frac{\Delta T}{\Delta d_\mathrm{s}} d_\mathrm{s} \qquad (2.4)$$

where, T_0 is the temperature at the seafloor.

3 *Gas composition* refers to the mole percentage of different gases in the sampled gas.

4 *Pore water salinity* means the concentration of dissolved salts in the pore water. Usually the pore water salinity is measured in the laboratory using recovered cores.

5 *Sedimentology data* in this project include the porosity, permeability, bulk density, thermal conductivity, and the geomechanical properties such as shear strength. The physical properties provide a lithological and geotechnical description of the sediment (Breitzke, 2006).

I also collected the geotechnical data such as Atterberg limits (water content, liquid limit, and plastic limit) of hydrate-bearing sediments measured during various expeditions and in laboratory research. The Atterberg limits are used to classify the sediment as clays or silts. The liquid limit and plastic limit are used extensively, either individually or together with other soil physical properties, to correlate with engineering behavior such as compressibility, permeability, compactability, swell and shear strength.

The important Atterberg limits are defined as follows:

1 *Water content:* Ratio of water mass to solid mass in a sediment specimen

2 *Liquid limit* is the water content where a soil changes from liquid to plastic behavior. Soil is placed into the metal cup portion of a standardized device called Casagrande cup. A groove is made in the soil sample (placed in the metal cup) with a standardized tool. The cup is repeatedly dropped 10 mm on to a hard rubber base until groove is closed. The moisture content at which it takes 25 drops of the cup to cause the groove to close is called the liquid limit.

3 *Plastic limit* is the water content at which the soil starts to exhibit the plastic behavior. A thread of soil is at its plastic limit when it is rolled to a diameter of 3 mm and crumbles.

In the following chapter, I discuss the important data collected at different offshore gas hydrate exploration sites.

CHAPTER III

OFFSHORE HYDRATE DEPOSITS

3.1 Introduction

Gas hydrates are distributed around the Continental margins. Fig. 3.1 illustrates various areas around the world where the hydrates are thought to exist (Makogon et al., 2007).

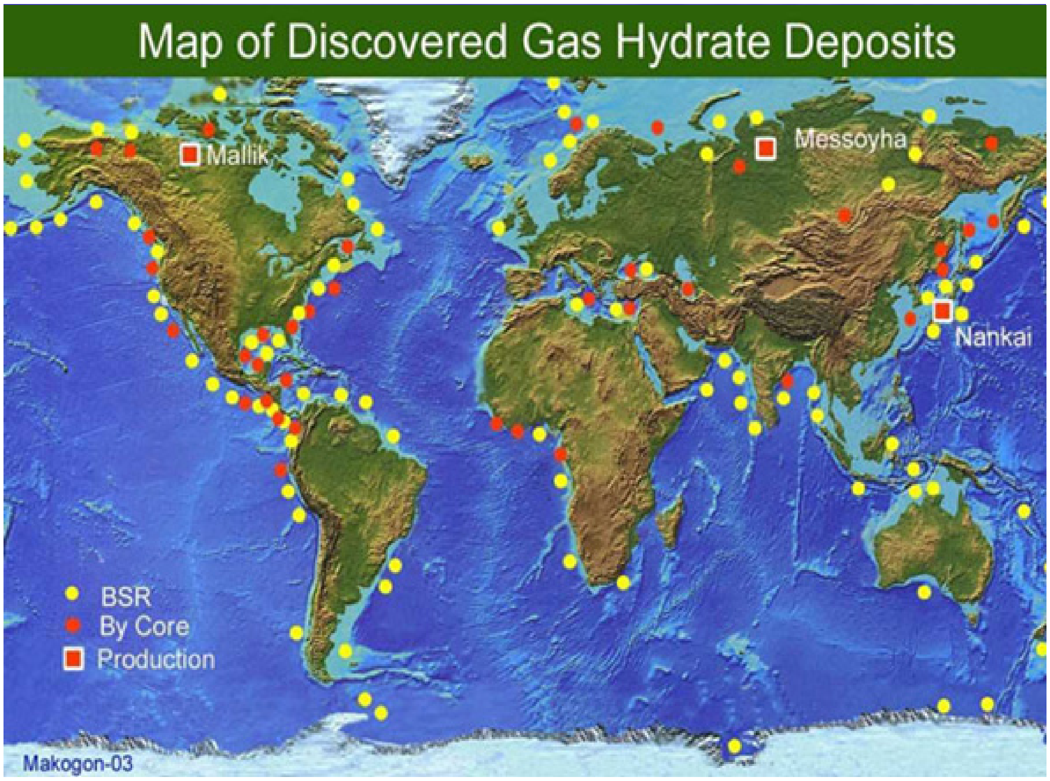

Fig. 3.1. Distribution of hydrates around the world (from Makogon et al., 2007).

The known gas hydrate deposits were discovered either from a BSR or by drilling wells into the sediments. The oceanic hydrate resource is believed to be huge as compared to onshore hydrates in the arctic permafrost (Sloan and Koh, 2008).

Oceanic hydrates have been found in different geological settings such as convergent and divergent margins (Milkov, 2005). Although numerous small expeditions conducted have studied the-near-seafloor hydrates, only a limited number of expeditions have been conducted where deep boreholes were drilled and have acquired samples from various depths. There is still a great deal of uncertainty surrounding the location and volume of gas hydrate deposits in the ocean. We know where some deposits exist because we have found them. However, most of the ocean is unexplored for gas hydrates.

I have collected the important data such as water depths, geothermal gradients, gas compositions and sediment properties from various literature sources for the offshore gas hydrate deposits. I collected the data and concentrated our efforts only for offshore hydrate deposits because of our interest in studying the seafloor stability issues in hydrate bearing sediments. All the important data are described in the following sections.

Various hydrate expeditions have been carried out by the Ocean Drilling Program (ODP), the Japanese Government (Nankai Trough) and the Chevron/US Department of Energy (DOE) joint industry project (JIP) (Gulf of Mexico). The lithological and mineralogical details are reported for the hydrate bearing sediments in the following sections.

3.2 Blake Ridge

3.2.1 Geologic setting

The Carolina rise, particularly along the Blake Ridge, was one of the first areas where marine gas hydrate was first identified on the basis of bottom simulating reflector (BSR) data.

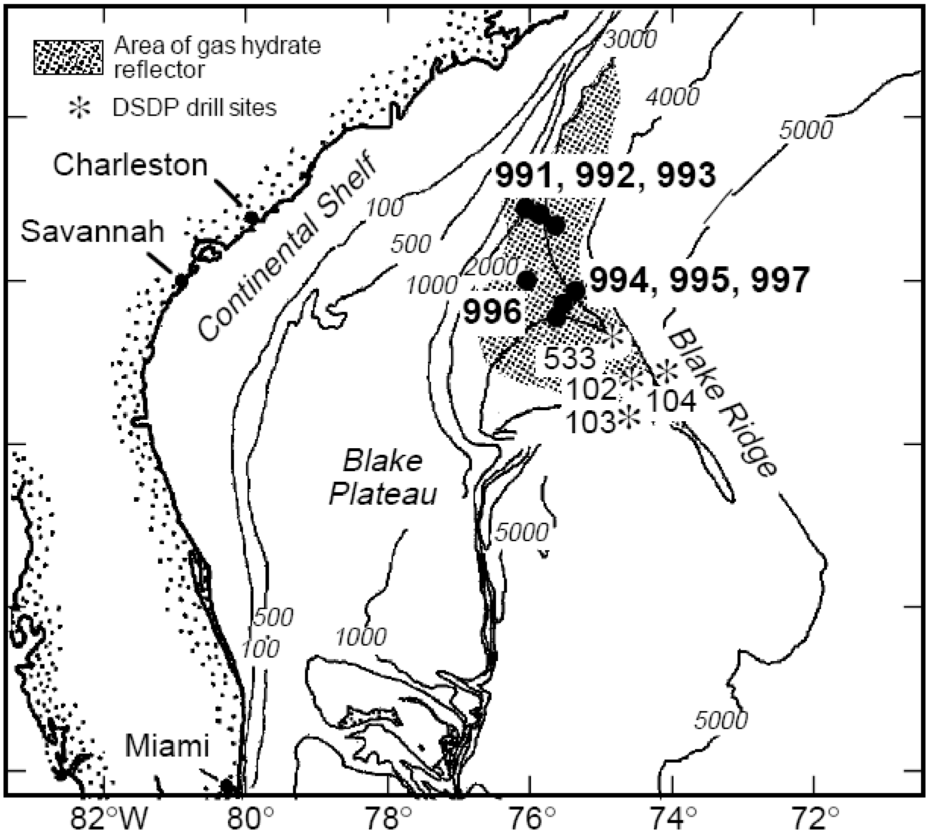

Fig. 3.2.Map of the Blake Ridge (from Shipboard Scientific Party, 1996).

Fig. 3.2 shows the map of the possible area of gas hydrate occurrence on the basis of where the BSR can be identified from seismic. A total of seven sites (991 to 997) and 17 wells were drilled in the Blake Ridge region. A number of large solid gas hydrates samples were recovered from sites 994, 996, and 997. The samples from sites 994 and 997 were either nodular or thick massive pieces of gas hydrate. X-ray computed tomography, diffraction, nuclear magnetic resonance and Raman spectroscopy gave results that indicated the gas was essentially 100% methane. Thermal conductivity values of gas hydrates from Blake Ridge range from 0.3 to 0.5 W/m/K. Equilibrium dissociation indicated that the equilibrium curve is almost the same as that of pure synthetic methane hydrate.

A large amount of microbial gas was encountered at the previous Deep Sea Drilling Project (DSDP) drill sites on the Blake Ridge and no indications of thermogenic gases were noted in these holes. At site 994, the sediments were very gassy. The probability of finding gas hydrate in this hole was high (>50%) at depths from 100 to 450 meters below the sea floor (mbsf) because of low chlorinity values in the pore water. The average geothermal gradient in this area was found to be 35.4 °C/km. The gas hydrates were recovered from nanofossil-rich clay at a sub-bottom depth of 260 to 330 m, about 200 to 120 meters above the BSR. The traditional method of core description does not work for gas hydrates because the hydrates are unstable at surface conditions. For this reason, different proxy techniques were used for the estimation of hydrate concentration in the pores. Using the chloride values, the gas hydrate concentration of some samples was as high as 14%. On the average, the values of 1.3%, 1.8% and 2.4% of the sediment above 450 mbsf was filled with gas hydrates at sites 994, 995, and 997. Gas volumes from the Pressure Core Sampler (PCS) indicated the range of hydrate concentration to be in between 0% and 9%. Seismic data from vertical seismic profiles indicate that the sediments contain at least 2% gas hydrates.

Nearly as much gas hydrate was inferred to occur at site 994 (no BSR present) as with sites 995 and 997 (where extensive BSR was present). This demonstrates that gas hydrates may be present at a given location even if a BSR is not identified by seismic. Sites 991, 992, and 993 were the diapir sites. Shallow holes (50 to 60 mbsf) were drilled on the flanks and crest of the Cape Fear Diapir and Blake Ridge Diapir. The sediments from these three sites were strongly deformed.

3.2.2 Water depths and geothermal gradient

Table 3.1 summarizes the water depths and penetrated depth and Table 3.2 shows the measured geothermal gradients in different wells at theBlake Ridge during ODP cruise 164.

The gas composition measured in gas hydrates recovered at Blake Ridge consists mainly of methane (>99.95%).

Table 3.1

Water depths and penetration for the Blake Ridge (from Shipboard Scientific Party,)

Well number	Water Depth (m)	Penetration (mbsf) Mbsf: meters below seafloor
994A	2797.6	36.4
994B	2797.6	6.9
994C	2799.1	703.5
994D	2799.1	670.0
995A	2778.5	704.6
995B	2776.9	700.0
996A	2169.6	63.0
996B	2184.1	3.4
996C	2184.7	2.6
996D	2169.7	52.2
997A	2770.1	434.3
997B	2770.1	750.7

Table 3.2

Geothermal gradients measured at Blake Ridge (from Shipboard Scientific Party, 1996))

Well number	Thermal gradient (°C/100m)
994C	3.87
995A	3.20
997A	3.91

3.2.3 Sedimentology data

Table 3.3 shows the sediment types recovered at different sites at Blake Ridge. The recovered cores constitute mainly of clays and silty-clays. The important feature of the recovered sediments is the presence of nanofossils and foraminifers. Table 3.4 describes the average mineralogy at different sites in Blake Ridge. Figs 3.3 to 3.5 describe the important physical properties of Blake Ridge sediments at different drilled sites.

Table 3.3

Sediment types at the Blake Ridge (from Shipboard Scientific Party, 1996)

Site	Major lithology	Other constituents
994	Silty Clay	Nanofossil, foraminifers
995	Silty Clay	Nanofossil, foraminifers
996	Silty-clay	Nanofossil
997	Silty Clay	Nanofossil, foraminifers

Table 3.4

Major mineralogy at the Blake Ridge (from Shipboard Scientific Party, 1996)

Site	Major mineralogical constituents		
	Clay	Quartz	Calcite
994	50-75%	5-15%	10-30%
995	50-85%	5-10%	10-30%
996	45-70%	10-20%	15-35%
997	60-80%	<10%	15-30%

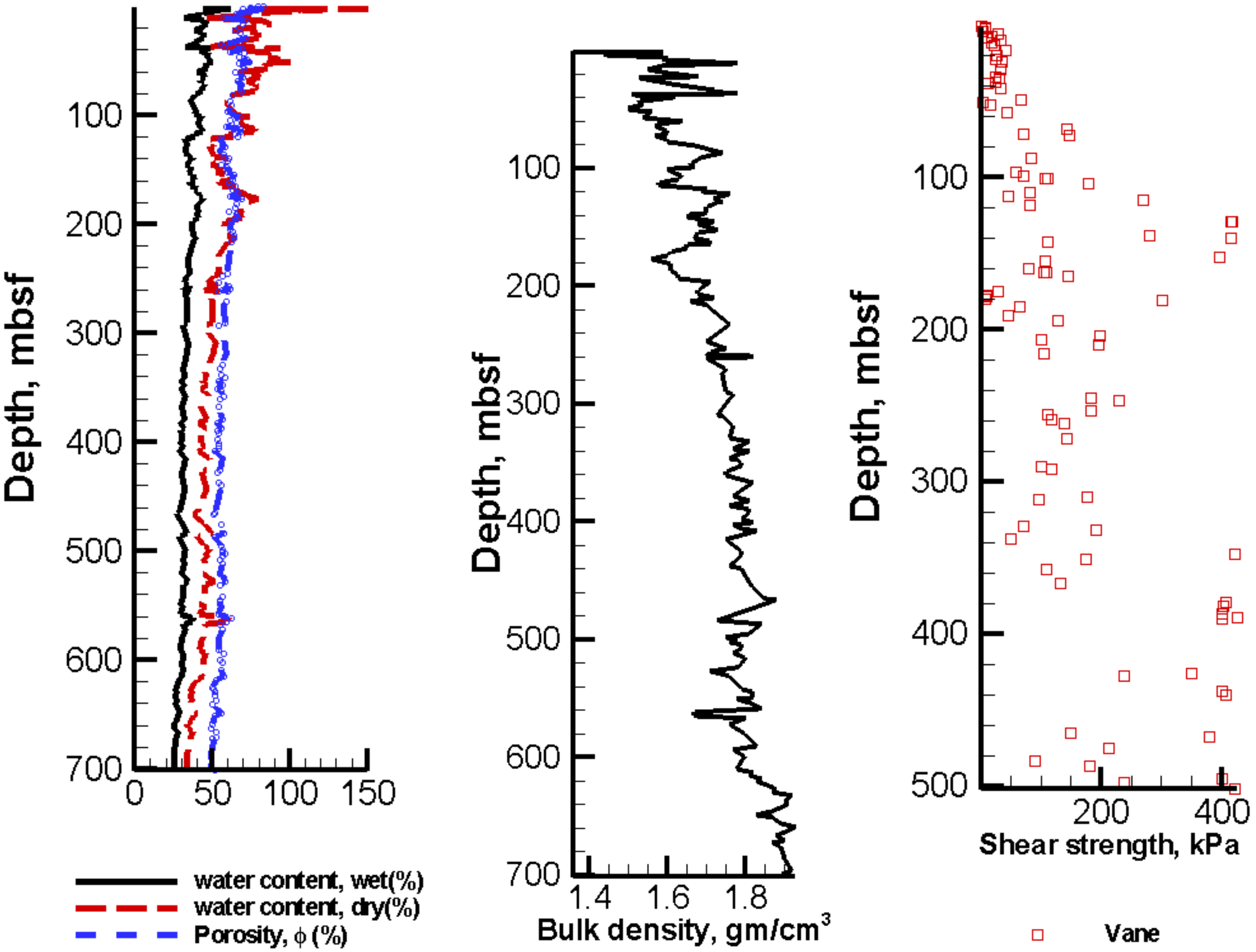

Fig. 3.3. Physical properties of the sediments from Hole 994 C (from Shipboard Scientific Party, 1996).

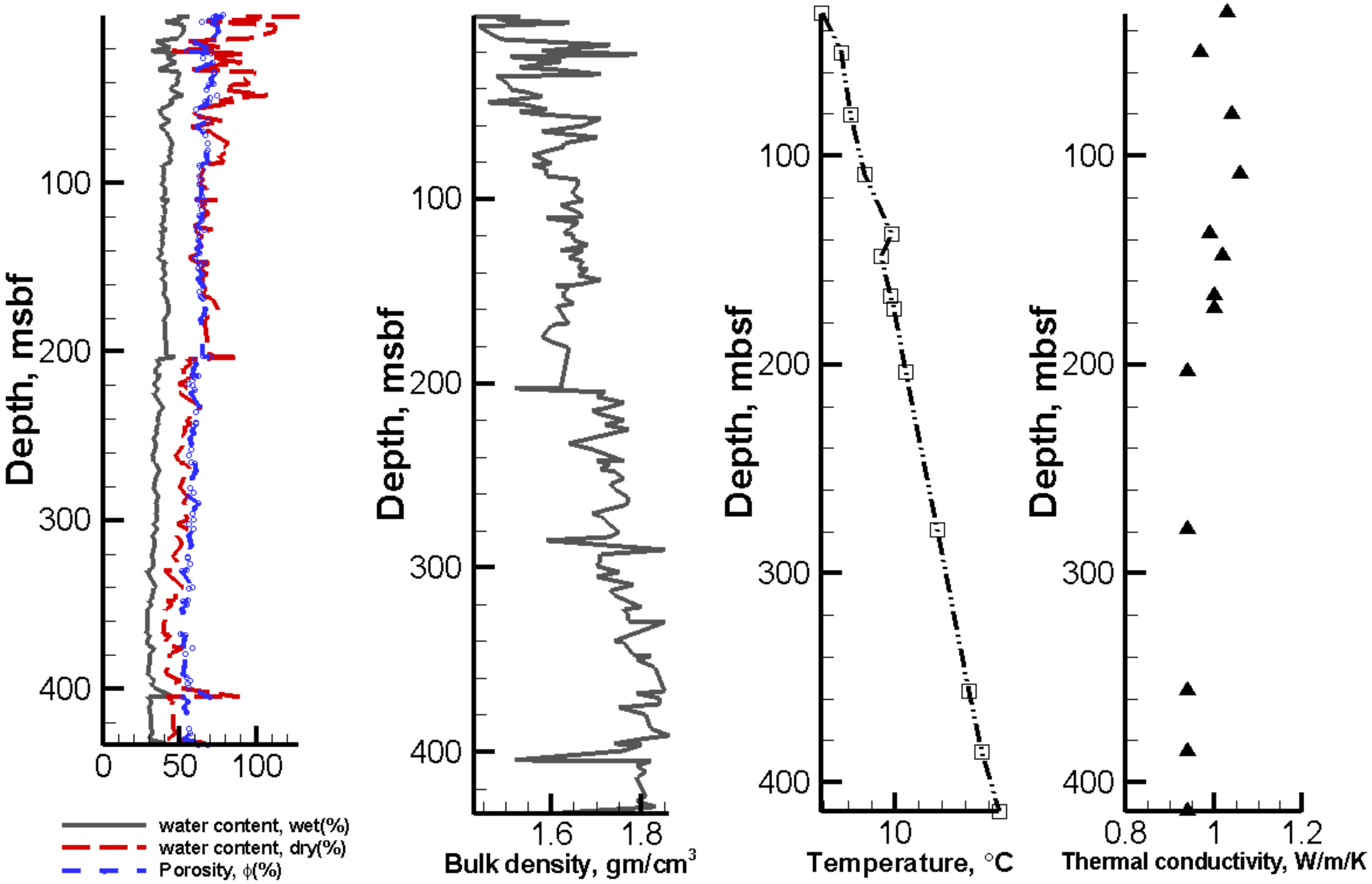

Fig. 3.4. Physical properties of sediments from Site 997A (from Shipboard Scientific Party, 1996).

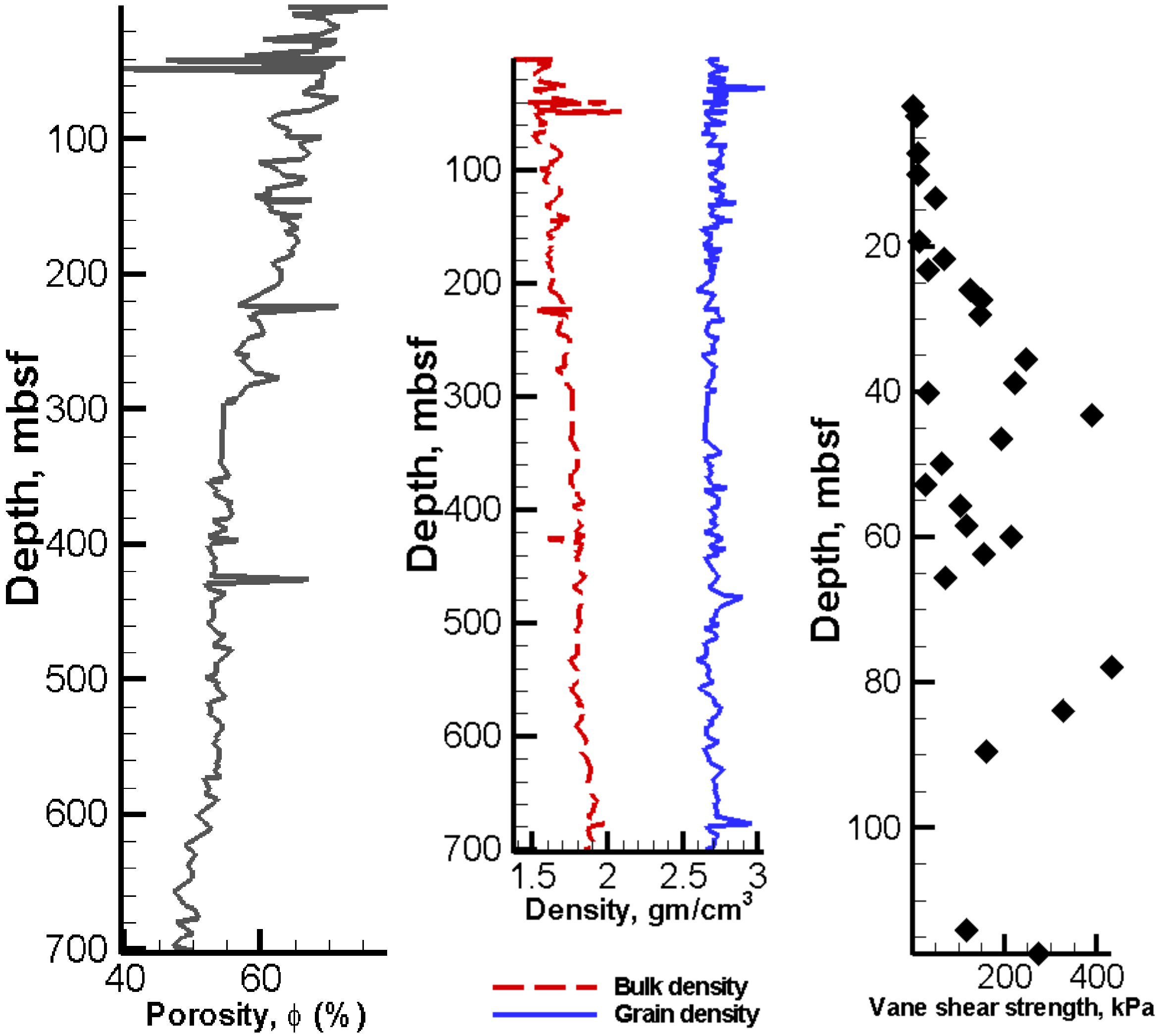

Fig. 3.5. Physical properties of sediments from Hole 995 A (from Shipboard Scientific Party, 1996).

3.2.4 Hydrate patterns in sediments

The gas hydrates recovered at Blake Ridge were white and occurred in three different forms:

- massive pieces, cylindrical to round in shape and as much as 5 to 8 cm long, in sediments recovered from the uppermost 9 mbsf
- platy, 1 to 4 mm thick veins that filled wavy vertical fractures
- vertically oriented rod-shaped nodules ~ 1 cm in diameter and 3 to 12 cm long that tapered down the core

3.2.5 Grain size control

Ginsburg et al (2000)studied the grain size distribution at sites 994, 995 and 997 drilled at Blake Ridge during ODP cruise 164. According to 375 samples collected, the depth intervals where pore-water chlorinity anomalies occur are in relatively coarse-grained sediments. The pore-water chlorinity is a proxy indicator for the presence of gas hydrates. Fig. 3.6 shows the grain-size distributions from sites 994, 995 and 997 along with the chlorinity anomalies. The grain size fractions are divided into five ranges defined as:

1 = (>0.05 mm), 2 = (0.05-0.01 mm), 3 = (0.01-0.005 mm), 4 = (0.005-0.001 mm), and 5 = (<0.001 mm)

The data presented in Fig. 3.6 suggests that the gas hydrate distribution is more common in coarser grained sediments. This observation is based on the chlorinity anomaly measured in various cores recovered from Blake Ridge. According to data, the sediment grain size distribution of sediments in the hydrate stability zone ranges from 0.005 to 0.001 mm.

The most abundant clay minerals in the Blake Ridge sediments are illite/kaolinite.

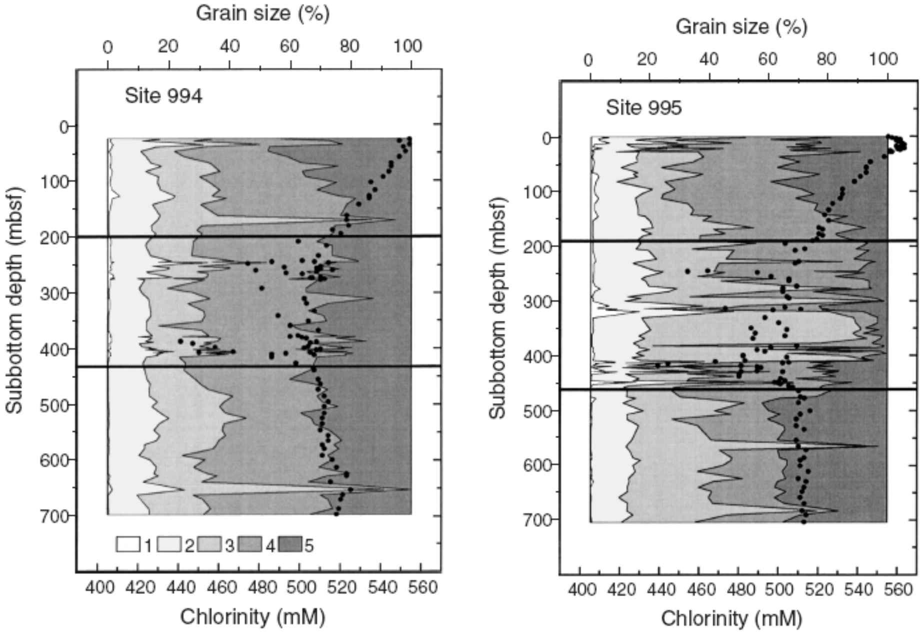

Site 994

Site 995

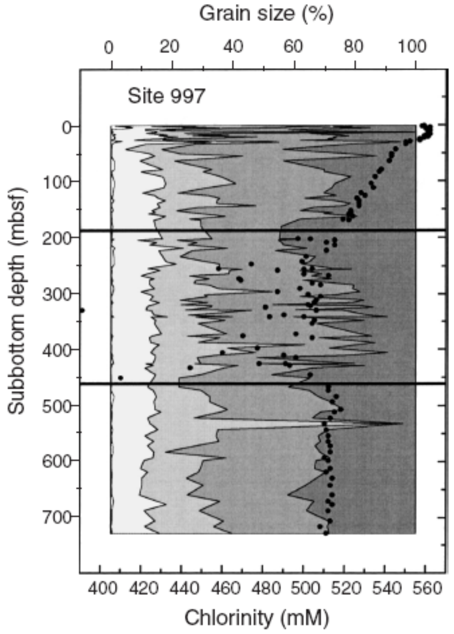

Site 997

Fig. 3.6. Sediment grain size control on hydrate distribution at the Blake Ridge (from Ginsburg et al., 2000).

3.2.6 Index properties

Table 3.5 shows the index properties measured in the laboratory from the well 995A at Blake Ridge. Table 3.6 shows the typical strength properties of the sediments from well 995A

Table 3.5

Index properties of the sediments from well 995 A (from Winters, 2000)

Depth (mbsf)	Water content	Porosity (%)	Liquid limit	Plastic limit	Liquidity index	Plasticity index
3.09	69	64.7	68	24	0.89	44
148.5	62	62.3	99	35	0.39	64
350.8	44	54	83	35	0.19	48
546.1	52	57.2	82	40	0.29	42

Table 3.6

Strength properties of sediments from well 995A (from Winters, 2000)

Depth (mbsf)	Shear strength (kPa)		
	Vane	Remolded	Penetrometer
3.09	25	4	22
148.5	135	34	120
350.8	145	N/A	230

3.3 Cascadia Margin

3.3.1 Geologic setting

Fig. 3.7 shows the expeditions performed in the Cascadia Margin, by the Ocean Drilling Program (ODP) Leg 168, 204 and International Ocean Drilling Program (IODP) Expedition 311.

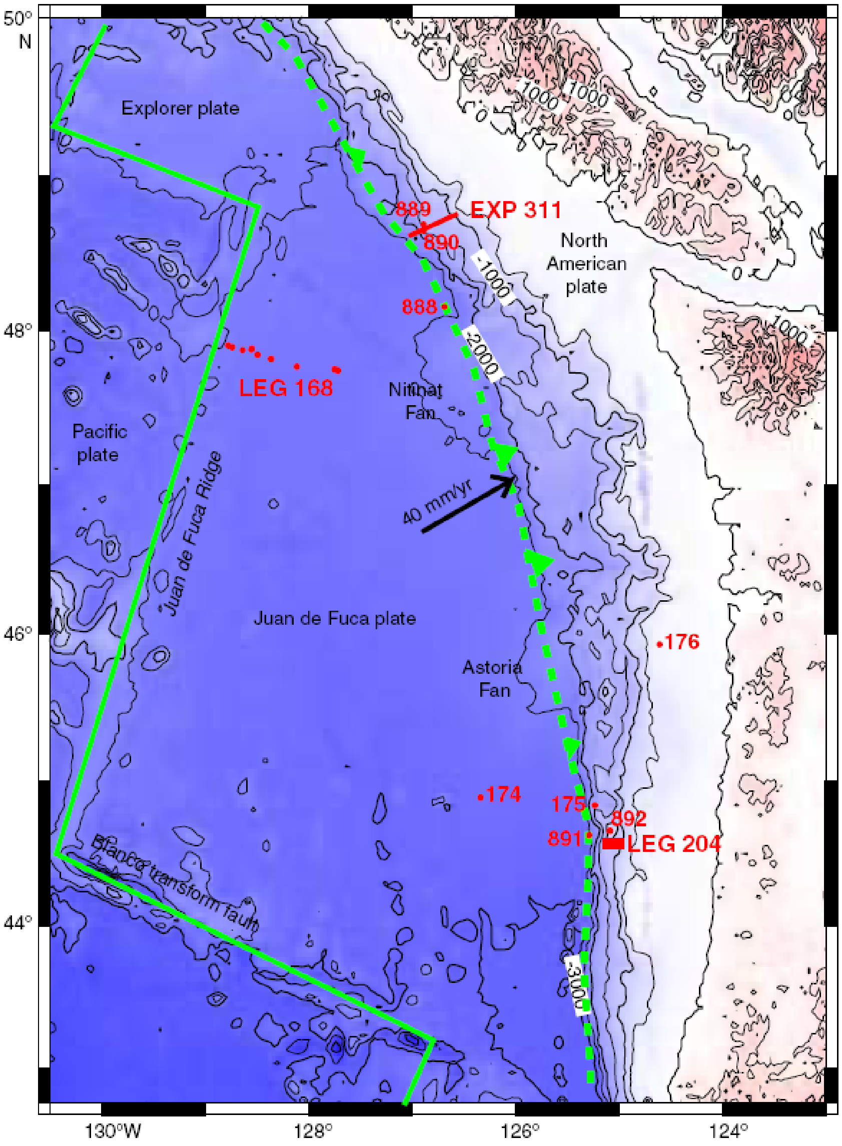

Fig. 3.7. Map of drilling sites at Cascadia Margin (from Trehu et al., 2006).

Leg 311 targeted a segment of northern Cascadia Margin where the sediments were coarser grained. The sediments encountered during the Leg 204 were finer grained. Leg 204 was carried out at Hydrate Ridge.

Hydrate Ridge is a 25-km long and 15-km wide ridge in the Cascadia accretionary complex, formed as Juan De Fuca plate subducts obliquely beneath North America at a rate of ~4.5 cm/year (Shipboard Scientific Party, 2003). Sediment on the subducting plate contains large volumes of sandy and silty turbidites. Hydrate Ridge is characterized by a northern summit at a water depth of ~600 m and a southern summit at a water depth of ~800 m (Fig. 3.8).

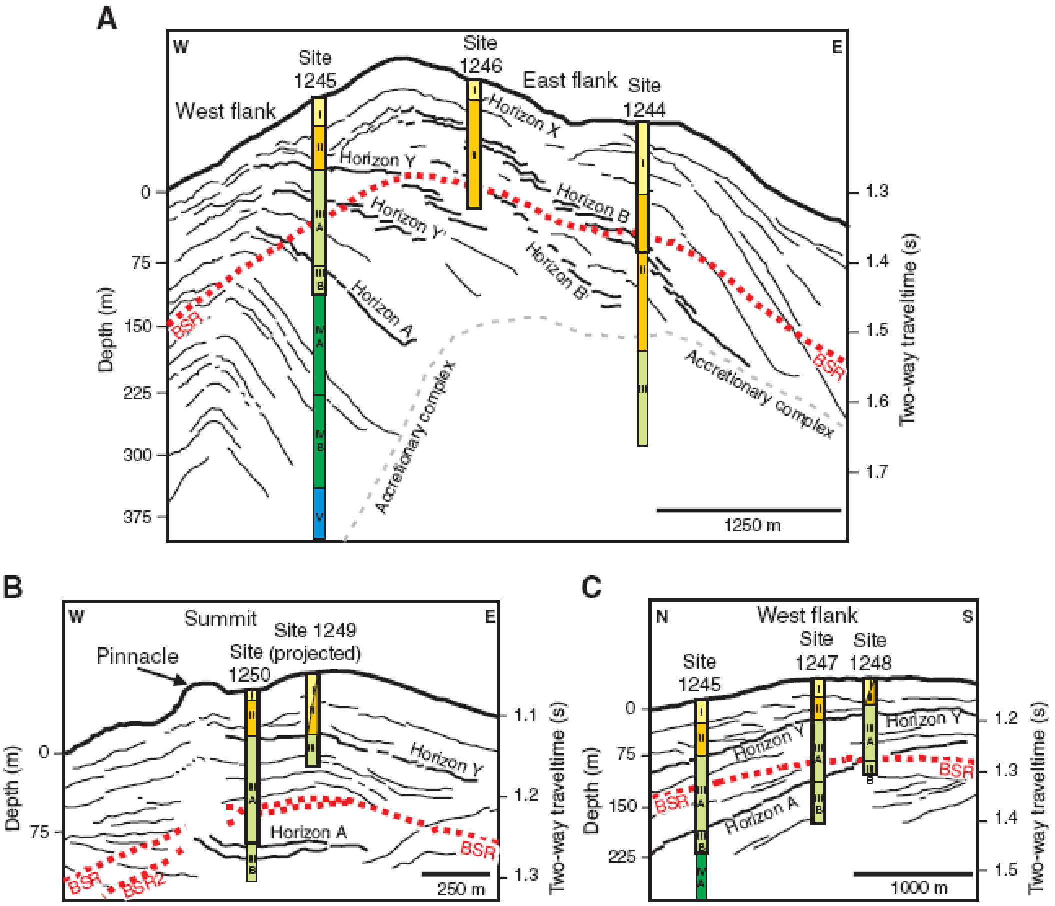

Fig. 3.8. Drilling sites during Leg 204 (from Gracia et al., 2006).

ODP Leg 204 was the first expedition to evaluate gas hydrates distribution in accretionary complexes. The distribution of gas hydrates in the nine sites and 45 wells is very heterogeneous, both laterally and vertically. The gas hydrates are present in the form of lenses and nodules of sub-millimeter to centimeter thickness. These lenses and nodules occur in clusters, and are several meters thick, and have orientations ranging from horizontal to vertical (Janik et al., 2003; Trehu et al., 2004; Abegg et al., 2006). Gas hydrates are usually present along the vertical fractures and do not significantly alter the sediment stiffness. The gas hydrate distribution at Cascadia Margin is a result of two different regimes of gas transport in the sediments, low flux settings and high flux settings (see Chapter II).

The water depths at Cascadia Margin drilled wells range from 790 to 1200 meters. The calculated geothermal gradient from the temperature measurements at different wells has an average value of 55°C/km. The BSR is present ubiquitously throughout the Hydrate ridge. A total of 13 hydrate bearing samples were subjected to X-ray Diffraction (XRD) measurements. Out of the 13 samples, 8 samples showed the hydrate concentration ranging from 1 to 7%. Five samples showed higher gas hydrate concentrations ranging from 20 to 70%. Detailed fabric analysis of the recovered samples showed that the gas hydrates were present in layers with different dips. In the shallow sediments (<40 m below seafloor) the gas hydrate layers were found to be parallel or subparallel to the bedding planes. At depths greater than 40 m, gas hydrate layers were found to be present at steeper dip angles (30° to 90°). The gas hydrates were interpreted to be fracture filling at these steeper angles.

Fig. 3.9 illustrates the drilled wells at Cascadia Margin during Leg 204. The BSRs are shown in the cross-section and the color contours show the calculated gas hydrate saturations.

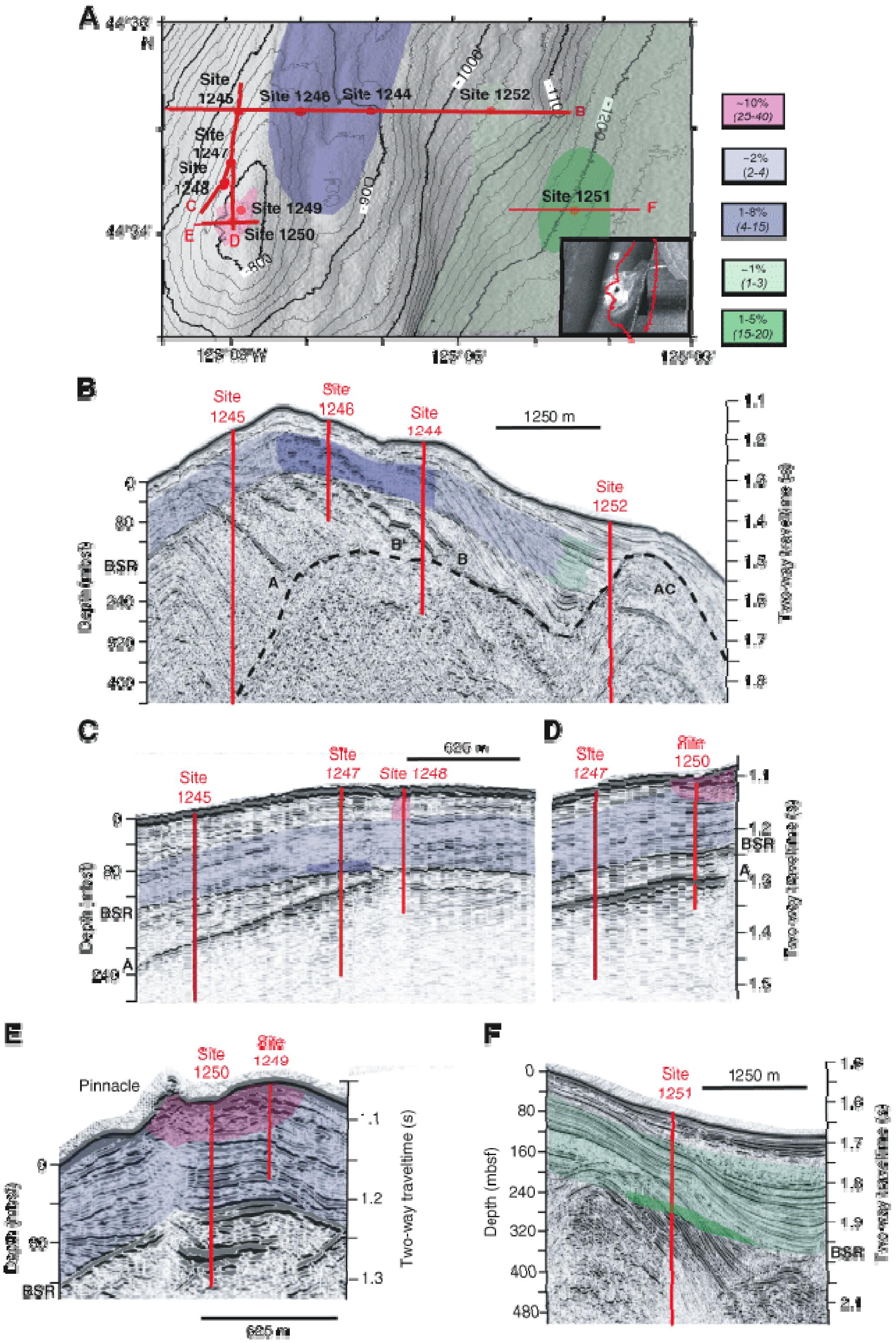

Fig. 3.9. ODP Leg 204 drill sites. Color contours refer to calculated gas hydrate saturations. Numbers in paranthesis refer to figure parts B-F (from Trehu et al., 2006).

3.3.2 Water depths and geothermal gradients

Table 3.7 describes the water depths and the penetrated depth at various sites in Cascadia Margin and Table 3.8 shows the measured geothermal gradients at different sites.

Table 3.7

Water depths, BSR and penetration at Cascadia Margin (from Su et al.,2006; Trehu et al., 2006)

Site	Water depth (meters)	BSR depth (meters)	Number of wells drilled	Penetration (mbsf) Mbsf: meters below seafloor
1244	895	125	5	0 – 380
1245	870	134	5	24 - 540
1246	850	114	2	136.7 – 180
1247	835	N/A	2	220 – 270
1248	830	124	3	17 – 194
1249	775	115	12	11 – 90
1250	792	114	6	145 – 210
1251	1210	196	8	9.5 – 445

Table 3.8

Geothermal gradients measured at the Cascadia Margin (from Trehu et al., 2006)

Site	Geothermal gradient (°C/100m)
1244	6.21
1245	5.4
1247	5.3
1248	5.4
1250	5.8
1251	5.2

3.3.3 Sedimentology data

Gracia and co-workers (2006) have analyzed the samples from seven Hydrate Ridge sites, and the grain sizes were defined as coarse-grained (above 50 μm) or silt and clay (below 50 μm).

Table 3.9 shows the sediment composition and Table 3.10 shows the clay mineralogy of the Cascadia Margin sediments. Figs. 3.10 to 3.12 show the important physical properties measured at three different sites during the Cascadia Margin expedition i.e. 1244, 1249 and 1251.

Table 3.9

Sediment composition at the Cascadia Margin (from Shipboard Scientific Party, 2003)

Site	Major lithology	Clays %	Silt %	Sand %
1244	Clay/Silty-clay	40-65	30-60	<5
1245	Clay/Silty-clay	60-90	0-20	<5
1246	Clay/Silty-clay	70-80	5-25	<5
1247	Clay/Silty-clay	70-90	5-30	<10
1248	Clay/Silty-clay	60-90	5-30	<5
1250	Clay/Silty-clay	40-65	35-50	<5
1251	Clay/Silty-clay	60-80	15-30	<5
1252	Clay/Silty-clay	70-95	5-30	<10

Table 3.10

Calculated clay mineralogy at the Cascadia Margin (from Gracia et al., 2006)

Hole	Detrital mica	Smectite	Kaolinite	Chlorite
1244 E	30-60	5-30	15-30	10-30
1250 C	30-50	10-30	5-15	10-20
1245 B	~50	5-10	10-15	10-30

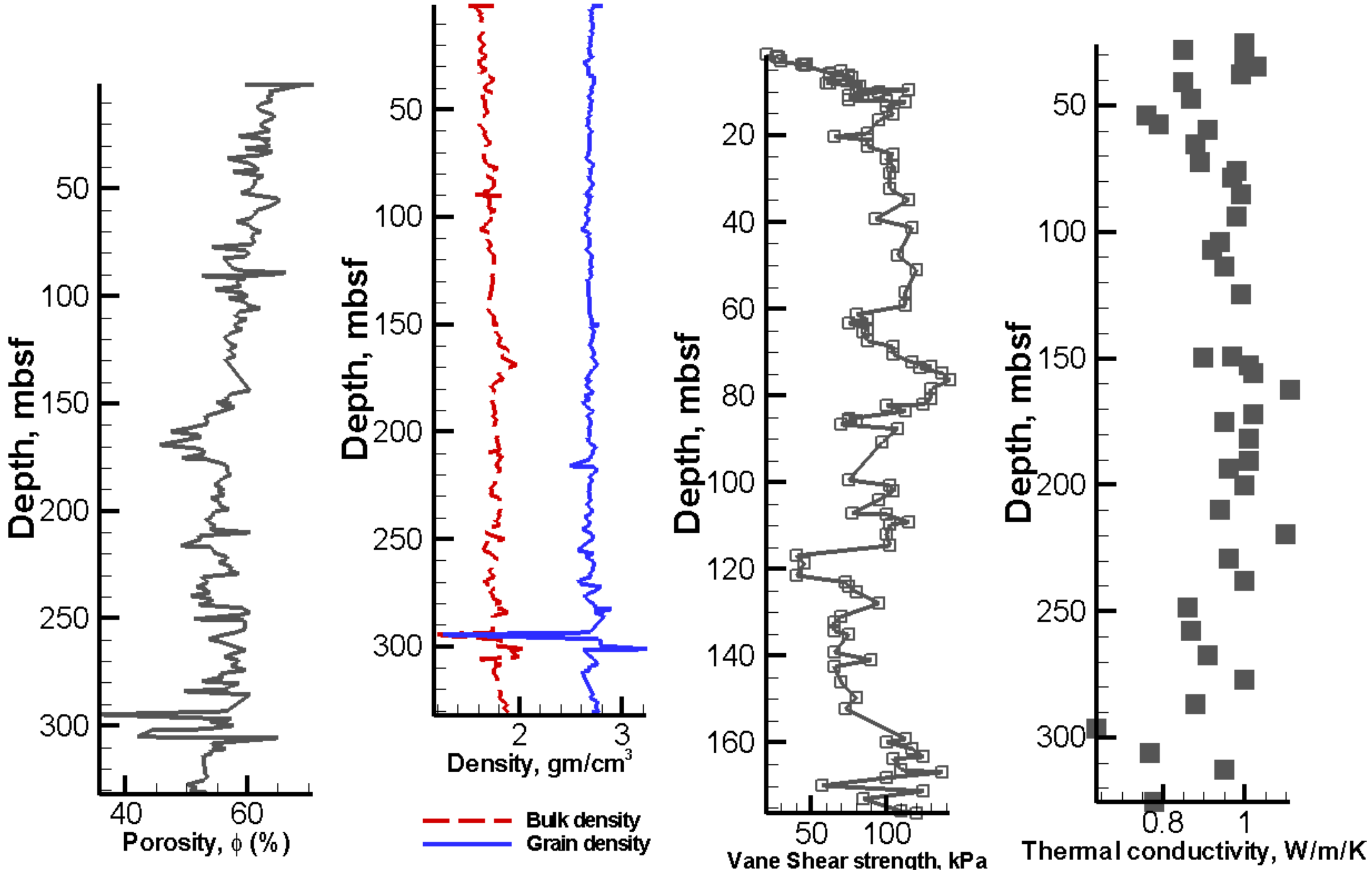

Fig. 3.10. Physical properties of sediments at Hole 1244 C (from Shipboard Scientific Party, 2003).

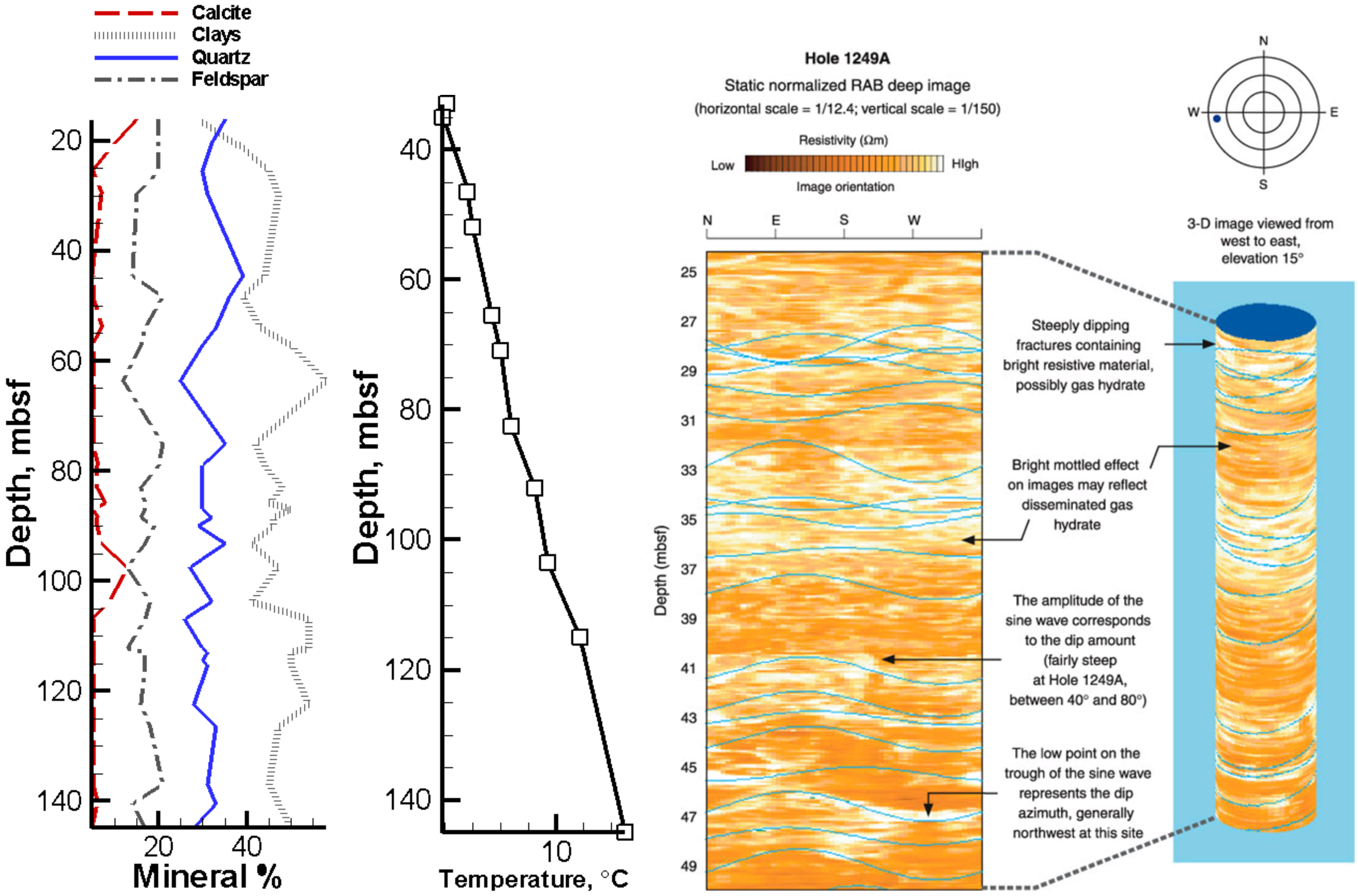

Fig. 3.11. Some properties of the sediments at Site 1249 (from Shipboard Scientific Party, 2003).

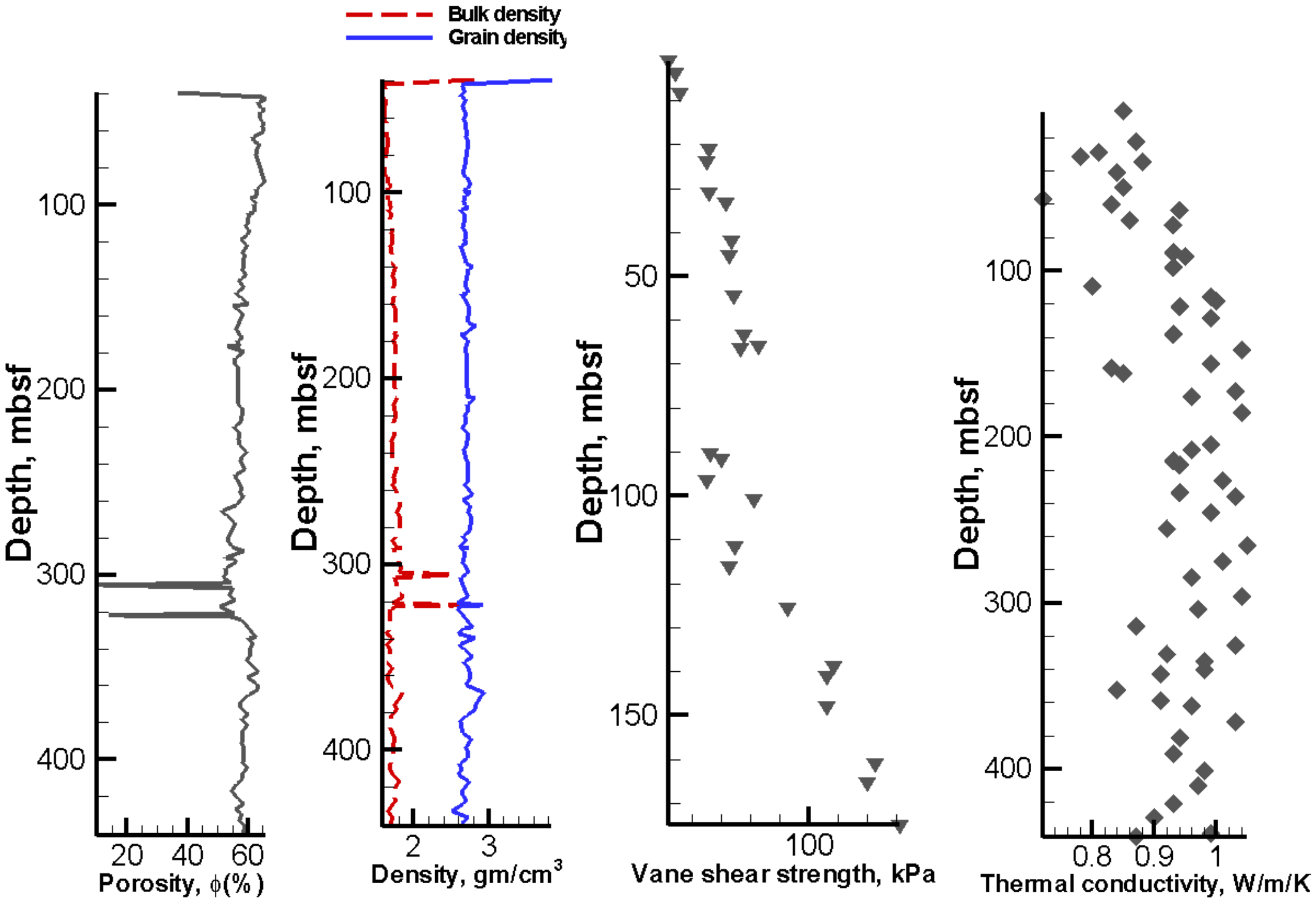

Fig. 3.12. Physical properties of the sediments at Hole 1251 B (from Shipboard Scientific Party, 2003).

3.3.4 Grain-size control

"Sediments from southern Hydrate Ridge show small fluctuation in grain-size distribution dominated by fine-grained (clay and silty-clay) sequences locally interbedded with clayey silt to silty layes"(Gracia et al., 2006)

The correlation between existence of gas hydrates and grain-size compositions has been studied in detail (Su et al., 2006). Fig. 3.13 illustrates the location of the cores and the grain size distribution from collected cores at Cascadia Margin. The results illustrate that the studied samples fall into the grain-size range of 1-148 μm. The presence of gas hydrates generally correlate well with the sediment layers with >0.5 to 5% sand. However, gas hydrates were also observed in layers containing <0.5% sand (but more silt) (Su et al., 2006).

The strength characteristics of the sediments recovered at Cascadia Margin have also been measured in the laboratory (Tan et al., 2006). The friction angle ranges from 27 to 37°.Table 3.11 describes the laboratory measured gas and water permeability of Cascadia Margin sediments.

Table 3.11

Permeability in Cascadia Margin sediments (from Kitajima et al., 2007)

Area	Sediment	Gas permeability	Water permeability
Cascadia Margin	Siltstone	10^{-14} to 10^{-16} m2 (10 to 0.1 md)	10^{-17} to 10^{-19} m2 (0.01 to 0.0001 md)
	Sandstone	10^{-12} to 10^{-13} m2 (1000 to 100 md)	10^{-15} to 10^{-16} m2 (1 to 0.1 md)

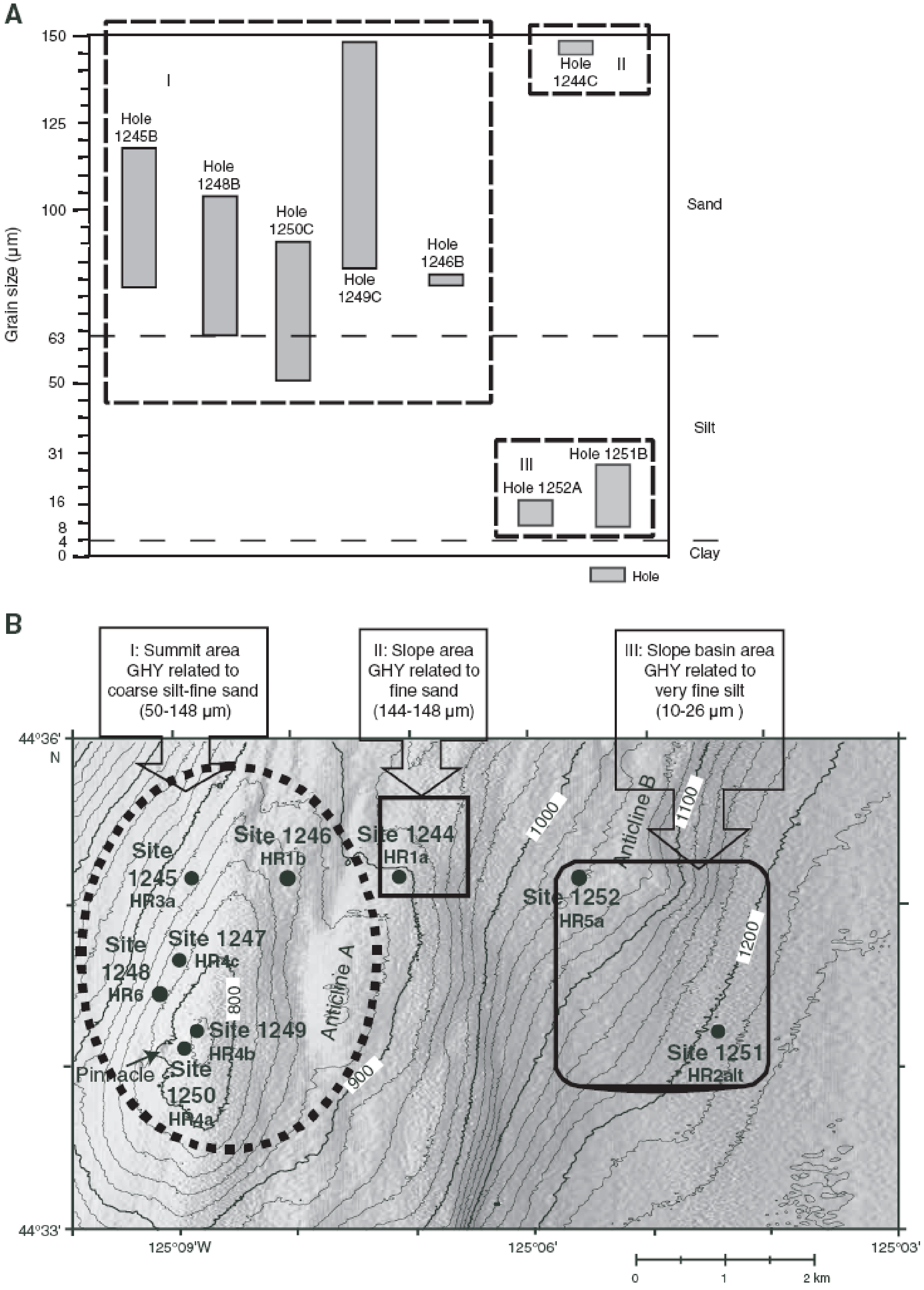

Fig. 3.13. Grain size controls on hydrate distribution at the Cascadia Margin (from Su et al., 2006).

3.3.5 Index properties

The representative values of index properties of Cascadia Margin sediments recovered at site 1244 are described in Table 3.12.

Table 3.12

Index properties from the sediments at site 1244 (from Tan et al., 2006)

Depth (mbsf)	Water content (%)	Liquid limit (%)	Plastic limit (%)	Plasticity index	Liquidity index
5.7	60	71	32	39	72
20.3	63.8	82	37	45	60
32.98	62.7	87	42	45	46
52.81	60.05	85	38	47	47
70.88	58.1	86	40	46	39
135.5	48.85	77	35	42	33

Based on the index properties, the Cascadia Margin sediments can be classified as high plasticity silt (Tan et al., 2006).

3.4 Gulf of Mexico

3.4.1 Geological setting

Gas hydrates have been recovered in more than 53 sites in the northwest portion of the Gulf of Mexico (GOM) at water depths of 440 to 2400 m (Sassen et al., 1999a). According to Krason and Ciesnik (1985), the total volume of hydrate-bound gas in the GOM is estimated to be between ~0.5 and 255 x 10^{12} m^3. BSRs are rare in the GOM and no relationship has been observed between the presence of actual hydrates and the geophysical signatures. Sassen et. al. have performed numerous field sample studies from the shallow sediments from the GOM. There have also been two cruises in the GOM, namely Leg 96 of Ocean Drilling Program and the Chevron/DOE JIP work in 2005.

Although the GOM originated as a passive Continental margin, it is tectonically-active with complex geological features. These features are faults, folds and salt piercements. The main characteristic in the GOM that is different from other continental margins is that hydrates are found in the shallow sediments. In other Continental margins (e.g. Blake Ridge, Costa Rica margin, Cascadia margin and Nankai accretionary margin) the top of the GHSZ for methane gas is found from tens to hundreds of meters below seafloor. Figs. 3.14 to 3.21 (Milkov and Sassen, 2003) illustrate some of the areas studied for hydrates in the Gulf of Mexico.

Gas hydrates in Gulf of Mexico occur in various forms; from seafloor to deeper sediments.

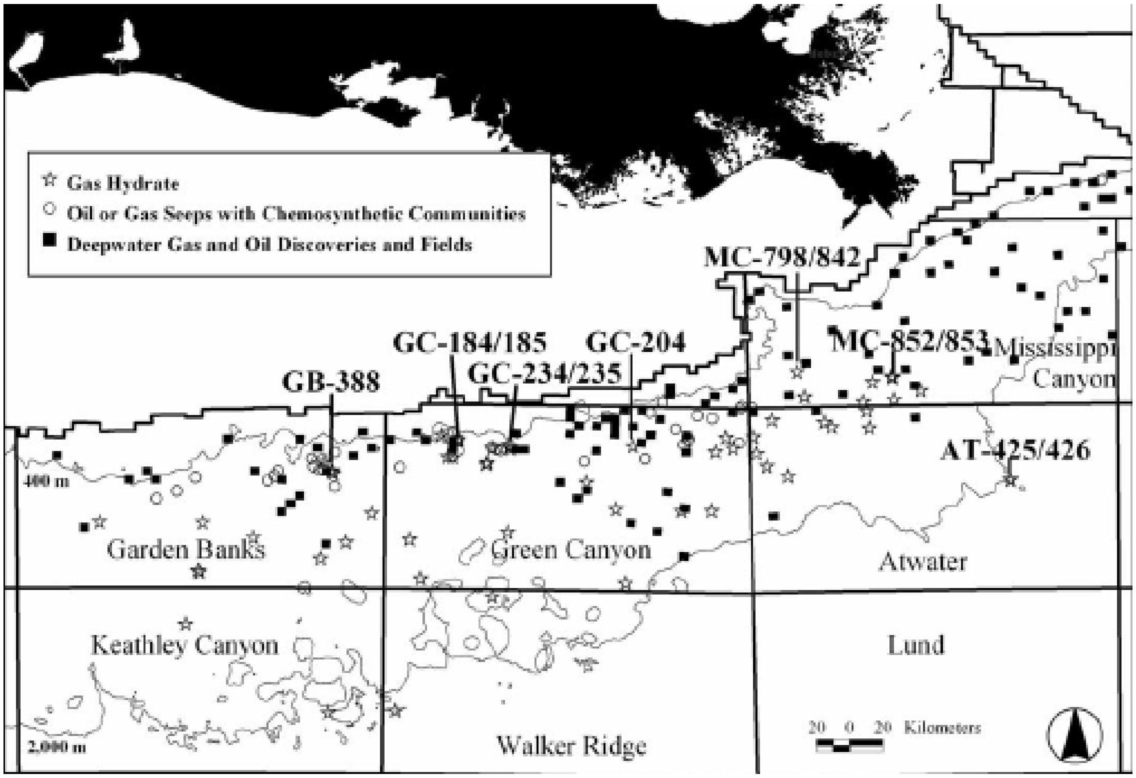

Fig. 3.14. Hydrate study locations at Gulf of Mexico (from Milkov and Sassen, 2003).

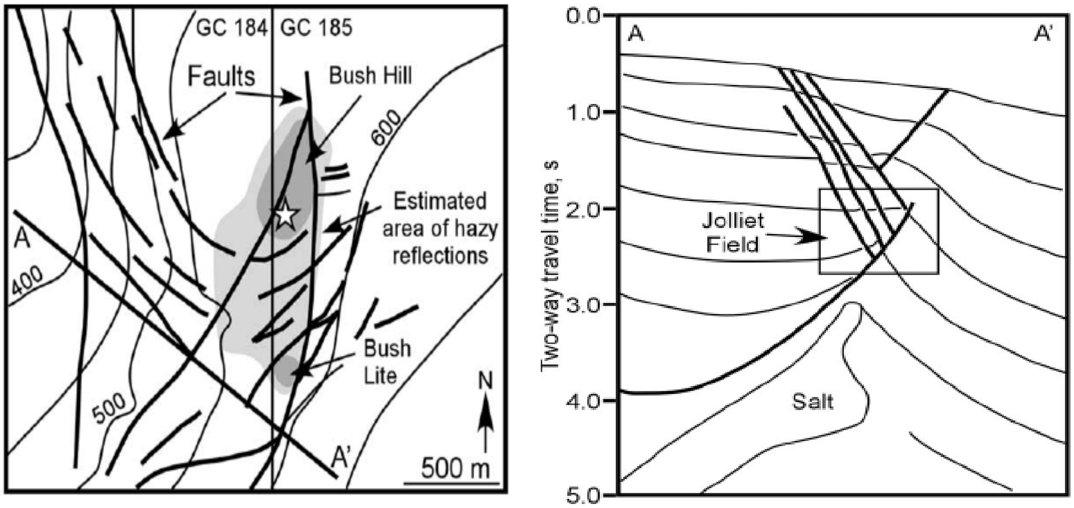

Fig. 3.15. Green Canyon 184/185 map and cross section (from Milkov and Sassen, 2003).

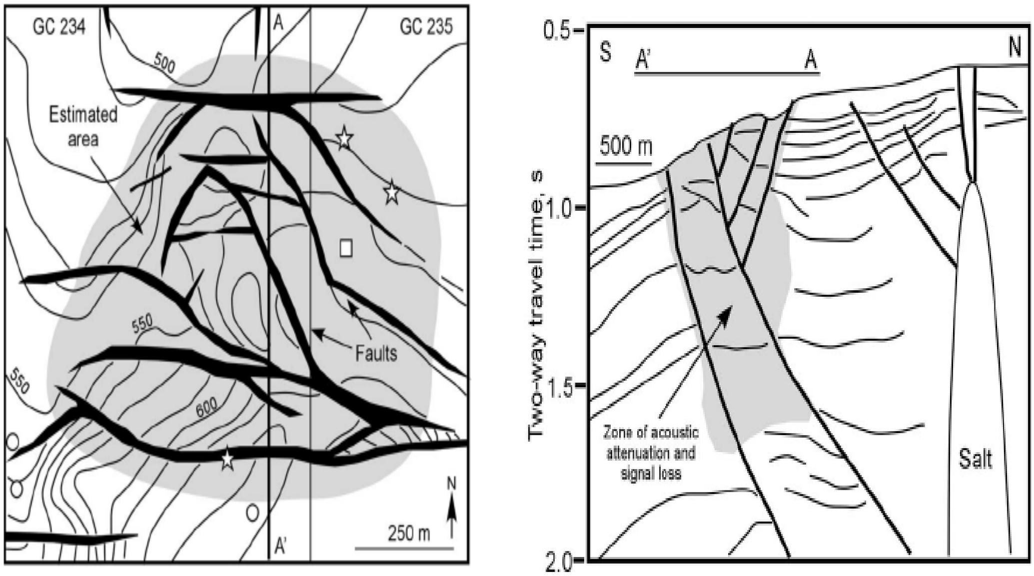

Fig. 3.16. Green Canyon 234/235 map and cross section (from Milkov and Sassen, 2003).

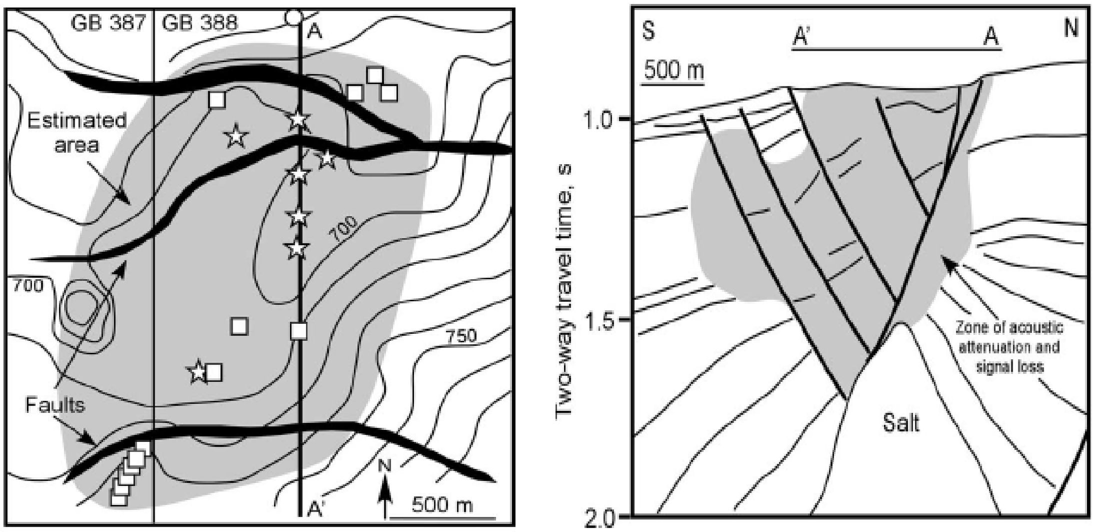

Fig. 3.17. Garden Banks 387/388 map and cross section (from Milkov and Sassen, 2003).

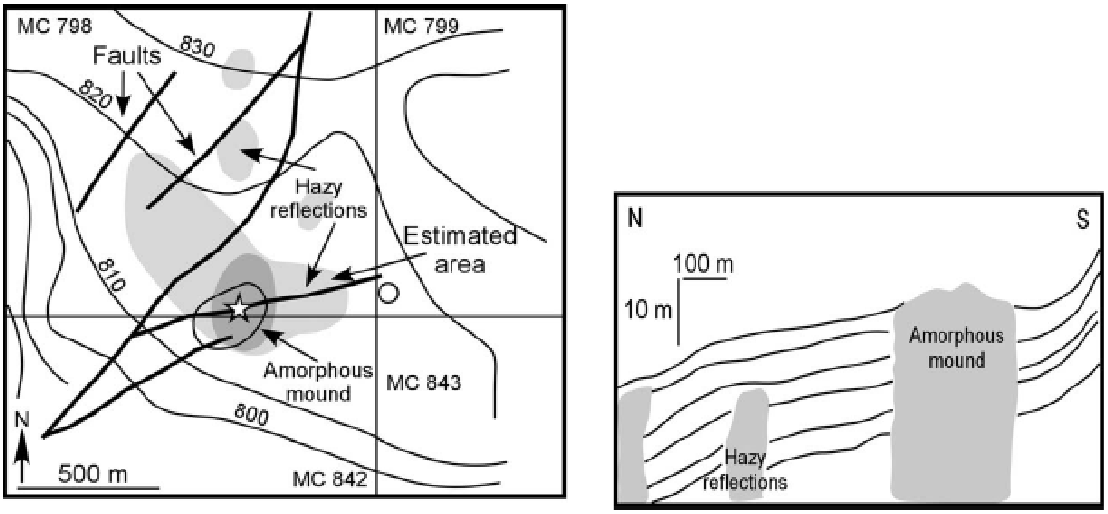

Fig. 3.18. Mississippi Canyon 798/842 map and cross section (from Milkov and Sassen, 2003).

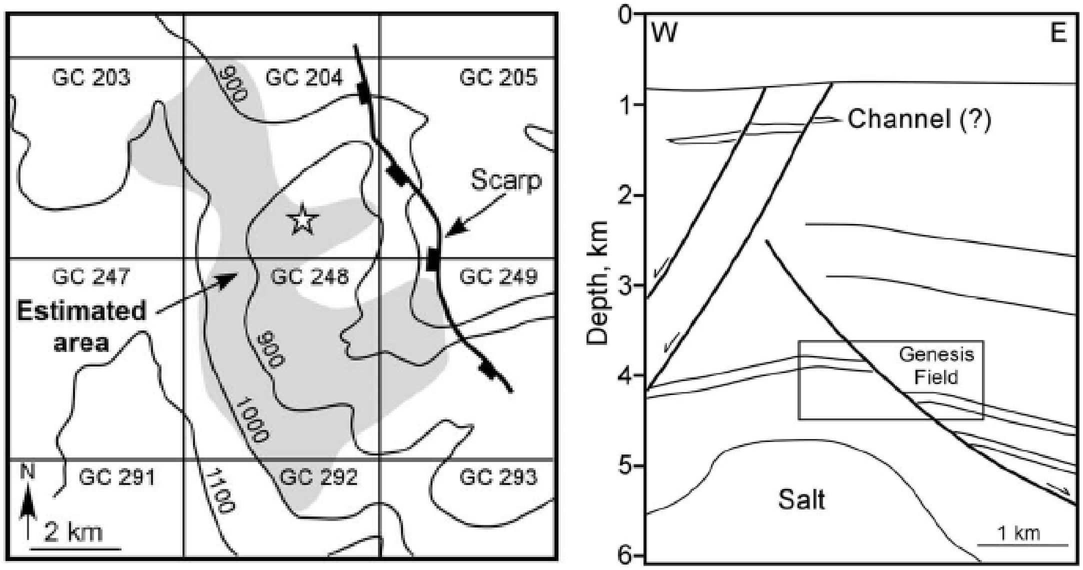

Fig. 3.19. Green Canyon 203/204 map and cross section (from Milkov and Sassen, 2003).

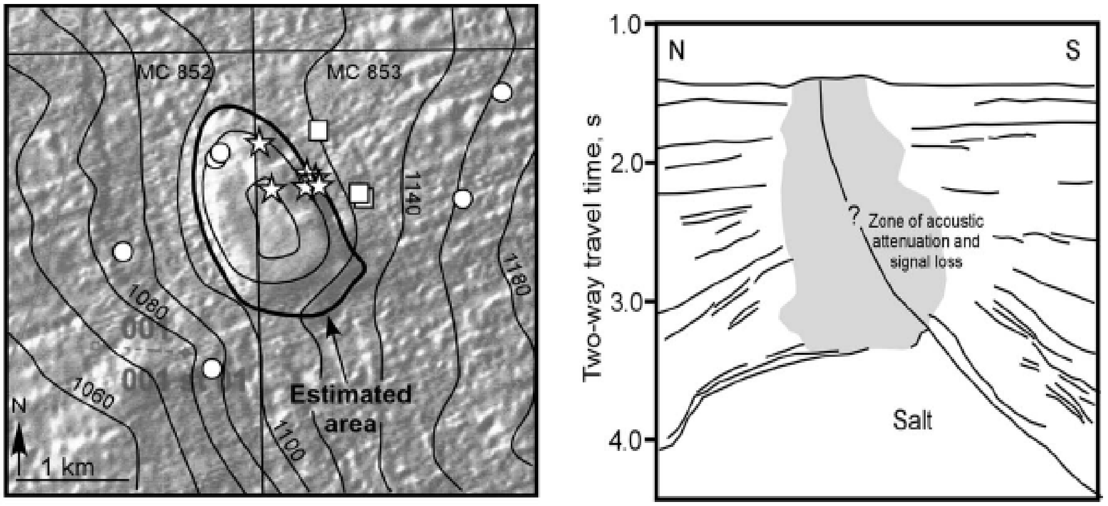

Fig. 3.20. Mississippi Canyon 852/853 map and cross section (from Milkov and Sassen, 2003).

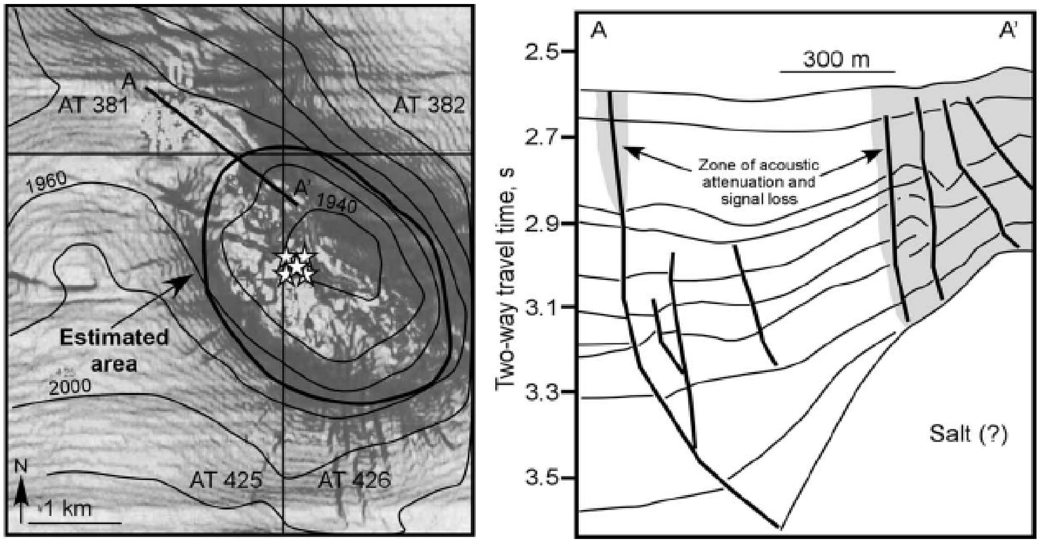

Fig. 3.21. Atwater Valley 425 map and cross section (from Milkov and Sassen, 2003).

In addition to the above sites mentioned above, two sites have been drilled by US-DOE/Chevron JIP. Those two sites are Atwater Valley 13/14 and Keathley Canyon 151 (Fig. 3.22). A total of seven wells were drilled during this expedition at water depths ranging from 1290 – 1320 meters.

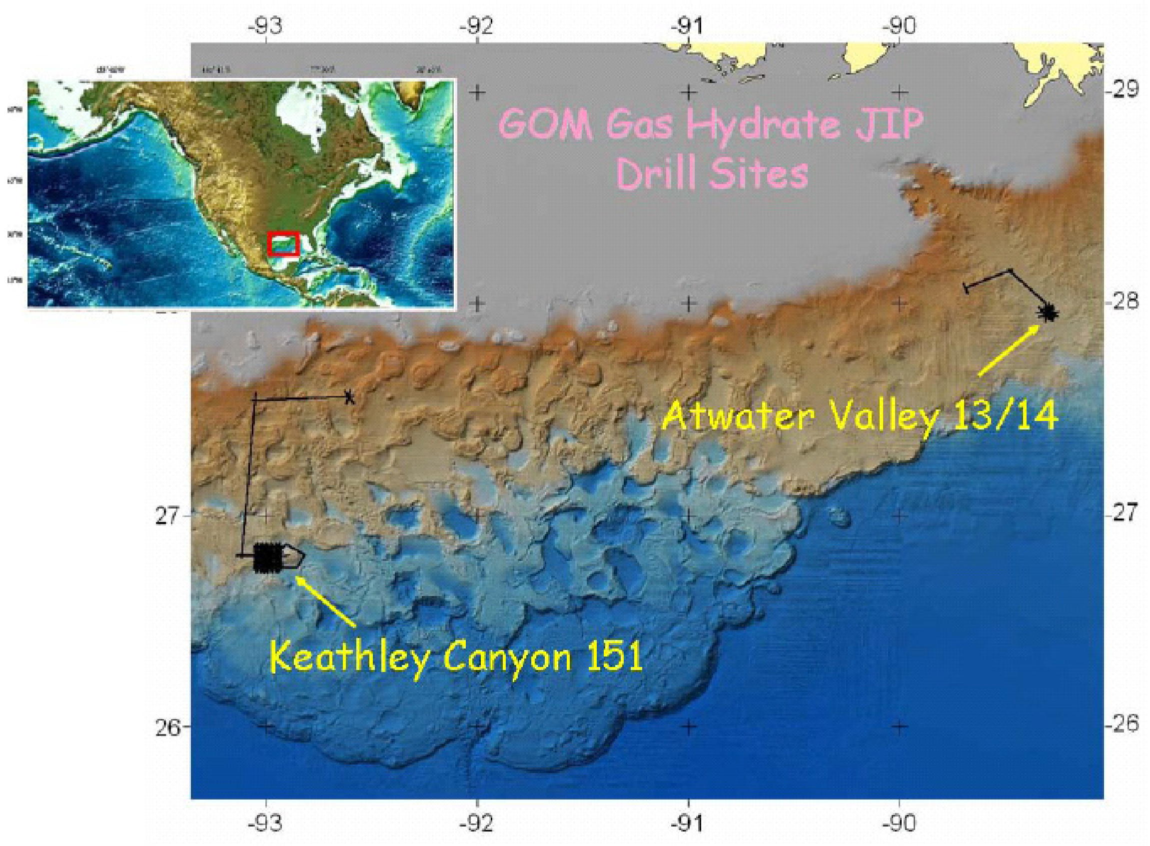

Fig. 3.22. US-DOE/Chevron JIP gas hydrate drill sites (from Conte and Bloyes, 2005).

3.4.2 Water depths and geothermal gradients

Tables 3.13 -3.15 presents the water depths and measured geothermal gradients at different sites in Gulf of Mexico

Table 3.13

Water depths for the GOM sites (from Milkov and Sassen, 2003)

Accumulation	Estimated Area	Water Depth (m)	Area (m^2)	HSZ thickness (m)	Assumed gas hydrate concentration (%)
GC 184/185	Bush Hill	540-560	101,300	370	5-10
GC 234/235	Faults	500-670	350,700	400	5-10
GB 388	Faults	650-750	3,200,200	495	5-10
				130	5-10
MC 798/842	Mound Wipeout	807-813	55,600	575	5-10
		810-820	217,400	580	5-10
GC 204	Wipeout	850-1000	26,130,700	640	1-5
MC 852/853	Mound	1080-1120	1,935,500	780	5-10
AT 425/426	Mound	1920-1940	5,650,000	380	5-10

Table 3.14

Water depths and penetrations for US-DOE/Chevron JIP sites (from Conte and Bloyes, 2005)

Site	Well number	Water depth (m)	Penetration (m)
Atwater Valley 13	AT13 #1	1290.5	246.6
(AT)13	AT13 #2	1291.1	200
Atwater Valley 14	AT14 #1	1300.3	286.5
(AT)14	ATM 1	1296	26.8
Keathley Canyon 151	KC151 #2	1330	459.3
(KC)151	KC151 #3	1322.5	438.9

Table 3.15

Geothermal gradients at the GOM (from Conte and Bloyes, 2005)

Site	Geothermal gradient (°C/100m)
Atwater Valley 13	3.2
Keathley Canyon 151	3.0
Mississippi Canyon	3.7

3.4.3 Sedimentology data

The Green Canyon sites and Mississippi Canyon sites in the GOM are reported to have the composition of the sediments described in Table 3.16 (Francisca et al., 2005):

Table 3.16

Sediment data from three sites in the GOM (from Francisca et al., 2005)

Sediment constituents	Sites		
	GC 185	GB 425	MC 852
Sand fraction (%)	4.9	2.6	3.5
Clay fraction (%)	55.0	52.5	48.5
Carbonate range (%)	4-55	6-35	7-72

The data in Table 3.16 indicate that these gas hydrate sediments are silty clay to clay. Yun et al. (2007a) have measured the physical characterization of core samples recovered from the Atwater Valley and Keathley Canyon drilling sites in Gulf of Mexico (Yun et al., 2007a). They classified the sediments as high plasticity clays. A more detailed cruise was carried out to study the distribution of gas hydrates in GOM in 2005 with DOE/Chevron JIP.

3.4.4 Patterns of gas hydrates in GOM sediments

Gas hydrates have been found in different geometries in GOM sediments. Table 3.17 describes different geometries found at different sites. Fig. 3.23 illustrates the deposition model of gas hydrates at Keathley Canyon site in Gulf of Mexico (Cook et al., 2007).

Table 3.17

Hydrate patterns and gas origin in the GOM sites (from Boothe et al., 1996)

Site	Mode of occurrence	Apparent origin of included gas
Green Canyon Block 184	Chunks and nodules	Thermogenic
Green Canyon Block 204	Chunks, dispersed	Thermogenic
Green Canyon Block 234	Massive	Thermogenic
Garden banks Block 388	Small white nodules, Flat sheet-like layers	Biogenic
Green Canyon Block 257	Small white nodules, Flat sheet-like layers	Biogenic
Green Canyon Block 320	Small white nodules, Flat sheet-like layers	Biogenic
Mississippi Canyon	Small pieces	Thermogenic
Bush Hill	Large Mounds	Thermogenic

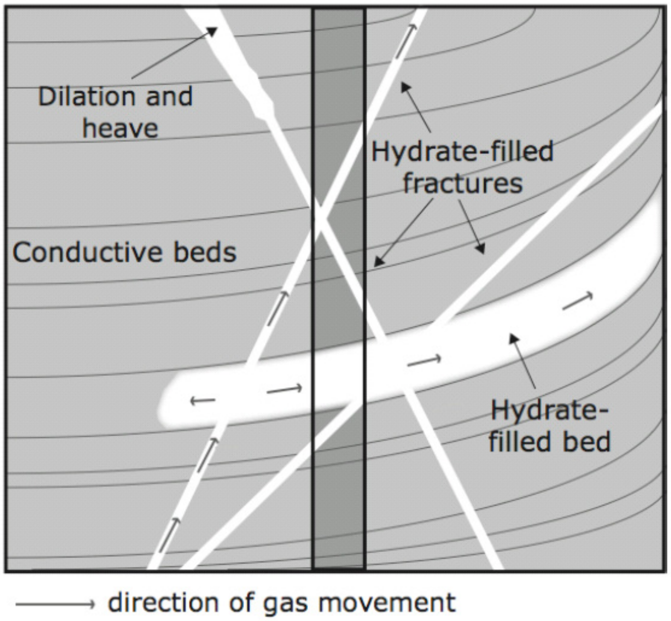

Fig. 3.23. Gas hydrates deposition model at the Keathley Canyon, GOM (from Cook et al, 2007).

3.4.5 Index properties

Tables 3.18 and 3.19 describe the index properties at Atwater Valley #13 and Keathley Canyon site 151 in the Gulf of Mexico.

Table 3.18

Index properties at Atwater Valley #13 (from Yun et al., 2007a)

Depth (mbsf)	Water content (%)	Liquid limit	Plastic limit
14.2	55.5	74.9	27
148.3	51.7	77	30.5

Table 3.19

Index properties at Keathley Canyon site 151 (from Yun et al., 2007a)

Depth (mbsf)	Water content (%)	Liquid limit	Plastic limit
23.4	53.2	66.6	27.7
224.8	30.3	51.2	20.7

3.5 Nankai Trough

The Nankai Trough is a convergent margin offshore southwest Japan. It is situated along the subduction zone between the Philippine Sea Plate and the island arc system of Japan. This area has been the focus of geologic and geophysical investigations for gas hydrates. Convergent margins are favorable locations for the formation of gas hydrates and it is estimated that two-thirds of total worldwide marine hydrates are found in these geological structures. According to Krason (1994), total gas resources in the form of gas hydrates in Nankai Trough is around 15 to 148 Tcf. Fig. 3.24 (He et al., 2006) describes the geological setting of Nankai Trough. Gas hydrates were indicated by the detection of BSRs in the early 1980s. However, the first samples of cores containing gas hydrates were collected in 1990 during ODP Leg 131. During the Nankai Trough expedition, hydrates were noted in cores between 90 to 140 meters below the seafloor (mbsf). The methane in the cores was considered to be of biological origin because of the low concentration of higher hydrocarbons.

The ODP carried out another expedition in Nankai Trough in 2000 and drilled seven holes. Japan National Oil Company and Japan Petroleum Exploration Corporation drilled three boreholes in eastern Nankai Trough as a part of Japan's effort to study the feasibility of gas production from the marine hydrate deposits. The world's first offshore natural hydrate exploratory wells were drilled from November 1999 to February 2000 at a single location at the water depth of 945 meters. Up to about 100 mbsf the sediments are composed of flat-lying mudstone-siltstone with occasional ash beds. Below 100m, the formation is mudstone and with increasing depth, the number and thickness of sandstone beds increases.

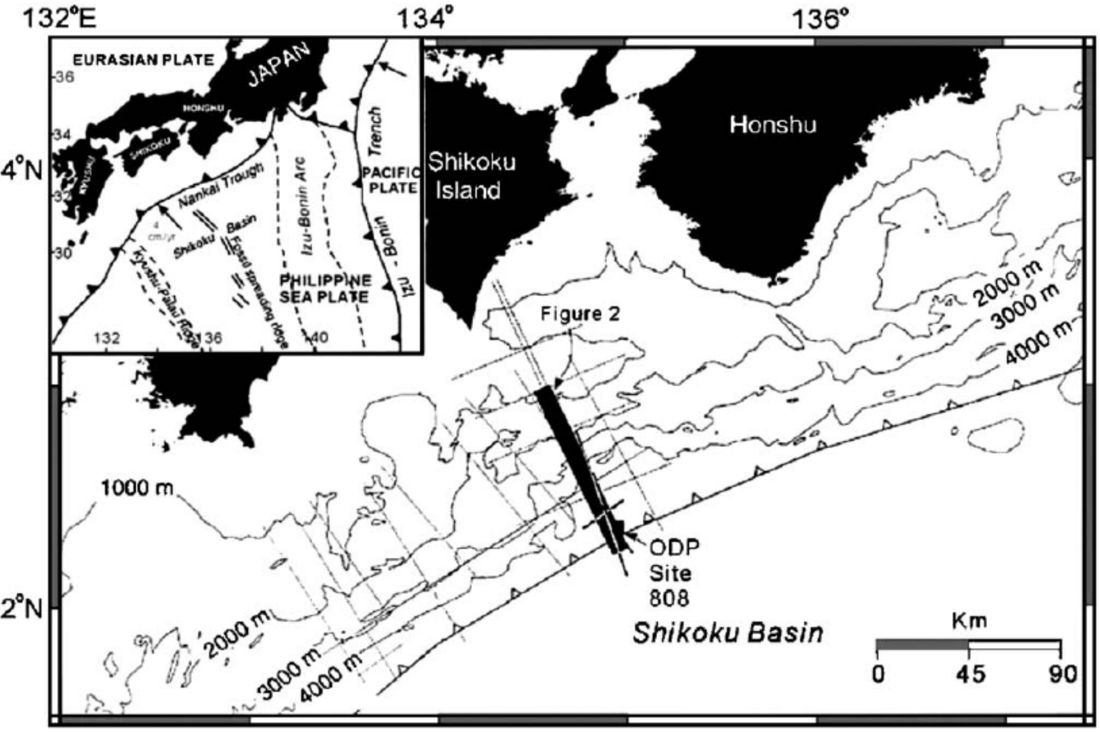

Fig. 3.24. Geological setting of Nankai accretionary prism (from He et al., 2006).

Table 3.20 (Kitajima et al., 2007) describes the permeability measured in the laboratory for Nankai Trough sediments

Table 3.20

Permeability measured in laboratory for Nankai Trough sediments (from Kitajima et al., 2007).

Area	Sediment	Gas permeability	Water permeability
Nankai Trough	Siltstone	10^{-14} to 10^{-16} m2 (10 to 0.1 md)	10^{-15} to 10^{-18} m2 (1 to 0.001 md)

3.6 Making synthetic cores in laboratory for gas hydrate testing

Table 3.21 describes various types of sediments used and their grain size/pore size distribution by different researchers in a chronological order. Most of the experiments have been done in coarse sediments (sand, glass beads).

Table 3.21

Grain size/pore size of sediments used in different hydrate experiments

Researcher	Sediment used	Grain size/Pore size	
		GS/PS	Value
Makogon, 1966	Sands, real cores		Different real
Handa and Stupin, 1992	Porous silica gel	PS	23-70 Å
Kunerth et al., 2001	Sand (Garnet sand)	GS	500-850 μm
Tohidi et al., 2001	Glass micro-models	GS	0.094-0.5 mm
Zatsepina and Buffett, 2001	Lane mountain sand	GS	0.4-0.6 mm
Kono et al., 2002	Glass beads	GS	100 , 5000 μm
Smith et al., 2002	Silica gel	PS	7.5, 5, 3 nm
Uchida et al., 2002	Glass beads	GS	20-200 μm
Waite et al., 2002	Quartz sand		
Kumar et al., 2004	Platte Valey sand	GS	250-500 μm
	Blake Ridge		
Santamarina et al., 2004	Ottawa sand	GS	1-120 μm
	Crushed silica flour		
	Kaolinite		
Uchida et al., 2004	Toyoura sand (TS)	GS	60-150 μm
	Berera sandstone		50-200 μm
	Clays		0.1-9 μm
	Glass beads		20, 100 μm
Winters et al., 2004	Ottawa sand		
Dicharry et al., 2005	Controlled pore glass	PS	25-40 nm
Huang and Fan, 2005	Sand	GS	300-125 μm
Liang et al., 2005	Activated carbon	PS	1.9 nm
Spangenberg et al., 2005	Glass bead	GS	250-500 μm
Yun et al., 2005	Fine grained sand	GS	120 μm
Kilner and Grozic, 2006	Ottawa sand	GS	20/30 mesh size
Kneafsey et al., 2007	Foundry 110 sand	GS	100-200μm
Winters et al., 2007	Medium sized sand	GS	0.25 mm
	Clayey silt		0.004 mm

Many different methods have been developed to form gas hydrates in sediments. The following three methods seem to be the most popular as published in various sources described in the Table 3.20.

In Method 1, the sediment completely saturated with water, is first cooled with liquid nitrogen. The water in the sediment is hence turned into ice. Then the ice and sediment mixture is pressurized with gas. Slowly the temperature is raised above the equilibrium temperature such that the ice is melted and the gas reacts with that water to form the hydrate in the sediment. This method is based on the original method devised by Stern et al. (1996; 2001).

In Method 2, the sediment is again first fully saturated with water. Gas is pushed through the sediment sample until the known amount of water is displaced. Then the temperature is decreased until the pressure and temperature conditions are within the hydrate stability zone.

In Method 3, the sediment is first sprayed with water until the wanted water content has been achieved. The partly saturated sediment is then pressurized with gas. The temperature is decreased until hydrates form in the pore space.

3.6.1 Recommendations to mix standard sediments in the laboratory for testing

Based on the review of sediment description in various offshore environments, I divided the sediment composition into three subgroups. I describe here three different types of sediments that can be used in the laboratory.

1 100% sand-sized particles of average diameter 100 μm

2 50% silt-sized particles of average diameter 10 μm and 50% clay sized of average diameter 1 μm

3 100% clay-sized particles of average diameter 1 μm

The reason to choose these three compositions of sediments is that these types of sediments are found in nature. For example, in Nankai Trough hydrates are found in the sandstone; at Blake Ridge they are found mostly in silty clay; and in the GOM they are found in both in silty clay and clay. For each of the subgroup, a procedure will be outlined to make the sediments in the laboratory.

3.6.2 Steps for Mixing Sediments in the Laboratory

The following recipes are for mixing 1 kg of dry sediment. The mixing rules are fairly straightforward; however, we needed to decide the basic soil samples we will use. Different types of clays can be used to represent different clay mineralogies, but we needed to decide upon a standard soil type for our experiments.

3.6.2.1 100% sand

1 Take 1 kg of sand of average size 100 μm, sand in this range can be collected using sieves.

2 Measure the water content of the sand specimen according to ASTM D2216 standards.

3 Add salt to the distilled water until the desired salinity value is obtained

4 To increase the water content of the sand specimen, spray water on the sand in steps and mix uniformly. Continue to do so until the required water content is reached.

5 Pack the sand to a porosity that is representative of that of natural sediments. To pack the sand to a particular porosity, give moistened sand a number of blows.

6 Once the desired porosity is reached and water saturation reaches the desired level, the partially saturated sand sample should be pressurized with methane.

7 After pressurization, lower the temperature until the hydrate is formed in the pore space.

3.6.2.2 Clay

1. Take the part of a specified soil sample that is 50% or more by weight with a nominal diameter smaller than 0.075 mm. The clay should be such that its plasticity index is greater than the "A" line in the plasticity chart (ASTM standard D2487) and liquid limit >50%.
2. Once this clay sample is procured, then the water content can be increased by spraying more water until it reaches the desired water content.

3.6.2.3 Silty Clay

1. From a specified soil mixture, sort out 750 gm of clay fraction (<5 μm) and 250 gm of silt sized fraction (75 μm to 5 μm), Mix these two proportions together. Different types of clays can be used to represent different clay mineralogies.
2. After mixing, measure the initial water content explained in the ASTM D2216 standard.
3. Add the salt to the distilled water until the salinity reaches the desired value.
4. To increase the water content of the soil specimen, spray water on the sample in steps and mix uniformly. Continue to do so until the required water content is reached.
5. Pack this sediment to a porosity which is representative of that of natural sediments. To pack the sediment to a particular porosity, the moistened sediment should be given a number of blows.
6. Once the desired porosity is reached and water saturation reaches the desired level, pressurize the partially saturated sediment sample with methane.

After pressurization, lower the temperature until the hydrate is formed in the pore space.

3.7 Use of collected data

3.7.1 Use of water depths and geothermal gradients

The information collected on water depths, temperature, and geothermal gradients can be used to find the thermodynamic state of a gas hydrate deposit with respect to the equilibrium curve (Fig. 3.25).

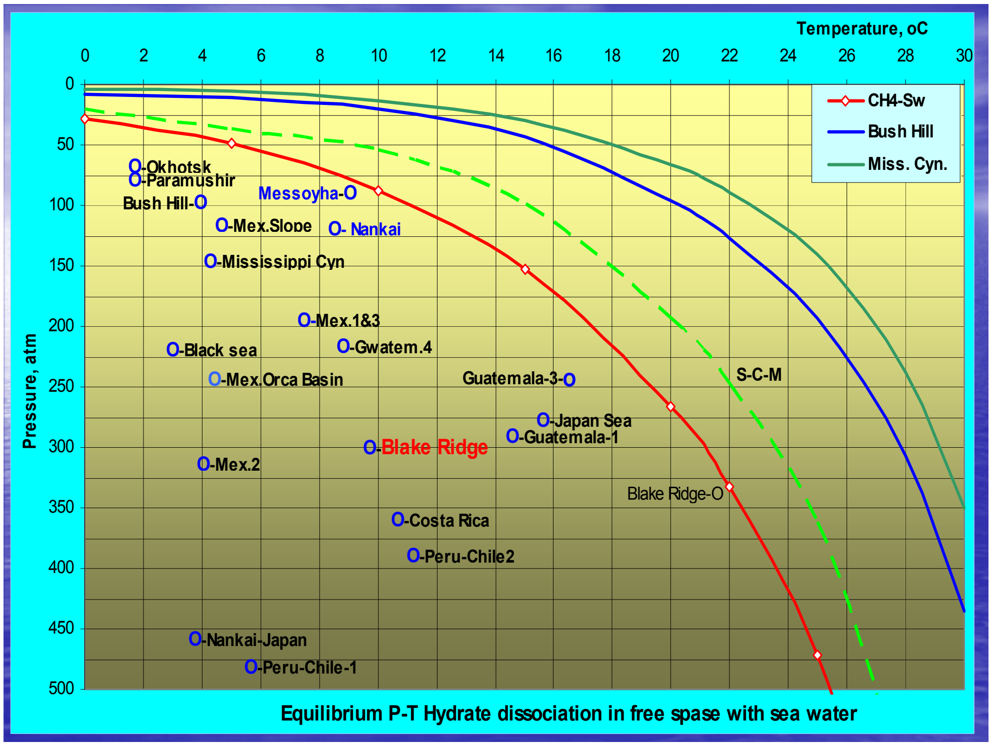

Fig. 3.25. Representation of various gas hydrate sites (from Makogon et al., 2007).

Fig. 3.25 illustrates various gas hydrate locations with respect to the different equilibrium curves. As discussed in Chapter II, if the gas composition contains the heavier components than methane, the equilibrium curve gets shifted. Gas composition is a primary control on the hydrate stability. The presence of heavier gases in the hydrate lattice has an opposite effect than presence of salts on the shifting of equilibrium curve. Usually, the hydrates formed from biogenic gas have methane as a major constituent. In thermogenic gases, heavier hydrocarbons are also present which may enter the hydrate lattice. However, unless the hydrates are recovered from the earth, their composition cannot be predicted. In Fig. 3.25, different equilibrium curves are shown for methane-seawater (red curve), the methane-water equilibrium curve with self conservation effect (green dashed curve), equilibrium curve for gas composition at the Bush Hill site at Gulf of Mexico (blue curve) and Mississippi Canyon (dark green curve). Similar graph has also been published by other researchers (Boothe et al., 1996).

The important point here is that the hydrates that are deep“inside” the phase envelope will require large depressurization and/or temperature increase to dissociate the hydrates (Makogon et al., 2007).

3.7.2 Use of sedimentology data

The gas hydrate expeditions have provided a very valuable database of hydrate bearing sediments. Various properties have been measured on the cores collected from different locations. Many new techniques of collection and analysis of cores were successfully implemented. The central point to each of these techniques is the description of hydrate-bearing sediments.

In situ stress in the sediments depends on the sediment characteristics (i.e. mineralogy and physical properties) as well as stress history of the sediments. The importance of in situ stress can be explained by Fig. 3.26.

In Fig. 3.26, when the pressure increase in the hydrate bearing sediments crosses the in situ stress gradient, sediment failures can occur. Note that this type of stresses can develop in response to thermal loading when there is no outlet for the gas released from hydrate dissociation. Significant stresses can also develop during depressurization (in the process of gas production), but their evolution follows a different mechanism and pathway. The stresses in the hydrate deposits and their evolution with time depend on the geomechanical properties of the system, the initial stress regime, and the magnitude and the direction of pressure changes.

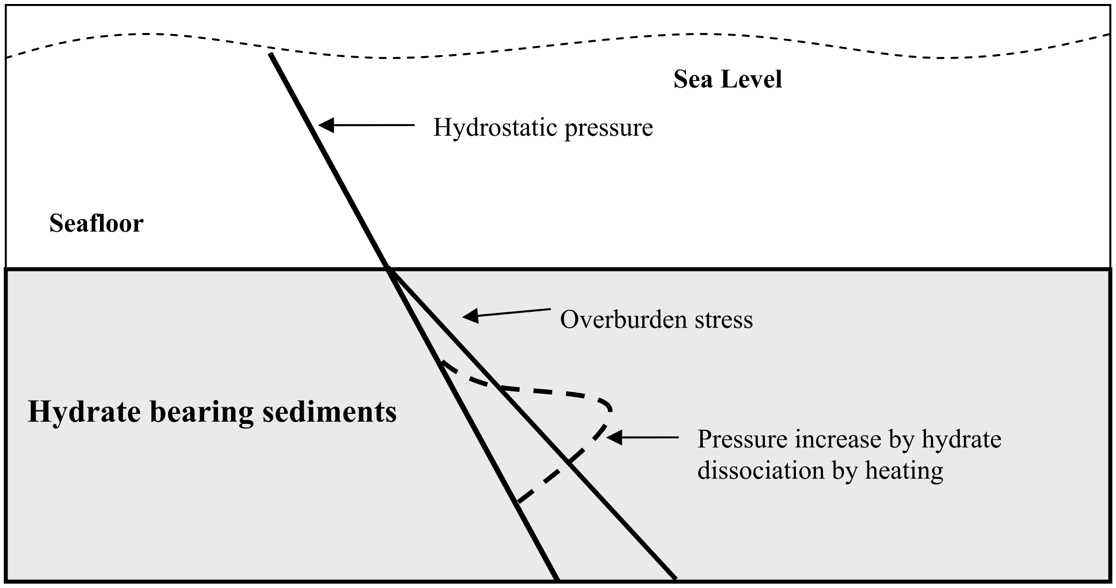

Fig. 3.26. Impact of pressure increase by heating hydrate deposit.

In offshore environments, hydrates exist in different types of sediments. A majority of hydrates, however have been found in clayey sediments with associated surficial gas seeps (Boswell et al., 2007; Sassen, 2007).

The geomechanical data collected and measured at different hydrate expeditions is of critical importance for slope stability, hydrate dissociation and formation, wellbore stresses, platform foundations, transportation pipelines, etc. Each of the geomechanical parameters important to study the performance of hydrate bearing sediments are discussed in the following section.

Clay mineralogy is an important parameter for geomechanical performance of hydrate bearing sediments (Nakagawa, 2007). Different types of clays have different mechanical properties. When these sediments are unloaded, they have different geomechanical responses because of the differences in their properties. Note that unloading means an increase in the pore pressure to a level that equals or exceeds the total stress, as determined by the lithostatic pressures (see Section 7.4), leading to zero or negative effective stresses.

Grain size has an important effect on the patterns of hydrates in sediments. For coarser grain sizes, hydrates can be pore filling. For the finer grained sediments, hydrates are present in the form of nodules or fracture filling (Winters et al., 2007). The hydrates are much more concentrated in fractures and faults in clayey sediments. This is because of very high surface charges in clays and high capillary pressures for gas in fine grained sediments (Fig.3.27). The high surface charge acts as an inhibitor for hydrate formation and hence hydrates are concentrated along easier pathways such as fractures and faults (Kneafsey, 2007). Each of the hydrate geometries will affect the geomechanical failure in a different manner. Grain size also has a strong affect on the seismic signatures of hydrate bearing sediments(Winters et al., 2007).

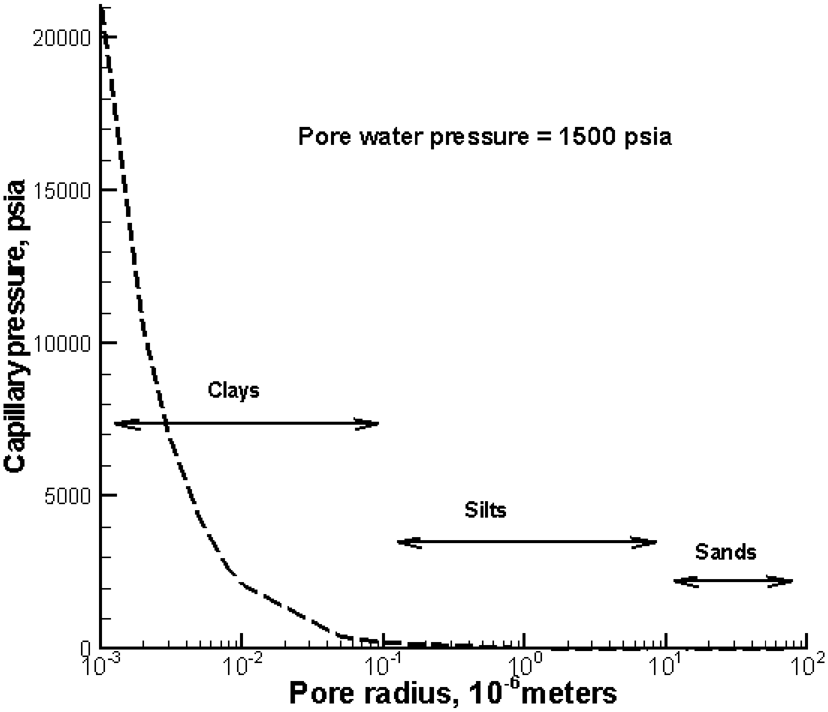

Fig. 3.27. Capillary pressure for methane-water system as a function of pore size (data from Sun et al., 2004).

Overburden stress is an important parameter to study the geomechanical stability of hydrate-bearing sediments. The overburden stress (σ_{v}) can be calculated by integrating the bulk density (ρ_{b}) of the sediments over the subsurface depth (d_{s}).

$$\sigma_{\mathrm{v}} = \int_{0}^{d_{\mathrm{w}}} \rho_{\mathrm{w}} g d(d_{\mathrm{w}}) + \int_{d_{\mathrm{w}}}^{d_{\mathrm{s}}} \rho_{\mathrm{b}} g d(d_{\mathrm{s}}) \tag{3.1}$$

The bulk density data of sediments with depth is available in the database of various hydrate expeditions. The bulk density is measured by well logs or in the laboratory tests on the cores collected.

3.7.3 Strength properties of sediments

The most important strength properties for hydrate bearing sediments are (Rutqvist and Moridis, 2007) shear strength, bulk modulus, cohesion and the friction angle.

The shear strength of sediment is the most important property to be considered for the sediment failures. Shear strength is defined as the maximum resistance of a soil to shear. Shear strength depends on many factors such as presence of gas, mineralogy, confining stress and subsurface depth. For hydrate bearing sediments, shear strength also depends on the percentage of hydrate present in the sediment. When the hydrate dissociates, gas and water will be generated and will change the shear strength of the sediment. The flow of the generated gas and water will ultimately depend on the flow properties of the sediments.

3.7.3 Use of flow properties of sediments

The most important flow property of the sediments is the permeability. Permeability is difficult to measure for unconsolidated sediments because it depends on the compressibility of the sediments (i.e. types of sediments). Also, permeability of the sediments depends on the confining pressure to which the sediments are subjected. As discussed before, the hydrate dissociation in low permeability sediments has a different effect than hydrate dissociation in higher permeability sediments. This is extremely important if hydrates are dissociated by thermal stimulation and inhibitor injection because of the tremendous amount of pressure generated in low permeability environments.

Another important property is the capillary pressure in the sediments. When the gas hydrates dissociate, gas and water are released. The gas released during gas hydrate dissociation has to form a more interconnected gas zone more than the residual gas saturation in order to flow. The entry pressure depends on the pore size of the sediments. As the pore radii keep decreasing, the capillary pressure in the pores increases significantly.

To model the behavior of hydrate-bearing sediments for different perturbation scenarios, I used two numerical simulators. The important underlying principles and assumptions of these simulators are described in Chapter IV. The input data in these simulators is the data presented in this chapter.

CHAPTER IV

NUMERICAL SIMULATORS

4.1 Introduction

To model the behavior of hydrate bearing sediments, I have used two state-of-arts numerical simulators, TOUGH+Hydrate (T+H) and TOUGH+Hydrate-FLAC3D (T+F). These simulators have been developed at Lawrence Berkeley National Laboratory (LBNL) (Rutqvist and Moridis, 2007; Moridis et al., 2008). The equations presented in this chapter and the discussions on the numerical simulators follow from the information provided in the manuals of T+H (Moridis et al., 2008) and T+F (Rutqvist and Moridis, 2007). A number of important simulation studies have been conducted using T+H (Moridis, 2003; Moridis and Collettt, 2003; Moridis, 2004; Moridis and Collettt, 2004; Moridis et al., 2004).

4.2 TOUGH+Hydrate (T+H)

T+H (Moridis et al., 2008) is a code for simulating the behavior of hydrate bearing sediments. It is written in FORTRAN 95/2003 language. The basis of this code is TOUGH2 family of codes for the transport of multi-component, multiphase and heat flow (Pruess et al., 1991).

4.2.1 Modeling capabilities

T+H can model the phase behavior, fluid flow and heat flow processes in porous media during dissociation and formation of methane hydrates (Moridis et al., 2008). Using T+H, all the three mechanisms of hydrate dissociation (depressurization, thermal stimulation and inhibitor injection) and any of their combinations can be modeled. There are two options for modeling a methane hydrate reaction, kinetic and equilibrium. In the equilibrium option, the hydrate formation and dissociation occurs instantaneously when the thermodynamic conditions are favorable. In the kinetic option, the hydration reaction is treated as a chemical reaction with a defined reaction rate.

4.2.2 Important assumptions

The important simplifying assumptions in T+H as defined in (Moridis et al., 2008) are:

1. Darcy's law is valid in the model domain.
2. The hydrate forming gas is assumed to be 100% CH_4.
3. Hydrodynamic dispersion of dissolved gas and inhibitors is negligible as compared to advective transport.
4. Hydrate and ice are assumed to have the same compressibility and thermal expansivity. This assumption is dictated by the lack of measured data on these hydrate properties, and the chemical similarity between hydrates and ice.
5. There is no precipitation of dissolved salts if their concentration in the aqueous phase increases in the process of hydrate and/or ice formation. Thus, the aqueous phase does not disappear when salts are present.
6. The thermophysical properties of aqueous phase are not affected by the concentration of dissolved inhibitors. This alleviates the need to describe the complex (and computationally demanding) properties of binary water-inhibitor systems.
7. The inhibitor is assumed to be non-volatile, thus avoiding the high computational requirements needed to account for the inhibitor vapor pressure and its diffusion in the gas phase.
8. The pressure cannot exceed 100 MPa (14,500 psi). This is by no means a limitation because it exceeds that pressure in all known hydrate deposits and in all reported laboratory studies.

4.2.3 Numerical scheme and governing equations

T+H uses integral finite difference method (IFDM) to discretize the mass and heat balance equations. T+H is a fully implicit simulator and the resulting finite difference equations are solved by Newton-Raphson iterations. The details of the mass and heat balance terms and the numerical techniques used in the T+H code can be found in Moridis et al. (2008).

4.2.4 Components and phases

T+H accounts for up to four mass components, which are, water (w), methane (m), hydrate (h) and inhibitors (i) and one heat component , that is, a total of 5 components. These 5 components are partitioned amongst four possible phases, which are, gas (*G*), aqueous (*A*), ice (*I*) and hydrate (*H*). When the equilibrium option is used, hydrate is treated only as a phase. When the kinetic option is used, hydrate is treated both a component and a phase. A total of 26 phase combinations can be described by T+H; 13 phase combinations are available for equilibrium option and 13 for kinetic option. Tables 4.1 and 4.2 shows list of primary variables for equilibrium simulations without inhibitor and kinetic simulations without inhibitor respectively (Moridis et al., 2008).

Table 4.1

Primary variables in equilibrium hydrate simulations without inhibitor* (Moridis et al., 2008)

Phase	State Identifier	Primary Variable 1	Primary Variable 2	Primary Variable 3
1 – Phase: *G*	**Gas**	P_gas	Y_m_G	T
1 – Phase: *A*	**Aqu**	P	X_m_A	T
2 – Phase: *A+G*	**AqG**	P_gas	S_aqu	T
2 – Phase: *I+G*	**IcG**	P_gas	S_Ice	T
2 – Phase: *H+G*	**GsH**	P_gas	S_gas	T
2 – Phase: *A+H*	**AqH**	P	S_aqu	T
2 – Phase: *A+I*	**AqI**	P	S_aqu	X_m_A
2 – Phase: *I+H*	**IcH**	P	S_ice	T
3 – Phase: *A+H+G*	**AGH**	S_gas	S_aqu	T
3 – Phase: *A+I+G*	**AIG**	P_gas	S_aqu	S_gas
3 – Phase: *A+I+H*	**AIH**	P	S_aqu	S_ice
3 – Phase: *I+H+G*	**IGH**	S_gas	S_ice	T
Quadruple point *I+H+A+G*	**QuP**	S_gas	S_aqu	S_ice

P: Pressure, Pa

T: Temperature, C

P_gas: Gas phase pressure, Pa

X_m_A: mass fraction of methane in aqueous phase

Y_m_G: mass fraction of methane in the gas phase

S_aqu: Aqueous phase saturation; S_gas: Gas saturation; S_ice: Ice saturation

X_i_A: Mass fraction of inhibitor dissolved in the aqueous phase

∗ For inhibitor case, X_i_A becomes 3rd primary variable (as listed in Table 4.1) and the 3rd primary variable becomes the 4th primary variable

Table 4.2

Primary variables in kinetic hydrate simulations without inhibitor [*](Moridis et al., 2008)

Phase	State Identifier	Primary Variable 1	Primary Variable 2	Primary Variable 3	Primary Variable 4
1 Phase: *G*	**Gas**	P_gas	Y_m_G	S_hyd	T
1 Phase: *A*	**Aqu**	P	X_m_A	S_hyd	T
2 Phase: *A+G*	**AqG**	P_gas	S_aqu	S_hyd	T
2 Phase: *I+G*	**IcG**	P_gas	S_Ice	S_hyd	T
2 Phase: *H+G*	**GsH**	P_gas	S_gas	S_ice	T
2 Phase: *A+H*	**AqH**	P	S_aqu	X_m_A	T
2 Phase: *A+I*	**AqI**	P	S_aqu	X_m_A	X_m_A
2 Phase: *I+H*	**IcH**	P	S_ice	S_gas	T
3 Phase: *A+H+G*	**AGH**	P_gas	S_aqu	S_gas	T
3 Phase: *A+I+G*	**AIG**	P_gas	S_aqu	S_hyd	S_gas
3 Phase: *A+I+H*	**AIH**	P	S_aqu	S_ice	S_ice
3 Phase: *I+H+G*	**IGH**	P_gas	S_gas	S_ice	T
Quadruple point *I+H+A+G*	**QuP**	P_gas	S_aqu	S_gas	S_ice

∗ For inhibitor case, X_i_A becomes 4th primary variable (as listed in Table 4.2) and the 4th primary variable becomes the 5th primary variable

4.2.5 *Thermophysical properties*

T+H has built-in thermophysical properties for water, methane hydrate and methane gas. The property packages are described in detail in Moridis et al.(2008).

4.2.6 *Phase relations*

In the equilibrium model, the phase changes take place according to the equilibrium curve shown in Fig. 4.1 (Moridis et al., 2008). P_e refers to the equilibrium pressure and temperature, T is in Kelvin.

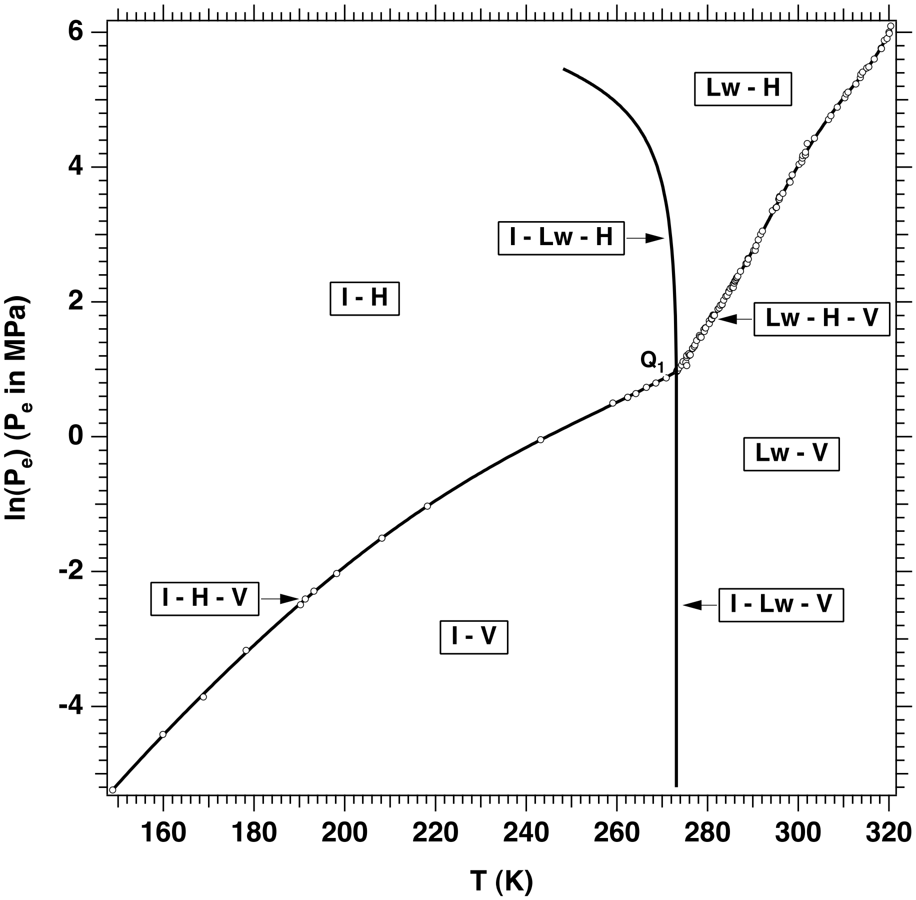

Fig. 4.1. Equilibrium relation for water/methane/hydrate system. *I* = Ice, *H*=hydrate, *V*=vapor, *Lw*=water, *Q* = quadruple point (from Moridis et al., 2008).

For the inclusion of the effect of inhibitors on the hydrate equilibrium, T+H uses equation 4.1 (Moridis et al., 2008).

$$\Delta T_{\mathrm{D}} = \Delta T_{\mathrm{D,r}} \frac{\ln(1 - x^{i}_{\mathrm{A}})}{\ln(1 - x^{i}_{\mathrm{Ar}})} \tag{4.1}$$

x^{i}_{A} is the mole fraction of the inhibitor in the aqueous phase,
x^{i}_{Ar} is the reference mole fraction of the inhibitor in the aqueous phase,
ΔT_{D} is the inhibitor induced temperature depression, and
$\Delta T_{\mathrm{D,r}}$ is the temperature depression at the reference mole fraction x^{i}_{Ar}

4.2.7 Wettability phenomena in hydrate bearing sediments (Moridis et al., 2008)

When the solids such as ice or hydrates precipitate in the porous media, there is a change in the wettability properties of porous media. When the solids are deposited in the pore space, the capillary pressure as well as relative permeability to gas and water changes. Permeability reduction can be thought to occur either because of change in absolute permeability or due to change in fluid relative permeability.

In T+H, the wettability processes can be described by two phenomenological models (Moridis et al., 2008). These models are termed as Original Porous Medium (OPM) model or the Evolving Porous Medium (EPM) model. In the OPM model, the permeability reduction during the formation of solid phases (hydrates and/or ice) is described in terms of relative permeability effects that are controlled only by the saturations of the mobile phases (gas and aqueous). The intrinsic porosity and permeability are assumed constant as these solid phases form. In EPM models, the precipitation of solid phases in porous media is equivalent to creation of new porous media with changing porosity and permeability.

4.2.8 Preparation of input data

The data needed to characterize a flow system include hydrogeologic parameters, thermal properties and constitutive relations of the permeable medium (absolute and relative permeability, porosity, capillary pressure, thermal conductivity, specific heat, etc.), the thermophysical properties of the fluids (defined internally), initial and boundary conditions of the flow system, and sinks and sources. In addition, T+H simulations require specification of the space-discretized geometry of the domain, computational parameters, and time-stepping information. T+H input is in fixed format and standard metric (SI) units such as meters, seconds, kilograms, °C, and the corresponding derived units, such as Newtons, Joules, and Pascal =N/m^2 for pressure. A detailed description of input data styles and formats can be found in Moridis et al (2008) A simplified flowchart depicting the input sequence and data requirements for T+H simulations is shown in Fig. 4.2.

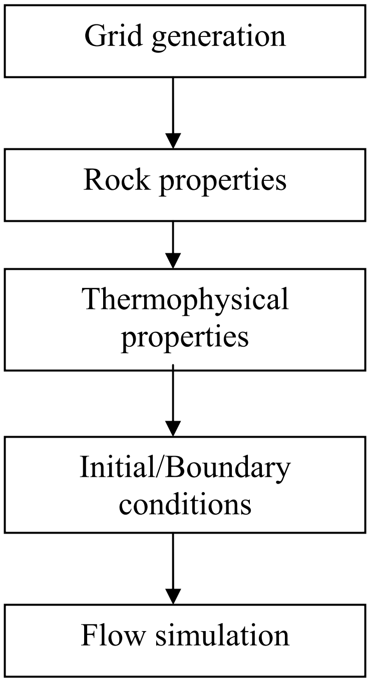

Fig. 4.2. Flowchart for running T+H model.

4.3 TOUGH+Hydrate-FLAC3D (T+F)

For the analysis of the geomechanical stability of HBS, I have applied a numerical model called T+F (Rutqvist and Moridis, 2007) that integrates a commercial geomechanical code (FLAC3D) into T+H. FLAC3D(Itasca Consulting Group, 2002) simulator is widely used in soil and rock mechanics engineering, and for scientific research in academia. FLAC3D has built-in constitutive mechanical models suitable for soil and rocks, including various elastoplastic models for quasi-static yield and failure analysis, and viscoplastic models for time dependent (creep) analysis, that could be used directly or modified for analysis of geomechanical behavior of hydrate bearing sediments (HBS) (Rutqvist and Moridis, 2007). The discussions on the coupled model follows the manual of T+F (Rutqvist, 2007; Rutqvist and Moridis, 2007)

4.3.1 Framework of the coupled model

In the resulting coupled simulator T+F, the two constituent codes—T+H and FLAC3D—are linked through a coupled thermal-hydrological-mechanical (THM) model of the HBS (Rutqvist and Moridis, 2007). This coupled model is shown in Fig. 4.3

The basic couplings between hydrological and mechanical processes in the deformable porous media are considered through:

(1) An effective stress law, that defines how a change in pore pressure affects mechanical deformation and stress, and

(2) A pore-volume model that defines how a change in stress or strain affects the fluid flow.

In addition, there are more couplings—including changes in mechanical and flow properties—that are consequences of changes in effective stress and pore-volume. The relationship between flow and geomechanical properties can become significantly more complicated by couplings related to temperature changes and the possible effects of inhibitors.

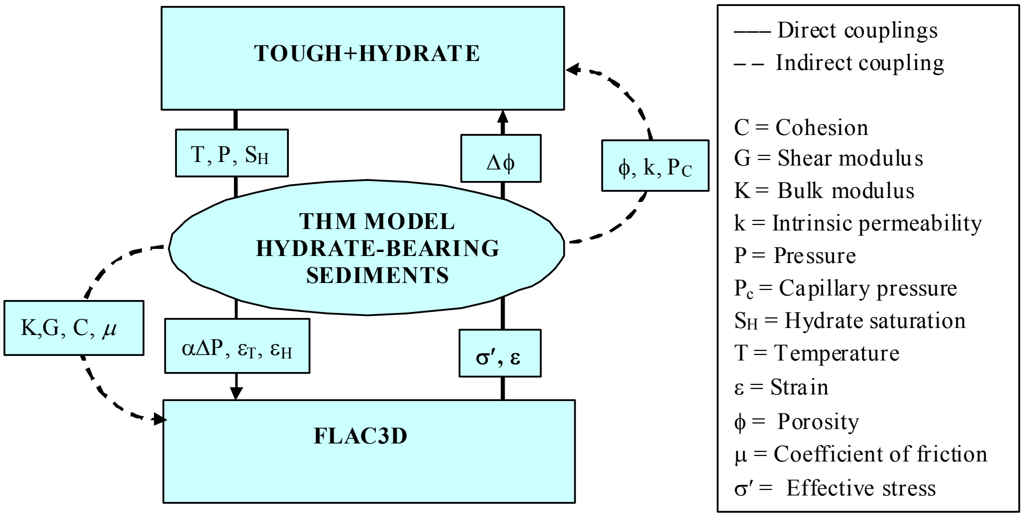

Fig. 4.3. Coupling of TOUGH+Hydrate and FLAC3D model (from Rutqvist and Moridis, 2007).

Fig. 4.3 illustrates the data exchanges between T+H and FLAC3D. The information on different parameters is exchanged through the central THM model. The arrow on the right hand side of Fig. 4.4 shows the information of the effective stress σ' and strain ε (that are computed in FLAC3D) to T+H for the calculation of the updated porosity ϕ, and of the corresponding change in porosity $\Delta\phi$. (Rutqvist and Moridis, 2007) The porosity change $\Delta\phi$ (induced by change in stresses and strains) has an immediate effect on the fluid flow behavior. For example, if a change in σ' and ε causes ϕ to decrease, the pore pressure is expected to rise, especially if the permeability is low (Rutqvist and Moridis, 2007).

The arrow on the left side of Fig. 4.4 depicts the flow of data obtained from T+H (that is, the pressure p, temperature T, and phase saturations S_β) to FLAC3D for calculating their impact on the effective stress $\alpha\Delta p$ (α is the Biot's effective stress parameter), as well as on the thermal and swelling strains (ε_θ and ε_{sw}, respectively) (Rutqvist and Moridis, 2007) Additionally, changes in p, T and S_β result in changes in other HBS mechanical properties that are listed in Fig. 4.4. These include the bulk modulus K, the shear modulus G, the cohesion C_m, and the coefficient of internal friction μ. The T+F model uses an empirical relationship to calculate the geomechanical properties of HBS for changes in the solid phase saturations, that is., hydrate and ice saturations (S_H and S_I, respectively) (Rutqvist and Moridis, 2007).

Two models for mechanically induced porosity changes are implemented in the current version of T+F as explained in Rutqvist and Moridis (2007) are:

(1) A poroelastic model (based on the approach proposed by Settari and Mourits that considers macroscopic stress/strain changes and grain deformability (Settari and Mourits, 1998), and

(2) An empirical model (proposed by Rutqvist and Tsang) that describes a non-linear change in porosity as a function of the effective mean stress (Rutqvist and Tsang, 2003)"(Rutqvist and Moridis, 2007).

The $\Delta\phi$ computed from either of these models is used to estimate changes in k by means of empirical equations (Rutqvist and Moridis, 2007). The updated ϕ and k values are then used to estimate changes in the flow and wettability properties of the sediments (i.e., aqueous and gas phase relative permeabilities k_{rA} and k_{rG}, and capillary pressure p_{cap}) by using appropriate scaling equations (Moridis et al., 2008) that are available as options in T+H (Rutqvist and Moridis, 2007).

4.3.2 Coupling schemes

Three coupling schemes are available in T+F as explained in Rutqvist and Moridis (2007):

(1) Jacobian: In this scheme, all the geomechanical and flow parameters are continuously updated (in every Newtonian iteration of every timestep), and their changes are accounted for in the computation of the Jacobian matrix.

(2) Iterative: In this scheme, the geomechanical and flow parameters are updated at the end of each Newtonian iteration of each timestep, and the contribution of their changes between Newtonian iterations are not accounted for in the computation of the Jacobian matrix.

(3) Time-step: This represents the weakest coupling option, and involves correction of the geomechanical and flow parameters only once in (and at the end of) each time step. As in the iterative scheme, the parameter changes do not contribute to the computation of the Jacobian matrix.

The full Jacobian option is a *sequentially implicit* scheme, whereas the iterative and the time-step coupling options are *sequentially explicit* schemes (Rutqvist and Moridis, 2007). The Jacobian scheme is necessary in problems where pore-volume (direct) couplings dominate, that is, when porosity change $\Delta\phi$ (induced by change in stresses and strains) results in a relatively strong and fast change in pore pressure, and where the fluid mass and heat balances must be preserved (Rutqvist and Moridis, 2007). In problems where the so-called property changes (indirect couplings) dominate, iterative or time-step coupling schemes have a practically negligible effect on mass balance, and are sufficient to describe the geomechanical evolution of the system (Rutqvist and Moridis, 2007).

4.3.3 Developing and running T+F simulation (Rutqvist, 2008)

A coupled T+F analysis for a particular problem is typically developed according to the steps shown in Fig. 4.4. Thus, user would begin by constructing the numerical grid and input data for T+H and FLAC3D according to the standard procedures for each code, following the steps below:

4.3.3.1 Grid generation (Rutqvist, 2008)

The geometry and element numbering should be consistent in T+H and FLAC3D for a particular problem. This can be achieved by generating the meshes using the standard MESHMAKER attached to the T+H code and by special FISH routines in FLAC3D that can be programmed such that mechanical mesh is consistent with the MESHMAKER (Rutqvist, 2008). Another possibility is to use an external mesh generator, e.g. FEM mesh generator, and routines that can translate this FEM mesh into T+H and FLAC3D meshes (Rutqvist, 2008).

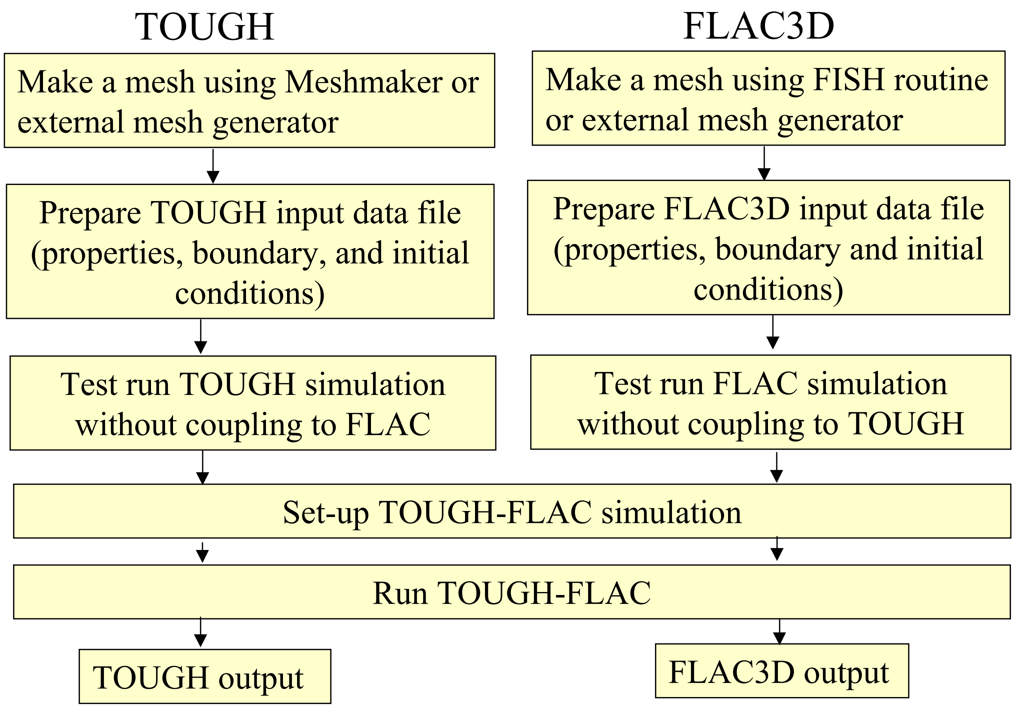

Fig. 4.4. Setting-up of a coupled T+F simulation (from Rutqvist, 2007).

4.3.3.2 Initialization (Rutqvist, 2008)

With the input files defined for T+H and FLAC3D, analyses should be conducted to assure that the problem can be solved and that the input data is correctly prepared. If gravitational effects are accounted for, an initial (gravity-equilibration) T+H simulation is conducted to attain the initial steady state and determine the corresponding initial conditions, including the P, T, and phase saturation profiles. Similarly, a FLAC3D simulation is conducted to establish initial mechanical stress profiles, if they cannot be exactly defined in the input data. Once the T+H and FLAC3D models are initialized, the simulation run can be started.

CHAPTER V

RESERVOIR PERFORMANCE OF THE MESSOYAKHA FIELD

5.1 Introduction

In the permafrost settings, hydrates have been recovered during expeditions at McKenzie Delta in Canada (Dallimore and Collett, 2005) and Alaska North Slope (US Department of Energy, 2007). The first instance of finding gas hydrates in the Messoyakha field on the eastern border of Siberia was published by Makogon and his co-workers (1970; 1971). The Messoyakha gas field was described as a gas reservoir overlain by gas hydrates and underlain by an aquifer of unknown strength. Many observed phenomena at the Messoyakha Field during its production operations appear to indicate the presence of gas hydrates (Makogon, 1981). Important observations reported by Makogon (1981) included:

1. An increase in the average reservoir pressure during the shutdown of production from the field. Note that there is no information on how this average pressure was estimated, and on the measurements upon which it was based.
2. No change in the elevation of the gas-water contact during the last 30 years of production
3. The wells completed within the hydrate layer flowed at very low rates compared to the wells completed in the free gas zone
4. Methanol injection into low-producing wells resulted in significantly increased production at higher wellhead pressures

In this study I have used the T+H simulator to analyze the reservoir and production performance of Messoyakha field.

5.2 Objectives and methodology

The main objective of this study was to determine whether it is possible to obtain a numerical description of the Messoyakha reservoir behavior that is similar to (or at least consistent with) the system response observed during production, and to evaluate the importance of various parameters on this behavior. Such proximity of system behaviors would provide evidence supporting the thesis that hydrates were a significant component of this field, and that their dissociation provided a substantial portion of the produced gas. A corollary to the main objective was that consistently dissimilar behaviors (observed and simulated) that persisted despite any variation of the important parameters would cast serious doubts on the hypotheses of the existence of hydrates and/or their contribution to production from the Messoyakha field.

To the best of the author’s knowledge, this attempt to analyze by means of numerical simulation the Messoyakha field response to gas production is the first study of its kind. I began the analysis with a detailed reservoir engineering analysis of the Messoyakha. The main of purpose of these calculations was to reconcile the available data on the Messoyakha with conceptual and fundamental knowledge of hydrates. The reconciliation study essentially was important to delineate the uncertainties in the available data. These uncertainties prompted me to develop a series of 2D cylindrical models that were potentially representative of the various aspects of the Messoyakha Field. I then simulated gas production from these models and compared them to the field observations. Finally, I conducted an analysis of the sensitivity of the behavior of this Class 1 deposit (hydrate-capped gas reservoir) to a variety of reservoir and operational parameters

Section 5.3 describes the geology, trap, operations, natural gas hydrates and the production at Messoyakha. Section 5.4 provides some of the basic reservoir engineering calculations. These calculations were necessary to construct the model. Section 5.5 describes the model setup, initialization and production parameters. Section 5.6 describes the results of the simulation runs and comparison with field observations. Ultimately, I present conclusions and recommendations for gas production from hydrate deposits.

5.3 The Messoyakha Field

5.3.1 Thermodynamic state

Fig. 5.1 shows the thermodynamic state of the top and bottom of the Messoyakha gas reservoir with respect to the equilibrium P-T curve (describing coexistence of the gas, aqueous and hydrate phases) of the methane hydrate. This figure indicates a typical Class 1 deposit (Moridis and Collett, 2002), with the upper part of the hydrate layer deeply in the hydrate stability zone, equilibrium conditions at the bottom of the hydrate layer (which coincides with the bottom of the stability zone), and a zone with free mobile gas (outside the hydrate stability zone) below the hydrate.

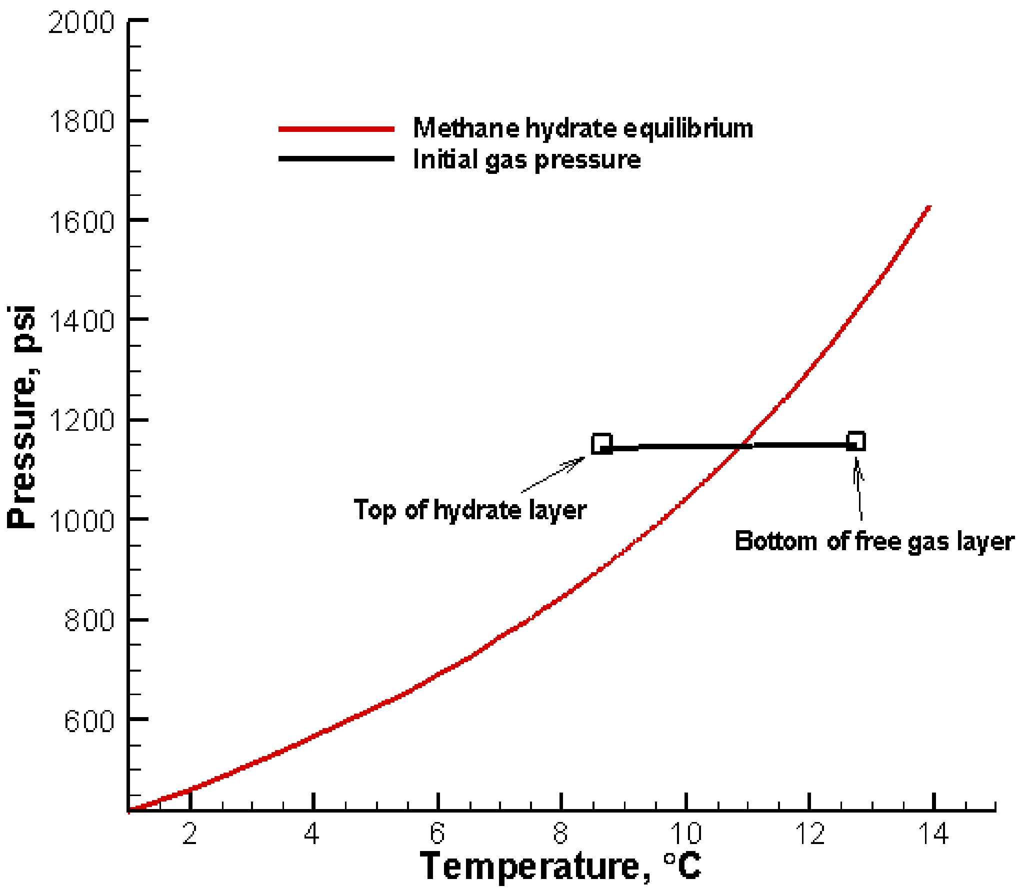

Fig. 5.1. Initial thermodynamic state of the Messoyakha reservoir.

5.3.2 The geology

A cross-sectional schematic of the Messoyakha field is shown in Fig. 5.2 (Makogon et al., 2005).The Messoyakha gas field is enclosed in an anticlinal structural trap and is overlain by a 420 to 480 m thick permafrost zone. The producing intervals are located in Dolgan formation (sandstone) which is sealed by an overlying shale layer. The Dolgan formation is frequently interbedded with shale streaks (Makogon, 1981; Krason and Ciesnik, 1985; Krason and Finley, 1992; Makogon, 1997).

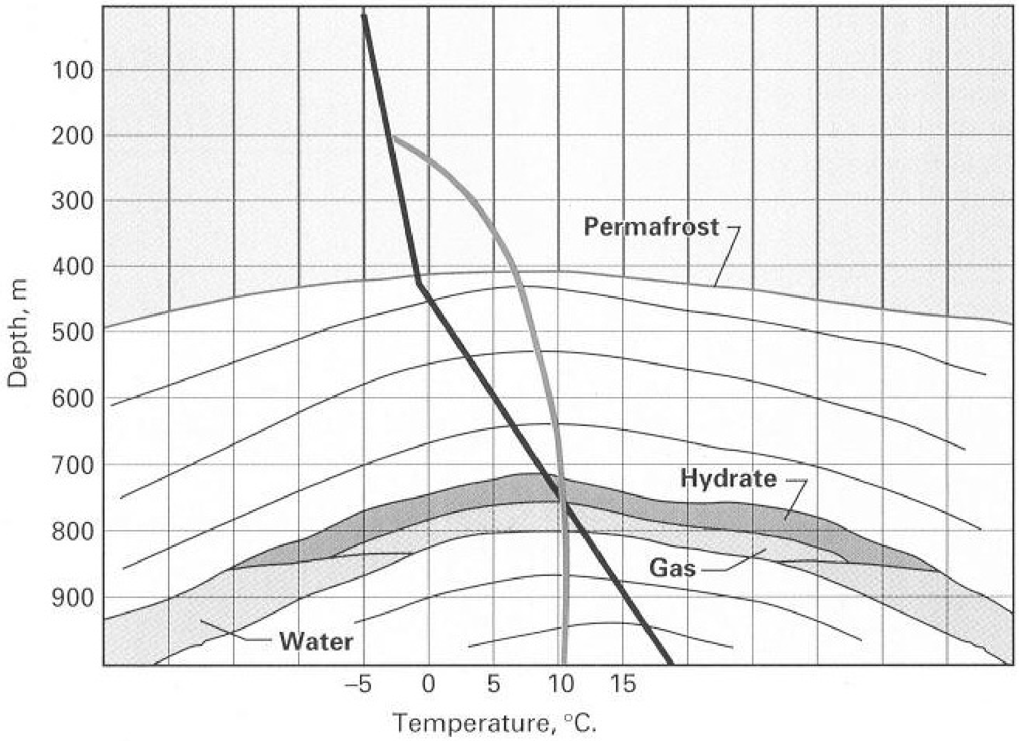

Fig. 5.2. Cross section of the Messoyakha reservoir (from Makogon et al., 2005).

The structural enclosure of the field is 84 meters and the areal extent of the field is 12.5 km x 19 km (Makogon et al., 2005). A contour map of the top of the Cenomanian Dolgan Formation at the Messoyakha field is shown in Fig. 5.3 (Krason and Finley, 1992). The depths (in meters) refer to the elevation below mean sea level. Fig. 5.4 shows two cross sectional views of the Messoyakha Field (Makogon et al., 1971) and depicts the 10°C isotherm, as inferred from the elevation of the base of the hydrate stability zone.

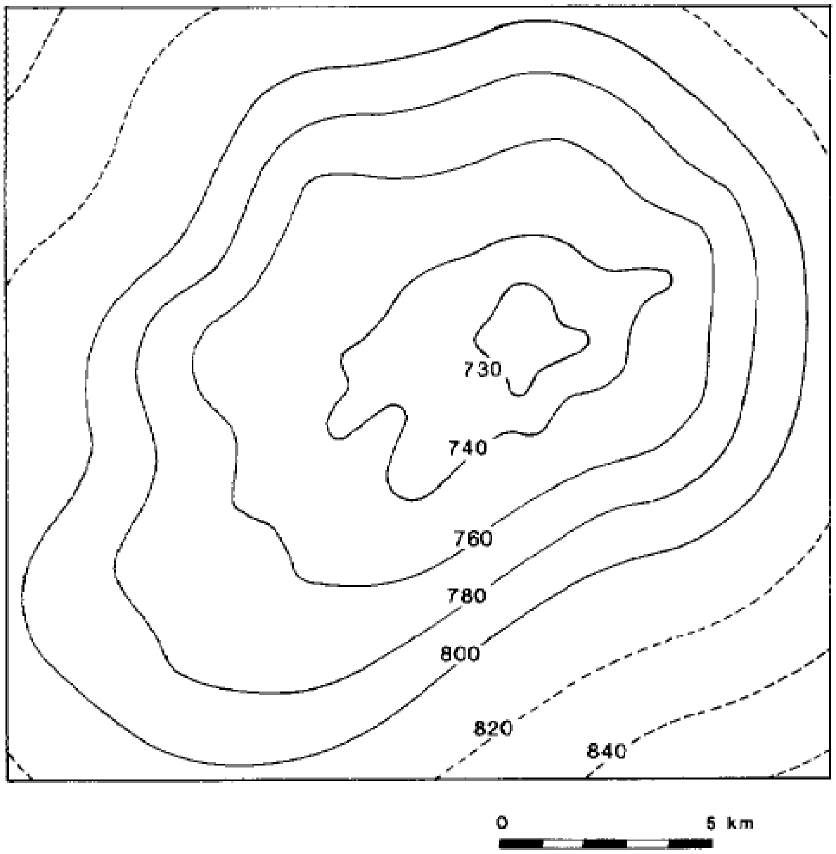

Fig. 5.3. Contour map of the Messoyakha Field (from Sapir et al., 1973).

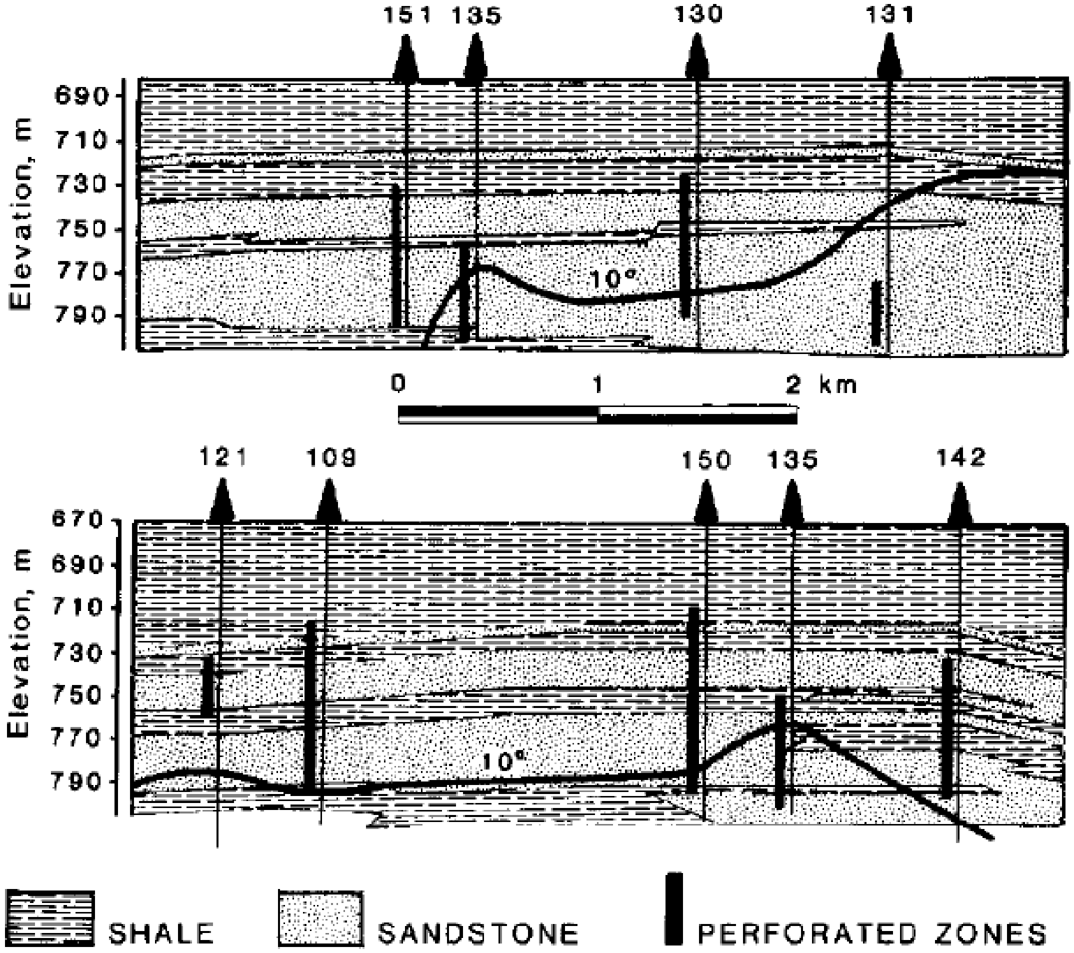

Fig. 5.4. Cross section of completions at the Messoyakha reservoir (from Makogon et al., 1971b).

5.3.3 Operations

More than 60 wells have been drilled in this field on a pattern that involved of 500 m x 1000 m well spacing. Production began in 1970 and continued until 1977. Initial production rate per well was reported to range from 111 Mscf/day to 6275 Mscf/day. The production in the Messoyakha field was ceased from 1979-82. During the shutdown period, the reservoir pressure increased (although how this was estimated is unclear), and this pressure increase was interpreted to have been caused by the continued dissociation of hydrates (Makogon, 1981). Fig. 5.5 (Makogon et al., 2005) shows the reservoir pressure behavior and the corresponding gas production history at the Messoyakha Field. This figure illustrates that when the production ceased at the Messoyakha, the average pressure kept on increasing. However, there is no information about how this average pressure was defined and estimated, what types of measurements were involved, at what locations, and using what kind of sensors.

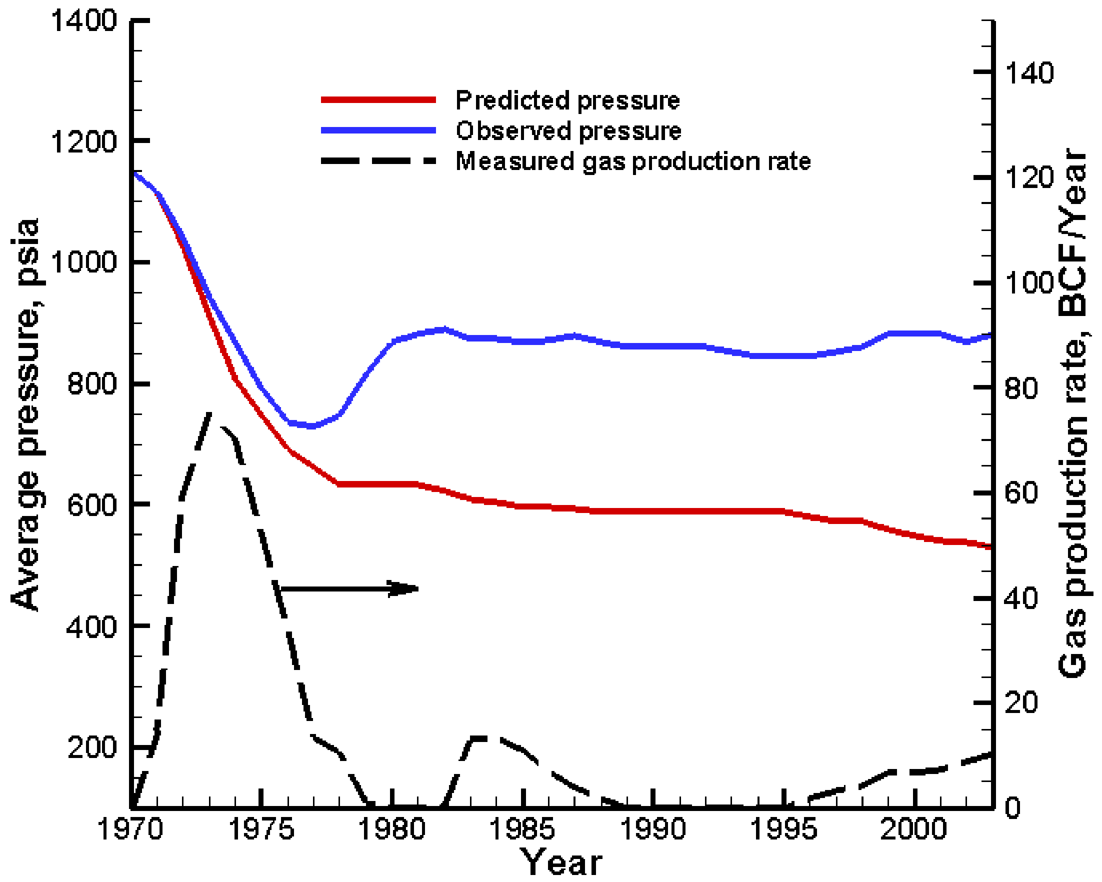

Fig. 5.5. Production behavior at the Messoyakha (from Makogon et al., 2005).

5.3.5 Gas reserves

The volumetric gas reserves (free gas + hydrated gas) at the Messoyakha field estimated by different researchers range from 1.3 to 14 Tcf, as illustrated in Fig. 5.6 (Krason and Finley, 1992). There is also significant uncertainty in the estimates of gas trapped in the hydrate layer of the Messoyakha Field. Sheshukov (1973) calculated that 2.2 Tcf of gas was in hydrate form in upper portion of Messoyakha and 0.6 Tcf gas present as free gas in the lower portion of the Messoyakha. Makogon et al. (2005) reported that initial in-place gas (free-gas) at Messoyakha was 848 Bcf and the producible reserves from hydrate state were 424 Bcf. Fig. 5.6 illustrates the uncertainty in the total gas reserves (free gas + hydrate gas) at the Messoyakha field. Using the geometry described in Makogon et al. (2005), my calculations predicted the in-place gas reserves (both as hydrate and as free gas) to be 5 to 7 times greater than that published by Makogon et al. (2005).

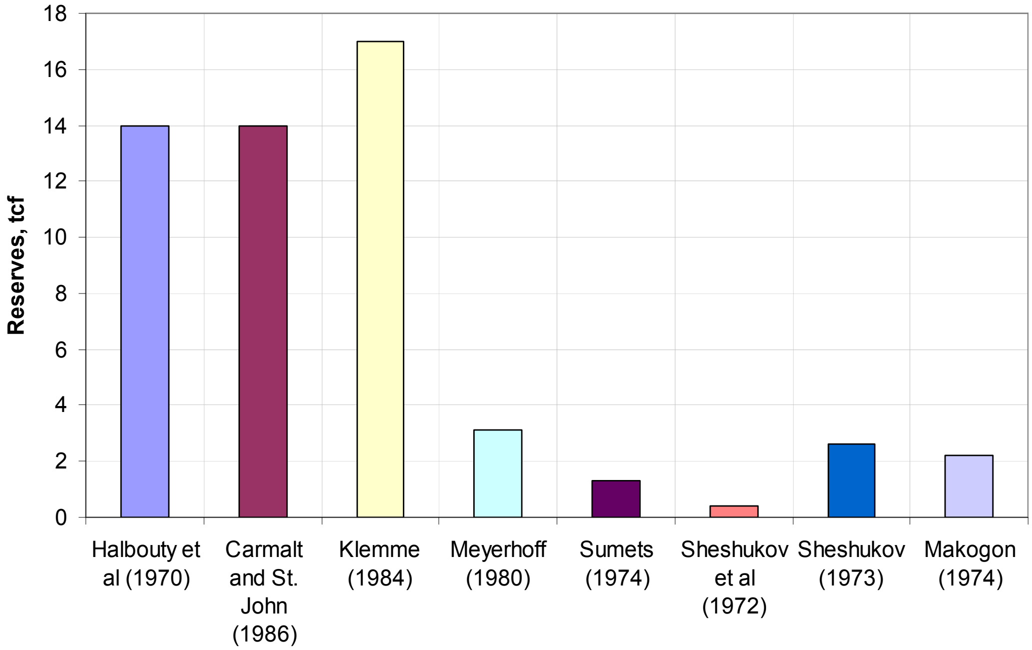

Fig. 5.6. Various estimates of gas in place in the Messoyakha field (data from Krason and Finley, 1992).

5.3.6 Production

The production rates from the wells that were completed within the hydrate layer were significantly lower than those from the wells that had been perforated deeper in the free gas zone of the reservoir. Table 5.1 lists the gas production rates from selected wells (Makogon et al., 1971) as well as the location of the corresponding perforated intervals with respect to the original elevation of the base of the hydrate layer. The base of the hydrate layer (BHL) is assigned a value of “0”; the elevations above the BHL are “+” and below the BHL are “–”.

Table 5.1

Production from various perforation locations at the Messoyakha (from Makogon et al., 1971b)

Well No.	Proportion of perforation in hydrate zone	Distance from perforations to hydrate-gas interface (m)	Production rate (1000 m^3/D)
121	100	+64	26
109	100	+6	133
150	81	-6	413
131	0	-59	1000

The wells that were completed in the hydrate zone were stimulated by using chemicals such as Calcium chloride and methanol. These chemicals are inhibitors for hydrate formation, or in other words, induce instability to the hydrates by causing the equilibrium curve to shift. This chemical stimulation helped destabilizing the hydrates near the well. After stimulation, the wells could operate at higher wellhead pressures because of higher effective permeability in the vicinity of the perforations. Fig. 5.7 (Makogon et al., 1971) demonstrates the effect of methanol injection on the production rate Q_p of a well in the Messoyakha Field.

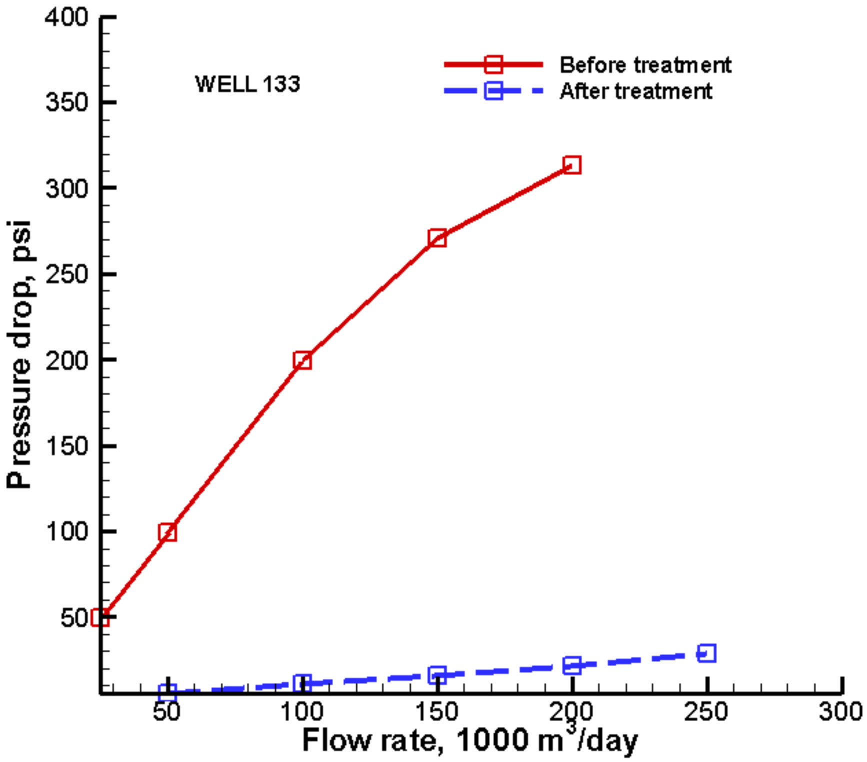

Fig. 5.7. Effect of chemical stimulation for Well 133 (data from Makogon et al., 1971).

5.3.7 Gas/water contact

Table 5.2 shows the various estimates of the depth to the gas/water contact reported in the literature (Krason and Finley, 1992).

Table 5.2

Gas/water contact values at the Messoyakha (from Krason and Finley, 1992)

Source	Gas/water contact
(Meyerhoff, 1980)	-805 m
(Makogon, 1984; Makogon, 1988; Makogon et al., 2005)	-819 m
(Sapir et al., 1973)	-779 to -811 m

According to Makogon et al. (2005) and Makogon (2007), the gas-water contact did not move during the entire period of gas production at the Messoyakha.

5.3.8 Rock properties

Although the rock properties at the Messoyakha are reported to be highly heterogeneous (Makogon et al., 1971; Meyerhoff, 1980; Krason and Ciesnik, 1985; Krason and Finley, 1992; Makogon et al., 2005), there is no information on their spatial distribution. The reservoir conditions and the range of the rock properties are listed in Table 5.3.

Table 5.3

Reservoir properties at the Messoyakha (from Makogon et al., 2005)

Property	Range
Porosity	16-38%
Permeability	10 to 1000 md
Geothermal gradient	4.2 °C/100m
Residual water saturation	29 to 50%
Initial reservoir pressure	1150 psia

5.4 Data reconciliation

To numerically represent the Messoyakha field in T+H, it was necessary to critically examine the different reservoir and thermodynamic parameters published in various sources. This section presents the arguments and comments on published parameters of the Messoyakha field. Based on these arguments, the representative values of different parameters were selected and used as inputs in the numerical model.

5.4.1 Saturations

The only data available on saturations of water, gas and hydrates in the respective zones (the upper hydrate zone and the lower free gas zone) is from Makogon et al. (2005). Average water saturation was described to be about 40%, salinity to be 1.5%, and initial hydrate saturation to be about 20%. The saturations data discussed in Makogon et al. (2005) is tabulated in Table 5.4.

Table 5.4

Average saturations at the Messoyakha (from Makogon et al., 2005)

Saturations	Hydrate layer	Free gas layer
$S_{hydrate}$	20	0
S_{water}	40	40
S_{gas}	40	60

There is an important point to be noted here. If these saturations do occur during the initial "undisturbed" state of the reservoir, the hydrostatic pressures should exactly follow the equilibrium hydration pressure (as defined by the gas + aqueous + hydrate phase coexistence in Fig. 2.3 and 4.1) at each point within the hydrate layer, i.e., this regime has to persist at every elevation despite different temperatures (as affected by the geothermal gradient). However, if methane and water coexist in such a 3-phase regime, they are expected to react and form hydrate until the exhaustion of one of the two. The only possibility of occurrence of three phases in the hydrate layer is an extremely finely balanced salt distribution, which would be next to impossible to maintain over long periods (as this would mean effective elimination of molecular diffusion). Because of the difficulty (if not impossibility) of meeting all these conditions, 3-phase coexistence cannot exist in the hydrate layer at the Messoyakha Field. Note that no information is available on the wettability properties (capillary pressures and relative permeability) of the various geologic media in the Messoyakha field, and on how these are affected by the presence of hydrates in the pores.

As is obvious from this discussion, Messoyakha is a typical representative of a Class 1G hydrate deposit (using the classification scheme of Moridis and Collett (2003)). Class 1G means that the hydrate layer consists of hydrate and gas and the lower free gas layer consists of gas and water. Such deposits are the most attractive targets for gas production, because while the free gas can be produced by conventional methods, the hydrate dissociation will keep on recharging the gas into the reservoir and will contribute to the overall gas production.

As the previous discussion indicates, the most reasonable description of the initial state of the Messoyakha field includes (a) a hydrate layer characterized by a 2-phase (gas and hydrate) regime, and (b) an underlying 2-phase zone of mobile fluids that include gas and water (often referred to as the “free gas zone”). This is how the numerical model of Messoyakha was initialized for this study.

5.4.3 Gas composition

Table 5.5 describes the gas composition at the Messoyakha field (Makogon et al., 2005), and indicates that it is overwhelmingly dominated by methane.

Table 5.5

Gas composition at the Messoyakha (from Makogon et al., 2005)

Gas	Percentage
CH_4	98.6
C_2H_6	0.1
C_3H_8	0.1
CO_2	0.5
N_2	0.7

5.5 Reservoir modeling

5.5.1 Model setup

Because the information on the Messoyakha field that can be obtained from public domain sources is limited, it was not possible to reconcile the limited published data with my reservoir engineering calculations and the gas hydrate fundamentals discussed earlier. The paucity of data sufficient for the task has also been reported previously (Krason and Ciesnik, 1985; Krason and Finley, 1992). These limitations and constraints did not allow the development of a full (3D) field model of the Messoyakha field. Instead, I constructed a series of 2-D cylindrical models (each describing the 500 x 1000 m units defined by the well spacing) representative of the various aspects of the Messoyakha Field. I analyzed the output from each of the models and compared to the different field observations.

Fig. 5.8 illustrates the modeled cylindrical domain used in this simulation study. The model radius was 400 m, resulting in a system with a volume equal to that of the Messoyakha well spacing of 500 x 1000 m (see Section 5.3.3). The thickness of the reservoir was 90 m. The model was discretized into 100 radial elements and 135 layers (a total of 13500 elements). The fine discretization scheme was necessary to capture the sharp front and rapid saturation changes occurring in the hydrate layer and in the vicinity of the well.

The base case in this study involved (a) impermeable shale overburden and underburden, and (b) no water drive. The input parameters for the base case are tabulated in Table 5.6.

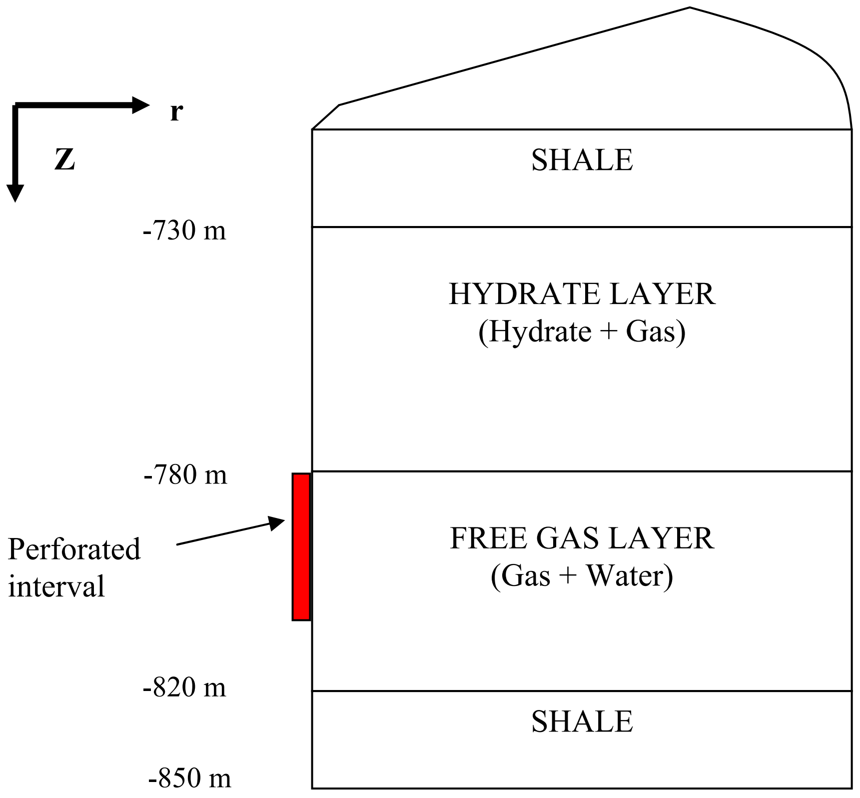

Fig. 5.8. Simulation model for the Messoyakha reservoir.

Table 5.6

Base case input parameters in T+H for the Messoyakha study

Property	Hydrate layer	Free gas layer
Thickness, m	50	40
Porosity	0.35	0.35
Gas production rate	1.96 m^3/sec (=6 MMscf/day)	
Absolute permeability, md	500 md	500 md
Initial hydrate saturation, S_H	0.5	0
Initial gas saturation, S_G	0.5	0.5
Water saturation, S_A	0	0.5
Irreducible water saturation	0.28	0.28
Relative permeability model - Modified Stone's model (Stone, 1970)	$k_{\mathrm{rA}} = \min\left\{\left[\frac{S_{\mathrm{A}} - S_{\mathrm{irA}}}{1 - S_{\mathrm{irA}}}\right]^{n}, 1\right\}$ $k_{\mathrm{rG}} = \min\left\{\left[\frac{S_{\mathrm{G}} - S_{\mathrm{irG}}}{1 - S_{\mathrm{irA}}}\right]^{n}, 1\right\}$ $k_{\mathrm{rH}} = 0$ $S_{\mathrm{irA}} = 0.28$ $S_{\mathrm{irG}} = 0.02$ $n = 3.57$	
Capillary pressure model - Van Genutchen function (Van Genutchen, 1980)	$p_{\mathrm{cap}} = -p_0\left[\left(S^*\right)^{-1/\lambda} - 1\right]^{-\lambda}$ with restriction $-p_{\max} \le p_{\mathrm{cap}} \le 0$ $S^* = \left[\frac{S_{\mathrm{A}} - S_{\mathrm{irA}}}{S_{\mathrm{mxA}} - S_{\mathrm{irA}}}\right]$ $\lambda = 0.45$ $S_{\mathrm{irA}} = 0.27$ $p_0 = 10^5$ Pascals $p_{\max} = 10^6$ Pascals $S_{\mathrm{mxA}} = 1$	

5.5.2 Model initialization

Before any numerical model is run, it is necessary to be initialized. Initialization process in T+H is a challenging task and has been discussed in detail in Moridis et al. (2007).

The following assumptions were made to initialize the model:

1 Salinity was assumed to be zero. Since the upper portion of the reservoir includes only gas and hydrate, we cannot define salinity in this type of system. In other words, neither the "gas phase" nor "hydrate phase" can account for salt. This is a reasonable approach, given that it is not known where the 1.5% salinity reported in Makogon et al (2005) was measured.

2 Initial pressure at the hydrate-gas interface is 7.92e6 Pa (1150 psia) which corresponds to the hydrostatic pressure at the base of the hydrate layer at the Messoyakha field. Based on the pressure at the base of the hydrate layer, the temperature is about 10.88°C (for 3-phase methane-hydrate-water) equilibrium which is close to 10°C isotherm defined in (Makogon et al., 2005).

The initialization process involves the determination of the correct initial p and T distribution along a single column that is used as a stencil for the entire domain. The column is subdivided into two separate subdomains: the hydrate layer subdomain and the free gas zone subdomain. Because the pressure in hydrate deposits follows very closely the hydrostatic (Moridis et al., 2008), the pressure in the entire profile and at the base of the hydrate layer is easily determined from its known elevation. Because Messoyakha is a Class 1 deposit, the base of the hydrate layer occurs at equilibrium. Consequently, the temperature at the base of the hydrate is determined as the hydration equilibrium T corresponding to p at the same location. From the known T at the base of the hydrate and the known geothermal gradient (= 0.042 °C/m), an initial temperature distribution in the profile of the upper subdomain is obtained. The p- and T- distributions are then finalized through an iterative process (owing to the dependence of fluid densities (and, consequently, the pressure) and composite thermal conductivities on p and T), and the heat flow through the bottom boundary is determined.

The process is repeated in the lower subdomain, but this time the temperature at the lowermost boundary is slightly adjusted to yield a heat flow through it upper boundary that exactly matches that determined in the upper subdomain. The two subdomains are connected, and the conditions in the resulting combined system (i.e., the entire column) are stable because of the equality of flows throughout the column.. Fig. 5.9 shows the initial conditions in the column. The shale boundaries at the top and bottom of the reservoir in the model were 30 meters thick. This thickness was based on the earlier scoping studies (Moridis, 2003; Moridis et al., 2007) and "was sufficient to accurately represent heat exchange with the hydrate deposit" (Moridis et al., 2007).

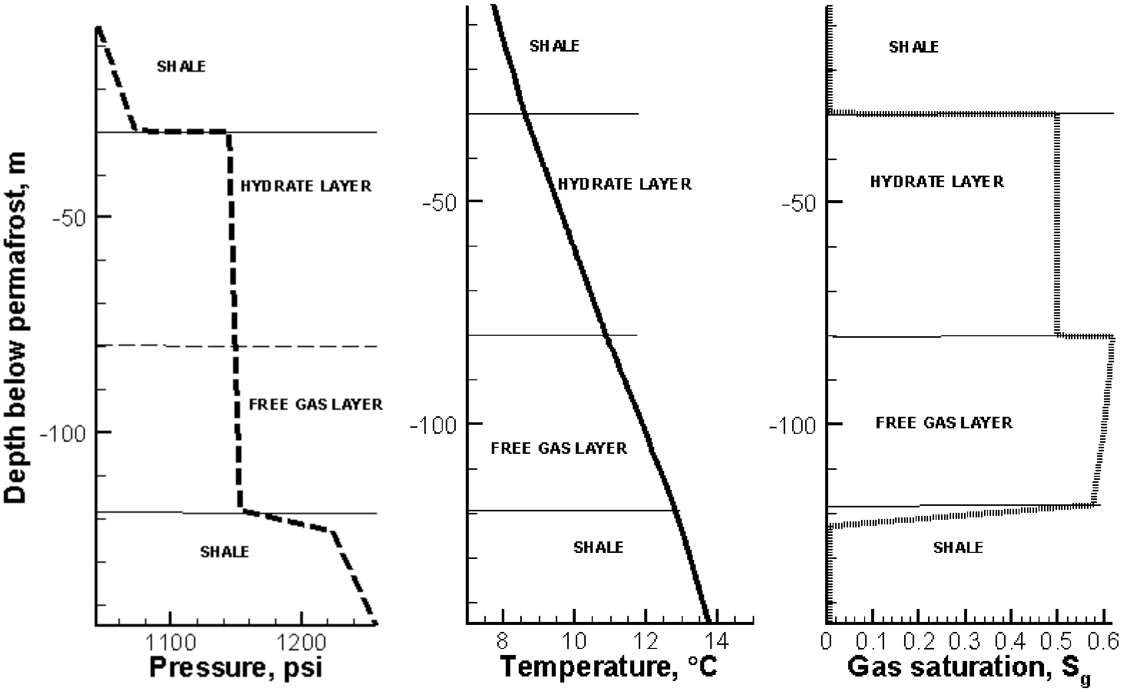

Fig. 5.9. Initial conditions for the base case in T+H.

5.5.3 Production parameters and well description

Gas was produced from the well of this 2-D model at a volumetric flow rate of Q_P = 170,000 Sm^3/Day (6 MMscf/day). The well was completed from 0.5 m below the base of hydrate layer (BHL) to 16.5 m below the BHL (thickness of the perforated interval is 16 m). I followed the approach of Moridis and Reagan (2007) for the description of well in T+H. The well was approximated to behave according to Darcy's equation instead of Navier-Stokes equation. Well was treated as a pseudo-porous medium with properties described in Table 5.7.

Table 5.7

Well description parameters

Property	Value
Porosity, $\varphi_{\text{wellbore}}$	1
Permeability, k	$k_z = 5*10^{-9}$ m^2 = 5000 darcy $k_r = 10^{-11}$ m^2 = 10 darcy
Capillary pressure	0
Relative permeability model • Modified Stone's first three phase model (Stone, 1970)	$k_{\text{rA}} = \min\left\{\left[\frac{S_{\text{A}} - S_{\text{irA}}}{1 - S_{\text{irA}}}\right]^n, 1\right\}$ $k_{\text{rG}} = \min\left\{\left[\frac{S_{\text{G}} - S_{\text{irG}}}{1 - S_{\text{irA}}}\right]^n, 1\right\}$ $k_{\text{rH}} = 0$ $S_{\text{irA}} = 0.01$ $S_{\text{irG}} = 0.005$ $n = 1$

The small gas saturation value was necessary to allow emergence of gas phase in the wellbore (Moridis and Reagan, 2007). The total mass production rate Q_p = 6 MMscf/day was applied to the single element located at the top of rock material which defines the wellbore. Moridis and Reagan (2007) have shown that the approach (described above) to numerically define the well deviates by less than 5% from the Navier-Stokes solution and cuts the computation time by more than a factor of 2.

5.5.4 Contribution of hydrates to overall gas production

Moridis et al. (2007) introduced the concept of “Rate replenishment ratio (RRR)” and “Volume replenishment Ratiof (VRR)” for production from Class 1 hydrate deposits. These two are defined as follows

$$RRR = \frac{Q_r}{Q_p} \tag{5.1}$$

$$VRR = \frac{V_r}{V_p} = \frac{\int_0^t Q_r(t)dt}{\int_0^t Q_p(t)dt} \tag{5.2}$$

where Q_r is the CH_4 release rate in the reservoir, Q_p is the CH_4 production rate at the well, V_r is the cumulative volume of CH_4 released and V_p is the cumulative volume of CH_4 produced.

5.6 Base case results and analysis

This section deals with the detailed analysis of various simulation results of T+H simulator.

5.6.1 Base case with no water drive

I ran the base case for 8 years at constant production rate and then shut it down for next 3 years. The results are shown in Figs. 5.10 to 5.11.

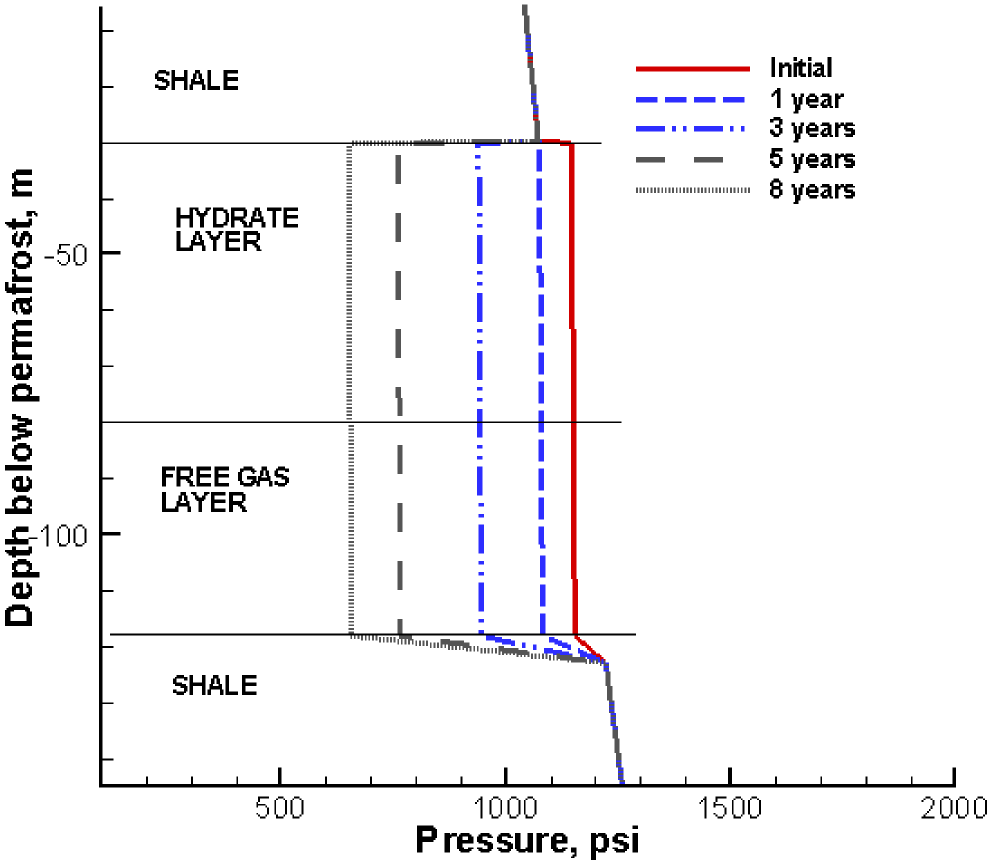

Fig. 5.10. Evolution of the pressure distribution of the gas phase along the z-axis at r = 50 m in the base case of the Messoyakha study.

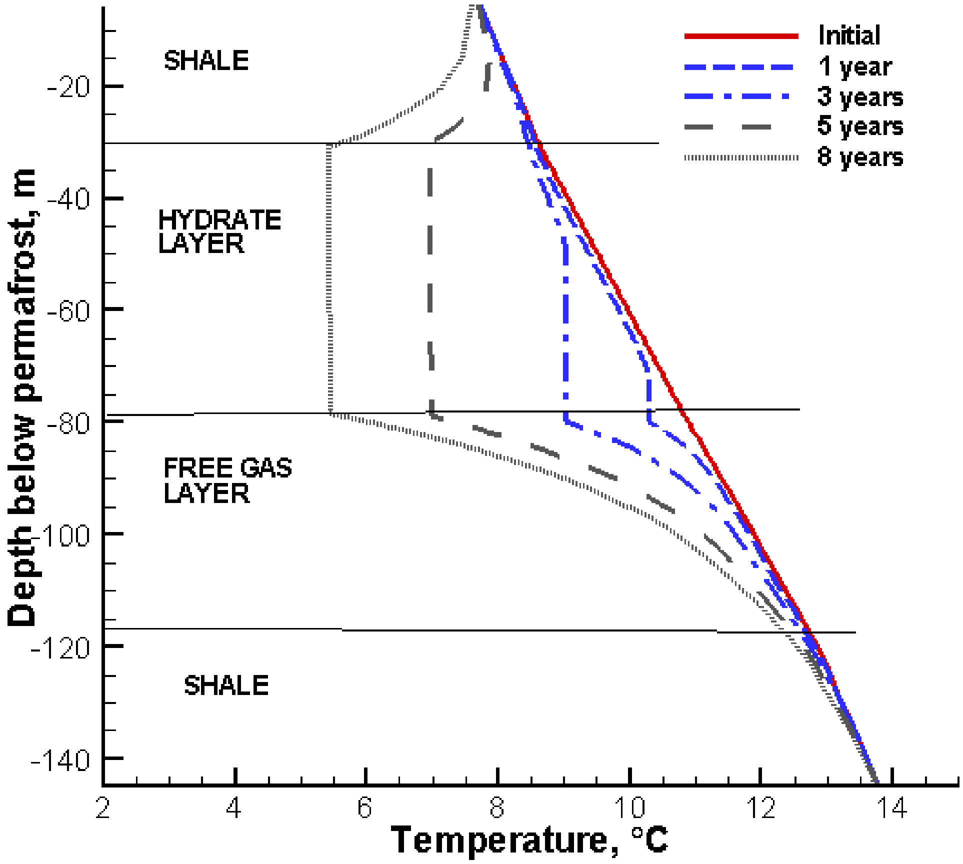

Fig. 5.11. Evolution of the temperature distribution along the z-axis at r = 50 m in the base case of the Messoyakha study.

The gas-phase pressure distribution (along the z-axis at r = 50 m) in Fig. 5.10 indicates that, when production is initiated, the gas pressure is practically uniform in the entire profile, i.e., in both the hydrate layer and the underlying free gas zone. This was expected, given the relatively low density of the gas at the initial p and T. Fig. 5.11 illustrates that the temperature in the reservoir continues to decrease because of the dissociation of hydrates. The decreasing temperature exhibits the "bottleneck" to gas production from hydrates and means that lesser heat is available to transfer to hydrates for their continued dissociation.

Fig. 5.12 shows the thermodynamic path followed by conditions at two points (at the bottom and at the top of the hydrate layer, respectively) at r = 50 m. Fig. 5.13 shows the S_H profiles at different times. Initially, the hydrate-gas interface is at the equilibrium curve and the top of the hydrate layer is away from the equilibrium curve (as it is at a lower temperature). When the gas is produced from the free gas portion of the reservoir, gas hydrate in the hydrate layer dissociates due to depressurization and starts charging the free gas portion of the reservoir.

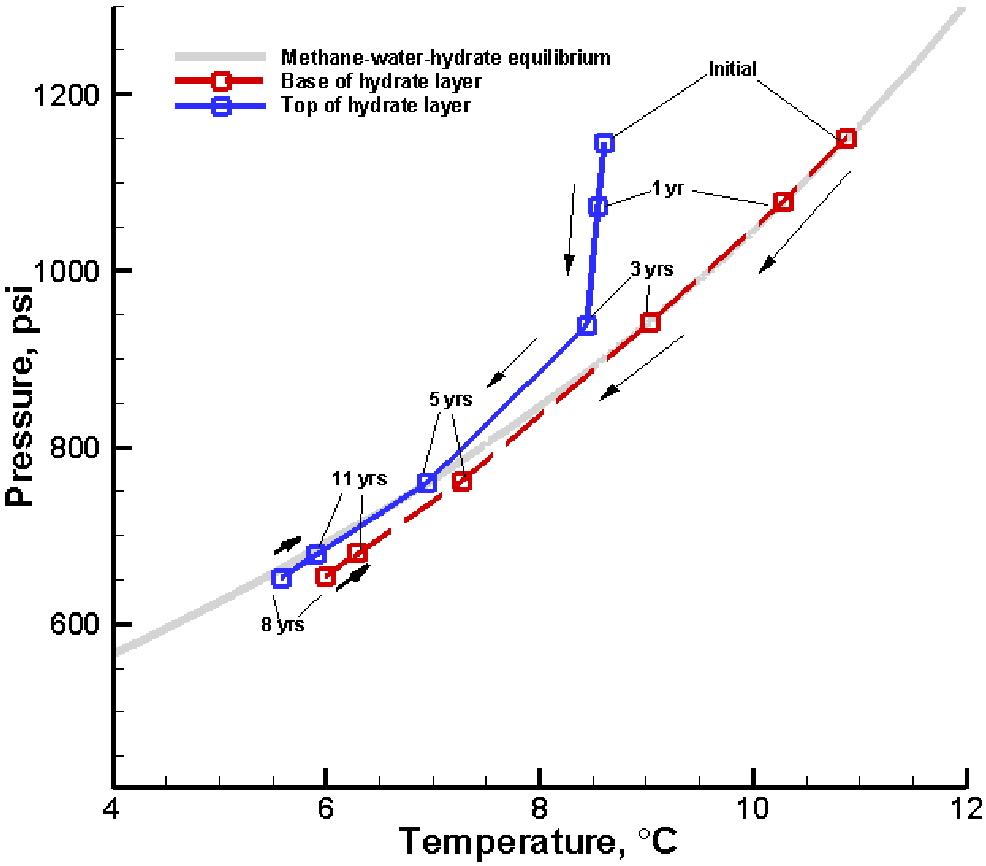

Fig. 5.12. Thermodynamic path during gas production for the base case.

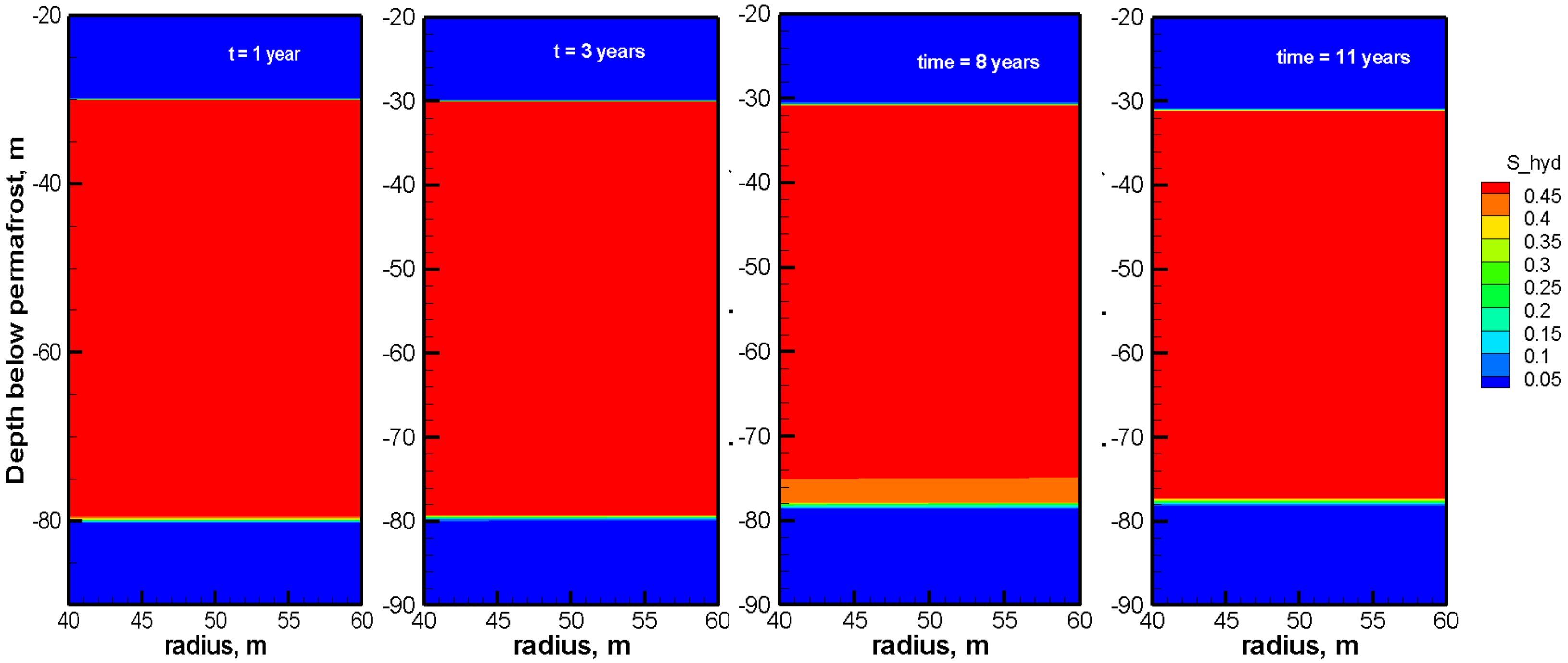

Figure 5.13. S_H distributions at different times for the base case

The pressure and temperature regime in the hydrate layer follows the equilibrium curve as production continues (shown by lighter arrows in Fig. 5.12), until the hydrate is completely dissociated. The hydrate gets completed dissociated at the base of hydrate layer after slightly over 3 years of production. After production stops at t = 8 years, the temperature begins to increase because of (a) continuous geothermal heat flow from the top and bottom boundaries towards the hydrate zone, (b) drastic reduction (and possible cessation) of dissociation with the interruption of production, and (c) practical elimination of flow, and of the corresponding Joule-Thomson cooling. In addition to the temperature, the pressure increases because of several reasons (the exact contribution of which is difficult to determine): temperature increase in a system with a fixed volume, pressure equilibration within the reservoir, continued net hydrate dissociation. The bolder arrows in Fig. 5.12 illustrate the increase in pressure at the two points during the shut-in period, which is from 8 years till 11 years.

At the Messoyakha gas field, the reservoir pressure increased during the shut-in period. Makogon et al. (2005) proposed that the pressure increased until the equilibrium curve at the corresponding temperature. As mentioned before, no information is available on how and where the pressure was measured at the Messoyakha field. The simulation results presented are for single well behavior. It might be possible that the pressures reported in Makogon et al. (2005) were not average but single well observations. Note that heat transfer is the main mechanism controlling hydrate dissociation in (and, consequently, gas production from) this Class 1G deposit.

Fig. 5.14 shows the methane release rate from the hydrate dissociation *in the reservoir*. The spikes in the methane release rates in Fig. 5.14 are related to the discretization and indicate that a hydrate layer in the model has dissociated completely. As the gas is produced (at a constant rate) from the free gas portion, the release rate continues to increase. The increase in release rate means that the gas hydrates are dissociating more vigorously as time advances.

The effective gas permeability in the hydrate layer continues to increase as hydrates continue to dissociate. When the well is shut-in after 2880 days of production, the hydrates still continue to dissociate in the reservoir, albeit at a very low rate. During the shutdown period (for t > 8 years), the contribution of dissociation is not strong enough to have a large pressure increase as observed at the Messoyakha field. Again, there is no mention in public literature about where the pressure was measured and how the average pressure was calculated in the field.

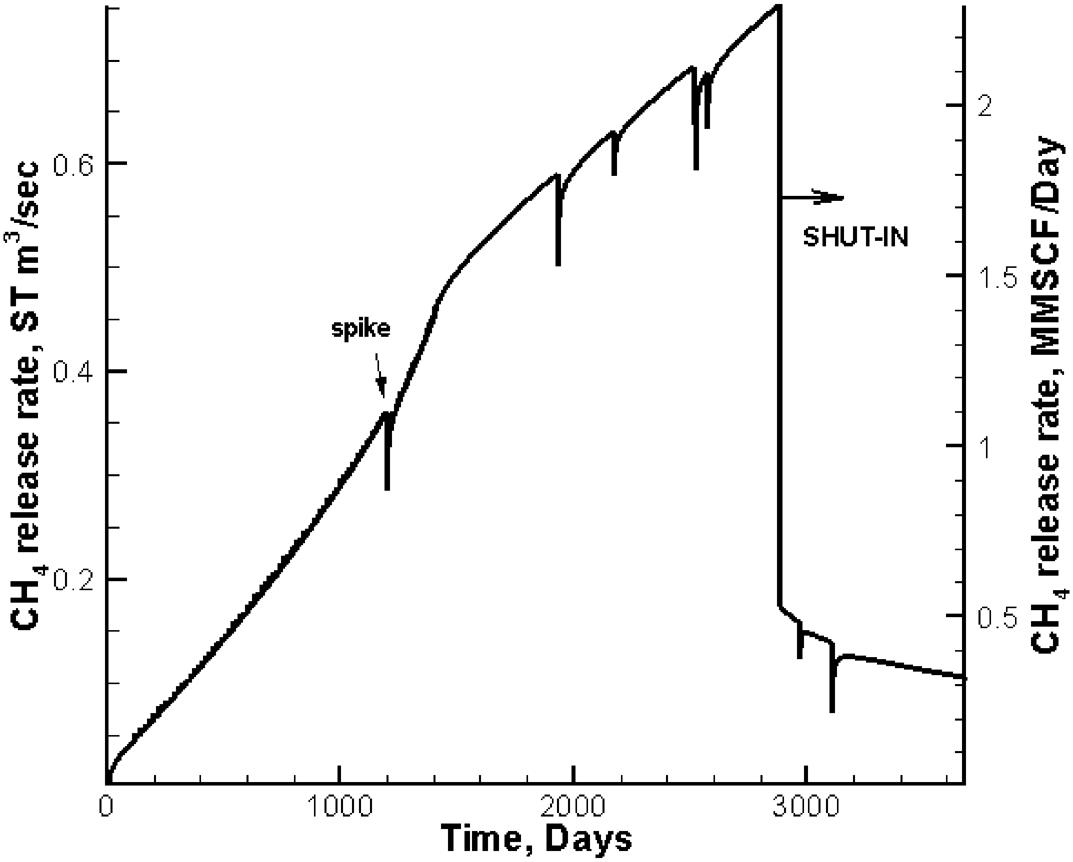

Fig. 5.14. Methane release rate for the base case.

At 2880 days of gas production, the release rate of gas in the reservoir Q_r reaches about 2.5 MMscf/day. The gas production rate at the well Q_p is 6 MMscf/day. Hence, the rate replenishment ratio (RRR) at the end of 2880 days is about 42%. The VRR reaches about 22% after 8 years of production (Fig. 5.15). Given the consistent upward trend of the VRR, this number is not inconsistent with that of Makogon et al. (2005) who estimated a VRR of 36% after 30 years of gas production at the Messoyakha. However, the methodology used to calculate the contribution of hydrates to gas production at the Messoyakha has not been published.

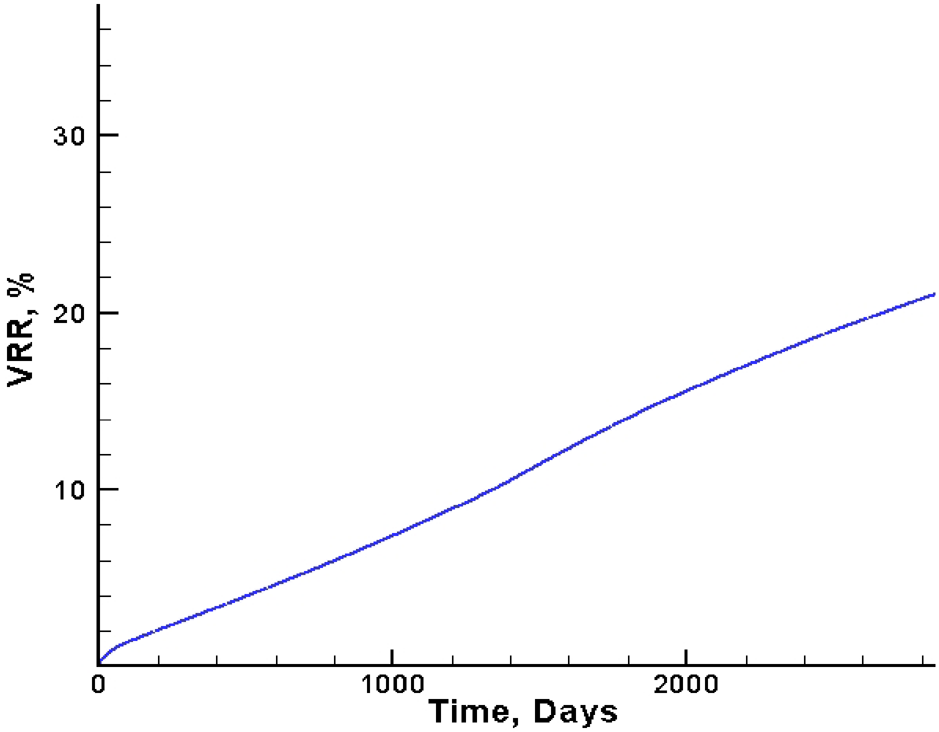

Fig. 5.15. VRR for the base case.

Another important effect observed in the simulations was the formation of secondary hydrates in the vicinity of the top of the perforations of the well, i.e. close to the hydrate-gas interface. In the base case, the top of the perforated interval is about 0.5 m away from the hydrate-gas interface. When gas is produced, cooling occurs because of the endothermic nature of the gas-releasing hydrate dissociation, and because of Joule-Thomson cooling caused by depressurization and high gas velocities near the well. The availability of gas and water (either native or originating from hydrate dissociation) and the continuing cooling lead to the formation of secondary hydrate near the well, where the gas velocity is at its highest and the temperature at its lowest level in the reservoir. The formation of secondary hydrates can lead to higher pressure drops around the perforations and eventually choking of the well, i.e, near complete blockage of flow. The formation of secondary hydrates is illustrated in Fig. 5.16, which shows such hydrates around the well after 180 days of production. However, for the base case, their effect was not important later during the production because of fluid mixing with the warmer gas from the free gas portion of the reservoir. The perforations very close to the hydrate-gas interface may exhibit secondary hydrate formation around the well during initial the early stages of production.

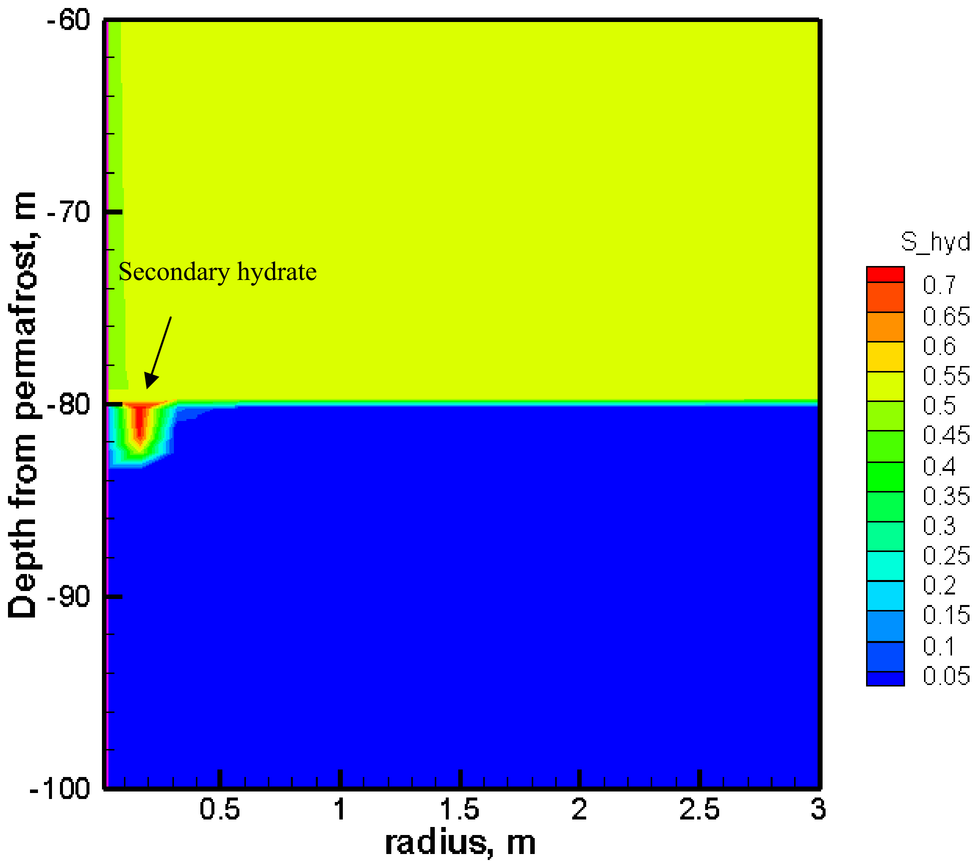

Fig. 5.16. Formation of secondary hydrate for base case at 180 days.

5.6.2 Base case with water drive

The literature is not clear about the strength of the aquifer at Messoyakha. Makogon et al. (2005) suggests that the gas-water contact has not moved during the last 30 years of production. To model this behavior, I had to develop cylindrical model with different initial conditions. Fig. 5.17 shows the initial pressure and temperature conditions in the reservoir. The capillary pressure parameters for the Van Genutchen function (Table 5.6) were changed so as to give the initial gas saturation and water saturation profiles shown in Fig. 5.18. $p_{\max}$ was changed to 3.0e5 Pa for the simulation study of the water drive case.

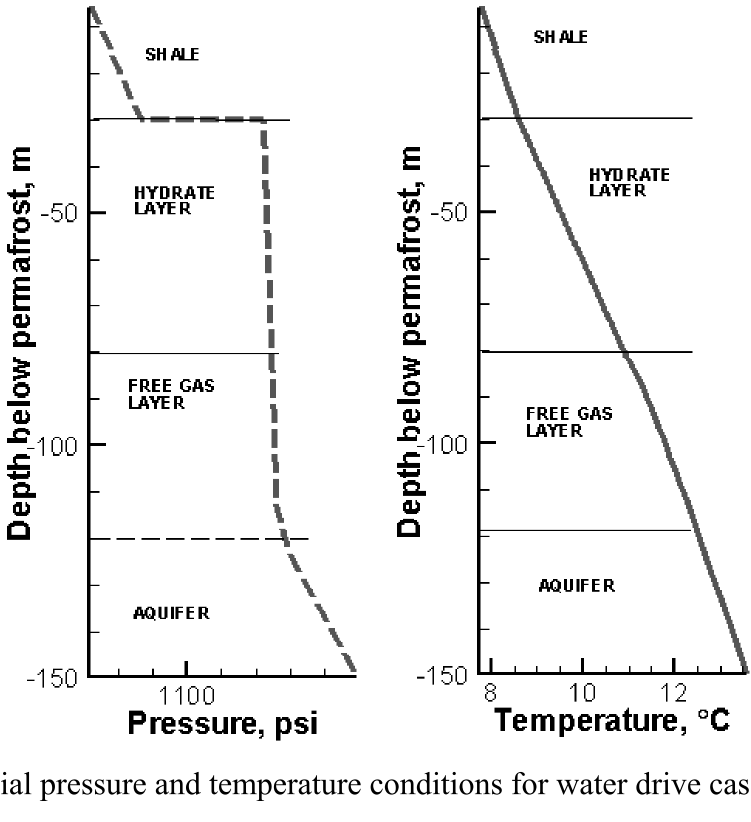

Fig. 5.17. Initial pressure and temperature conditions for water drive case.

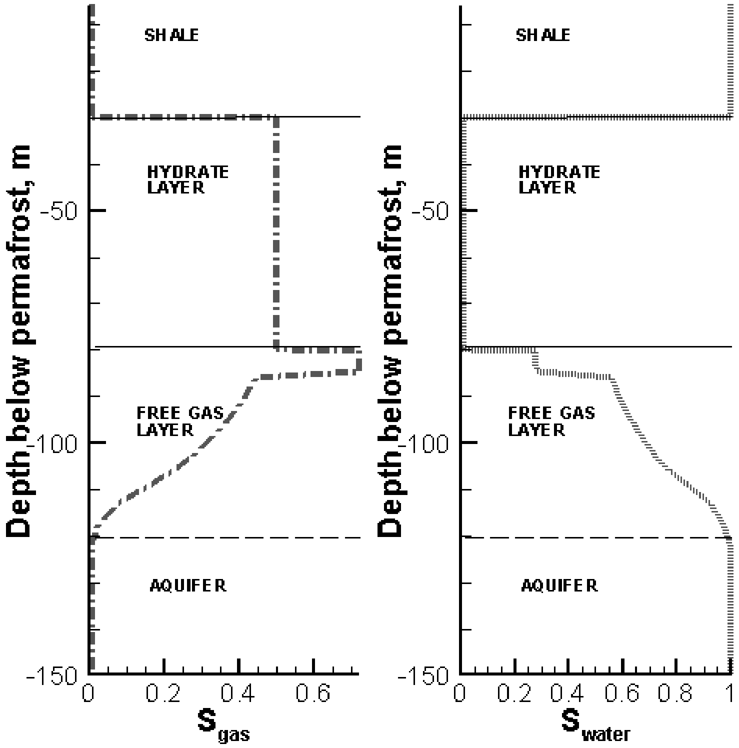

Fig. 5.18. Initial gas saturation and water saturation profiles for water drive case.

Following initialization, a simulation of long-term production was attempted. This was not possible because of rapid formation of large amounts of secondary hydrates near the well that choked the well within a short time from the initiation of production. If the aquifer is modeled as a strong aquifer, it displaces the gas very quickly. When Q_p = 1.7×10^5 STP m^3/day (= 6MMscf/day), it takes about 10 days for the production cessation to occur. Because of the low temperature (for the reason discussed in Section 5.6.1) and the increased availability of water, secondary hydrates form near the well, and reach saturations that are sufficiently high to block flow, thus resulting in the cessation of production (Fig. 5.19). Essentially, the formation of hydrates around the perforations is expedited in the presence of strong water drive Moreover, in the simulation results it was observed that the rapidly rising water, when comes in contact with gas in the hydrate layer, starts forming more hydrate in the hydrate layer.

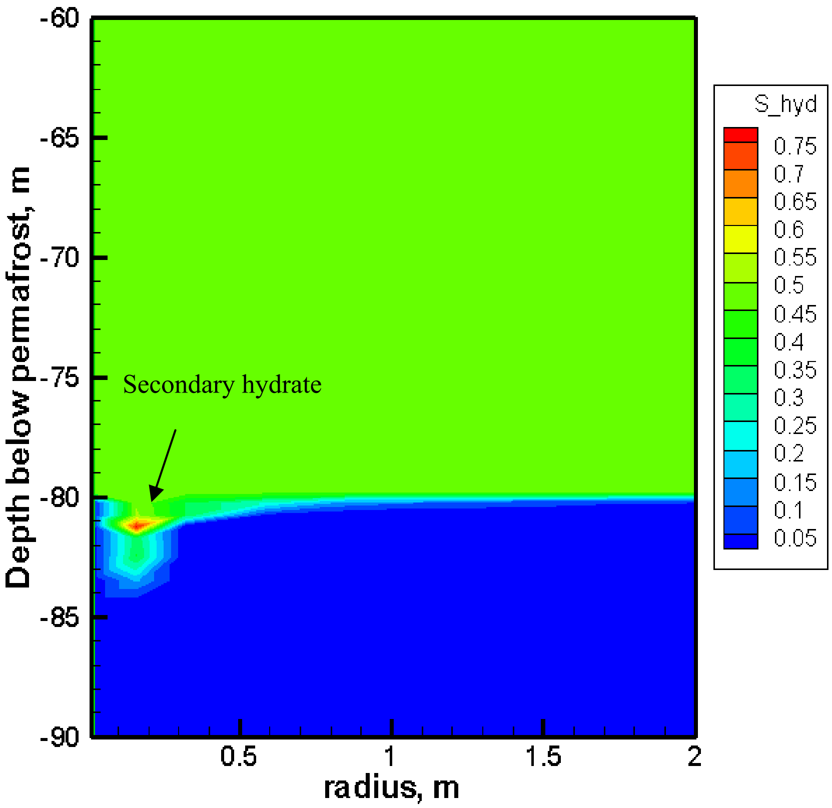

Fig. 5.19. Pressure map for the water drive case after 10 days.

Because secondary hydrate formation is characterized (in terms of mathematics and physics) by very large gradients and very dynamic phenomena and processes, simulations involving evolution of secondary hydrates are very computationally intensive. I also ran the cases of water drive for different production rates of 1 MMscf/day and 4 MMscf/day. Table 5.8 shows time when the production ceases for different gas flow rates as secondary hydrates form. These results show that water drive is very weak at the Messoyakha. Also, Makogon (2007) suggested that the aquifer at the Messoyakha is in a low permeability rock.

Comparing the simulation results and the observations at the Messoyakha about water drive (no movement in gas-water contact for last 30 years) it can be concluded that the aquifer at the Messoyakha was weak and did not play any significant role during the gas production from the Messoyakha field.

Table 5.8

Effect of flow rate on the stopping of flow for water drive case

Production rate	Production cessation
6 MMSCF/D	10 days
4 MMSCF/D	165 days
1 MMSCF/D	463 days

5.7 Sensitivity analysis

In this section the results of sensitivity analysis of gas production from the Messoyakha field are presented. The base case provided a reference frame in the evaluation and analysis of the system behavior in this Class 1G deposit (i.e., hydrate capped gas reservoir). In an effort to reproduce some of the observations at the Messoyakha Field (given the dearth of information on its geology, properties and initial conditions), sensitivity analysis was conducted.

5.7.1 Sensitivity to hydrate layer permeability

This study was fueled by preliminary investigations that tended to indicate that lower intrinsic permeability k in the hydrate layer tended to result in enhanced pressure recovery after the cessation of production. By determining the pressure response of the system to various levels of k in the hydrate layer, it was also possible to test the claim of Makogon et al (2005) that the reservoir pressure continued to increase a long time after the interruption of production. The k values used in this study are listed in table 5.9. All other parameters remained as in the base case. The rest of the reservoir properties were same as that of the base case.

Table 5.9

Parameters for sensitivity to hydrate layer permeability

Parameter	Case ID	Value(s)
Absolute permeability-Hydrate zone	Case 2A	0.01 md
	Case 2B	0.10 md
	Case 2C	1.00 md

Fig. 5.20 shows the thermodynamic path of conditions at two points (at the top and bottom of the hydrate layer) in Case 2B at r = 50 m from the well. Fig. 5.21 shows the S_H

contour plots at different times. When compared with the thermodynamic path for base case, it can be seen that as the production continues, the pressure difference (Δp_{tb}) between the top of the hydrate layer and the bottom of the hydrate layer continues to increase. (Δp_{tb}) is the result of very low effective gas permeability in the hydrate.

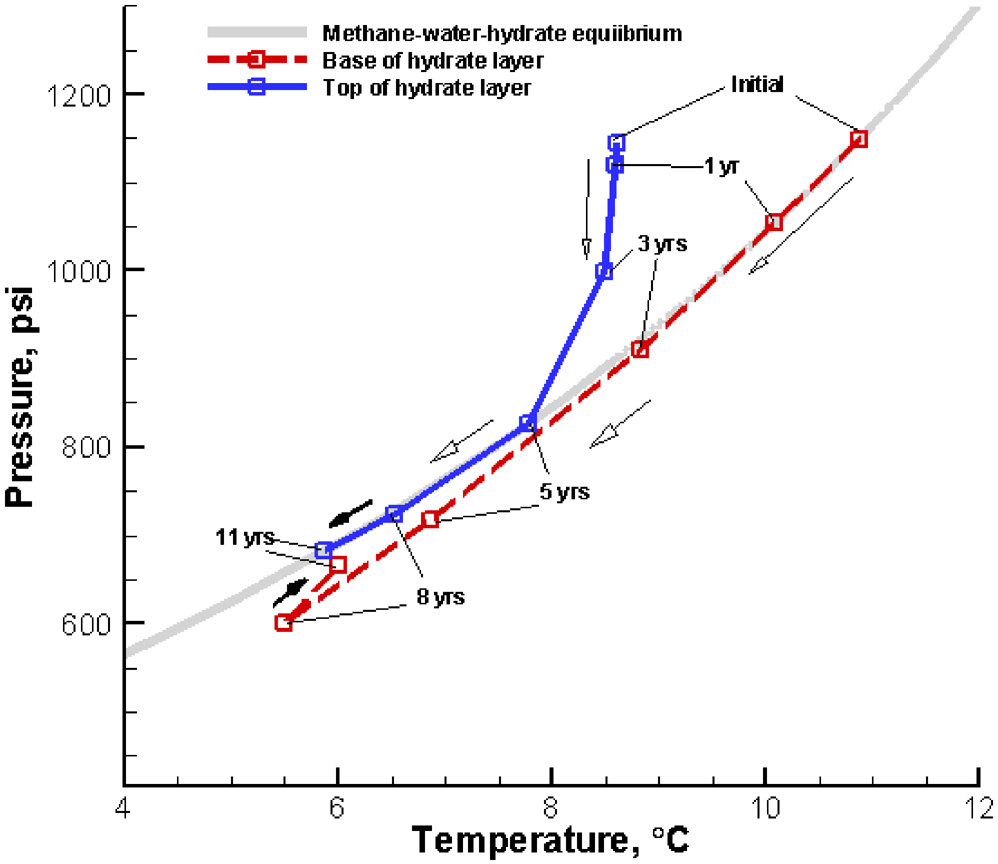

Fig. 5.20. Thermodynamic path of conditions at two points at r = 50 m during gas production in Case 2B.

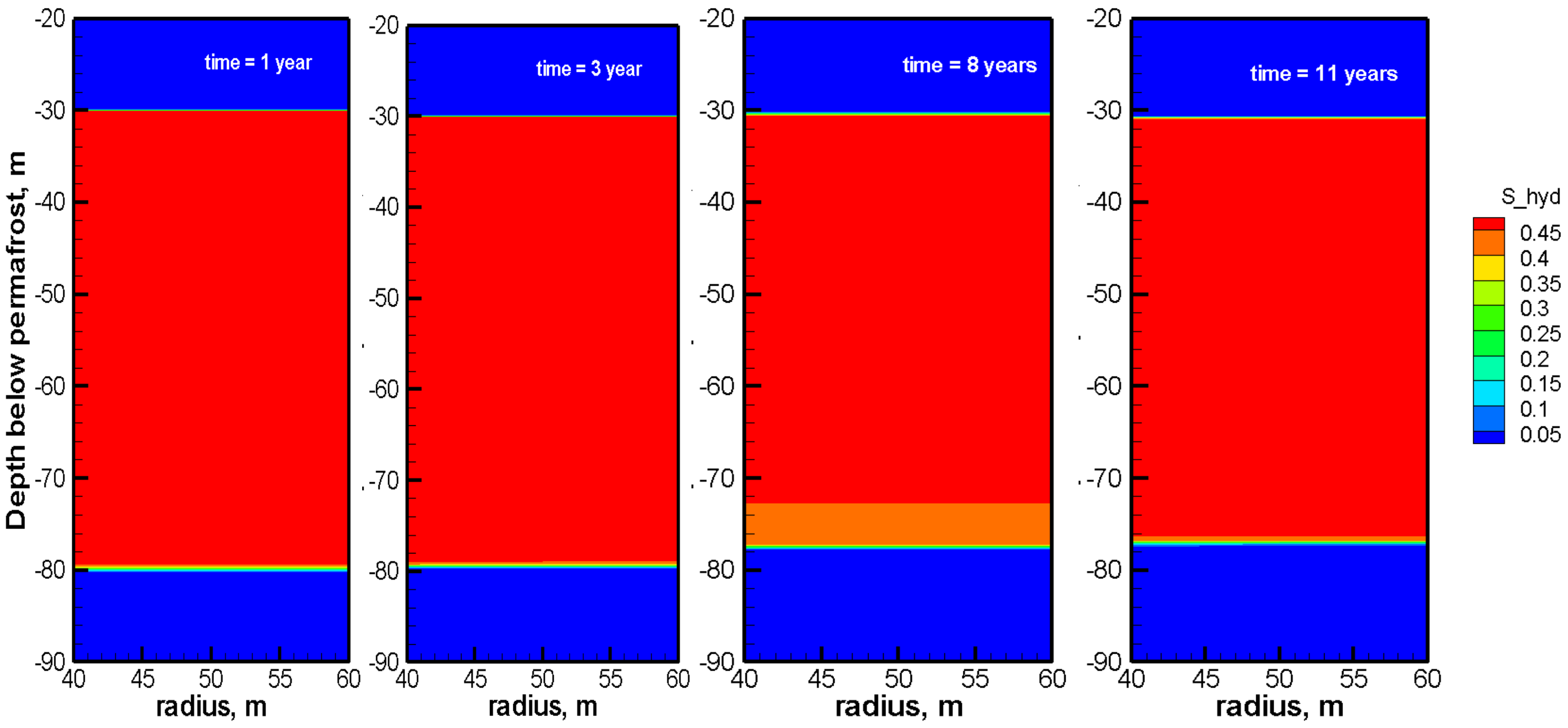

Figure 5.21. Evolution of S_H for the Case 2B at different times.

Because of lower effective permeability in the hydrate layer for Case 2B (as compared to that of base case), the gas flow through the hydrate layer is reduced; whereas at the bottom of the hydrate layer (and in the free gas layer), the gas flows much easily because of high effective permeability. Therefore, the difference between the effective gas permeabilities between hydrate layer and free gas layer results in high (Δp_{tb}).

The bottom of the hydrate layer (h_{bottom}) dissociates in less than 3 years and the thermodynamic conditions for h_{bottom} start to deviate away from the equilibrium curve. The thermodynamic conditions of top of the hydrate layer (h_{top}) are still on the 3-phase equilibrium curve. After 3 years of shut-in (at time = 11 years) the conditions of h_{bottom} moved very close to the equilibrium curve (Fig. 5.20). The temperature increases because of the heat flow during the shut-in period, which results in continued hydrate dissociation and hence pressure increases in the h_{bottom} and free gas layer. The conditions of h_{top} are such that after shut-in, the pressure and temperature still follows the equilibrium curve downwards (solid arrow) and pressure and temperature continues to decrease at h_{top}. The permeability is so low in the hydrate layer that a pressure gradient persists between the top and the bottom of the hydrate layer, leading to flow and continuing dissociation. The temperature profile for Case 2B (Fig. 5.22) is such that after the shut-in of the well, the temperature differential exists between h_{top} and $h_{\mathrm{bottom.,}}$ which results in more dissociation at h_{top} and charging of that gas towards h_{bottom}.

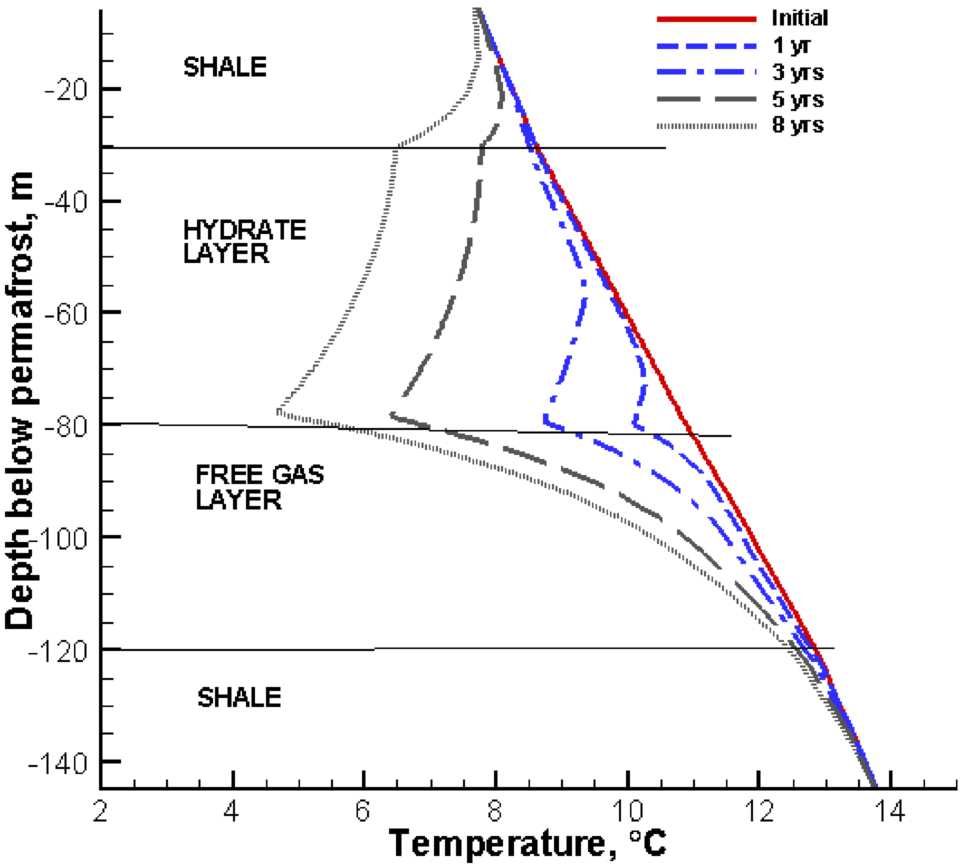

Fig. 5.22. Evolution of the temperature distribution along the z-axis at r = 50 m in Case 2B of the Messoyakha study.

Fig. 5.23 illustrates the average pressure (p_{avg}) in the free gas layer (FGL) plotted as a function of time. p_{avg} increases when the well is shut off, when the permeability of the hydrate layer is lower than that of the free gas zone. When the well is shut-in, there is a substantial pressure differential between the hydrate layer and the free gas layer below keeps hydrates dissociating vigorously even after shut-in. This is similar to the pressure behavior observed at Messoyakha field. Note that the average pressure is dampened by the inclusion in the computation of the no-flow but heat conducting overburden and underburden. Pressure in these shale layers do not change with time and the computed average pressures are slower to decline and to rebound.

Even if some portion of the hydrate bearing layer at the Messoyakha Field has low permeability, it could have led to higher measured pressures in the free gas layer during the shut-in.

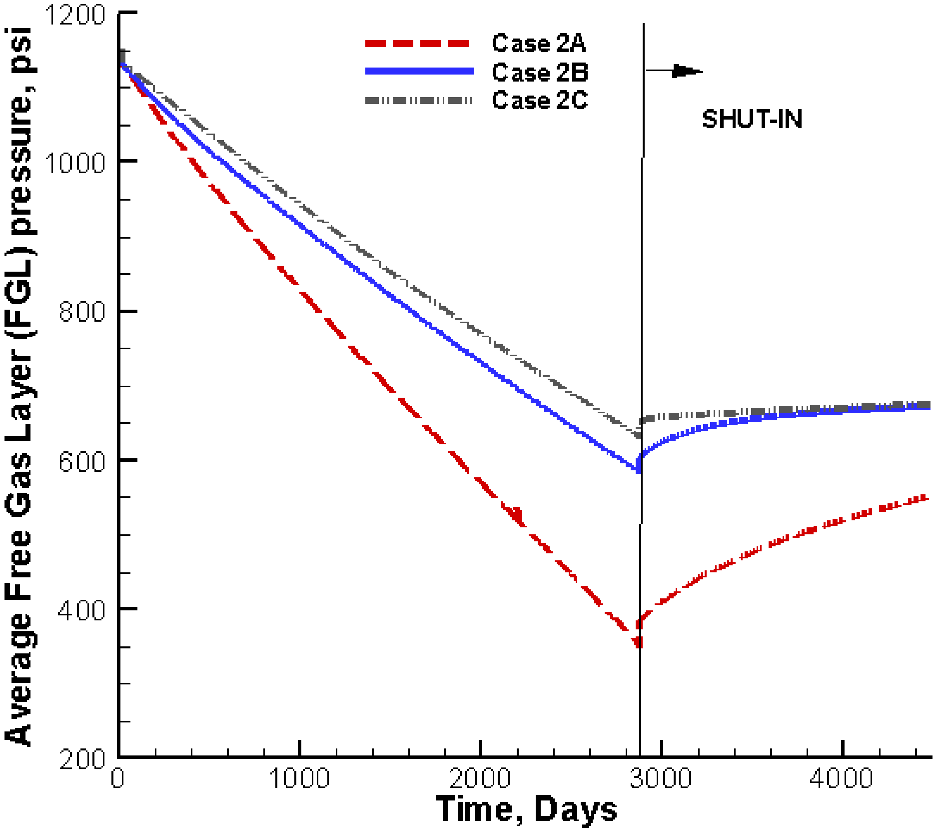

Fig. 5.23. Average free gas layer pressure profiles for Cases 2A, 2B and 2C.

Fig. 5.24 shows the methane release rate in the reservoir during production and after shut-in for Cases 2A, 2B and 2C. Fig. 5.25 shows VRR for the three cases. Initially, the lower permeability cases have better performance (greater VRR) but after producing for longer period, the higher permeability case (Case 2C) wins over Case 2A and 2B and shows larger VRR. Low k means intense localized depressurization and dissociation, and a limited affected radius. Initially, this releases more gas, but also results in faster cooling (with a corresponding reduction in dissociation). A higher k means lower initial depressurization and gas release, a larger radius of influence, and larger release rates in the long run.

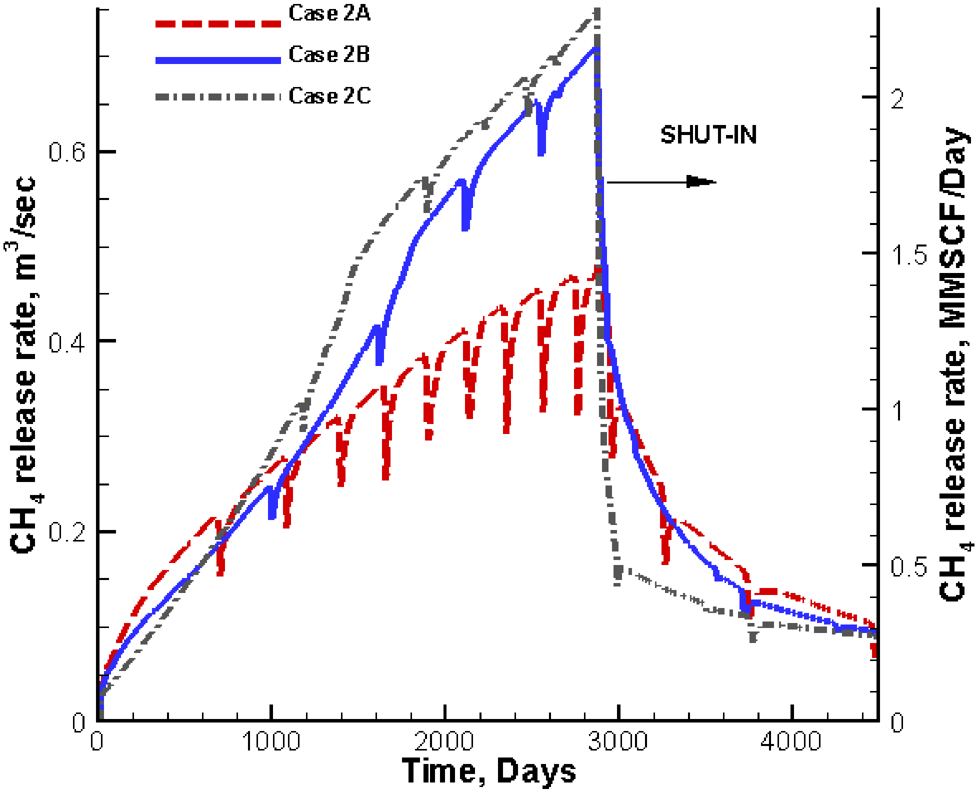

Fig. 5.24. Methane release rates in reservoir for Cases 2A, 2B and 2C.

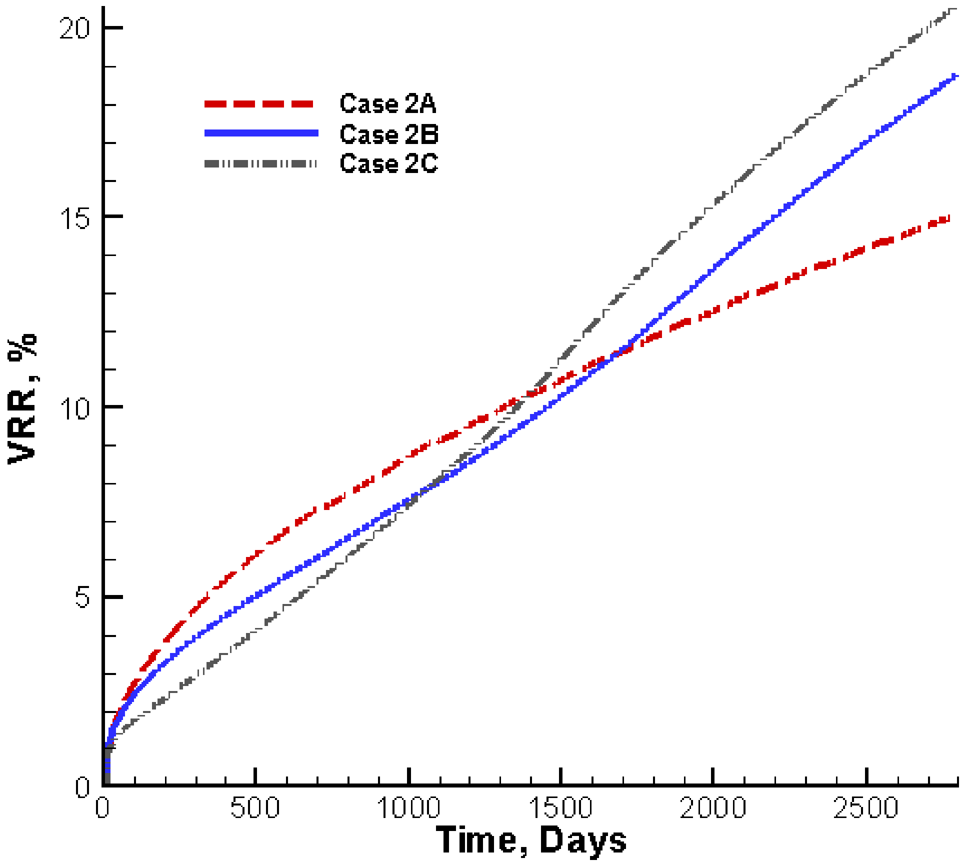

Fig. 5.25. VRR for Cases 2A, 2B and 2C.

5.7.2 *Sensitivity to absolute permeability in the free gas layer*

I studied the gas production sensitivity to absolute permeability in the free gas layer. The intrinsic permeability of the reservoir was reduced to 100 md, keeping all the other reservoir properties the same as those of the base case. Production ceased only 9 days after its initiation because of flow blockage by high-saturation secondary hydrates that had formed around the well. Formation of secondary hydrates is promoted by the low permeability in the free gas zone (where the well production interval is located), which results in significant depressurization near the well, and substantial cooling because of the intense localized depressurization. This simulation result of rapid formation of secondary hydrates in low permeability porous media is consistent with Makogon's

(1971) observation of difficulty in gas production from wells completed within the hydrate layer (where the effective permeability was very low). The pressure drop at the perforations is very high when the well is completed very close or inside the hydrate layer. The production rate (6 MMSCF/Day) applied at the well cannot be supported by rapidly declining permeability. Thus cavitation occurs and production stops. These types of simulations where perforation choking occurs, take very small timesteps and hence very large clock time to run.

5.7.3 Sensitivity to hydrate saturation

With the exception of Makogon et al. (2005), who provided some estimates of the S_H distribution in the Messoyakha Field, there is no relevant information in any other publications on the subject. I investigated the effect of S_H on gas production at the Messoyakha deposit by reducing S_H to 0.25 from the reference value of 0.5. All other parameters and conditions in this simulation were as in the base case. The simulation results indicated that production at the constant rate of Q_P = 6 MMSCFD continued for t = 825 days, but was then interrupted because of secondary hydrate formation that resulted in well choking (Fig. 5.26).

The gas effective permeability (k_{eff}) is larger for $S_H = 0.25$ as compared to that of the base case. Because of the larger effective permeability and the larger mass of native (and highly compressible) gas in the reservoir, depressurization (and, consequently, dissociation) is less effective. This is evident in Figure 5.27, which shows the RRR curves for S_H = 0.25 and 0.50. Gas velocity is lower than in the base case because of the higher k_{eff}, and Joule-Thomson cooling is less pronounced because of higher pressures and lower gas velocities. However, the increased permeability to water allows interaction of gas and water near the well at a location that is sufficiently cold to lead to the formation of secondary hydrate that eventually blocks fluid flow to (and production from) the well.

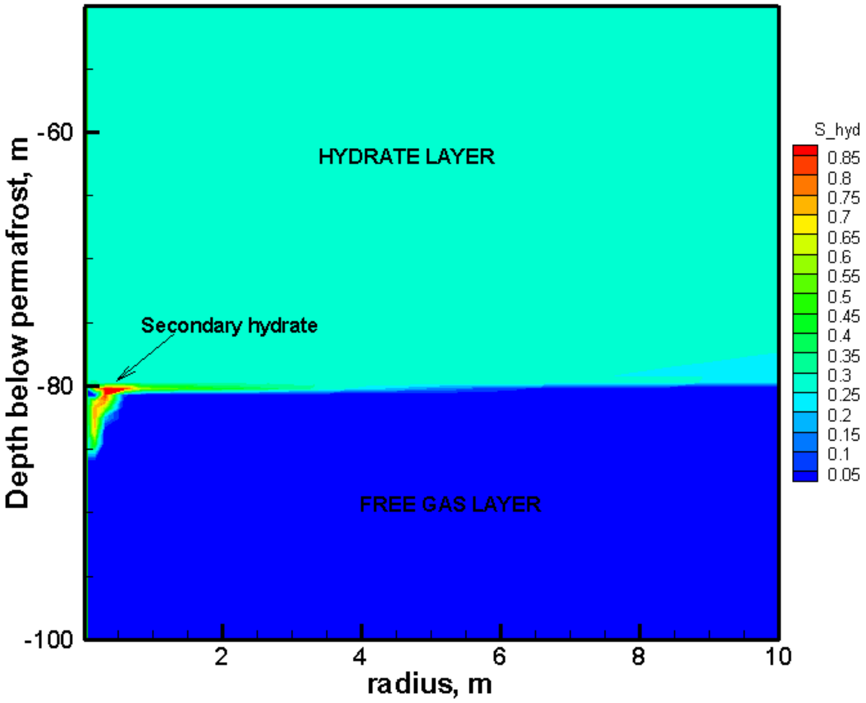

Fig. 5.26. Well choking for case of S_H = *0.25*.

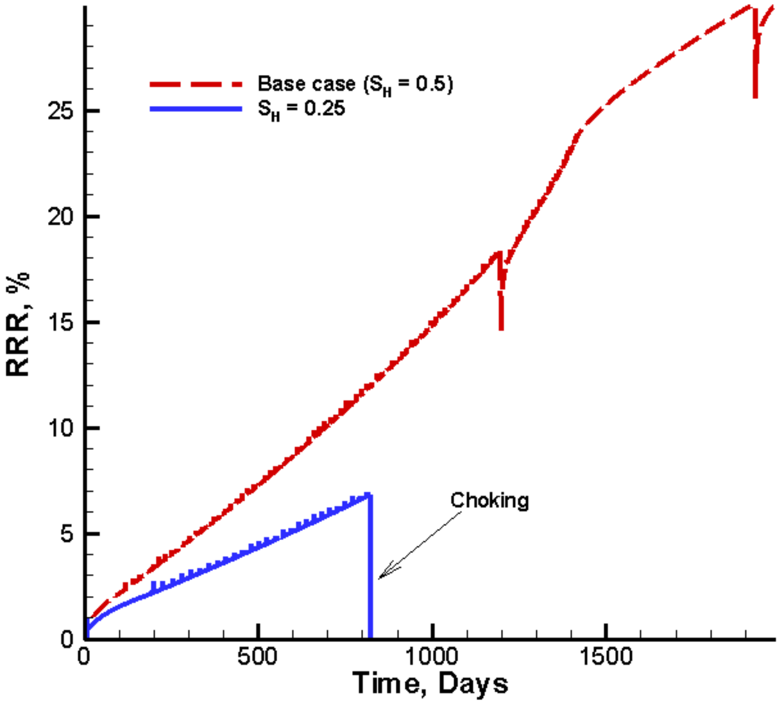

Fig. 5.27. Comparison of methane release rate for base case and S_H = *0.25*.

5.7.4 Sensitivity to well completion interval

As discussed in section 5.2, the low flow rates in the hydrate zone that had been observed by Makogon (1971) were attributed to the percentage of completion of well in the hydrate zone. I ran different cases of producing from perforations at different locations in the reservoir. The maximum pressure drop ($\Delta p_{\max}$) at the wellbore as a function of perforation locations was recorded (Table 5.10).

Fig. 5.28 shows $\Delta p_{\max}$ for different completion intervals. The higher the pressure drop, the greater the cooling because of the high gas velocity and rapid hydrate dissociation, and the higher the likelihood of secondary hydrate formation and flow blockage (well choking). Such strong pressure drop comes with the additional risk of substantial sand production and formation collapse near the well. At Messoyakha, the flow rate was such that the pressure drop was not allowed to increase more than 40 psia because of low rock strength (Makogon et al., 2005; Makogon, 2007). The wells completed deeper in the free gas portion had lower $\Delta p_{\max}$ and exhibited no formation of secondary hydrates around the perforations. These perforations (located away from the hydrate-gas interface) have a smooth pressure gradient. The simulation results are consistent with the observations of Makogon et al. (1971).

Table 5.10

Maximum pressure drop across perforations as a function of location

Distance of top of perforation from interface, m	Pressure drop across perforations, Pa
+49	Immediate choking
+10	4.7×10^5 Pa (68 psia)
+8	2.3×10^5 Pa (33 psia)
+0.5	8×10^4 Pa (12 psia)
-12	7.8×10^4 Pa (10 psia)

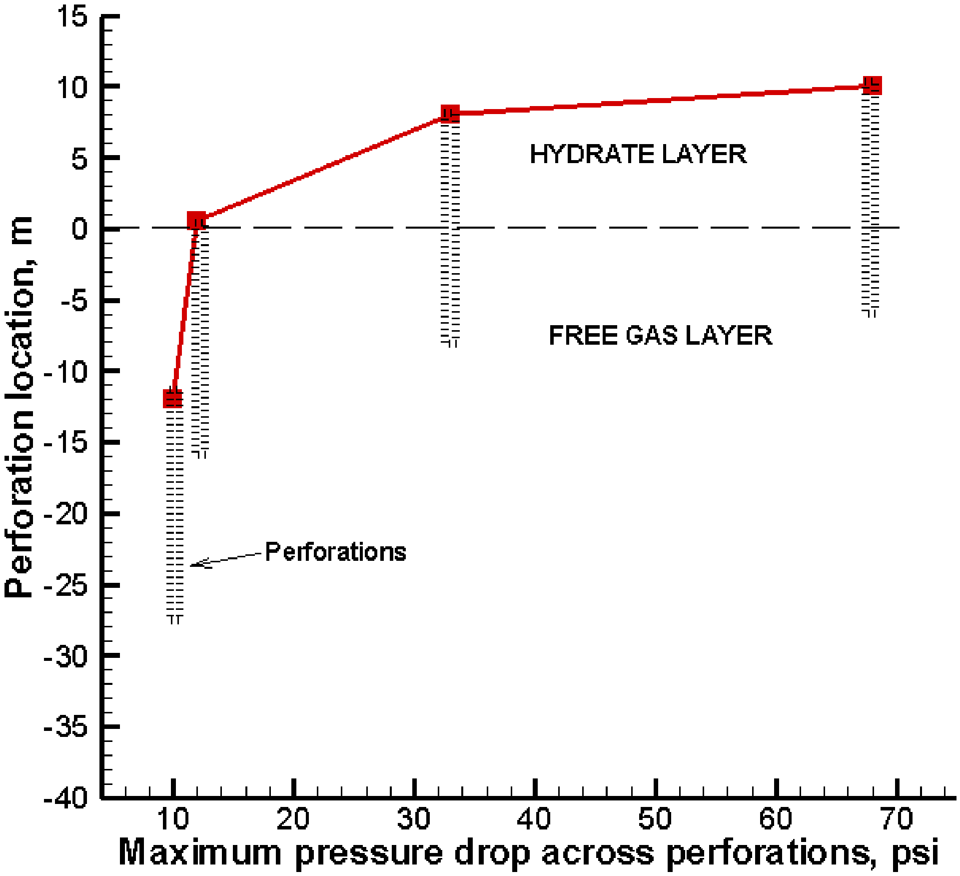

Fig. 5.28. Sensitivity to well completion interval.

5.7.5 Sensitivity to flow rate

I also investigated the sensitivity of gas production to the production flow rate Q_p A lower production rate Q_p = 3 MMscf/day was used. Figs. 5.29 and 5.30 show the RRR and VRR respectively for different flow rates. Comparison of the corresponding RRR and VRR curves in Figs 5.29 and 5.30 clearly indicates that a higher Q_P enhances the dissociation of hydrates and increases their contribution to production. This was expected because a higher Q_P is associated with a larger depressurization, i.e., the driving force of dissociation.

However, it should be noted that if the gas is produced at higher production rate, the temperature of the system will drop rapidly. Fig. 5.31 shows the evolution of temperature of a point at r = 50 m and at the base of the hydrate layer.

The faster temperature drop means that the increased dissociation rate (brought about by the higher Q_P) results in a heat loss (needed to fuel dissociation) that is larger than that for the lower Q_P, and which cannot be replenished by the slow (conduction-based) rate of heat addition from the boundaries despite the larger temperature gradient. The fast temperature drops can lead to problems of well choking if the well is completed very close to the hydrate layer.

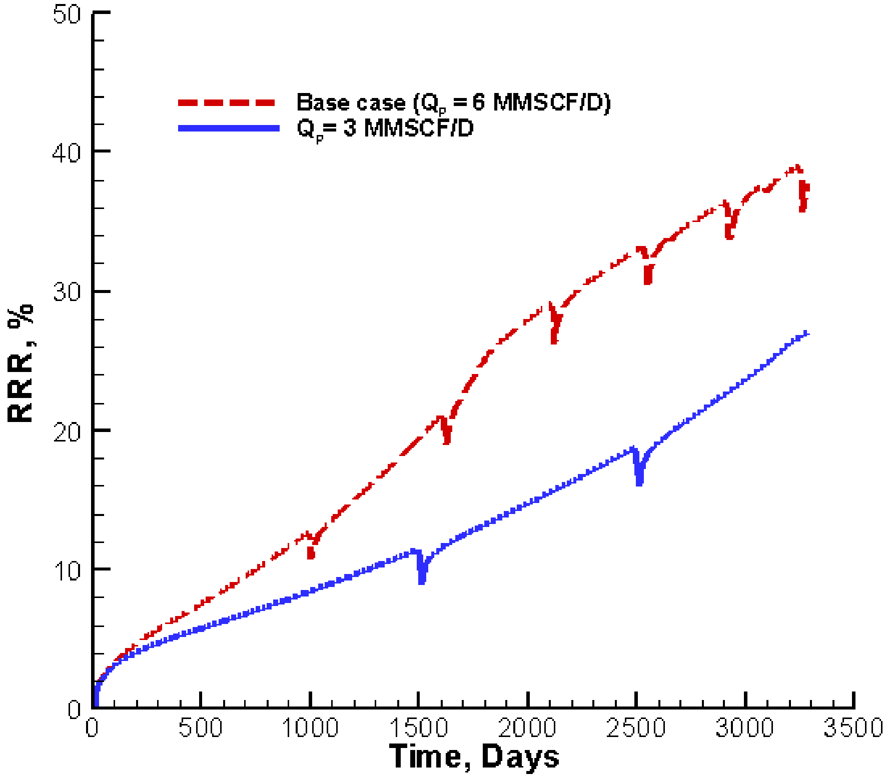

Fig. 5.29. RRR for the flow rate sensitivity analysis.

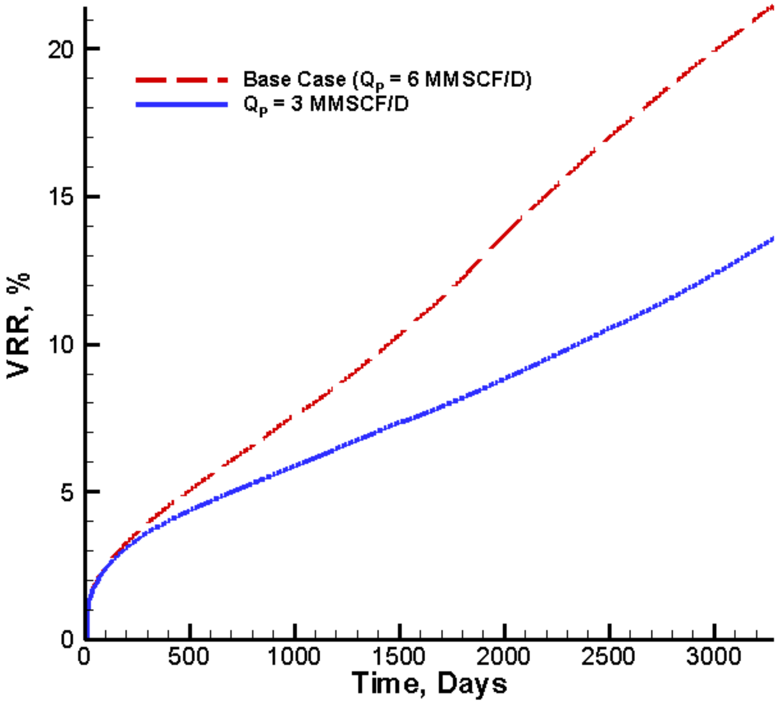

Fig. 5.30. VRR for the flow rate sensitivity analysis.

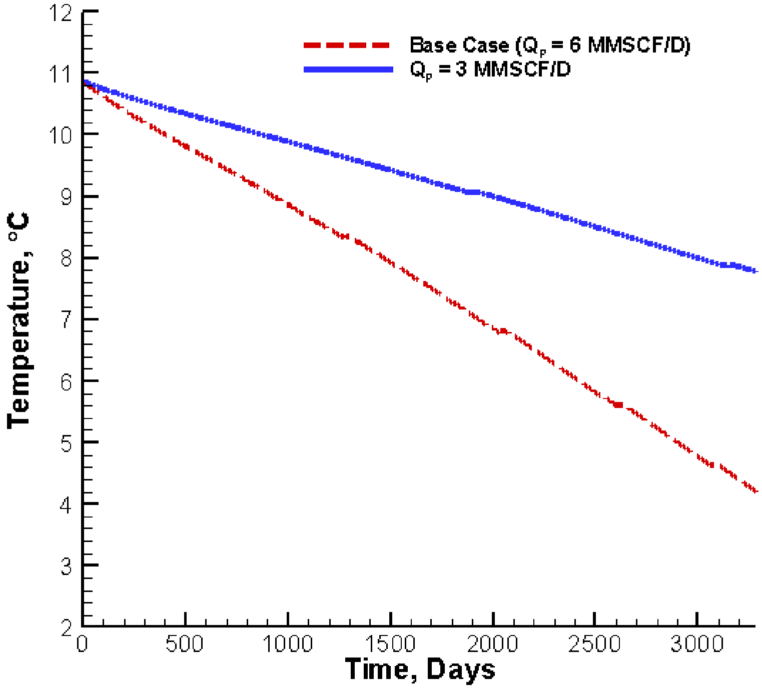

Fig. 5.31.Temperature at base of hydrate layer at r = 50 m for different flow rates.

5.8 Variable rate simulation

At the Messoyakha field, the gas production was resumed at lower rates after the shut-in period. Makogon et al. (2005) discussed that when the gas production was resumed at lower flow rates, the decline rate of reservoir pressure was slow because the gas production rate was nearly equal to the gas charging rate of the reservoir by hydrate dissociation

Therefore, I attempted a simulation scenario with the a production at 6 MMscf/day for 2880 days (8 years), followed by shut-in of the well till 4500 days (12.5 years) and then again resuming of production at a lower rate of 0.5 MMscf/day till 7200 days (20 years). Fig. 5.32 illustrates the average pressure and the RRR values for this variable rate. When the flow rate is high, the RRR increases as effective permeability (k_{eff}) continues to increase. The pressure continues to decrease as gas is produced from the reservoir. During the shut-in period, heat continues to flow towards the hydrate layer from both the overburden and the underburden. When production resumes at a lower Q_{P}, the RRR is high (about 80%) because of higher thermal state of the reservoir (Fig. 5.33), which results in more effective dissociation of hydrates and higher effective permeability (k_{eff}). Fig. 5.34 shows the evolution of S_{H} during all the phases of (high Q_{p}, shut-in and lower Q_{p}) of production.

It is also observed that the reservoir pressure decline rate after the production is resumed at lower Qp is slow. This observation is also consistent with the pressure behavior at the Messoyakha reported by Makogon et al. (2005).

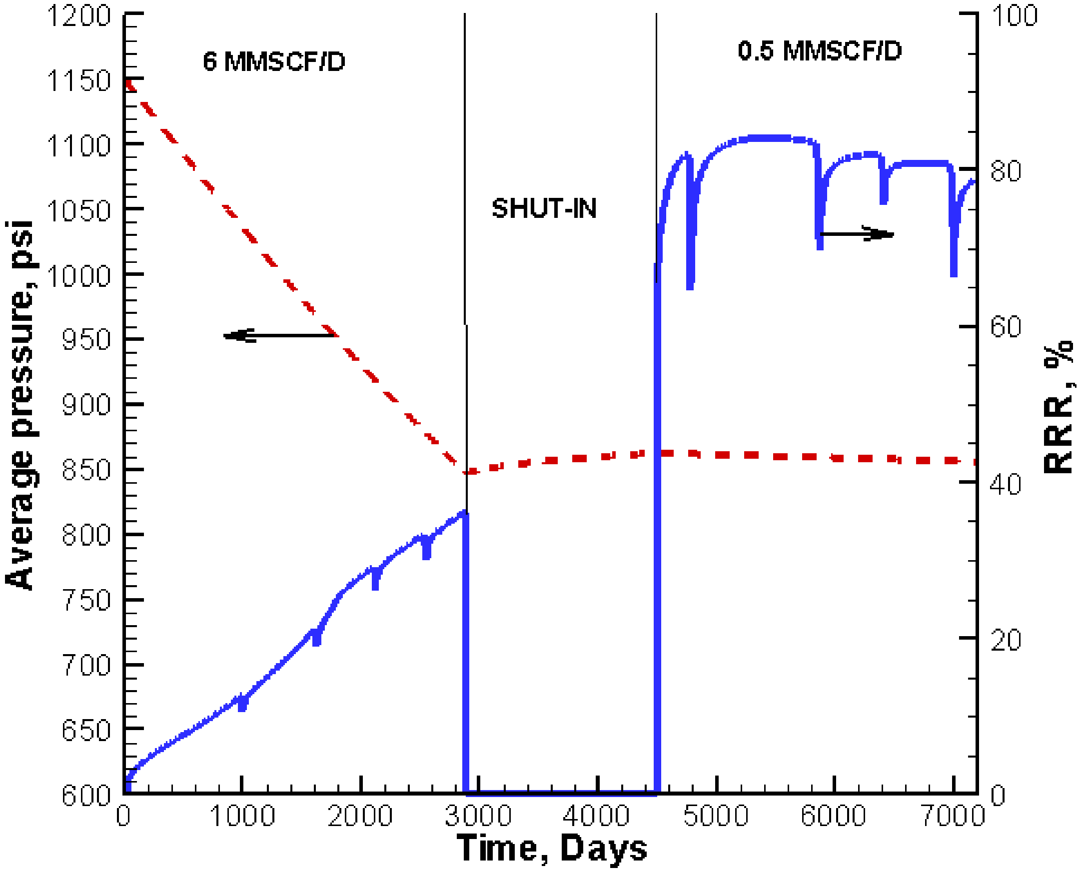

Fig. 5.32. Variable rate simulation results.

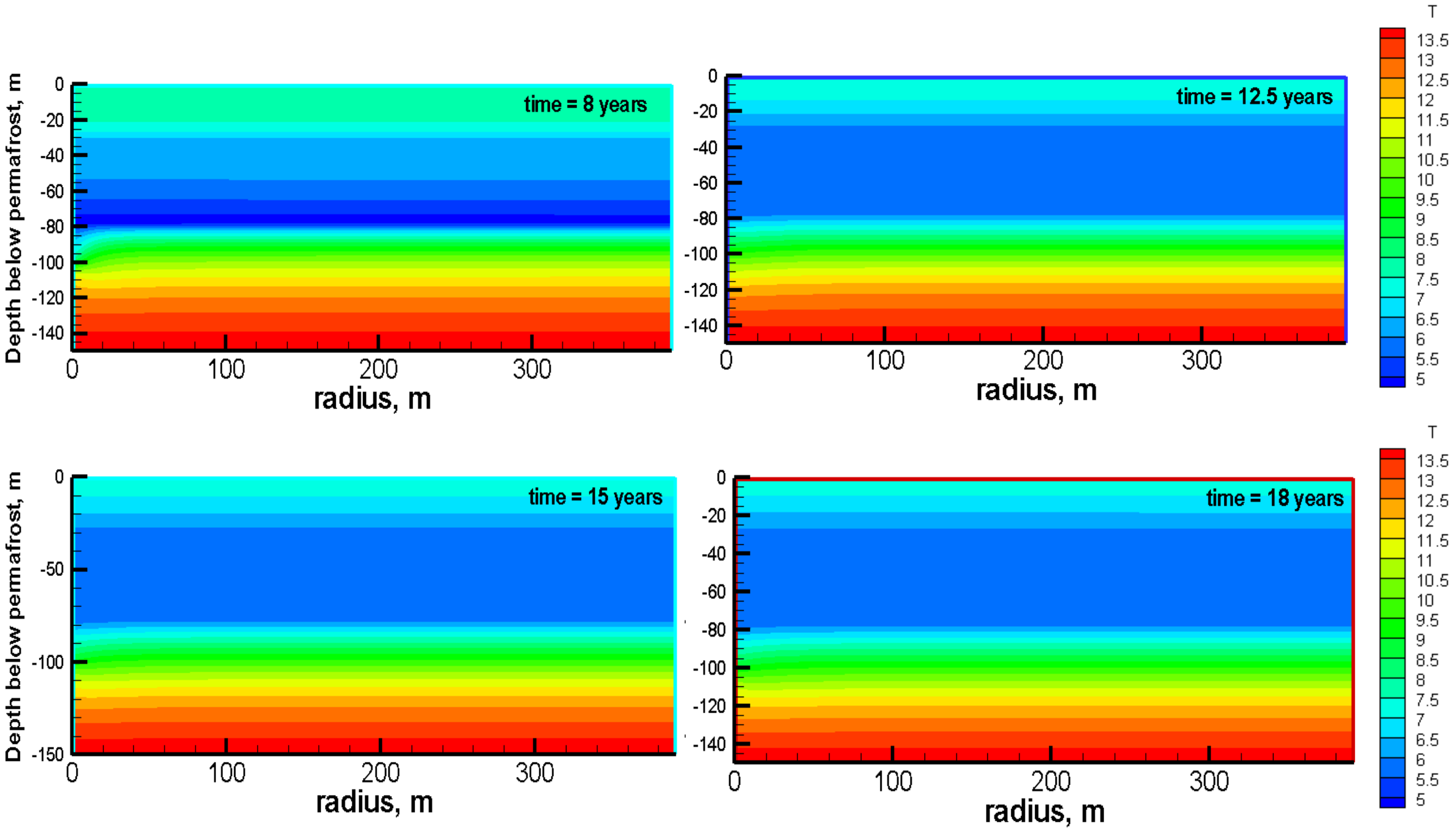

Fig. 5.33. The evolution of temperature in the reservoir with time for the variable rate simulation.

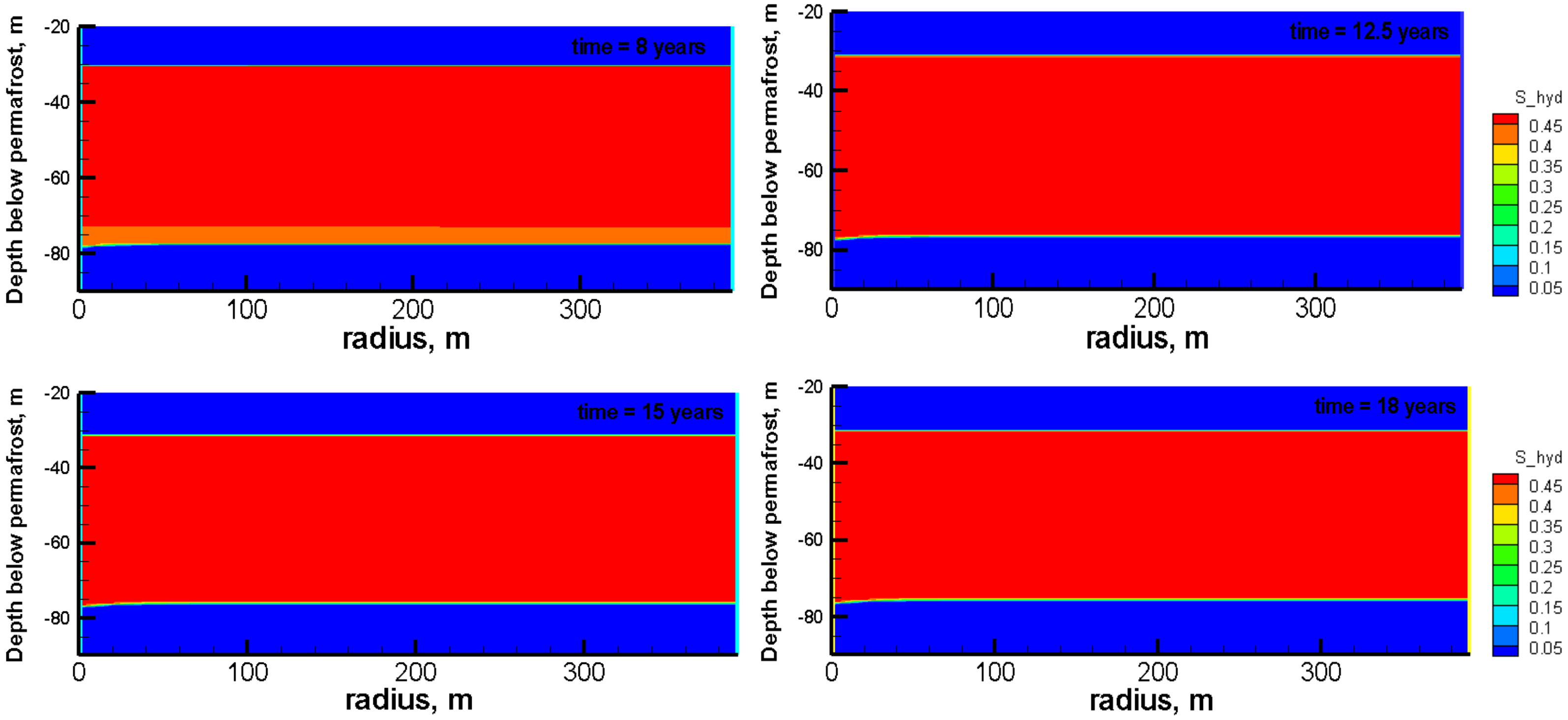

Fig 5.34. The evolution of S_H in the reservoir for the variable rate simulation case.

5.9 No hydrate case scenario

I wanted to test if the pressure response at the Messoyakha can be reproduced if it is assumed that there were no hydrates present in the reservoir. To set-up a model for no hydrate case, it was necessary to initialize it differently. Figs. 5.35 to 5.36 show the initialized conditions for the no-hydrate case. The temperature profile in the reservoir was assumed to be higher than that at Messoyakha to avoid hydrate formation in the reservoir. Gas and water were assumed to be present, overlain by shale and underlain by aquifer.

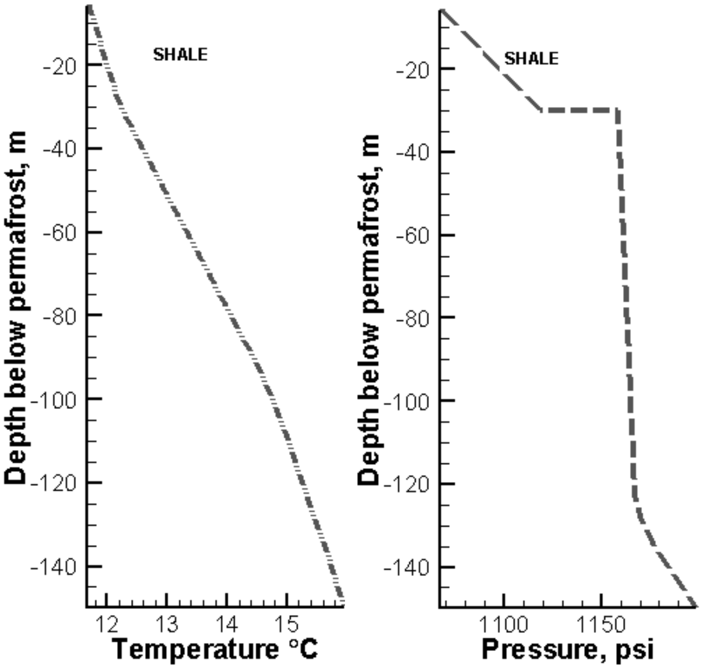

Fig. 5.35. Initial pressure and temperature for no hydrate case.

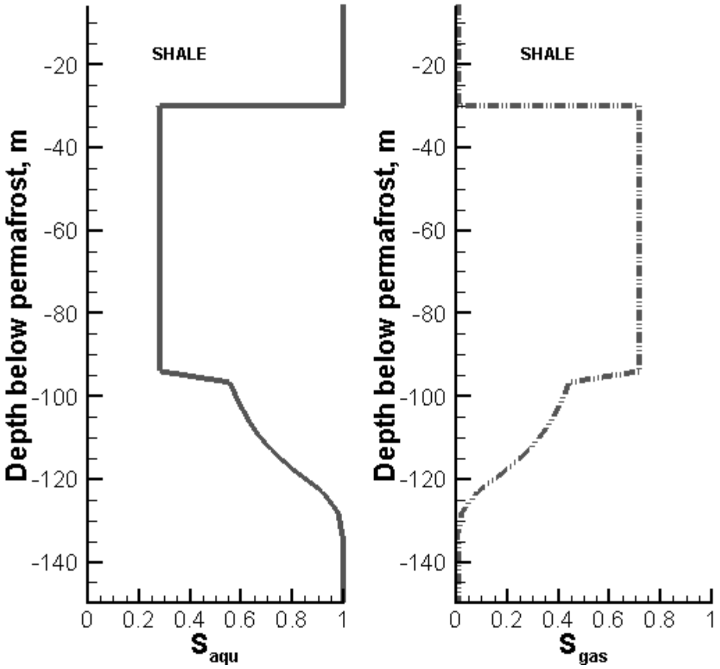

Fig. 5.36. Initial water saturation and gas saturation for no hydrate case.

In the analysis of the reservoir sensitivity to the aquifer strength when no hydrates are present, I investigated three cases. The first was very strong aquifer drive, the second an intermediate strength aquifer and the third a very weak aquifer. Table 5.11 gives the aquifer parameters input in T+H.

Table 5.11

Aquifer parameters for no hydrate case

Aquifer type	Aquifer permeability (k_{aqu})
Strong	500 md (Same as free gas layer)
Intermediate	1 md
Weak	0.001 md

Fig. 5.37 shows the average pressure in the reservoir as a function of time. The strong aquifer case is not shown because the pressure decline was very slow as compared to the other two cases. Fig. 5.37 shows that the pressure increase is also possible with time even without the presence of hydrates (as shown in intermediate strength aquifer). However, it is to be noted that along with the pressure increase, the water level also will rise because of pressure differential in the reservoir. At the Messoyakha field there was no gas-water contact change with time (Makogon et al., 2005). As discussed in section 5.3.7, there is significant uncertainty regarding the location of the gas-water contact at the Messoyakha Field.

Therefore, if we accept the thesis that gas-water contact did not move during the production lifetime of the Messoyakha, we can exclude the possibility of "no hydrate" case and it seems plausible that pressure increase at the Messoyakha occurred because of continued hydrate dissociation. Even with intermediate strength aquifer I observed that water encroachments do occur and hence water level rises with production.

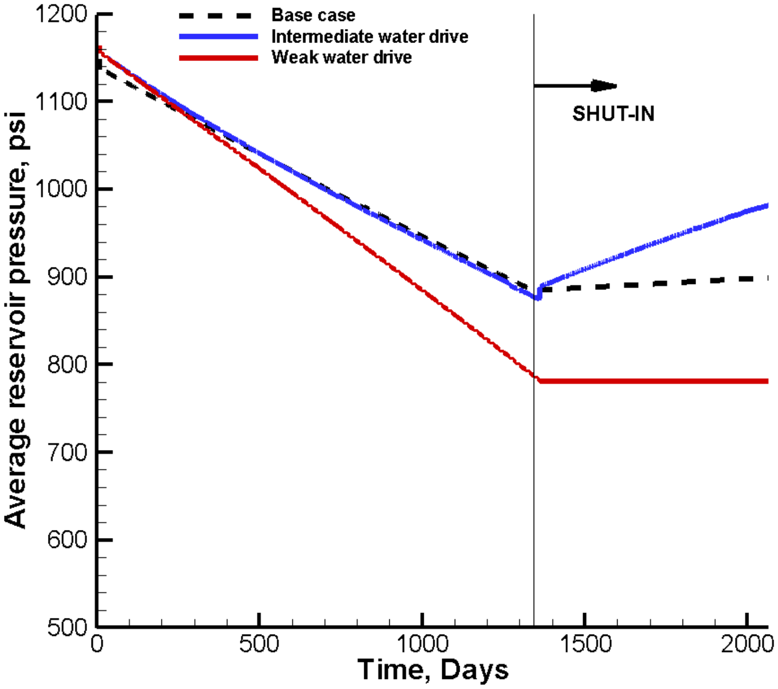

Fig. 5.37. Reservoir pressures for different aquifer strengths for no hydrate case.

5.10 Conclusions

Because of the limited data, I constructed a number of 2D cylindrical models to explain some plausible scenarios at the Messoyakha field. Important conclusions from this simulation study are listed below.

1. Water drive in a hydrate capped gas reservoir is not beneficial for producing gas from hydrates because it might lead to "choking" of the perforations if they are placed close to the hydrate-free gas interface. As demonstrated by the simulations, the water drive at the Messoyakha is very weak.
2. If the perforations are close to the hydrate-gas interface, the rapid cooling due to hydrate dissociation and Joule-Thomson cooling will lead to the formation of secondary hydrates around the perforation (perforation choking). The formation of secondary hydrates will lead to reduction in permeability that can lead to production cessation.
3. In a hydrate capped gas reservoir, the permeability of the free gas zone becomes a limiting factor if the perforations are located near the hydrate-gas interface. The low initial temperature of the system and the close proximity to the hydrate interface has production inhibition effects. Rapid ice or secondary hydrate will form around the perforations and will block the gas flow.
4. As the gas is produced from Class 1G hydrate deposits, the temperature of the system continues to decrease because of endothermic hydrate dissociation reaction. When the production is stopped (shut-in), the heat flow from the confining boundaries continues to flow towards the hydrate zone. The heat flow then increases the thermal state of the system which can increase the RRR values if the gas is produced at a lower flow rate.
5. The higher the flow rate of the well, the stronger will be the dissociation of the hydrates. The RRR and VRR values for higher flow rate (Q_p) are higher than that for lower Q_p. If the high production rates are desired in a reservoir similar to the Messoyakha, the production intervals should be placed far from the hydrate-gas interface. Otherwise, rapid cooling at the perforations (due to hydrate dissociation

and Joule-Thomson effect) and availability of gas and water will induce rapid formation of secondary hydrates.

6. Effective permeability (k_{eff}) is higher in the case of low hydrate saturation. If the same mass rate (same as high S_H) is applied in low S_H cases, the well choking phenomena is expedited due to higher effective permeability to water and the ready availability of gas.
7. If we believe that gas-water contact did not move with time, the increase in pressure due to continued hydrate dissociation after shut-in can be a plausible scenario. If we don't believe that gas/water contact was stationary during the production life of the Messoyakha field, the increase of reservoir pressure can be obtained using an intermediate strength aquifer.

CHAPTER VI

EFFECT OF HYDRAULIC FRACTURE IN A HYDRATE DEPOSIT

6.1 Introduction

In Chapter III, I discussed the various properties of sediments and typical permeabilities of sediments in offshore sediments. The permeabilities depend on the sediment type. In the offshore, hydrates have been found in sand, sandstone with a majority of them found in silty clays and clays (Boswell et al., 2007). In the permafrost, hydrates have typically been found in coarse sediments. However, the effective permeability in hydrate bearing sediments is very low because of presence of hydrates. In fine-grained sediments, the capillary pressure is high and permeability is low; whereas in coarse-grained sediments, the capillary entry pressure is low and permeability is high. Hydraulic fracture has been successfully used to stimulate thick, high pressure extremely low permeability gas sandstone reservoirs (Holditch, 2006).

At the Messoyakha gas field, the depressurization technique appeared successful because of the presence of free gas below the hydrate layer (Makogon et al., 2005). However, majority of the hydrate deposits are not underlain by thick free gas zones. To the best of author's knowledge, no one has done a simulation study of using a hydraulic fracture to stimulate the hydrate deposit for gas production.

6.2 Objectives and methodology

The main objective of this simulation study was to investigate the effect of a single hydraulic fracture on gas production from hydrate bearing sediments. A 2-D areal simulation model was developed using T+H. Because of the significant execution time requirements of this type and size of problem, all these simulations were conducted on a cluster using a parallel version of the T+H code.

I compared the gas production between two cases, that is fracture and no fracture cases. It was assumed that the fracture can be created and remain propped open during the gas production.

6.3 Simulation domain and grid discretization

The 2-D areal Cartesian model used in this study is shown in Fig. 6.1. The extent in the X, Y, and Z directions are 200 m, 200 m and 1 m respectively. The simulation domain was discretized into 100 x 100 x 1 elements in x, y and z direction using the MESHMAKER program that accompanies T+H. This discretization resulted in a total of 10,000 elements, with 3 equations per gridblock. The fracture width was 0.001 meters (0.4 inches) and the grid spacing was increased logarithmically in both x and y direction directions.

6.4 Simulation parameters

I used the evolving porous medium (EPM) model (refer to Chapter IV) for all the simulation runs in this study. Tables 6.1 and 6.2 describe the important simulation parameters for the hydrate bearing rock and fracture respectively.

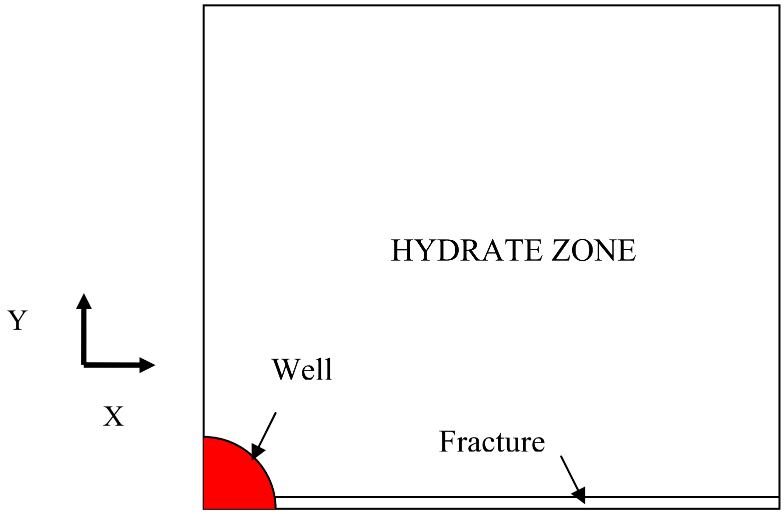

Fig. 6.1. Model domain for simulating production from a hydraulic fracture.

Table 6.1

Parameters used for simulating fracture performance

Property	Hydrate bearing sediment	Hydraulic fracture
Porosity	0.35	1
Absolute permeability	500 md (Simulation set I)	10000 md
Initial hydrate saturation	0.5	0
Water saturation	0.5	1
Irreducible water saturation	0.28	
Relative permeability model	Modified Stone’s first three phase model $k_{\mathrm{rA}} = \min\left\{\left[\frac{S_{\mathrm{A}} - S_{\mathrm{irA}}}{1 - S_{\mathrm{irA}}}\right]^n, 1\right\}$ $k_{rG} = \min\left\{\left[\frac{S_{\mathrm{G}} - S_{\mathrm{irG}}}{1 - S_{\mathrm{irA}}}\right]^n, 1\right\}$ $k_{\mathrm{rH}} = 0$ $S_{\mathrm{irA}} = 0.28$ $S_{\mathrm{irG}} = 0.02$ $n = 3.57$	
Capillary pressure model	Van Genutchen function $p_{\mathrm{cap}} = -p_0\left[\left(S^*\right)^{-1/\lambda} - 1\right]^{-\lambda}$ with restriction $-p_{\mathrm{max}} \leq p_{\mathrm{cap}} \leq 0$ $S^* = \left[\frac{S_{\mathrm{A}} - S_{\mathrm{irA}}}{S_{\mathrm{mxA}} - S_{\mathrm{irA}}}\right]$ $\lambda = 0.45$ $S_{\mathrm{irA}} = 0.27$ $p_0 = 2*10^4$ Pascals (Entry pressure) $p_{\mathrm{max}} = 10^6$ Pascals $S_{\mathrm{mxA}} = 1$	

Table 6.2

Fracture description parameters

Property	Value
Porosity, $\varphi_{\text{fracture}}$	1
Permeability, k	$k_x = k_y = k_z = 10^{-11}$ m^2 = 10000 md
Capillary pressure	0
Relative permeability model (EPM model)	Modified Stone's first three phase method $k_{\text{rA}} = \min\left\{\left[\frac{S_{\text{A}} - S_{\text{irA}}}{1 - S_{\text{irA}}}\right]^n, 1\right\}$ $k_{\text{rG}} = \min\left\{\left[\frac{S_{\text{G}} - S_{\text{irG}}}{1 - S_{\text{irA}}}\right]^n, 1\right\}$ $k_{\text{rH}} = 0$ $S_{\text{irA}} = 0.01$ $S_{\text{irG}} = 0.005$ $n = 1$

6.5 Initial and boundary conditions

The initial pressure of the system was 10^7 Pa (1450 psia) and the temperature was 10° C. There was no need for vertical equilibration because in the z-direction only one gridblock is present. Hence the gravity effects in this study were not accounted for. Gas was produced by means of depressurization-induced dissociation of the hydrates. The producing well was at constant pressure of 3.0e6 Pa (435 psi), which acted as an internal boundary condition in the model. The model boundaries are no-flow boundaries. Gas production, and cumulative production in the reservoir by hydrate dissociation was recorded at each time step. Fig. 6.2 shows the initial thermodynamic state of the problem.

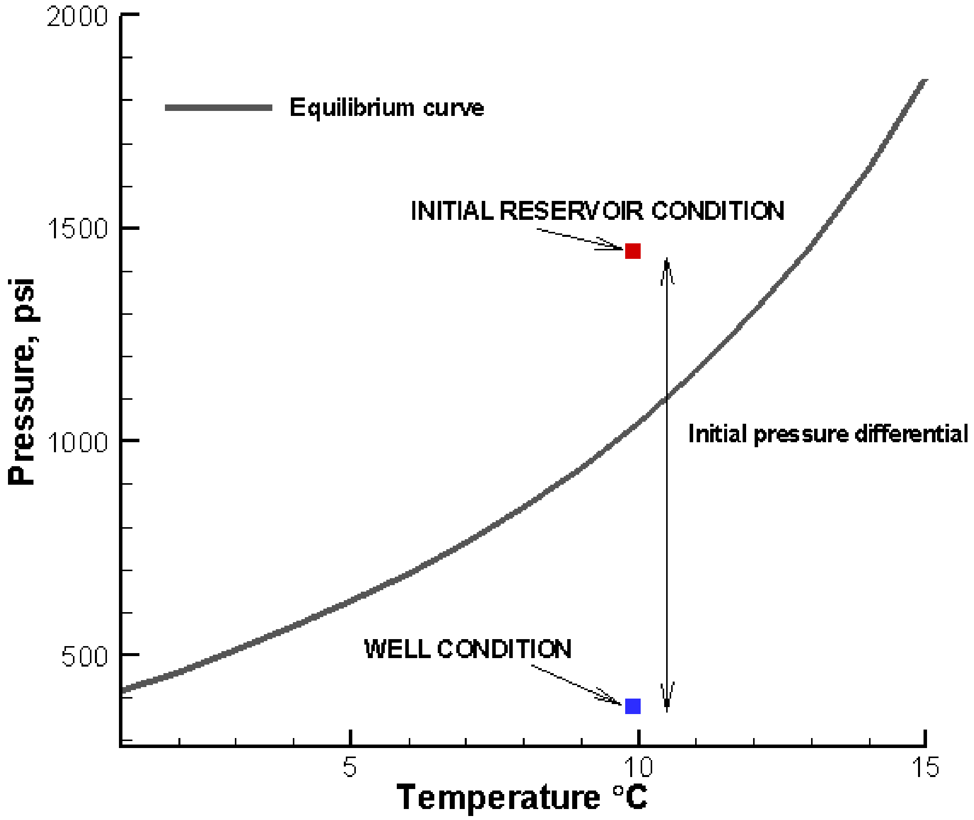

Fig. 6.2. Initial thermodynamic conditions for hydrate deposit and the well.

6.6 Simulation results

Case 1A refers to the fracture case and Case 1B refers to the no-fracture case.

Fig. 6.3 shows the methane production rate for Case IA and IB. Early production rate is high because of a maximum pressure differential applied to the well. The production rate (Q_p) then begins to rise because the effect of decreasing pressure differential is outweighed by the effect of continuously expanding zone of increasing effective permeability as dissociation advances. Finally, Q_p decreases continuously because the effect of increasing effective permeability is again overcome by decreasing pressure differential (Rutqvist and Moridis, 2007). The fracture performance shows just a 7% increase in Q_p as compared to that of radial case after 600 days of production. Further, after about 800 days, Q_p with the fracture drops below that of without fracture. Once hydrate starts dissociating around the fracture, its effective permeability becomes equal to absolute permeability k = 500 md. This large permeability around the fracture and the width of the expanding hydrate-free zone next to the fracture eliminate the flow advantages of the fracture. Fig. 6.4 shows the cumulative gas production for with fracture and without fracture. The two are practically identical.

Hydraulic fracture is not found to be useful in stimulating the high intrinsic permeability hydrate bearing sediments (e.g. sands and sandstone).

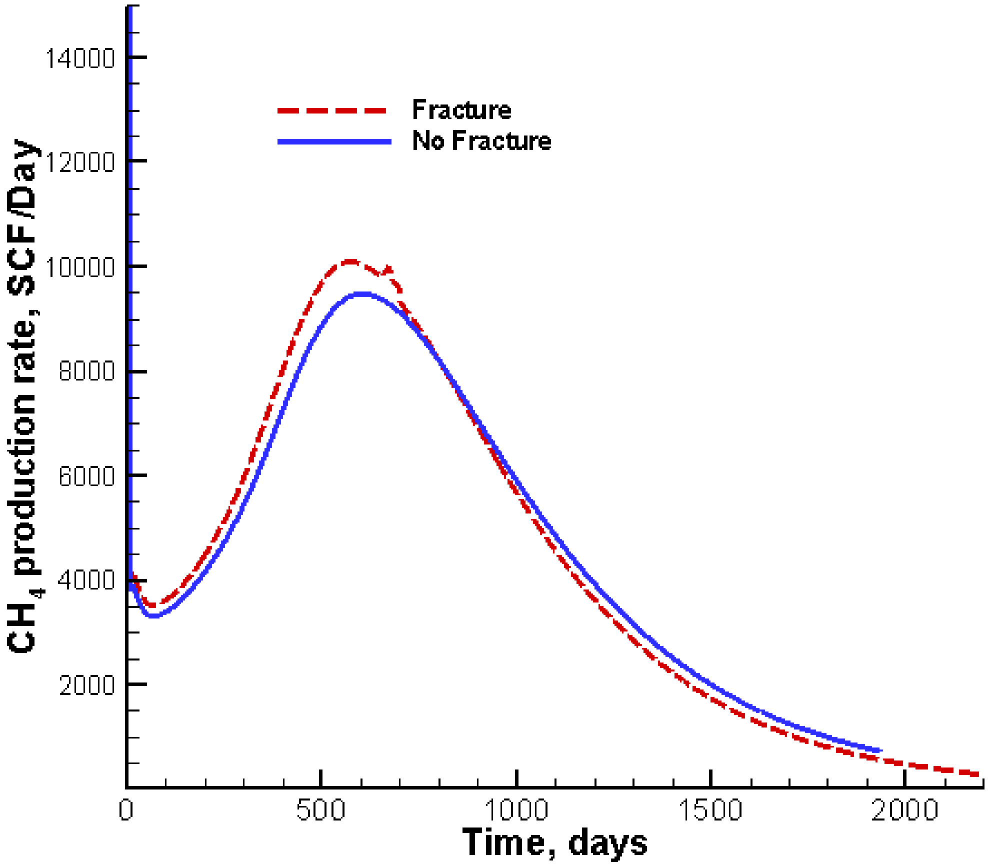

Fig. 6.3. Methane production rate per unit meter of well depth for fracture study.

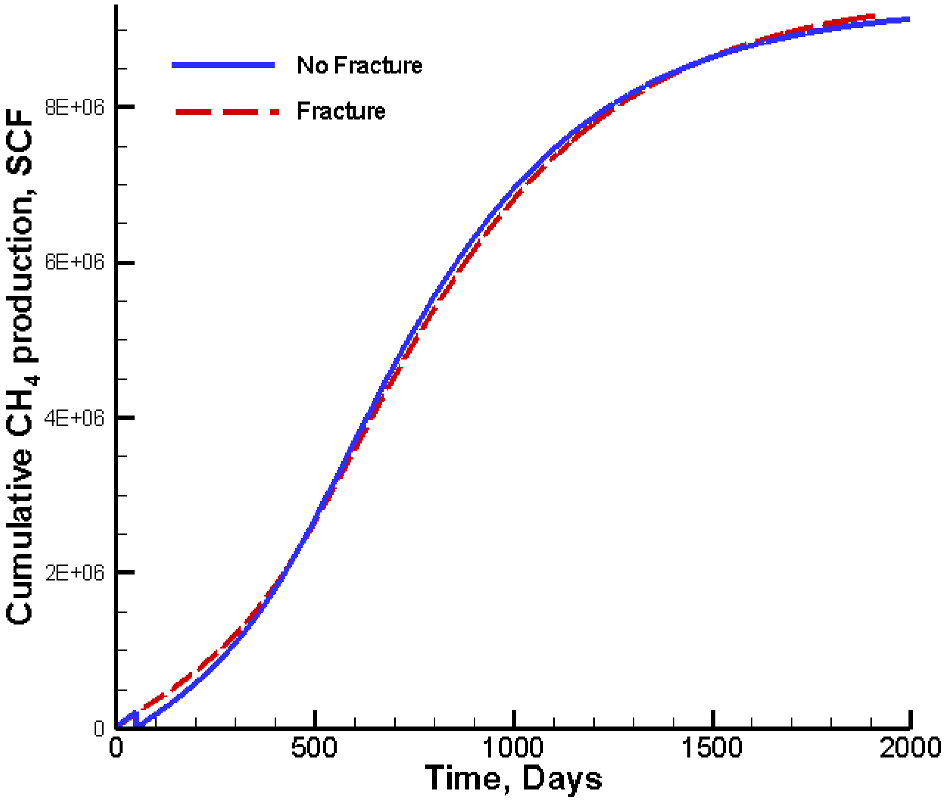

Fig. 6.4. Cumulative gas production per unit meter of well for fracture study.

The other important phenomenon is the formation of secondary hydrate all around the fracture. This occurs because of significant Joule-Thomson in the vicinity of the fracture (see Fig. 6.5). This is caused by the high gas velocity in the highly permeable fracture. The lower temperatures, coupled with the availability of gas and water originating from dissociating hydrates in the formation along the fracture, lead to formation of secondary hydrate along the entire length of the fracture. This development negates the early advantages of the presence of the fracture (Fig. 6.3).The simulation results suggest that hydraulic fracture in high permeability hydrate bearing sediments becomes self sealing and closes because of formation of secondary hydrate (Fig. 6.6) around the fracture.

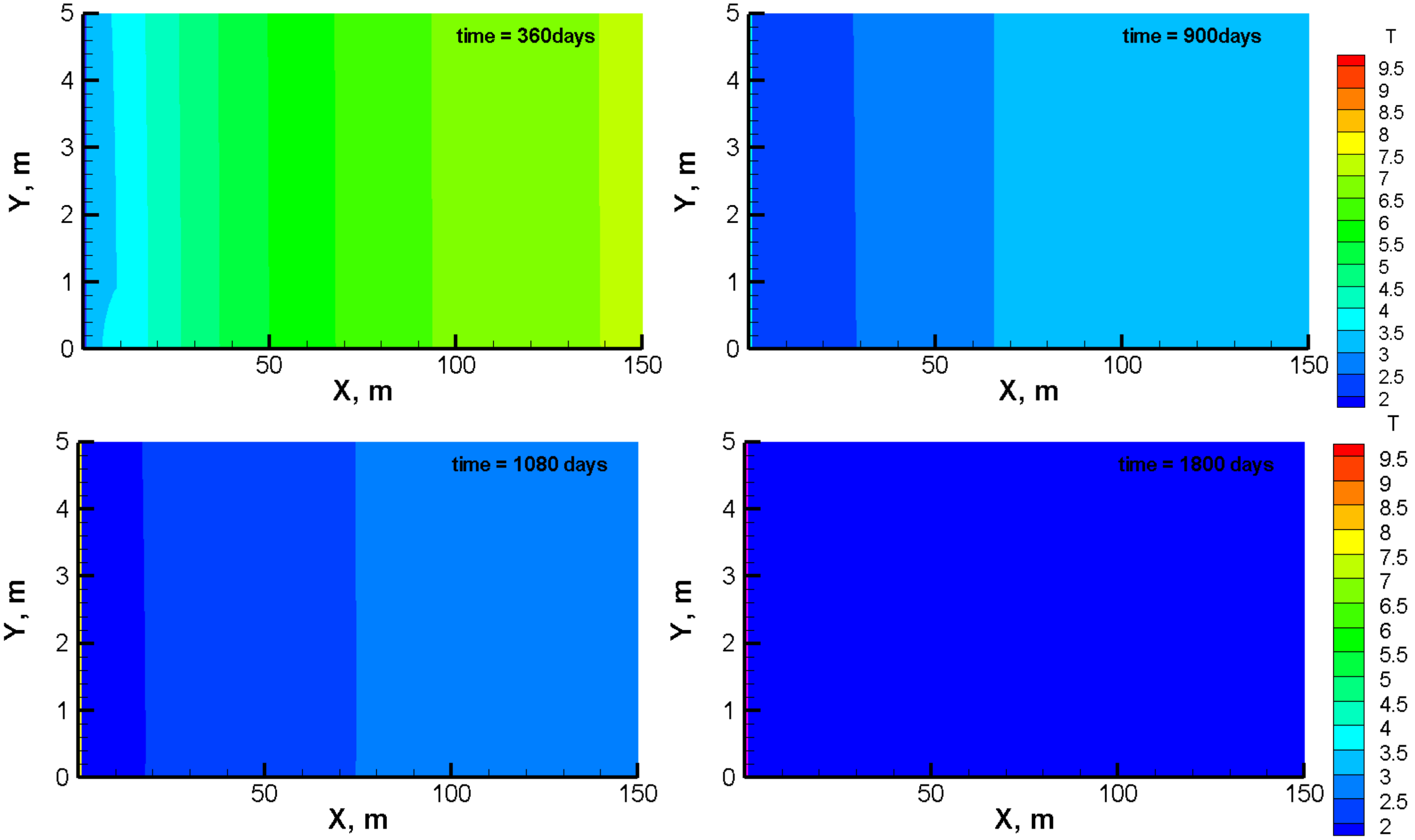

Fig. 6.5 Evolution of temperature in the reservoir during gas production from a hydraulic fracture.

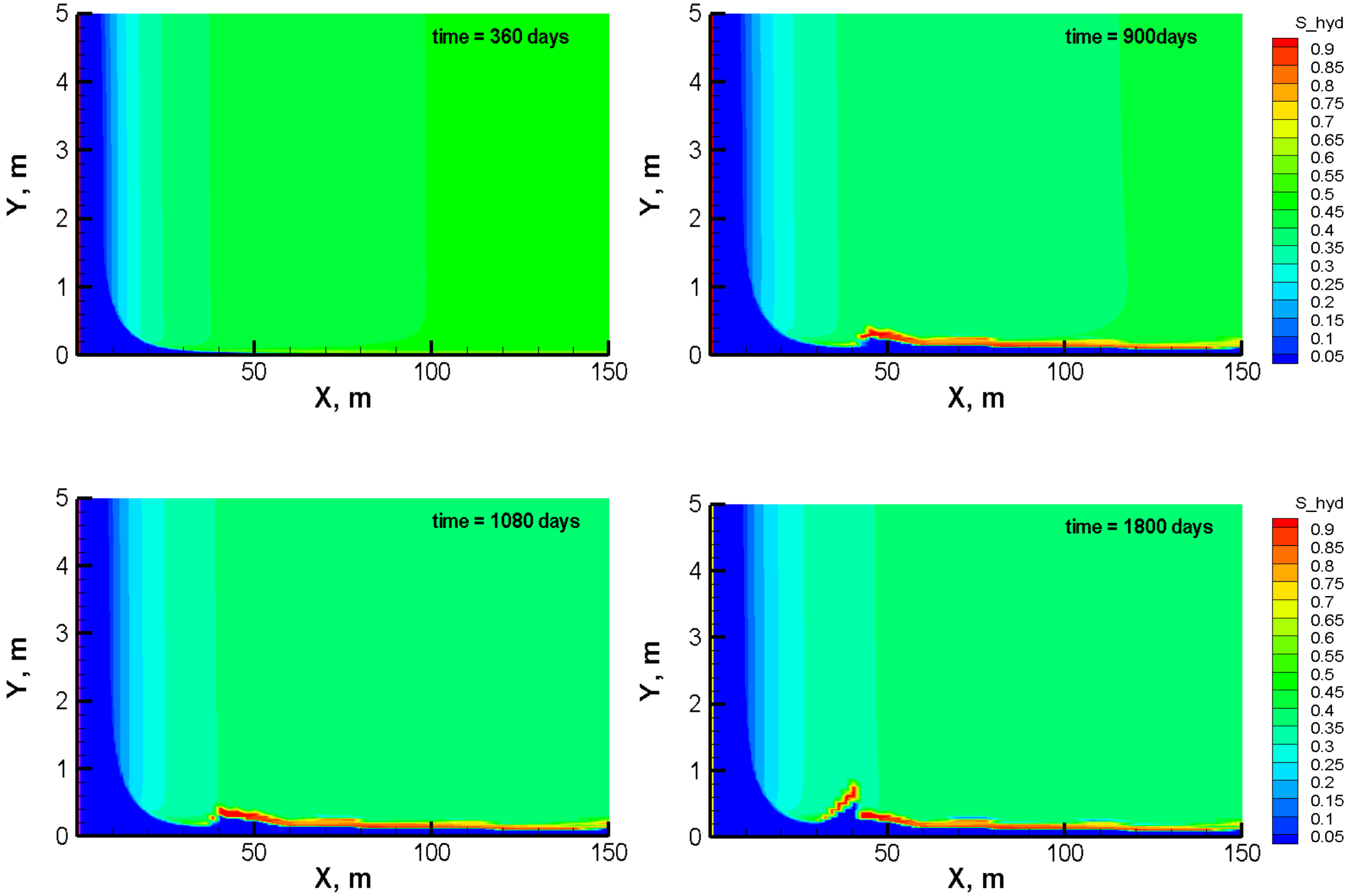

Fig. 6.6. Evolution of secondary hydrate around the fracture during gas production from a hydraulic fracture.

6.7 Conclusions

The main conclusion from this simulation study is that hydraulic fractures do not appear effective in increasing gas production from hydrate-bearing sediments because they are self-healing. Evolution of secondary hydrate along the entire length of the fractures blocks fluid flow and negates their advantages.

CHAPTER VII

GEOMECHANICAL PERFORMANCE OF HYDRATE BEARING SEDIMENTS

7.1 Introduction

Hydrate bearing sediments are typically unconsolidated. The shear strength of the sediments impregnated with hydrates is higher than when no hydrates are present(Winters et al., 2007). Hydrate dissociation thus results in sediments with constantly declining strength characteristics that can lead to sediment failures. The sediment failures can lead to wellbore instability, loss of oil and gas platform foundations or on a large scale, slope failures Different case studies have been conducted showing the possibility of hydrate dissociation as the triggering sources for slope failures (Carpenter, 1981; Field and Barber, 1993; Popenoe et al., 1993; Crutchley et al., 2007).

Many researchers have studied the effect of hydrates on Storegga Slide offshore Norway (Vogt and Jung, 2002; Sultan et al., 2004a; Sultan et al., 2004b; Bryn et al., 2005; Kvalstad et al., 2005; Mienert et al., 2005). The slope stability studies require a full suite of geotechnical properties and the detailed analysis of sliding forces down the slope. Important geotechnical properties are discussed in Chapter III. Some mathematical models estimating slope failures have been recently developed, e.g., Sultan et al. (2004b), Nixon and Grozic (2007). The approaches by these researchers are based on the geotechnical principles and the calculated estimates of excess pore pressure generated because of hydrate dissociation but they do not include a built-in model of dynamic hydrate behavior. Xu and Germanovich (2006) have developed theoretical relationships for the estimation for excess pore pressures resulting from hydrate dissociation.

During gas production from hydrate deposits, the likelihood of developing geomechanical instability is at its highest intensity in the vicinity of the wellbore where the largest changes are concentrated. The changes in pressure and temperature can significantly change the stress state in the sediments.

In Chapters V and VI I discussed in detail the flow behavior of hydrate-bearing sediments. Some important issues related to the gas production from the hydrate-bearing sediments were modeled. The evolution of pressure in the hydrate bearing sediments (which depends on flow characteristics of the sediments) has the strongest effect on the geomechanical performance of sediments (Rutqvist, 2008).

7.2 Objectives and methodology

The primary objective of this study was to use the coupled model "T+F" to estimate the likelihood of geomechanical failures during hydrate dissociation. The geomechanical stability in two different types of sediments (sands and clays) was investigated. I studied three problems to estimate the geomechanical instability problems in hydrate bearing sediments. In problem 1, I studied the evolution of stresses in the HBS during the temperature increase. In problem 2, I addressed the geomechanical issues related to the gas production from a hydrate deposit using a horizontal well. In Problem 3, I addressed the geomechanical issues related to gas production using a vertical well in a similar hydrate deposit as that studied in problem 2.

7.3 Geomechanical properties of hydrate bearing sediments (HBS)

Very few experimental studies published on the strength of sediments in the presence of hydrates. The most relevant studies on strength of methane hydrate bearing sediments has been done by Masui et al. (2005), Winters et al. (2004) and Winters et al. (2007). Experimental work using tetrahydrofuran (THF) hydrates has provided some qualitative insight into the effect of hydrates on mechanical properties of different types of sediments (Yun et al., 2007b). Although THF hydrate is not a good proxy for methane hydrate, it does yield some important results on strength characteristics of hydrate bearing sediments.

In this study, I used two host sediments with distinctly different geomechanical properties: Toyoura sand (Masui et al., 2005) and clays. These were the same media used in the study of Rutqvist and Moridis (2007).

To simulate the mechanical behavior of the HBS, I applied an elastoplastic mechanical model, with a modified Mohr-Coulomb failure criterion. Rutqvist and Moridis (2007) indicate that “the elastic-plastic properties of the HBS are dependent on the properties of the host medium (e.g. sand or clay), which were modified to take into account the cementing effects of pore-filling hydrates”.

Fig. 7.1 (Rutqvist and Moridis, 2007) describes the geomechanical properties of the two types of sediments considered in this study, Toyoura sand (Masui et al., 2005) and clay. The parameters describing the mechanical properties of the Toyoura sand are assumed to vary linearly with the hydrate saturation (S_H) because of dearth of information on this matter from laboratory or field tests (Rutqvist and Moridis, 2007). The friction angle was considered independent of the hydrate saturation S_H and equal to 30° for Toyoura sand and 20° for clays.

Among the properties shown in Fig. 7.1, only the properties for Toyoura sand were rigorously determined from laboratory experiments on hydrate bearing sediments. As Rutqvist and Moridis (2007) indicated, “Toyoura sand properties are the most internally consistent with the hydraulic and thermal properties used in the multi-phase flow and heat transport calculations”. The properties of the unconsolidated soft clay were approximated as being 25% of the corresponding Toyoura sand values (Rutqvist and Moridis, 2007). In this study, I assumed the flow properties of sand and clays to be the same, and did not account for the effect of geomechanical changes on the permeability and porosity of the geologic media (i.e., I only investigated a one-way coupling).

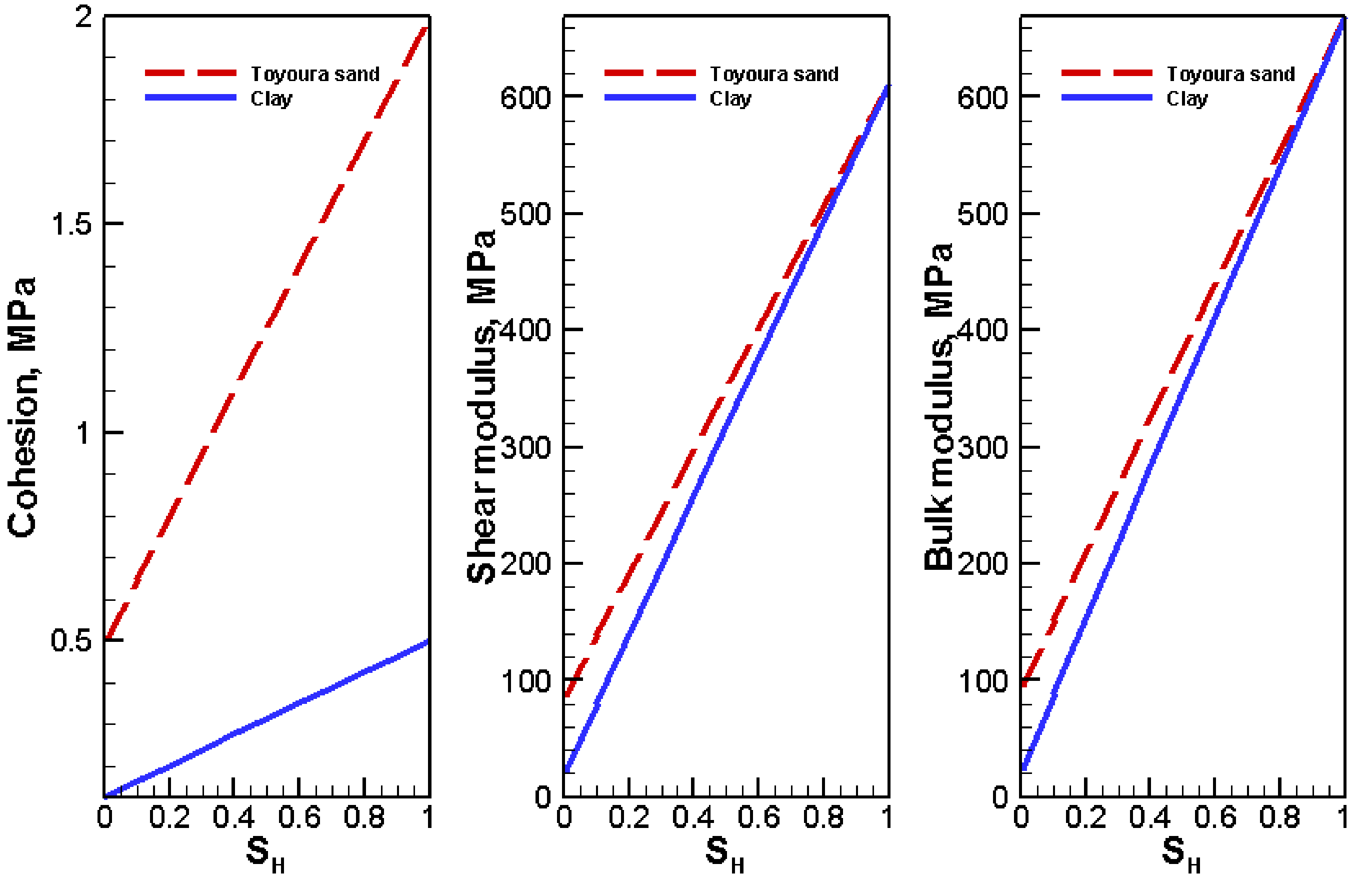

Fig. 7.1. Strength properties of hydrate bearing sediments (modified from Rutqvist and Moridis, 2007).

7.4 Modeling methodology using T+F

To solve a problem using T+F, I have followed the flowchart shown in Fig. 7.2

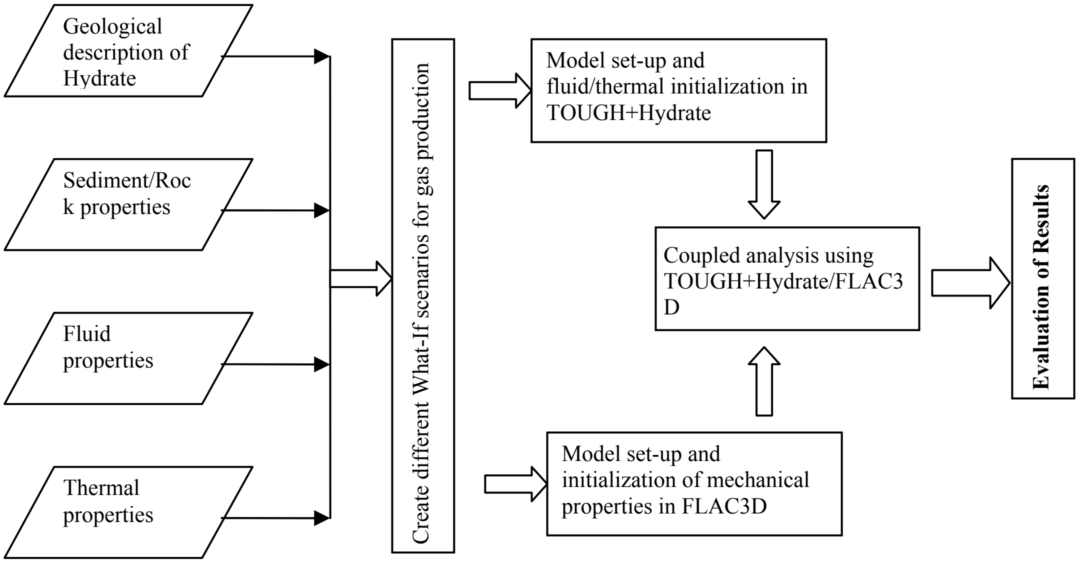

Fig. 7.2. Flowchart to solve the problems in T+F (modified from Rutqvist, 2008).

Solving a problem in the coupled model requires initialization, which is a two step process (Rutqvist, 2008)

1. Construction of the grid for T+H simulations and initializing the model for flow simulation using hydrothermal initial and boundary conditions.
2. Construction of exactly the same grid in FLAC3D and initializing the model for different mechanical initial and boundary conditions.

Once the model is initialized, it is ready for the simulation study. The T+F simulation process in this study involves providing data (temperature, pressure and saturations) from the T+H simulation to FLAC3D to update stresses, strains and all other geomechanical properties. However, the study was limited to one-way coupling, i.e., the

FLAC3D data (effective stresses and strains) were not fed back to T+H to update the porosity and permeability distributions (as affected by the geomechanical changes).This is because the significant change in permeability was not expected; moreover this coupling significantly increases the computation time (Rutqvist, 2008).

7.5 Material models

The mechanical calculations can be run using different constitutive material models. FLAC3D has different built-in constitutive models that are suitable for various rock and soil mechanics studies. The constitutive models can be elastic, elastoplastic (Mohr-Coulomb, Cam-Clay) or viscoplastic. Each of these models has different advantages over the others under different circumstances.

The elastic model is simple to use but is insufficient to predict the behavior of soft sediments. The elastic model is characterized by reversible deformation upon unloading, follows linear stress-strain law and is path-independent.

The elastoplastic model involves more parameters to handle than elastic model but can more closely predict the behavior of soft sediments. All the elastoplastic models obey non-linear stress-strain law and hence involve some degree of permanent, path-dependent deformations (failures). The important characteristic of elastoplastic models is their yield functions, or the combinations of stress and strains for which plastic deformation takes place i.e. the material fails. The yield functions are generally represented as one or more limiting surfaces in a generalized stress space. Fig. 7.3 illustrates the yield-function for Mohr-Coulomb failure criterion in σ_1- σ_3 stress space. σ_1 is the maximum principal stress and σ_3 the minimum principal stress. The yield surface for Mohr Coulomb model is given by

$$\sigma'_{1c} = C_0 + m\sigma'_3 \tag{7.1}$$

where σ'_{1c} is the maximum compressive effective principal stress and σ'_3 is the minimum effective principal stress. C_0 is the uniaxial compressive strength which can be calculated from cohesion, S_0 and the coefficient of friction, $\mu = tan\ (\psi)$ where ψ is the friction angle

$$C_0 = 2S_0\left[\left(\mu^2 + 2\right)^{0.5} + \mu\right] \tag{7.2}$$

The slope *m* of the failure line calculated from the coefficient of friction as

$$m = \left[\left(\mu^2 + 2\right)^{0.5} + \mu\right]^2 \tag{7.3}$$

This strength criterion described by equation 7.3 is shown in the Fig. 7.3

Effective stress is defined as the difference between total stress and pore pressure.

$$\sigma' = \sigma - p_p \tag{7.4}$$

where σ is the total stress and p_p is the pore pressure. Whenever pore pressure increases above the total stress value, effective stress becomes zero and hence tensile failures occur. As discussed in Section 7.2, the geomechanical parameters of hydrate-bearing sediments (such as C_0) are functions of the hydrate saturation. Consequently, the intercept of the failure line in Fig. 7.3 is expected to change as hydrate saturation changes in the sediment.

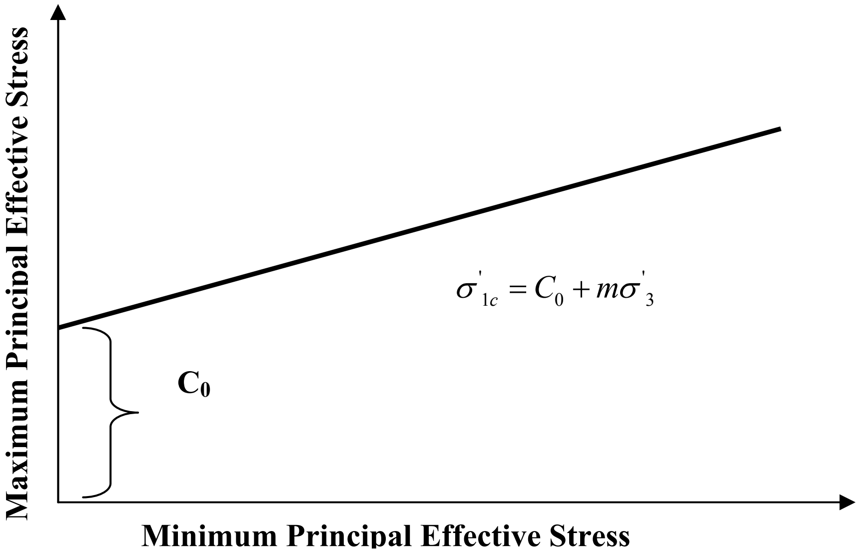

Fig. 7.3. Mohr-Coulomb failure criterion.

7.6 Stress change in hydrate bearing sediments during heating

The idea of sediment failure from heating a hydrate deposit was first proposed and experimentally verified by Makogon (1966). Recently, Moridis and Kowalsky (2006) and Rutqvist and Moridis (2007) have used T+F to numerically simulate the sediment failures in hydrate-bearing sediments during wellbore heating. In this study, I have simulated a system to demonstrate the failure zones that result from heating in hydrate-bearing sediments. I plotted the stress paths that show clearly the yielding (failure) due to heating hydrate-bearing sediments.

7.6.1 Problem description

As discussed in Chapter II, hydrate dissociation by heating can lead to large excess pressures in the sediments if there is limited (or no) outlet for the released gas, e.g., in low-permeability marine sediments.

This is dependent on the permeability of the sediments. The pressure evolution during hydrate dissociation by heating will change the effective stresses in the sediments. The main aim of this problem was to study the types of failures occurring during heating of a hydrate deposit. The failure types depend on the stress evolution with time in the sediments, which ultimately depends on geomechanical properties of the sediments.

7.6.2 Simulation domain and grid set-up

The problem domain is of unit thickness (1 m along the Y axis), 20 m in the vertical (z) direction, 10 m in the horizontal (x) direction. The domain was discretized into 10 x 20 elements in x and z direction respectively. One element acted as a constant temperature boundary (Fig. 7.4). I used the flowchart in Fig.7.2 in the solution and analysis of this problem. Although this is a small problem, it is sufficient to demonstrate the geomechanical effects (including yielding and failure) of increasing pore pressure following the thermal dissociation of hydrates in low-permeability sediments.

7.6.3 Initial and boundary conditions

The initial and boundary conditions for this problem are listed in Table 7.1. I assumed the initial stress field to be isotropic and applied a vertical stress gradient based on the sediment bulk density (ρ_b = 2600 kg/m3). In terms of geomechanical boundary conditions, only vertical movement of the horizontal boundaries was allowed; the lateral model boundaries were fixed (immobile). I simulated two cases with the same thermodynamic conditions, but with different sediment types: Case A, involving Toyoura sand, and Case B, involving clay. The initial pressure and stress distributions are shown in Fig. 7.4b.

Table 7.1

Initial and boundary conditions for heating case (from Rutqvist, 2007)

Property	Value
Temperature	12.5° C
Pressure	9.8 MPa
Vertical stress	20 MPa
Horizontal stress	20 MPa
Water saturation	0.5
Hydrate saturation	0.5

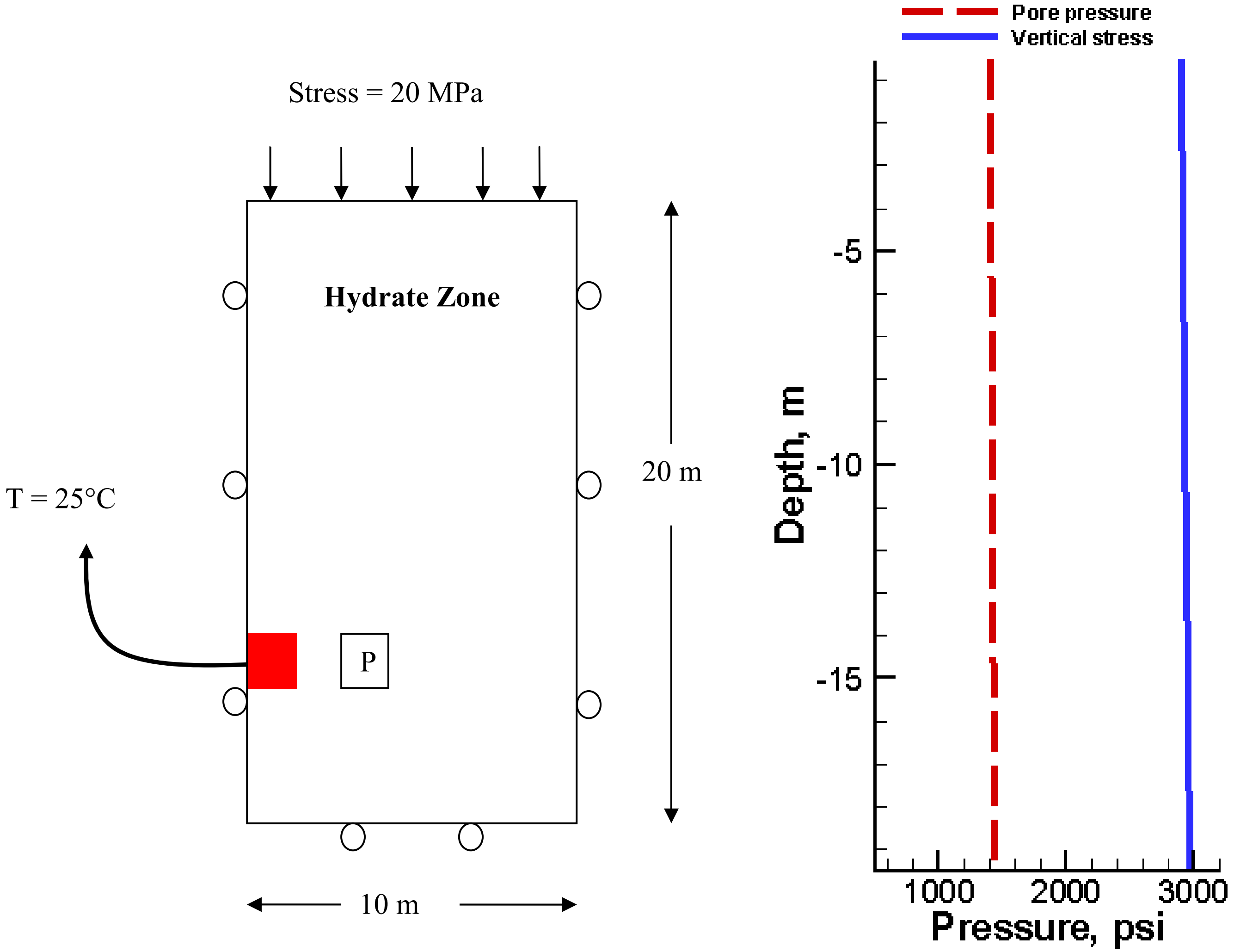

Fig. 7.4. .a) Model set-up for heating problem b) Initial pressure and stress gradients for heating problem.

7.6.4 Simulation results

The evolution of various parameters at point P (at a distance x=3 m from the heat source, see Fig. 7.4) were recorded. Fig. 7.5 shows the pressure and temperature evolution at point P. Pressure increases substantially in the sediment (doubling after about 1,130 days), significantly changing the effective stresses in the process.

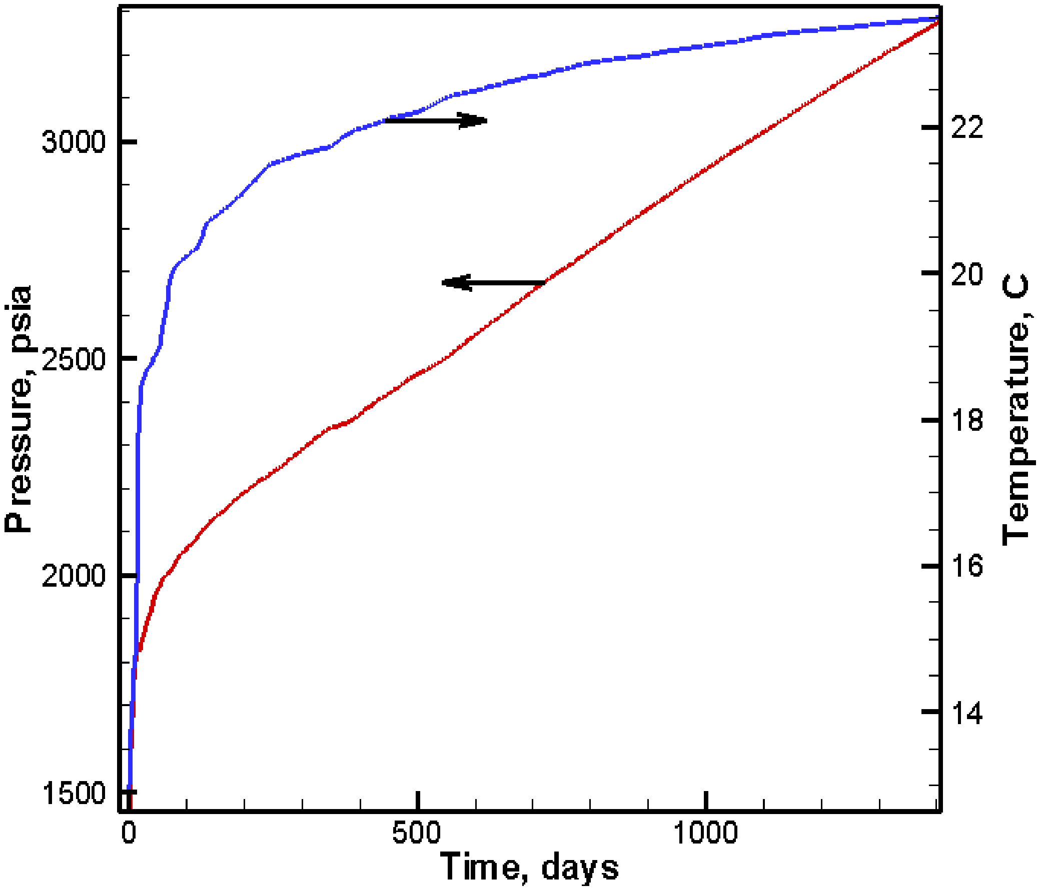

Fig. 7.5. Pressure and temperature change at point P for heating problem.

Fig. 7.6 shows the stress paths during hydrate dissociation in σ_1'- σ_3' (effective principal stress) space. The main point to note here is that different strength properties of the sediments control the shape of their stress paths. In both these cases, minimum effective stresses are almost zero which means that the pore pressure has reached such a high value that it is equal to the effective vertical stress (also the minimum effective stress). The reduction of effective stress to zero will lead to tensile failures or hydrofractures in the sediments. The tensile failures can also lead to shear failures in the sediments. The stress path not only depends on the sediment types but also the stress anisotropy.

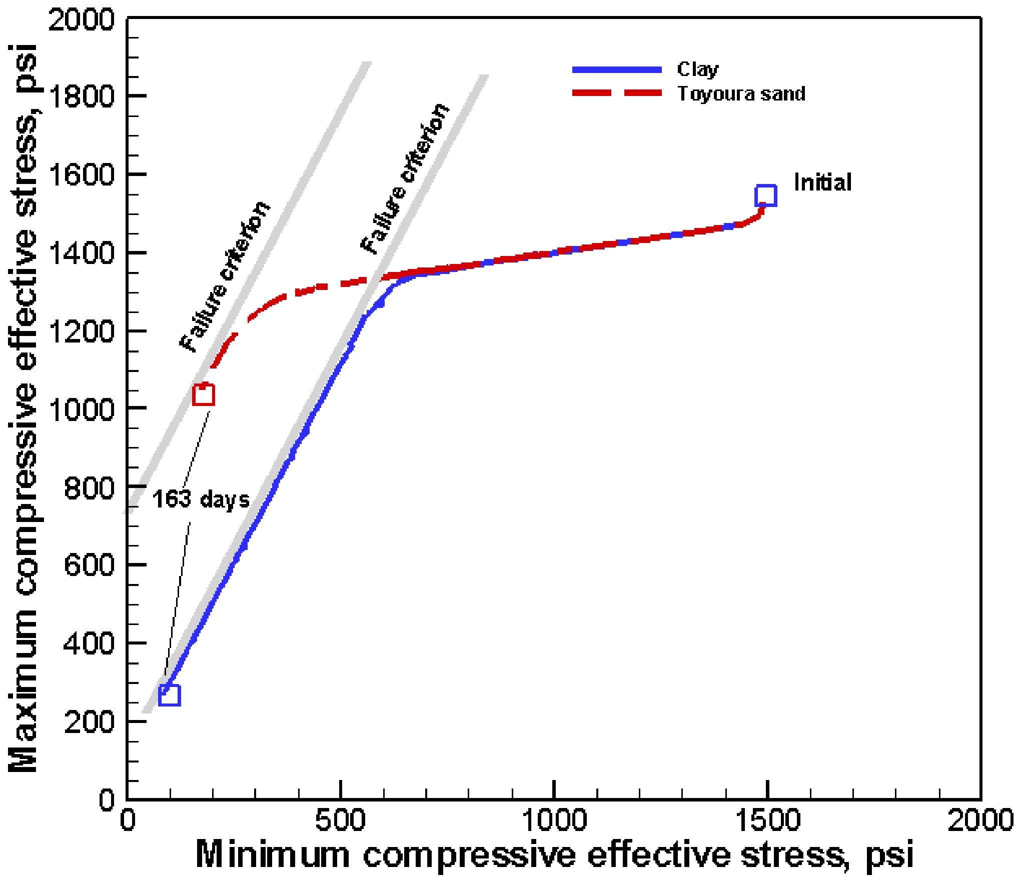

Fig. 7.6. Stress paths during hydrate dissociation for heating problem.

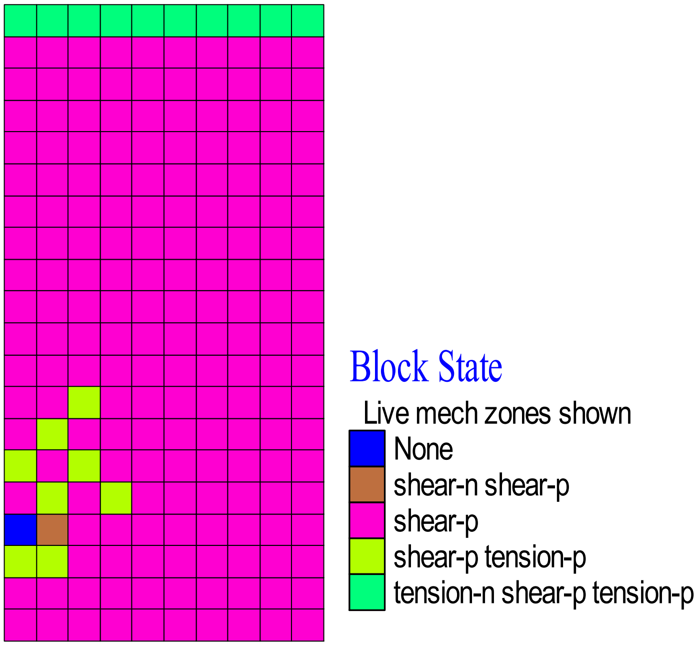

Fig. 7.7. Sediment failure zones for clay for heating problem after 163 days.

Fig. 7.7 shows various failure zones in the grid for clay sediments. The legends with “-n” means now and “-p” means past. These simulation results demonstrate that considerable sediment weakening and shear failures occur when a hydrate deposit is heated.

7.7 Geomechanical failure during gas production from offshore hydrate deposit

In this section I discuss the numerical simulation study of geomechanical failures occurring during gas production from a Class 3 hydrate deposit using a horizontal well and from a Class 2 hydrate deposit using a vertical well. In this geomechanical analysis, I used the studies of gas production from (a) a Class 3 oceanic hydrate deposit using a horizontal well (Rutqvist and Moridis, 2007), and (b) a Class 2 oceanic hydrate deposit using a vertical well (Moridis and Reagan, 2007). Using the coupled T+F model, I determined the stress changes in two different types of sediments, Toyoura sand and clay. The results of the geomechanical inverstigation are also included in Rutqvist et al. (2008).

7.7.1 Production induced geomechanical changes using horizontal well

7.7.1.1 Geological description

The geologic system in this study is based on that of the Tigershark area located in the Alaminos Canyon Block 818 of the Gulf of Mexico which was initially described by Smith et al. (2006) and was subsequently investigated by Rutqvist and Moridis (2007). The water depth at the exploration site is about 2750 m; the thickness of the hydrate-bearing sandy layer was estimated to be 18.25 m. The depth to the top of the hydrate zone below the seafloor was 460 meters (Smith et al., 2006). The porosity ϕ was estimated to be 0.30 and the absolute permeability was estimated to be close to 1 Darcy (Smith et al., 2006). Preliminary calculations by Smith et al. (2006) indicated that the hydrate saturation (S_H) ranges from 0.6-0.8.

7.7.1.2 Simulation model

To calculate the stress changes in the hydrate-bearing layer during gas production, I used the simulation model of Rutqvist and Moridis (2007). Fig. 7.8 (Rutqvist and Moridis, 2007) illustrates the simulation domain, the initial and boundary conditions and Fig. 7.9 illustrates the enhanced view of the horizontal well, which is operated at a constant pressure of 2.8 MPa (392 psi). The simulation domain is discretized into 97 x 106 elements in x and z direction (Rutqvist and Moridis, 2007).

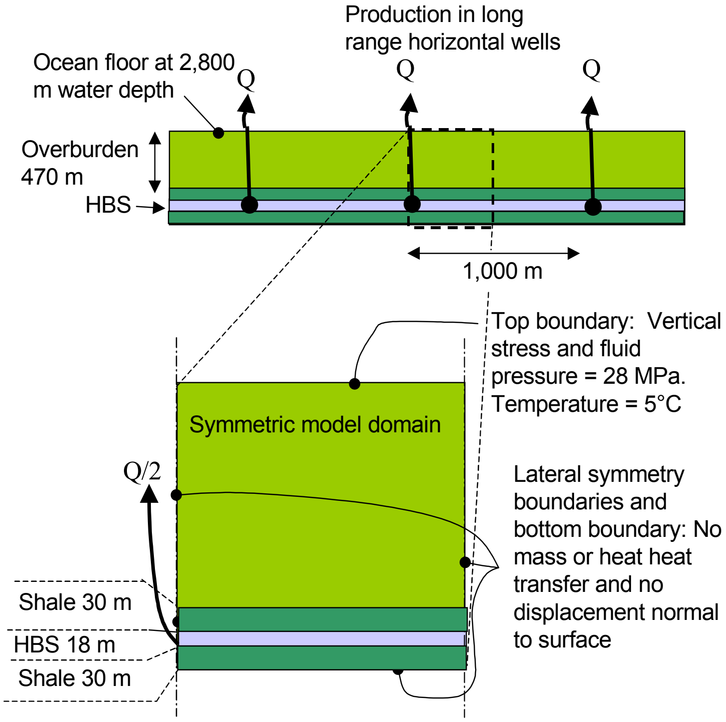

Fig. 7.8.Simulation domain for the horizontal well (Rutqvist and Moridis, 2007).

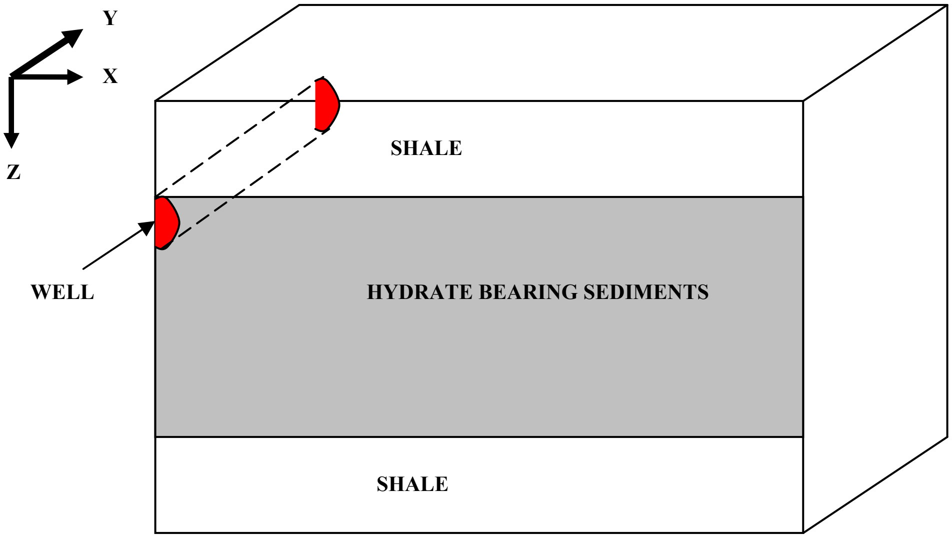

Fig. 7.9. Cross sectional view of the horizontal well.

Table 7.2 describes the simulation parameters input into the model as described in Rutqvist and Moridis (2007) and Fig. 7.10 shows the initial conditions in the model.

Table 7.2

Simulation parameters for the horizontal well and vertical well models (after Rutqvist et al., 2008; Rutqvist and Moridis, 2007)

Parameter	Value
Hydrate zone thickness	18.25 m
Initial saturations in Hydrate layer	$S_H = 0.7$, $S_A = 0.3$
Water salinity (mass fraction)	0.03
Intrinsic permeability, kx = kz	750 md
Well pressure (constant)	2.70e6 Pa (392 psi)
Capillary pressure model	Van Genutchen function $p_{cap} = -p_0\left[\left(S^*\right)^{-1/\lambda} - 1\right]^{-\lambda}$ with restriction $-p_{max} \le p_{cap} \le 0$ $S^* = \left[\frac{S_A - S_{irA}}{S_{mxA} - S_{irA}}\right]$ $\lambda = 0.45$ $S_{irA} = 0.20$ $p_0 = 10^5$ Pascals $p_{max} = 10^6$ Pascals $S_{mxA} = 1$
Relative permeability model (OPM model)	$k_{rA} = (S_A{}^*)^n$ $k_{rG} = (S_G{}^*)^n$ $S_A{}^* = \frac{S_A - S_{irA}}{1 - S_{irA}}$ $S_G{}^* = \frac{S_G - S_{irG}}{1 - S_{irA}}$ $n = 3.572;\ S_{irG} = 0.02;\ S_{irA} = 0.25$

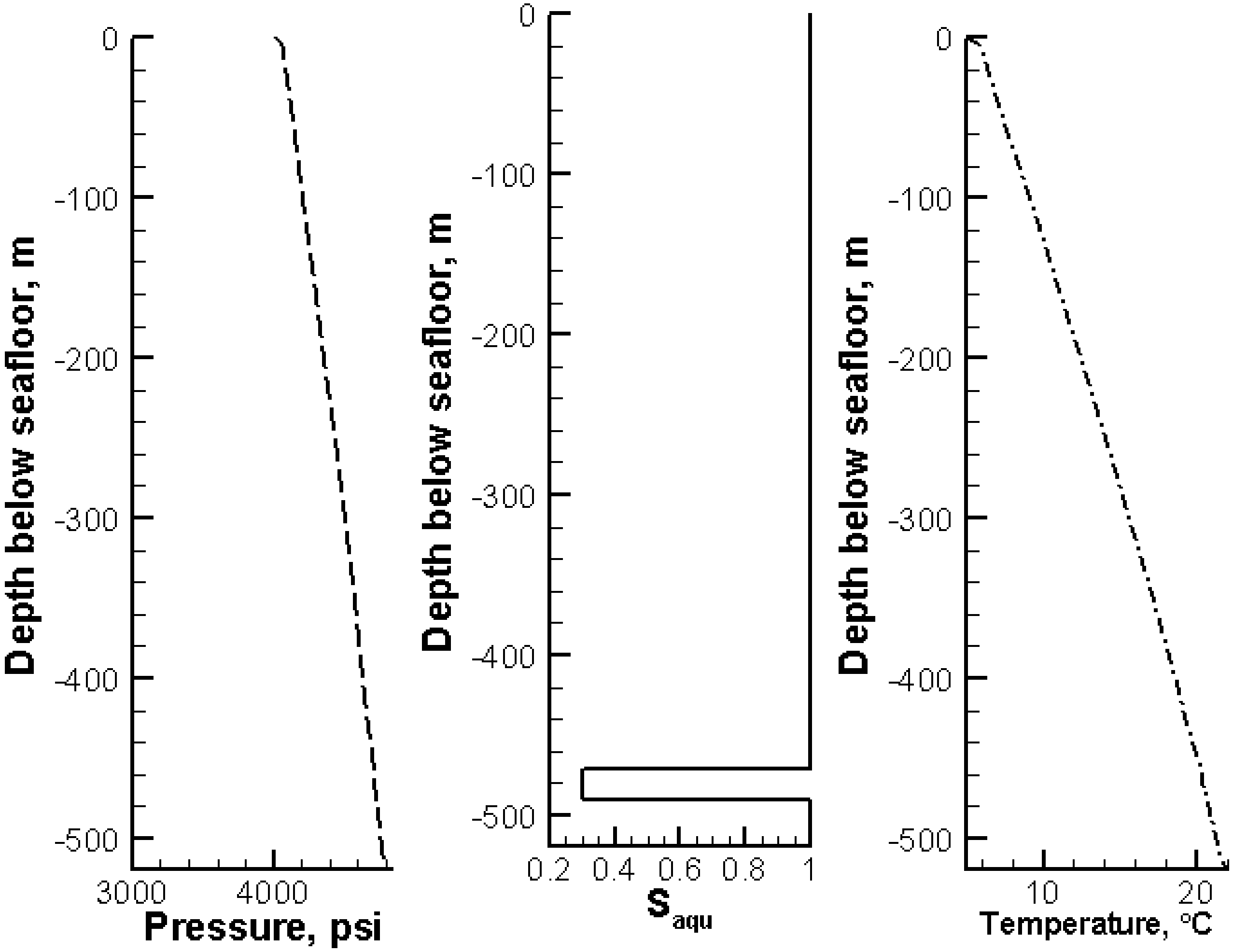

Fig. 7.10.Initial conditions for the horizontal well model.

7.7.1.3 Simulation results for horizontal well

Hydrate dissociation occurs due to depressurization. I conducted the simulation until 1 year of gas production as this time was sufficiently long to observe significant pressure and temperature conditions around the well along with significant hydrate dissociation in the sediments (Rutqvist and Moridis, 2007).

The production behavior from a horizontal well has been described in Rutqvist and Moridis (2007). Fig. 7.11 shows the evolution of gas production rate for a 500 m long horizontal well.

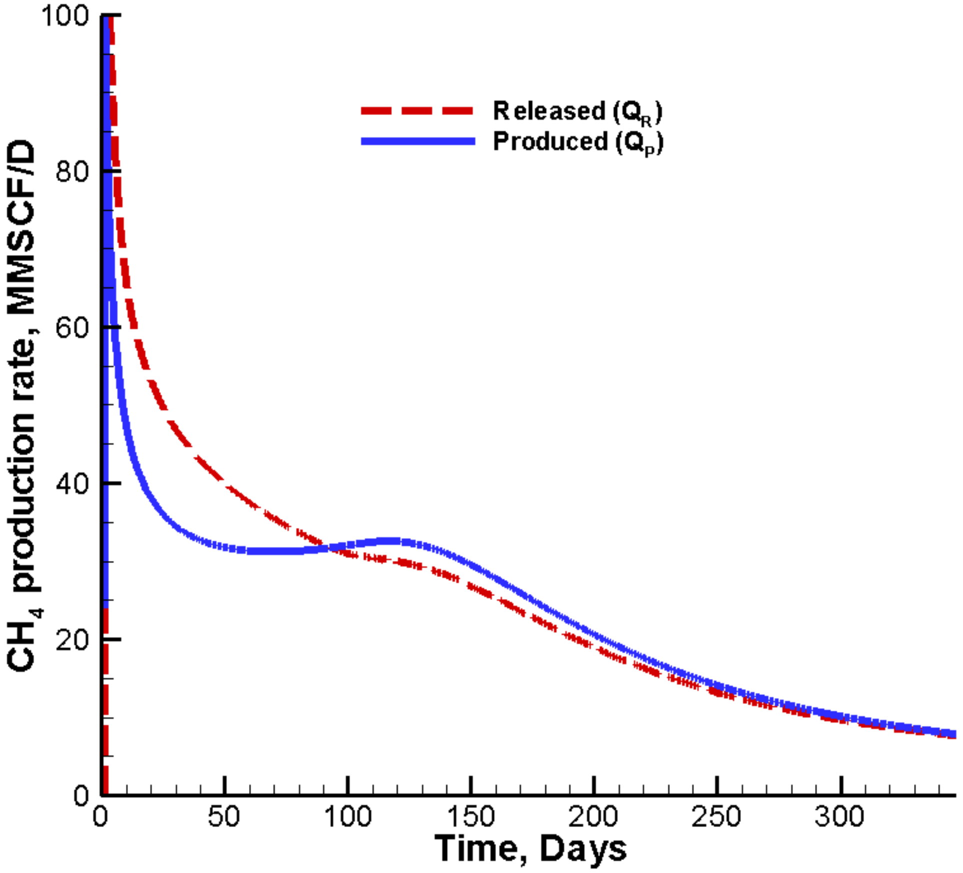

Fig. 7.11. Evolution of Q_r and Q_p for a 500 meter long horizontal well (after Rutqvist and Moridis, 2007).

The results in Fig. 7.11 indicate that both gas release into the reservoir and production from horizontal well are the highest very early after the initiation of the operation (when the maximum pressure differential Δp_w applies to the well) (Rutqvist and Moridis, 2007). Gas release rate (Q_r) continues to decline during the entire production period (of 1 year), but gas production rate (Q_p) stabilizes at about $t = 55$ days, and then rises slowly (as the effect of the decreasing Δp_w on production is overcome by the effect of a continuously expanding zone of increasing k_{eff} as dissociation advances). Finally Q_p begins a slow continuous decline (when a large HBS volume has dissociated, k_{eff} is either stabilized or increases very slowly, and the k_{eff} effect is overcome by that of the decreasing Δp_w) (Rutqvist and Moridis, 2007).

Fig.s 7.12 and 7.13 show the stress path followed during gas production in two different types of sediments, Toyoura sand and Clays.

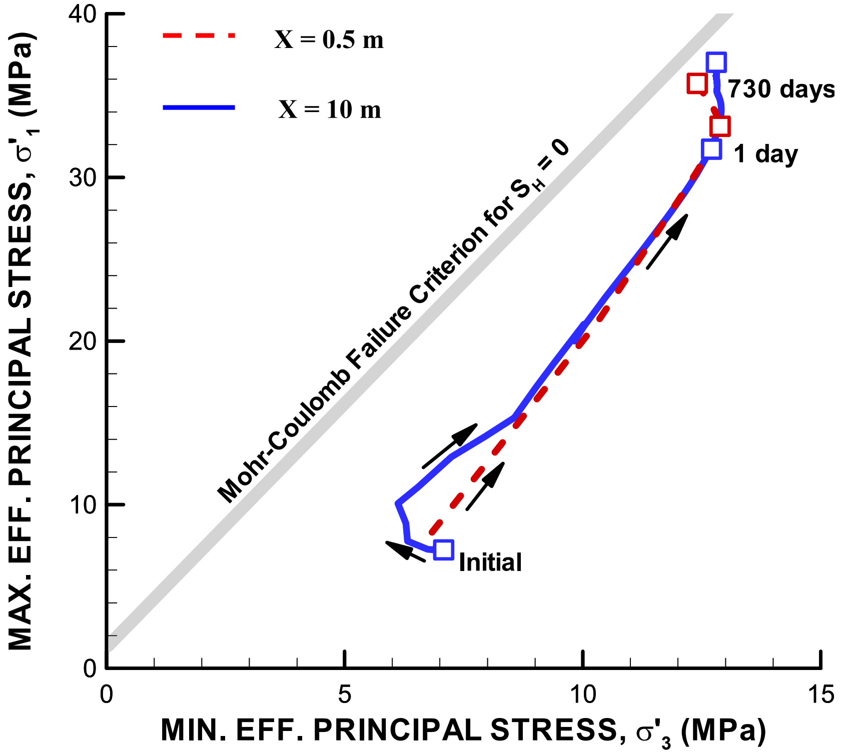

Fig. 7.12. Calculated effective stress path for horizontal well in Toyoura sand.

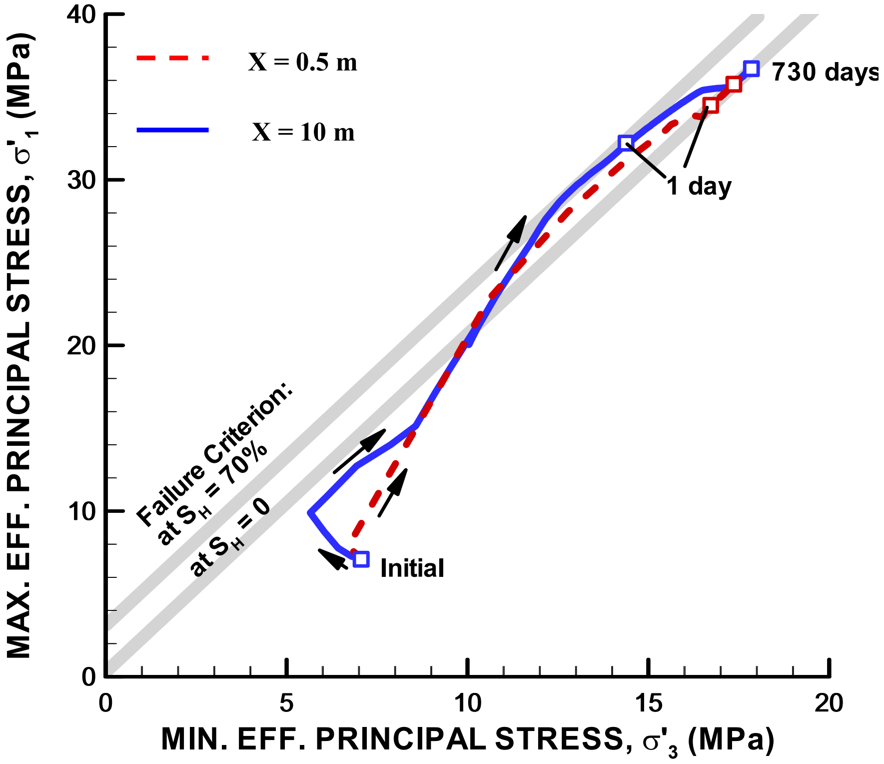

Fig. 7.13. Calculated effective stress path for horizontal well in clay.

The initial stress state in the hydrate deposits is isotropic. As the production continues the principal effective stresses in the sediments continues to increase and becomes progressively anisotropic. For the case of Toyoura sand, the maximum and minimum principal effective stresses quickly merge after 1 day and follow the same path of effective stress increase. However, the principal effective stresses never reach the failure line for weakest hydrate bearing sediments (that is, for $S_H = 0$). Therefore no failure occurs during the gas production from the Toyoura sand.

For the case of clay (mechanically weaker sediments), just within a day the stress path hits the failure line for clay. The principal effective stress path at $x = 0.5$ m crosses the $S_H = 0$ failure line early (i.e., in less than a day), continues to evolve in a region that indicates failure (still, in less than a day), before returning to follow again the $S_H = 0$ failure line to the end of the simulation. This indicates that the system failure occurs from day 1. For x = 10 m (further away from the well) crossing the $S_H = 0$ failure line when $S_H > 0$ at this point is not a problem because hydrate has not dissociated completely. The system will fail when SH = 0 and the stress pathway coincides with the SH = 0 failure. The other important observation is that the SH = 0.7 failure line is not crossed at any time because of rapidly declining S_H near the well. Similarly, for x = 10 m, the principal effective stress path first reaches the failure line for $S_H = 0.7$ and then falls down as hydrate dissociates and eventually effective stresses follow the failure line for $S_H = 0$ and the sediments are in the state of yielding.

The settlement calculated for the Toyoura sand was 0.8 m at the ocean floor and for clay was 4.3 m at the ocean floor. This large settlement for clays shows the detrimental effect of gas production on structures or pipelines placed on the seafloor. The weaker the sediments, the more are the chances of geomechanical failures.

7.7.2 Production induced geomechanical changes using vertical well

For the vertical well, I studied the geomechanical instability in same hydrate deposit, Tigershark Area in the Gulf of Mexico, as studied in the horizontal well (Section 7.7.1.1). The use of a vertical well for the Tigershark Area has been proposed by Moridis and Reagan (2007) assuming the deposit to be a Class 2 deposit, that is hydrate layer underlain by a water zone. Moridis and Reagan (2007) proposed a novel well design that I used in my simulation study to study the geomechanical instability.

7.7.2.1 Simulation domain and well design

A schematic of the problem domain is illustrated in Fig. 7.14 (Moridis and Reagan, 2007). To conduct the geomechanical simulation study, I used a modified 3D grid of the same problem (Rutqvist, 2008; Rutqvist et al., 2008). Fig. 7.15 shows the schematic of the well design used for the production of gas from the hydrate deposit (Moridis and Reagan, 2007). The well design involves a 6-m long perforated production interval. The interval extends 2 m into the HBS, and 4 m into the underlying water zone (WZ). The outer wellbore surface is heated over its vertical extent within the HBS.

As Moridis and Reagan (2007) indicated “this heating causes thermal dissociation of the hydrate and lead to the creation of a cylindrical dissociation interface around the well that can communicate with the production interval because of its enhanced permeability”. A constant mass rate of 10,000 barrels per day (BPD) was applied at the well

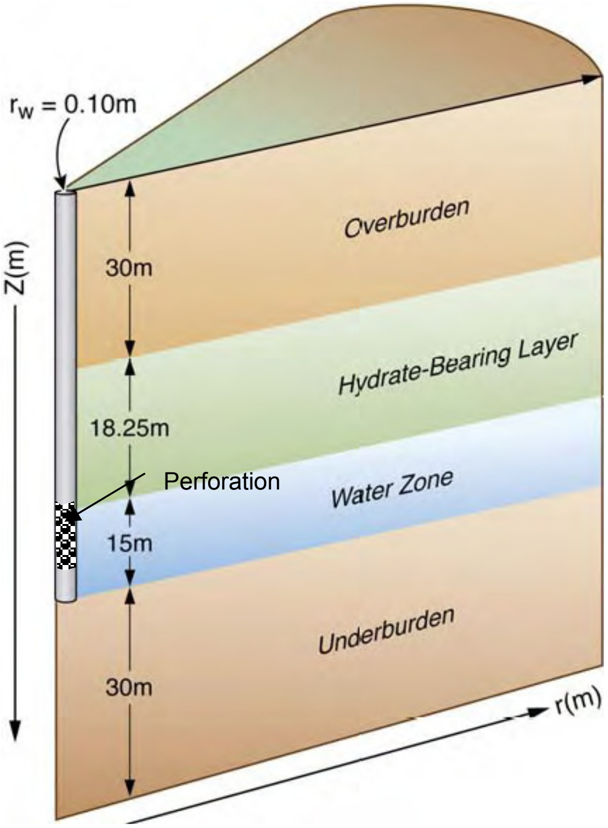

Fig. 7.14. Schematic of production from vertical well (from Moridis and Reagan, 2007).

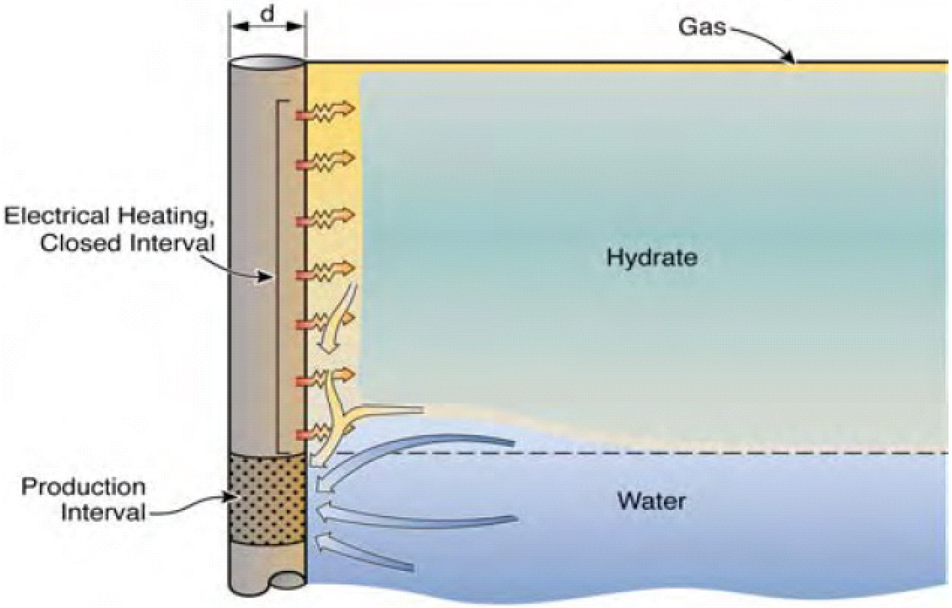

Fig. 7.15. Well design for vertical well proposed by Moridis and Reagan (2007).

7.7.2.2 Simulation results

Hydrate dissociation occurs because of the combination of the thermal stimulation and depressurization.

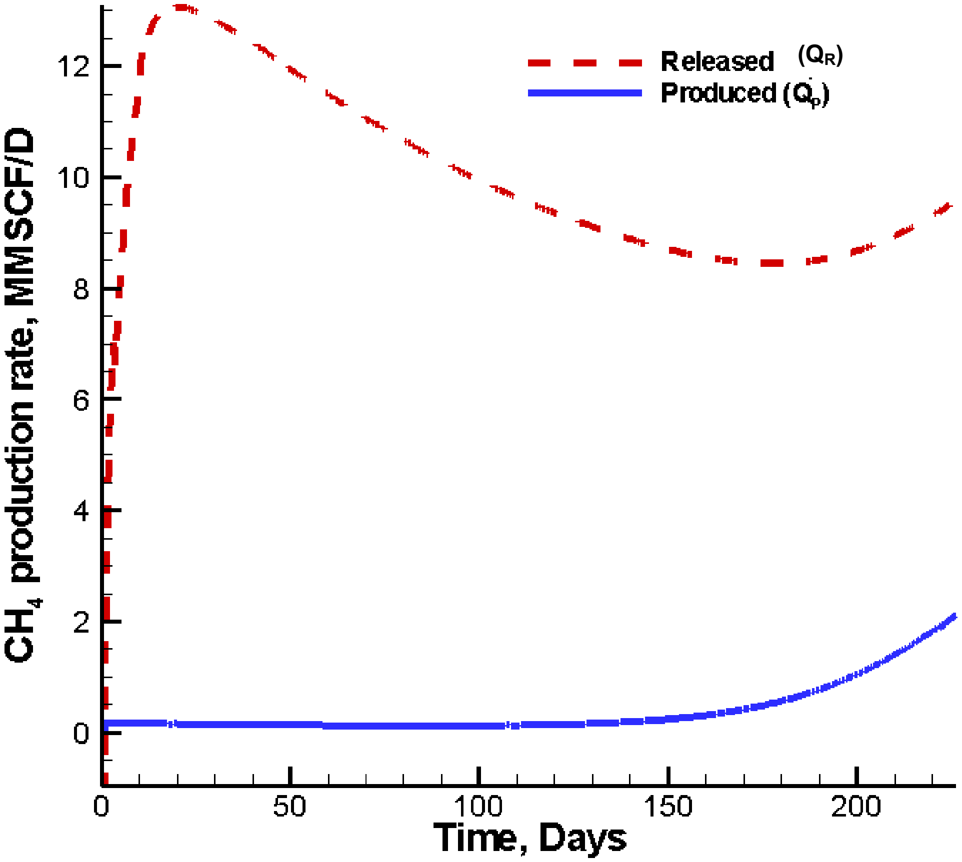

Fig. 7.16. Evolution of Q_r and Q_p for vertical well (after Moridis and Reagan, 2007)

Fig. 7.16 shows the evolution of Q_r *and* Q_p. Before about 150 days, the gas production is low as the produced gas originates (to a substantial degree) from the exsolution of gas from water (Moridis and Reagan, 2007). The electrical heating (and the corresponding localized dissociation) along the outer surface of the wellbore makes an insignificant contribution to the gas production because initially the effective permeability (k_{eff}) is low in this zone (Moridis and Reagan, 2007). After about 150 days, the gas production begins to increase rapidly. This rapid gas production occurs because of vigorous gas relaease by hydrate dissociation. The gas production continues to rise steeply until 230 days. After this time, cavitation occurs near the well and well pressure falls rapidly below the allowable limit (Moridis and Reagan, 2007). The reason for this caviation is that the low density gas replaces water in the reservoir and the prescribed mass rate cannot be sustained by low density gas (Moridis and Reagan, 2007).

Fig. 7.17 shows the effective principal stress path for Toyoura sand during gas production at distance of 0.5 and 10 m away from the well (at an elevation z = 517.5 m). The effective stresses increase during the gas production (as in the horizontal well case). No failure was observed during the gas production from Toyoura sand.

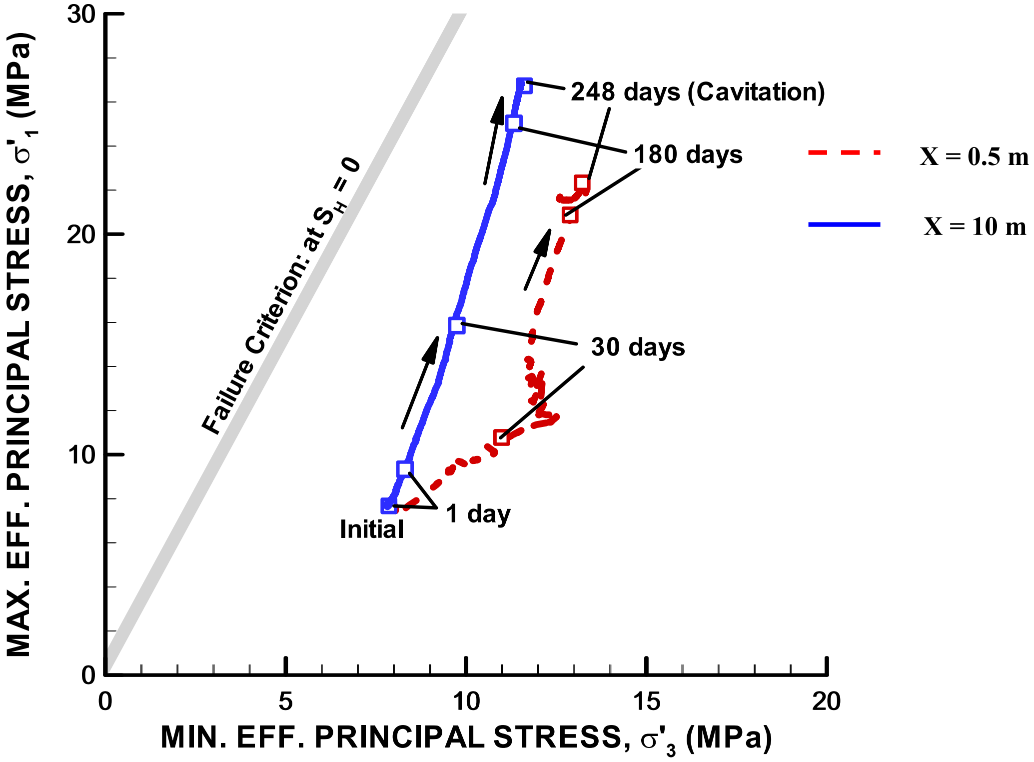

Fig. 7.17. Calculated effective stress path for vertical well in Toyoura sand.

Fig. 7.18 shows the calculated effective stress path during production in the low strength clay. At a distance x = 10 m away from the well, the principal effective stresses reach the failure line, whereas near the wellbore (i.e. at x = 0.5 m) the sediments do not fail. In the case of the vertical well, the pressure depletion is such that the near wellbore failure is prevented, while the sediments away from the wellbore yield because of the plastic strain.

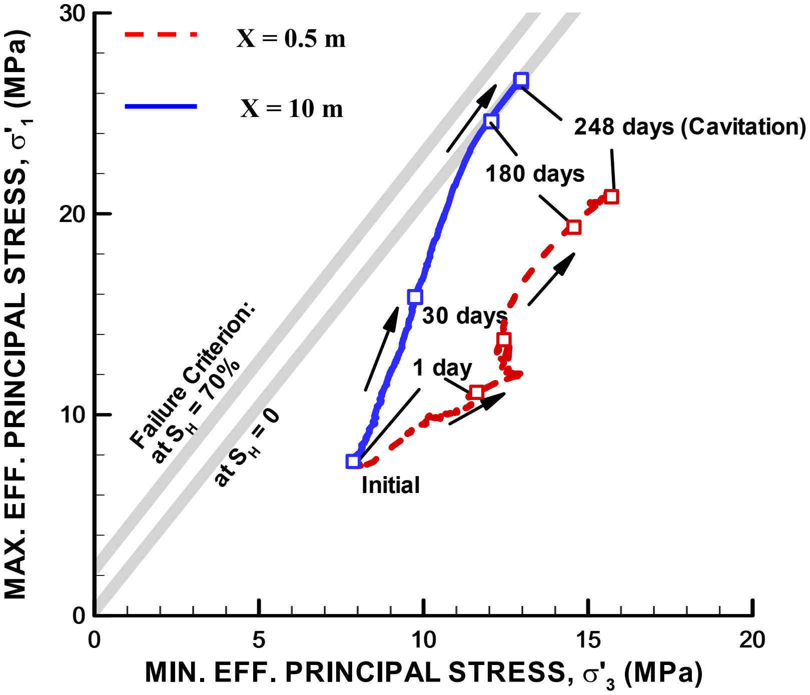

Fig. 7.18. Calculated effective stress path for vertical well in clay.

7.8 Conclusions

The conclusions from our simulation studies on geomechanics are:

1 Very high pore pressures can be reached in the hydrate-bearing sediments during the hydrate dissociation by temperature increase. This generation of excess pore pressure reduces the effective stresses in the sediments. When the effective stresses in the sediments approach zero, tensile failures can occur in the sediments.

2 During gas production from hydrate-bearing sediments by depressurization, the effective stresses get increased. The main failure criteria in the hydrate-bearing sediments will be shear failure.

3 Shear failures during the depressurization induced gas production from HBS are more prominent in lower-strength sediments such as clays.

4 During gas production from a horizontal well, near wellbore failures can occur whereas during gas production from a vertical well, the sediment shear failures occur away from the wellbore

5 Vertical subsidence caused by the depressurization depends on the sediment type; weaker the sediments, the larger will be the subsidence. Subsidence can be a serious issue during gas production from hydrate-bearing sediments.

CHAPTER VIII

CONCLUSIONS

Gas hydrates have been found in offshore sediments as well as Arctic permafrost. The understanding of the gas hydrate distribution in the scientific community has increased significantly over the last few years. The various expeditions carried out for studying gas hydrates have provided very important database. The fundamental flow and geomechanical properties of the hydrate bearing sediments are important if a typical hydrate deposit is to be exploited for gas production. From our detailed study of the database, we have learnt that the hydrates can be distributed in the sediments in different forms. A majority of the hydrates are found in the low permeability clays and silty-clay sediments in the offshore environments. Since oceanic hydrates are typically found in unconsolidated sediments, the strength of the hydrate bearing sediments plays an important role in studying the geomechanical failures.

The simulation work of the Messoyakha field showed that the intrinsic permeability and hence the effective gas permeability are an important factor for gas production from hydrate deposit. The temperature of the hydrate bearing sediments decreases when hydrates dissociate. In a hydrate-capped gas reservoir (such as the Messoyakha), when the wells are completed very near the hydrate-free gas interface, the formation of secondary hydrates plugs the perforations. Hence, the wells should be completed as far as possible from the hydrate layer to avert the formation of secondary hydrates. When gas is produced at high rates in a Class 1G hydrate deposit contribution of hydrates to overall gas production increases. However, with gas production at high rates, the temperature drops rapidly in the sediments and can have inhibitory effect on gas production if perforations are very close to the hydrate/gas interface. The contribution of hydrates to the overall gas production increases with time because of increasing effective permeability in the hydrate-bearing sediments.

The hydraulic fracture stimulation of a hydrate deposit in high permeability sediments is not effective and there is no gain in production rate. Instead, the fracture face gets plugged by the formation of secondary hydrates.

Heating a gas hydrate deposit can generate excess pore pressures. The generation of excess pore pressures leads to reduction in effective stress, and the tensile failures can occur in the sediments. During gas production by depressurization method in the hydrate-bearing sediments, the effective stresses in the sediments increase. If the sediments are weak like clays, the gas production can lead to rapid sediment yielding and shear failure. Subsidence can be a serious issue during gas production from hydrate deposits and can lead to the loss of platforms or other seafloor installations.

REFERENCES

Abegg, F., Bohrmann, G. and Kuhs, W., 2006. Data report: shapes and structures of gas hydrates imaged by computed tomographic analyses, ODP Leg 204, Hydrate Ridge. In: A.M. Trehu, G. Bohrmann, M.E. Torres and F.S. Colwell (Editors), Proceedings of Ocean Drilling Program, Scientific Results, 204, College Station, Texas, pp. 1-11.

Boothe, J.S., Rowe, M.M. and Fischer, K.M., 1996. Offshore gas hydrate sample database: Open file report 96-272, United States Geological Survey, http://pubs.usgs.gov/of/1996/of96-272/index.html.

Boswell, R., Kleinberg, R.L., Collett, T. and Frye, M., 2007, Exploration priorities for marine gas hydrate resources. Fire in The Ice: Methane Hydrate R&D Newsletter, Spring/Summer 2007, 11-13, http://www.netl.doe.gov/technologies/oil-gas/FutureSupply/MethaneHydrates/newsletter/newsletter.htm.

Breitzke, M., 2006. Physical properties of marine sediments. In: H.D. Schultz and M. Zabel (Editors), Marine Geochemistry. Springer, Berlin, pp. 27-71.

Brooks, J.M., Cox, H.B., Bryant, W.R., Kennicutt, M.C., Mann, R.G. et al., 1986. Association of gas hydrates and oil seepage in the Gulf of Mexico. Organic Geochemistry. 10, 221-234.

Bryn, P., Berg, K., Forsberg, C.F., Solheim, A. and Kvalstad, T.J., 2005. Explaining the Storrega Slide. Marine and Petroleum Geology. 22(1-2), 11-19.

Carpenter, G.B., 1981. Coincident sediment slump/clathrate complexes on the U.S Atlantic slope. Geo-Marine Letters. 1, 29-32.

Center for Gas Hydrate Research - Heriot Watt University, 2007. What are gas hydrates?, http://www.pet.hw.ac.uk/research/hydrate/hydrates_what.htm.

Claypool, G.E. and Kaplan, I.R., 1974. The origin and distribution of methane in marine sediments. In: I.R. Kaplan (Editor), Natural Gases in Marine Sediments. Plenum Press, New York, pp. 99-139.

Collett, T., Lewis, R.E. and Dallimore, S.R., 2005. Mallik 5L-38 gas hydrate production research well downhole well-log and core montages. In: S.R. Dallimore and T. Collett (Editors), GSC Bulletin 585: Scientific results from the Mallik 2002 gas hydrate production well program, Mackenzie Delta, Northwest Territories, Canada. Geological Survey of Canada, pp. 23.

Conte, A. and Bloys, B., 2005. Cruise report - The Gulf of Mexico gas hydrate joint industry project, National Energy Technology Laboratory - US Department of Energy http://www.netl.doe.gov/technologies/oil-gas/FutureSupply/MethaneHydrates/rd-program/GOM_JIP/hydrates_main.html.

Cook, A.E., Goldberg, D. and Kleinberg, R.L., In Press. Fracture-controlled gas hydrate systems in Gulf of Mexico. Marine and Petroleum Geology.

Crutchley, G.J., Gorman, A.R. and Fohrmann, M., 2007. Investigation of the role of gas hydrates in continental slope stability west of Fiordland, New Zealand. New Zealand Journal of Geology and Geophysics. 50, 357-364.

Dallimore, S.R. and Collett, T.S., 2005. Summary and implications of the Mallik 2002 gas hydrate production research well program. In: S.R. Dallimore and T.S. Collett (Editors), GSC Bulletin 585: Scientific results from the Mallik 2002 gas hydrate production research well program, Mackenzie Delta, Northwest Territories, Canada. Geological Survey of Canada, pp. 36.

Davie, M.K. and Buffett, B.A., 2001. A numerical model for the formation of gas hydrate below the seafloor. Journal of Geophysical Research. 106(B1), 497-514.

Dicharry, C., Gayet, P., Marion, G., Graciaa, A. and Nesterov, A.N., 2005. Modeling heating curve for gas hydrate dissociation in porous media. Journal of Physical Chemistry B. 2005(109), 17205-17211.

Field, M.E. and Barber, J.H.J., 1993. A submarine landslide associated with shallow seafloor gas and gas hydrates off Northern California. In: W.C. Schwab, H.J. Jee and D.C. Twichell (Editors), Submarine Landslides: Selected Studies in the U.S. Exclusive Economic Zone. U.S Geological Survey, pp. 971-972.

Francisca, F., Yun, T.S., Ruppel, C. and Santamarina, J.C., 2005. Geophysical and geotechnical properties of near-seafloor sediments in the northern Gulf of Mexico gas hydrate province. Earth and Planetary Science Letters. 237, 924-939.

Ginsburg, G., Soloviev, V., Matveeva, T. and Andreeva, I., 2000. Sediment grain-size control on gas hydrate presence, Sites 994, 995 and 997. In: C.K. Paull, R. Matsumoto, P.J. Wallace and W.P. Dillion (Editors), Proceedings of Ocean Drilling Program, Scientific Results, 164, College Station, Texas, pp. 237-245.

Gracia, E., Martinez-Ruiz, F., Pinero, E., Larrasoana, J.C., Vizcanio, A. et al., 2006. Data Report: Grain-size and bulk and clay mineralogy of sediments and the presence of gas hydrate in Hydrate Ridge. In: A.M. Trehu, G. Bohrmann, M.E. Torres and F.S. Colwell (Editors), Proceedings of Ocean Drilling Program, Scientific Results, 204, College Station, Texas, pp. 1-19.

Hammerschmidt, E.G., 1934. Formation of gas hydrates in natural gas transmission lines. Industrial and Engineering Chemistry. 26(8), 851-855.

Handa, Y.P. and Stupin, D., 1992. Thermodynamic properties and dissociation characteristics of methane and propane hydrates in 70 Å radius silica gel pores Journal of Physical Chemistry. 96(21), 8599-8603.

He, L., Matsubayashi, O. and Lei, X., 2006. Methane hydrate accumulation model for the Central Nankai accretionary prism. Marine Geology. 227, 201-214.

Hesse, R. and Harrison, W.E., 1981. Gas hydrates (clathrates) causing pore-water freshening and oxygen isotope fractionation in deepwater sedimentary sections of terrigenous continental margins. Earth and Planetary Science Letters. 55, 453-462.

Holditch, S., 2006. Tight gas sands. Journal of Petroleum Technology. 58(6), 86-93.

Huang, D. and Fan, S., 2005. Measuring and modeling thermal conductivity of gas hydrate bearing sand. Journal of Geophysical Research. 110(B01311), 1-10.

Hyndman, R.D. and Davis, E.E., 1992. A mechanism for the formation of methane hydrate and seafloor bottom simulating reflectors by vertical fluid expulsion. Journal of Geophysical Research. 97(B5), 7025-7041.

Itasca Consulting Group, 2002. FLAC3D: Fast Lagrangian Analysis of Continua in 3 Dimensions, Minneapolis.

Janik, A., Goldberg, D., Collett, T. and Leg 204 Scientific Party, 2003. Azimuthal variability in gas hydrate concentration using LWD resistivity and density images EOS Transactions, 84(46/Supplement), Abstract OS51C-0875.

Kilner, J.R. and Grozic, J.L.H., 2006. Determination of synthetic hydrate content in sand specimens using dielectrics Canadian Geotechnical Journal. 43, 551-562.

Kitajima, H., Noda, H., Chester, F.M. and Shimamoto, T., 2007. Hydraulic and frictional properties of natural clay-rich sediments from OPD Leg 190 Nankai Trough and IODP expedition 311 Cascadia Margin EOS Transactions, 88(52), Abstract S21B-0569.

Klauda, J.B. and Sandler, S.I., 2005. Global distribution of methane hydrate in ocean sediment. Energy and Fuels. 19, 459-470.

Kleinberg, R.L., 2006. New deposit accumulation model for marine gas hydrates, Offshore Technology Conference. Society of Petroleum Engineers, Houston, Texas.

Kneafsey, T.J., 2007. Staff Scientist, Lawrence Berkeley National Laboratory, Personal Communication.

Kneafsey, T.J., Tomutsa, L., Moridis, G.J., Seol, Y., Friefeld, B.M. et al., 2007. Methane hydrate formation and dissociation in a partially saturated core-scale sand sample. Journal of Petroleum Science and Engineering. 56(1-3), 108-126.

Kono, H.O., Narasimhan, S., Song, F. and Smith, D.H., 2002. Synthesis of methane gas hydrate in porous sediments and its dissociation by depressurizing Powder Technology. 122, 239-246.

Krason, J. and Ciesnik, M., 1985. Geological evolution and analysis of confrmed or suspected gas hydrate localities. DOE/MC/21181-1950, US Department of Energy, Morgantown, West Virginia.

Krason, J. and Finley, P.D., 1992. Messoyakh Gas Field - Russia West Siberian Basin, American Association of Petroleum Geologists - Treatise of Petroleum Geology, Structural Traps VII, pp. 197-220.

Kumar, P., Turner, D. and Sloan, E.D., 2004. Thermal difffusivity measurements of porous methane hydrate and hydrate-sediment mixtures. Journal of Geophysical Research. 109(B01207), 1-8.

Kunerth, D.C., Weinberg, D.M., III, J.W.R., Scott, C.L. and Johnson, J.T., 2001. Acoustic laboratory measurements during the formation of a THF hydrate in unconsolidated porous media. Journal of Seismic Exploration. 9, 337-354.

Kvalstad, T.J., Andresen, L., Forsberg, C.F., Berg, K., Bryn, P. et al., 2005. The Storegga Slide: evaluation of triggering sources and slide mechanics. Marine and Petroleum Geology. 22(1-2), 245-256.

Kvenvolden, K.A. and McMenamin, M.A., 1982. Hydrates of natural gas: A review of their occurence. US Geological Survey Circular 825, pp. 11.

Liang, M., Chen, G., Sun, C., Yan, L., Liu, J. et al., 2005. Experimental and modeling study on decomposition kinetics of methane hydrates in different media. Journal of Physical Chemistry B. 109, 19034-19041.

Liu, X. and Flemings, P.B., 2007. Dynamic multiphase flow model of hydrate formation in marine sediments. Journal of Geophysical Research. 112(B3), B01301.

Macdonald, I.R., Guinasso, N.L., Sassen, R., Brooks, J.M., Lee, L. et al., 1994. Gas hydrates that breaches the seafloor on the continental slope of the Gulf of Mexico. Geology. 22, 699-702.

Makogon, Y.F., 1965. Hydrate formation in gas bearing beds under permafrost conditions. Gazovaia Promyshlennost. 5, 14-15.

Makogon, Y.F., 1966. Specialties of exploitation of the natural gas hydrate fields in permafrost conditions. Vniiegazprom. 11(4), 1-12.

Makogon, Y.F., 1974. Hydrates of natural gases. NEDRA, Moscow.

Makogon, Y.F., 1981. Hydrates of natural gases. PennWell, Tulsa, Oklahoma.

Makogon, Y.F., 1984. Production from nautral gas hydrate deposits. Gazovaya Promishlennost. 10, 24-26.

Makogon, Y.F., 1988. Natural gas hydrates - the state of study in the USSR and perspectives for its use, Third Chemical Congress of North America, Toronto, Canada.

Makogon, Y.F., 1997. Hydrates of hydrocarbons. PennWell, Tulsa, Oklahoma.

Makogon, Y.F., 2007. Professor Emeritus - Petroleum Engineering Department, Texas A&M University, Personal Communication.

Makogon, Y.F., Holditch, S.A. and Makogon, T.Y., 2005. Russian field illustrates gas-hydrate production. Oil and Gas Journal. 103(5), 43-47.

Makogon, Y.F., Holditch, S.A. and Makogon, T.Y., 2007. Natural gas hydrates - A potential energy source for the 21st century. Journal of Petroleum Science and Engineering. 56(1-3), 14-31.

Makogon, Y.F., Trebin, F.A., Trofimuk, A.A. and Chersky, N.V., 1971. Detection of a pool of natural gas in a soild hydrated state. Doklady Akademii Nauk SSSR. 196(1), 197-200.

Makogon, Y.F., Tsarev, V.P. and Chersky, N.V., 1970. Gas-hydrate resource in the offshore, 17th World Gas Congress, Moscow.

Masui, A., Haneda, H., Ogata, Y. and Aoki, K., 2005. The effect of saturation degree of methane hydrate on the shear strength of synthetic methane hydrate sediments, 5th International Conference on Gas Hydrates, Trondheim, Norway, pp. 657-663.

Max, M.D., Johnson, A.H. and Dillon, W.P., 2006. Economic Geology of Natural Gas Hydrates (Coastal Systems and Continental Margins). Springer, Dordrecht, 341 pp.

Meyerhoff, A.A., 1980. Petroleum basins of the Soviet Arctic. Geological Magazine. 117(2), 101-210.

Mienert, J., Vanneste, M., Bunz, S., Andreassen, K., Haflidason, H. et al., 2005. Ocean warming and gas hydrate stability on the mid-Norwegian margin at the Storrega Slide. Marine and Petroleum Geology. 22, 233-244.

Milkov, A.V., 2000. Worldwide distribution of submarine mud volcanoes and associated gas hydrates. Marine Geology. 167, 29-42.

Milkov, A.V., 2005. Molecular and stable isotope compositions of natural gas hydrates: a revised global dataset and basic interpretations in the context of geological settings. Organic Geochemistry. 36, 681-702.

Milkov, A.V., Claypool, G.E., Lee, Y.-J. and Sassen, R., 2005. Gas hydrate systems at Hydrate Ridge offshore Oregon inferred from molecular and isotopic properties of hydrate-bound and void gases. Geochimica et Cosmochimica Acta. 69(4), 1007-1026.

Milkov, A.V. and Sassen, R., 2000. Thickness of the gas hydrate stability zone, Gulf of Mexico continental slope. Marine and Petroleum Geology. 17, 981-991.

Milkov, A.V. and Sassen, R., 2002. Economic geology of offshore gas hydrate accumulations and provinces. Marine and Petroleum Geology. 19, 1-11.

Milkov, A.V. and Sassen, R., 2003. Preliminary assessment of resources and economic potential of individual gas hydrate accumulations in the Gulf of Mexico continental slope. Marine and Petroleum Geology. 20, 111-128.

Moridis, G.J., 2003. Numerical studies of gas production from methane hydrates. SPE Journal. 8(4).

Moridis, G.J., 2004. Numerical studies of gas production from Class 2 and Class 3 hydrate accumulations at the Mallik site, Mackenzie Delta, Canada. SPE Reservoir Evaluation and Engineering. 7(3), 175-183.

Moridis, G.J. and Collettt, T., 2003. Strategies for gas production from hydrate accumulations under various geologic conditions. LBNL-52568, Lawrence Berkeley National Laboratory, Berkeley, California.

Moridis, G.J. and Collettt, T., 2004. Gas production from Class 1 hydrate accumulations. In: C. Taylor and J. Kwan (Editors), Recent Advances in the Study of Gas Hydrates, pp. 75-88.

Moridis, G.J., Collettt, T., Dallimore, S.R., Satoh, T., Hancock, S. et al., 2004. Numerical studies of gas production from several CH4 hydrate zones at the

Mallik site, Mackenzie Delta, Canada. Journal of Petroleum Science and Engineering. 43(3-4), 219-238.

Moridis, G.J., Kowalsky, M.B. and Pruess, K., 2007. Depressurization-induced gas production from Class 1 hydrate deposits. SPE Reservoir Evaluation and Engineering. 10(5), 458-481.

Moridis, G.J., Kowalsky, M.B. and Pruess, K., 2008. TOUGH+Hydrate v 1.0 User's Manual: A code for the simulation of system behavior in hydrate bearing geologic media. Lawrence Berkeley National Laboratory, Berkeley, California.

Moridis, G.J. and Reagan, M., 2007. Gas production from oceanic Class 2 hydrate accumulations, Offshore Technology Conference, Houston, Texas.

Moridis, G.J. and Sloan, E.D., 2007. Gas production potential of disperse low-saturation hydrate accumulations in oceanic sediments. Energy Conversion and Management. 48(6), 1834-1849.

Nakagawa, S., 2007. Staff Scientist, Lawrence Berkeley National Laboratory, Personal Communication.

Nixon, M.F. and Grozic, J.L.H., 2007. Submarine slope failure due to gas hydrate dissociation: a preliminary quantification. Canadian Geotehcnical Journal. 44, 314-325.

Paul, C.K. and Ussler, I.W., 2001. History and significance of gas sampling during DSDP and ODP. In: C.K. Paul and W.P. Dillon (Editors), Natural Gas Hydrates: Occurrence, Distribution and Detection. American Geophysical Union, pp. 53-66.

Popenoe, P., Schmuck, E.A. and Dillon, W.P., 1993. The Cape Fear landslide: slope failure associated with salt diapirism and gas hydrate decomposition. In: W.C. Schwab, H.J. Lee and D.C. Twichell (Editors), Submarine Landslides-Selected Studies in the U.S. Exclusive Economic Zone: U.S. Geological Survey Bulletin B 2002, pp. 40-53.

Pruess, K., Oldenburg, C. and Moridis, G.J., 1991. A general purpose numerical simulator for multiphase fluid and heat flow. LBNL-29400, Lawrence Berkeley National Laboratory, Berkeley, California.

Rempel, A.W. and Buffett, B.A., 1997. Formation and accumulation of gas hydrate in porous media. Journal of Geophysical Research. 102(B5), 10,151-10.

Ruppel, C., Dickens, G.R., Castellini, D.G., Gilhooly, W. and Lizzarlde, D., 2005. Heat and salt inhibition of gas hydrate formation in the northern Gulf of Mexico. Geophysical Research Letters. 32(L04605), 1-4.

Rutqvist, J., 2007. Staff Scientist, Lawrence Berkeley National Laboratory, Personal Communication.

Rutqvist, J., 2008. Staff Scientist, Lawrence Berkeley National Laboratory, Personal Communication.

Rutqvist, J., Grover, T. and Moridis, G.J., 2008. Coupled hydrological, thermal and geomechanical analysis of wellbore stability in hydrate bearing sediments, Offshore Technology Conference, Houston, Texas.

Rutqvist, J. and Moridis, G.J., 2007. Numerical studies on the geomechanical stability of hydrate-bearing sediments, Offshore Technology Conference, Houston, Texas.

Rutqvist, J. and Tsang, C.F., 2003. Analysis of thermal-hydrologic-mechanical behavior near an emplacement drift at Yucca Mountain. Journal of Contaminant Hydrology. 62-63, 637-652.

Santamarina, J.C., Francisca, F.M., Sun, T.S., Lee, J.Y., Martin, A.I. et al., 2004. Mechanical, thermal, and electrical properties of hydrate bearing sediments, AAPG Hedberg Conference. AAPG, Vancouver, BC, Canada.

Sapir, M.H., Khramenkov, E.N., Yefremov, I.D., Ginsburg, G.D., Beniaminovich, A.E. et al., 1973. Geologic and gephysical features of the gas hydrate deposits in the Messoiakh field. Geologiia Nefti i Gaza. 6, 26-34.

Sassen, R., 2007. Deputy Director, Resource Geochemistry, Geochemical and Ennvironmental Research Group, Texas A&M University - College Station, Personal Communication.

Sassen, R., Brooks, J.M., Macdonald, I.R., KennicuttII, M.C., Guinasso, N.L. et al., 1994. Association of oil seeps and chemosynthetic communities with oil discoveries, upper continental slope, Gulf of Mexico. Gulf Coast Association of Geological Societies Transactions. 44, 349-355.

Sassen, R., Joye, S., Sweet, S.T., DeFreitas, D.A., Milkov, A. et al., 1999a. Thermogenic gas hydrates and hydrocarbon gases in complex chemosynthetic communities, Gulf of Mexico continental slope. Organic Geochemistry. 30, 485-497.

Sassen, R., Joye, S., Sweet, S.T., DeFreitas, D.a., Milkov, A.V. et al., 1999b. Thermogenic gas hydrates and hydrocarbon gases in complex chemosynthetic communities, Gulf of Mexico continental slope. Organic Geochemistry. 30, 485-497.

Sassen, R. and Macdonald, I.R., 1994. Evidence of structure H hydrate, Gulf of Mexico continental slope. Organic Geochemistry. 22(6), 1029-1032.

Settari, A. and Mourits, F.M., 1998. A coupled reservoir and geomechanical simulation system. SPE Journal. 27(9), 219-226.

Sheshukov, N.L., 1973. Features of gas bearing strata with the hydrates. Geologiia Nefti i Gaza. 6, 20-26.

Shipboard Scientific Party, 1996. In: C.K. Paul, R. Matsumoto, P.J. Wallace, N.R. Black, W.S. Borowski et al. (Editors), Proceedings of Ocean Drilling Program, Initial Reports, 164, College Station, Texas.

Shipboard Scientific Party, 2003. Leg 204 Summary. In: A.M. Trehu, G. Bohrmann, F.R. Rack, M.E. Torres, N.L. Bangs et al. (Editors), Proceedings of Ocean Drilling Program, Initial Reports, 204, College Station, Texas, pp. 1-75.

Sloan, E.D. and Koh, C.A., 2008. Clathrate Hydrates of Natural Gases. CRC Press, Boca Raton, 752 pp.

Smith, D.H., Wilder, J.W. and Seshadri, K., 2002. Methane hydrate equilibria in silica gels with broad pore-size distributions AIChE Journal. 48(2), 393-400.

Smith, S., Boswell, R., Collett, T., Lee, M. and Jones, E., 2006. Alaminos Canyon Block 818: A documented example of gas hydrate saturated sand in Gulf of Mexico. Fire In The Ice: NETL Methane Hydrate R&D Newsletter. 12.

Spangenberg, E., Kulenkampff, J., Naumann, R. and Erzinger, J., 2005. Pore space hydrate formation in a glass bead sample from methane dissolved in water. Geophysical Research Letters. 32(L24301), 1-4.

Stern, L., Circone, S., Kirby, S. and Durham, W.B., 2001. Anolamous preservation of pure methane hydrate at 1 atm Journal of Physical Chemistry B. 105, 1756-1762.

Stern, L., Kirby, S. and Durham, W.B., 1996. Peculiarities of methane clathrate hydrate formation and solid-state deformation, including possible superheating of water-ice. Science. 273, 1843-1848.

Stone, H.L., 1970. Probability model for estimating three phase relative permeability. Journal of Petroleum Technology. 22(2), 214-218.

Su, X., Song, C.B. and Fang, N.Q., 2006. Relationship between sediment granulometry and the presence of gas hydrate on Hydrate Ridge. In: A.M. Trehu, G. Bohrmann, M.E. Torres and F.S. Colwell (Editors), Proceedings of Ocean Drilling Program, Scientific Results, 204, College Station, Texas, pp. 1-30.

Sultan, N., Cochonat, P., Canals, M., Cattaneo, A., Dennielou, B. et al., 2004a. Triggering mechanisms of slope instability processes and sediment failures on continental margins: a geotechnical approach. Marine Geology. 213, 291-321.

Sultan, N., Cochonat, P., Foucher, J.P. and Mienert, J., 2004b. Effect of gas hydrates melting on seafloor slope stability. Marine Geology. 231, 379-401.

Sun, C.-Y., Chen, G.-J. and Yang, L.-Y., 2004. Interfacial tension of methane+water with surfactant near the hydrate formation conditions. Journal of Chemical Engineering Data. 49, 1023-1025.

Tan, B., Germaine, J.T. and Flemings, P.B., 2006. Data report: consolidation and strength characteristics of sediments from ODP Site 1244, Hydrate Ridge, Cascadia continental margin. In: A.M. Trehu, G. Bohrmann, M.E. Torres and

F.S. Colwell (Editors), Proceedings of Ocean Drilling Program, Scientific Results, 204, College Station, Texas.

Tohidi, B., Anderson, R., Clennell, M.B., Burgass, R.W. and Biderkab, A.B., 2001. Visual observation of gas hydrate formation and dissociation in synthetic porous media by means of glass micromodels. Geology. 29(9), 867-870.

Trehu, A.M., Long, P.E., Torres, M.E., Bohrmann, G., Collett, T.S. et al., 2004. Three-dimensional distribution of gas hydrate beneath southern Hydrate Ridge: constraints from ODP Leg 204. Earth and Planetary Science Letters. 222, 845-862.

Trehu, A.M., Torres, M.E., Bohrmann, G. and Colwell, F.S., 2006. Leg 204 Synthesis: Gas hydrate distribution and dynamics in the Central Cascadia Accretionary Prism Complex. In: A.M. Trehu, G. Bohrmann, M.E. Torres and F.S. Colwell (Editors), Proceedings of the Ocean Drilling Program, Scientific Results, 2004.

Uchida, T., Ebinuma, T., Takeya, S., Nagao, J. and Narita, H., 2002. Effects of pore sizes on dissociation temperatures and pressures of methane, carbon dioxide, and propane hydrates in porous media. Journal of Physical Chemistry B. 106, 820-826.

Uchida, T., Takeya, S., Chuvilin, E.M., Ohmura, R., Nagao, J. et al., 2004. Decomposition of methane hydrates in sand, sandstone, clays and glass beads. Journal of Geophysical Research. 109(B05206), 1-12.

US Department of Energy, 2007. http://www.netl.doe.gov/technologies/oil-gas/FutureSupply/MethaneHydrates/about-hydrates/estimates.htm,

Ussler, I.W. and Paul, C.K., 2001. Ion exclusion associated with marine gas hydrate deposits. In: C.K. Paul and W.P. Dillon (Editors), Natural Gas Hydrates: Occurrence, Distribution and Detection. American Geophysical Union, pp. 41-51.

Van Genutchen, M.T., 1980. A closed-form equation for predicting the hydraulic conductivity of unsaturated soils. Soil Science Society of America Journal. 44, 892-898.

Vogt, P.R. and Jung, W.Y., 2002. Holocene mass wasting on upper non-polar continental slopes - due to post-glacial ocean warming and hydrate dissociation? Geophysical Research Letters. 29(9), 55-1 - 55-4.

Waite, W.F., deMartin, B.J., Kirby, S.H., Pinkston, J. and Ruppel, C.D., 2002. Thermal conductivity measurements in porous mixtures of methane hydrate and quartz sand. Geophysical Research Letters. 29(24), 2229-2232.

Weinberger, J.L., Brown, K.M. and Long, P.E., 2005. Painting a picture of gas hydrate distribution with thermal images. Geophysical Research Letters. 32(L04609), 1-4.

Winters, W.J., 2000. Stress history and geotechnical properties of sediment from the Cape Fear Diapir, Blake Ridge Diapir and Blake Ridge. Ocean Drilling Program, Scientific Results. 164, 421-429.

Winters, W.J., Pecher, I.A., Waite, W.F. and Mason, D.H., 2004. Physical properties and rock physics models of sediment containing natural and laboratory-formed methane gas hydrate American Mineralogist. 89, 1221-1227.

Winters, W.J., Waite, W.F., Mason, D.H., Gilbert, L.Y. and Pecher, I.A., 2007. Methane gas hydrate effect on sediment acoustic and strength properties. Journal of Petroleum Science and Engineering. 56(1-3), 127-135.

Xu, W. and Germanovich, L.N., 2006. Excess pore pressure resulting from methane hydrate dissociation in marine sediments: A theoretical approach. Journal of Geophysical Research. 111(B01104), 1-12.

Xu, W. and Ruppel, C., 1999. Predicting the occurrence, dsitribution, and evolution of methane gas hydrate in porous marine sediments. Journal of Geophysical Research. 104(B3), 5081-5095.

Yun, T.S., Francisca, F.M., Santamarina, J.C. and Ruppel, C., 2005. Compressional and shear wave velocities in uncemented sediment containing gas hydrate. Geophysical Research Letters. 32(L10609), 1-5.

Yun, T.S., Narsilio, G.A. and Santamarina, J.C., 2007a. Physical characterization of core samples recovered from Gulf of Mexico. Marine and Petroleum Geology. In Press.

Yun, T.S., Santamarina, J.C. and Ruppel, C., 2007b. Mechanical properties of sand,silt and clay containing tetrahydrofuran hydrate. Journal of Geophysical Research. 112(B04016), 1-13.

Zatsepina, O.Y. and Buffett, B.A., 2001. Experimental study of the stability of CO2 hydrate in a porous medium. Fluid Phase Equilibria. 192, 85-102.

VITA

Name: Tarun Grover

Address: B-4/278, Sector – 8,
Rohini,
New Delhi – 110085
India

Email address: tgrover@tamu.edu

Education: B.En., Chemical Engineering, Panjab University, 2001
M.S., Chemical Engineering, University of Mississippi, 2004
Ph.D., Petroleum Engineering, Texas A&M University, 2008